Studies of Laminar and Turbulent Combustion Using Particle Image Velocimetry

By

Mohamed Elsayed Mohamed Hassan Morsy

B.Eng., M.Sc (Eng.)

Submitted in accordance with the requirements for the degree of Doctor of Philosophy

University of Leeds

School of Mechanical Engineering

November, 2019

Intellectual Property and Publication Statements

The candidate confirms that the work submitted is his own, except where work which has formed part of jointly-authored publications has been included. The contribution of the candidate and the other authors to this work has been explicitly indicated below. The candidate confirms that appropriate credit has been given within the thesis where reference has been made to the work of others.

- Sections 4.2 and 5.2 of this thesis is based on a jointly-authored journal paper: Bradley, D., Lawes, M., Morsy, M. E. (2019). Flame speed and particle image velocimetry measurements of laminar burning velocities and Markstein numbers of some hydrocarbons. Fuel, 243, 423-432. The candidate performed major tasks including experimental works, analysing and presenting the results. The other authors, Prof. Derek Bradley and Dr. Malcolm Lawes, helped the candidate by providing valuable technical discussions and guidance.

- Sections 4.3 and 5.3 of this thesis is based on a jointly-authored journal paper: Bradley, D., Lawes, M., Morsy, M. E. (2019). Measurement of Turbulence Characteristics in a Large Scale Fan-Stirred Spherical Vessel. Journal of Turbulence, 20(3), 195-213. The candidate performed major tasks including experimental works, analysing and presenting the results. Prof. Bradley and Dr. Malcolm Lawes helped the candidate by providing valuable discussion.

- Sections 4.4 and 5.4 of this thesis is based on a jointly-authored journal paper: Bradley, D., Lawes, M., Morsy, M. E. Flow fields induced by spherically turbulent expanding flames. Pending submission to Fuel Journal. The candidate performed major tasks including experimental works, analysing and presenting the results. Prof. Bradley and Dr. Malcolm Lawes helped the candidate by providing valuable discussion.

Acknowledgements

First of all, I would like to express my sincere gratitude to my supervisors, Prof. Derek Bradley and Dr. Malcolm Lawes for the continuous support of my PhD study and related research, for their patience, motivation and immense knowledge. It has been a privilege and pleasure to work alongside them both. Their immense contribution towards my academic, intellectual and professional development is truly unrivalled and always kept me on course.

Acknowledgement and thanks must also be given to Prof. Alexey Burluka for giving me the opportunity to study at Leeds. I also thank the British Council, Egyptian Educational Bureau in London, and University of Helwan for funding the four years of this study.

My thanks are also due to all of the staff in the Thermodynamics Laboratory, it has been a pleasure working with you all. Onto the technical staff in the Thermodynamics Laboratory, who without them, I would have not completed this work. A massive thank you must go to Mark Bachelor and Brian Leach for their support and assistance during the preparation of the experimental work.

Through this journey, there is no doubt family and friends have helped me a lot. Many thanks are due to all my fellow PhD-students: Moustafa Shehata, Ahmed Pervez, Jeong-Do Kim, Peter Zhang and Ben Thorne whom I have great regard for their friendship and assistance throughout my time at the University of Leeds and for making it somewhat entertaining. I look forward to continuing collaboration with them in the future.

A massive thank you must also go to my beloved parents; without your continuous support, encouragement and love throughout my life, I would never have reached this stage in the first place. Also, special thanks go to my lovely daughters, Linda and Asya. Finally, my deepest gratitude to my wife, Khloud. It is fair to say, without your support, understanding, patience, kindness and love, I honestly could not have done this. I will be forever grateful. Thank you for everything.

Abstract

In the quest to mitigate demand for conventional petroleum-derived transportation fuels and reduce their associated emissions of various pollutants, there are an increasing number of alternative fuels are being proposed. Employing such alternatives necessitates a comprehensive understanding and accurate measurement of their combustion characteristics for effective commercial deployment. Particle Image Velocimetry (PIV) is amongst the advanced experimental techniques now in use to improve our understanding of combustion. It was therefore installed and employed in the course of the present work. Such a technique can directly measure key combustion characteristics with high accuracy, under both laminar and turbulent conditions.

This PIV technique was employed first for measuring laminar burning velocities during flame propagation in spherical explosions, by the measurement of flame speed and gas velocity just ahead of the flame. Measurements made in this way are compared with those obtained solely from the flame speed method, which is based on the flame front propagation speed and the ratio of unburned to burned gas densities. Different values arose between the two methods. The principal reason was the common assumption in the flame speed method that the burned gas density is at the equilibrium, burned gas, adiabatic temperature value. When allowance is made for the effects of flame stretch rate and Lewis number on this density, the differences in burning velocities are significantly reduced. Burning velocities and Markstein numbers have been measured for methane, *i*-octane, ethanol, and *n*-butanol over a range of equivalence ratios at atmospheric pressure and, in the case of *n*-butanol, also over a range of pressures. In measuring Markstein numbers, there is a dependency upon the isotherm employed for the measurement of the stretch rate. This aspect was studied by comparing measurements with two different isotherms. It was concluded that the measured PIV flame measurements might under-estimate the Markstein numbers by about 12%.

The PIV technique was employed also to measure the turbulence characteristics of the flow in fan-stirred vessel, using dry air in the absence of phase change and chemical reaction. Since a knowledge of the aerodynamic characteristics of the turbulent flow enables better analysis of the flame/turbulence interactions. Spatial and temporal distributions of mean and root mean square, rms, velocity fluctuations are investigated,

as well as integral length scales, L, Taylor microscales, λ, and Kolmogorov length scales, η, in the fan speed range, 1,000-6,000 rpm. Mean velocities are about 10 % of the turbulence velocity, u'. Importantly, turbulence is close to homogeneous and isotropy in the central volume, although this volume decreases with increasing fan speed. Its radius and other characteristics are expressed in terms of the fan speed. Relationships are presented for the variations of u' and L with fan speed, temperature and pressure. A novel relationship between the autocorrelation function and integral length scale is obtained, for when Taylor's hypothesis is invalid.

Finally, changes induced in the turbulent flow fields by methane/air flames were measured at different experimental conditions. In measuring turbulent burning velocity in spherical explosions, allowance must be made for the transient changes in the rms turbulent velocity, to which the flame is exposed. This rms turbulent velocity was measured a head of flame front. The influences of pressure, temperature and equivalence ratio on its value were investigated and a novel empirical expression obtained.

Table of Contents

List of Figures

List of Tables

Nomenclature

A	m^2	Flame surface area
B	-	Spatial spectral filtering function
c_p	KJ/Kg.K	Specific heat
D	m^2/s	Thermal diffusivity
Da	-	Turbulent Damköhler number
D_{im}	m^2/s	Minority species diffusion coefficient
D_k	m	Kernel diameter
$E(k)$	-	Energy spectrum
f	rps	Rotational fan speed
i	-	Number of vector maps in time
K	-	Karlovitz stretch factor
Ka	-	Karlovitz number
$\underline{k}$	-	Wavenumber vector with a magnitude k
K_{cl}	-	Critical Karlovitz number
$\bar{k}_\eta$	-	Dimensionless wave number
k_n	1/m	Minimum effective wave number
$K_c,\ K_s$	-	Karlovitz curvature and strain rate factors
K_u, K_v	-	Kurtosis factors of the velocity probability distribution functions
L	m	Mean longitudinal integral length scale
L_b	m	Flame speed Markstein length
Le	-	Lewis number
l_G	m	Gibson scale
L_{cr},L_{sr}	m	Curvature and strain Markstein lengths, respectively, associated with u_{nr}
L_u	m	Markstein length for u_n
L_{ux}, L_{vy}	m	Longitudinal integral length scales related to the velocity components *u* and *v*
L_{uy}, L_{vx}	m	Lateral integral lengths related to the velocity components *u* and *v*
Ma	-	Markstein number
Ma_b	-	Flame speed Markstein number
Ma_{cr},Ma_{sr}	-	Curvature and strain Markstein numbers, respectively, associated with u_{nr}
n	-	Total number of grid nodes in the vector map
N_{im}	-	Total number of vector maps
N_i	-	Total number of sectors
n_k	-	Number of integral length scale
n_{kG}	-	Value of n_k for Gibson scale

N_p	-	Total number of velocity vectors in each sector
P	Pa	Initial pressure
Pe_{cl}	-	Critical Peclet number
Pr	-	Prandtl number
R	-	Correlation coefficient
r_{cl}	m	Critical flame radius
R_H	m	Limiting radius of homogeneity and isotropy
R_j	m	General spherical radius
R_L	-	Reynolds number related to the integral length scale
R_λ	-	Reynolds number related to the Taylor length scale
R_r	m	Flame root radius
R_t	m	Flame tip radius
r_u	m	Cold flame front radius
r_v	m	Radius for equal volumes
R_u, R_v	-	Temporal correlation coefficients related to the velocity components *u* and *v*
R_{ux}, R_{vy}	-	Longitudinal correlation coefficients related to the velocity components *u* and *v*
R_{uy}, R_{vx}	-	Lateral correlation coefficients related to the velocity components *u* and *v*
R_0		Correlation coefficient with value of 0 $(R = 0)$
s	m/s	Mean cold gas speed / dimensionless stretch rate
S		Flame speed factor
$\bar{S}$	m/s	Pseudo-convective velocity
$\bar{S}(\bar{k}_\eta)$	-	Non-dimensional power spectral density
$S_{k,u}, S_{k,v}$	-	Skewness factors of the velocity probability distribution functions
S_n	m/s	Stretched laminar flame speed
S_s	m/s	Unstretched laminar flame speed
S_t	m/s	Turbulent flame speed
t	s	Time
T_b	K	Adiabatic equilibrium burned gas temperature
$\bar{T}_b$	K	Burned gas mean temperature
T_u	K	Unburned gas temperature
u, v	m/s	Instantaneous velocity components in the $x-$ and $y-$ directions
u_η	m/s	Kolmogorov turnover velocity
$\bar{u}, \bar{v}$	m/s	Mean velocity components in the $x-$ and $y-$ directions
$\bar{u}_g$	m/s	Mean gas velocity within each sector
u', v'	m/s	Root-mean-square (rms) velocity fluctuations in the $x-$ and $y-$ directions
u'_k	m/s	Effective rms turbulent velocity
u'_s	m/s	Spatial rms turbulent velocity

u_g	m/s	Outwards gas velocity
u_l	m/s	PIV, unstretched laminar burning velocity, u_n at $\alpha = 0$.
u_{la}	m/s	Adiabatic density, unstretched laminar burning velocity
u_{lr}	m/s	PIV u_l with no radiative loss
u_{ls}	m/s	Density corrected, unstretched laminar burning velocity
u_n	m/s	Flame entrainment laminar velocity
u_N, v_N	m/s	Normalised velocities in the $x-$ and $y-$ directions
u_{nr}	m/s	Stretched laminar mass burning velocity expressing mass burning rate
U_r	m/s	Local radial gas velocity
u_{tr}	m/s	Turbulent burning velocity
$\bar{u}_x, \bar{u}_y$	m/s	Mean velocity components of $\bar{u}$ In the $x-$ and $y-$ directions
$\bar{v}_x, \bar{v}_y$	m/s	Mean velocity components of $\bar{v}$ In the $x-$ and $y-$ directions

Greek symbols

α	1/s	Flame stretch rate
α_{cl}	1/s	Critical stretch rate for flame instability
α_{cr}	1/s	Curvature strain rate
α_{sr}	1/s	Strain rate
γ		Ratio of specific heats
δ_l	m	Flame thickness
ε	m^2/s^3	Turbulence dissipation rate
η	m	Kolmogorov length scale
λ	m	Taylor length scale
λ_{th}	KJ/m.K.s	Thermal conductivity
μ	Kg/m.s	Dynamic viscosity
ν	m^2/s	Kinematic viscosity
φ	-	Equivalence ratio
Φ_{xx}	-	Ratio of true to measured spectral density tensors
ρ_b	Kg/m^3	Adiabatic burned gas density
$\bar{\rho}_b$	Kg/m^3	Mean burned gas density
ρ_u	Kg/m^3	Unburned gas density
τ	s	Integral timescale
τ_u, $\tau_{v,}$	s	Integral timescale related to the velocity components *u* and *v*
ξ	m	Spatial lag

Subscripts, superscripts and notation

b	Burned gas
cl	Critical
cr	Curvature

l	Laminar
i	Initial condition
r	Radial
sr	Strain
t	Turbulent / Tip radius
th	Thermal

Abbreviations

ADC	Analogue digital converter
CCD	Charge-coupled device
DNS	Direct numerical simulation
FSM	Flame speed method
GHG	Greenhouse gases
IA	Interrogation area
ND:YAG	Neodymium-doped yttrium aluminum garnet
LCD	liquid crystal display
LDV	Laser doppler velocimetry
PC	Personal computer
PID	Proportional integral derivative
PIV	Particle image velocimetry
PSD	Power spectral density
ROI	Region of interest
rms	Root mean square
TTL	Transistor-transistor logic

Chapter 1 - Introduction

1.1 General Overview and Motivation

Under the recent "Paris Agreement", more than 190 countries suggested ambitious goals to mitigate the negative consequences of climate change and agreed to reduce their greenhouse gas (GHG) emissions (UNFCCC, 2015, Herman, 2019). The agreement aims at a 60% reduction in GHG emissions by 2050 from transportation sectors, compared to the 1990 levels. The main obstacle is that most of transportation sectors depend mainly on the conventional petroleum derived fuels, due to their high energy density, relatively safe nature, abundant low cost supply and ease of transportation and storage. Combustion of such fuels is one of the major sources of carbon dioxide emissions (Davis et al., 2010, Stellingwerf et al. 2018, Batur et al., 2019). Therefore, the former goal of using 10% of renewable fuels in the transportation sectors by 2020 has been changed to a minimum share of 14% by the end of 2019, with an annual growth, until it reaches 27% by 2050. These renewable fuels can be partially, if not fully, substitute conventional petroleum derived fuels and hence reduce their associated GHG.

Accurate characterisation of the combustion performance for both conventional fuels and renewable fuels is essential, to study and exploring the possibilities of optimising existing engine technologies and diverting them to other potentially viable alternative fuels. These involve burn rates (both laminar and turbulent), ignition, flame propagation, flame instabilities, the effects of flame stretch, extinction and many other aspects. Although, considerable research has already been conducted in these aspects, the

understanding of them is still incomplete and often very challenging. One of the main reasons is the limitations of the available diagnostic techniques. With the improvement of technology and computer aided post-processing algorithms, it is becoming possible to study these aspects with high accuracy.

The present work is devoted to study both laminar and turbulent premixed combustion of a variety of hydrocarbon fuels. These include the promising alternative bio-alcohols, ethanol and *n*-butanol. Measurements were conducted in fan- stirred spherical combustion vessel, using high repetition rate particle image velocimetry (PIV) technique with advanced post-processing algorithm (hereafter referred to as "Adaptive PIV algorithm"). Such techniques allow direct measurements of combustion characteristics, which help in improving our understanding of combustion and developing the existing conventional methods of measurements. More details are provided in the following sections.

1.2 Laminar Burning Velocity

Laminar burning velocity is one of the most important parameters of a combustible mixture and its accurate experimental and computational determination is extremely important for developing and validating chemical kinetic mechanisms (Chen, 2015). It has been defined by Andrews and Bradley, (1972), as the velocity at which the flame front propagates normal to its surface, relative to the flow of the unburned mixture. Peters (2000) described it as a physio-chemical property of a flame that depends primarily upon the reaction chemical kinetics, molecular transport processes, equivalence ratio, unburned mixture temperature, and pressure.

Historically, much time has been devoted to perfecting methods of measuring stretched laminar burning velocities. An early critical review of laminar burning velocity described six different measurement techniques, including particle tracking, for measuring velocities, yet it omitted any treatment of flame stretch rate (Andrews and Bradley, 1972). At an early stage, it became apparent that more complete data on flow velocities, from particle tracking (Lindow, 1968) and hot wire anemometry (Bradley and Hundy, 1971), yielded values of laminar burning velocity that differed from those obtained from more traditional techniques. Later, Direct Numerical Simulations (Jayachandran et al., 2014) showed that burning velocities based solely upon schlieren measurements of flame speeds in strongly radiating spherical explosion flames would be

under-predicted, and would be more accurately measured with particle image velocimetry, PIV.

Dong et al. (2002) employed PIV in the flow configuration ahead of a stagnation plate, whilst Balusamy et al. (2011) employed it to measure the laminar burning velocities of propane/air mixtures in spherical explosion flames. Varea et al. (2012) also used such flames to measure laminar burning velocities and Markstein lengths of methane, ethanol and *i*-octane/air. Measurements of laminar burning velocity by this technique are not widespread because of the inherent experimental difficulties and necessary post-processing of a large number of data points. As a result, the spherical flame explosion technique, based solely on flame speed measurements, has become widely employed for this purpose. This flame speed method necessitates assumptions about the adiabatic density of the burned gas that are not required with PIV, which simultaneously measures the flame speed and gas velocity just ahead of the flame. The difference in these values gives a burning velocity that can yield a mass rate of burning. In addition, both the flame curvature and strain rate contributions to the flame stretch rate, α, can readily be found, as described in Chapter (2).

The present work reports PIV measurements in spherical explosions, from which burning velocities can also be derived from the flame speed measurements. The velocity measurements also enable entrainment and mass rate of burning velocities to be found, along with flame stretch rates and associated Markstein numbers. In the flame speed method of measuring burning velocity, it is often assumed that the burned gas density at zero stretch rate is that of an adiabatic flame under equilibrium conditions, ρ_b. This tends to be an under-estimation, giving burning velocities that are shown to be about 4-11 % low. A modification of this approach is developed, involving the burned gas density of the stretched flame, entirely in the regime of stable propagation, prior to the development of unstable flames at low stretch rate. In the stable regime, the mean burned gas density, $\bar{\rho}_b$, is larger than ρ_b, and depends on the stretch rate, α, and Lewis number, Le. There is little change in $\bar{\rho}_b$ before the instability develops. Values of $\bar{\rho}_b$ yield values of burning velocities that are closer to those determined by PIV. The PIV method provides more complete information on flame propagation and, consequently, more accurate data on burning velocities, the influences of flame stretch rates, the onset of flame instabilities, and radiative energy exchanges. Burning velocities are presented from both of the flame

speed methods, as well as the PIV-derived values for methane, *n*-butanol, *i*-octane and ethanol mixtures with air and, in the case of *n*-butanol, over a range of pressures.

The present work also develops a methodology for correcting burning velocities, measured by the flame speed method, due to it not having an adiabatic value of burned gas density. Normal strain rate laws and Markstein numbers are only applicable during the propagation of stable flames and a methodology for defining this regime is explained. Errors arise in the determination of Markstein numbers, if the temperature of the associated isotherm is too low (Giannakopoulos et al., 2015), and this effect is quantified. Results are presented in Chapter (4) and discussed in Chapter (5).

In the case of combustion studies of spherical explosions, the vessel and windows must be large enough for a stable flame to be established and observed at near constant pressure. However, this might affect the initial characteristics of the flow, especially when dealing with turbulent premixed combustion. Thus, turbulent flow characterization by means of spatial or temporal spectral analysis is essential, as a first step in investigating turbulent premixed combustion. This has been discussed in the following section.

1.3 Characterisation of Turbulence

Not infrequently, it is convenient to suppress high convective velocities, in order to facilitate experimental studies of the influences of turbulence on such phenomenon as phase changes, chemical reactions, generation of sprays, and flame propagation. A suitable vessel contains the turbulent liquid or gaseous mixture, with turbulence generated by one or more rotating fans. The detail that can be revealed in such a fan-stirred, probably spherical, vessel is also valuable, when considered in parallel with direct numerical simulations of the effects of such turbulence. Useful generalisation can be achieved for turbulence that is homogeneous and isotropic, and this has been widely discussed (Hwang and Eaton, 2004, Ravi et al., 2013). The mean flow should be minimal, with spatial and temporal uniformity of the rms turbulent velocity, u', and turbulent length scale, with near-Gaussian turbulent velocity probability density functions, pdfs, all with good control, quantification, and repeatability.

The use of fans to control the turbulence, in a mixture initially at rest, was pioneered by Schlossing and de Mondesir in 1864, see (Andrews et al., 1975). Some stages in the sequential development of this technique are indicated in Table 1.1, along with details of the different vessels. Semenov (1965) showed that four identical, eight-bladed fans,

symmetrically disposed within a closed volume, rotating at the same speed, generated a central region of uniform isotropic turbulence. Sokolik et al. (1967) employed this technique, in a vessel of about 97 mm radius and rms velocity of up to 10 m/s, with pressure records and flame photography, to measure turbulent burning velocities. Andrews et al. (1975) employed a cylindrical explosion vessel, with fan speeds up to 5,000 rpm and rms turbulent velocities, u', up to 4 m/s. Hot wire anemometry confirmed a high degree of isotropy. Abdel-Gayed et al. (1984), in measuring turbulent burning velocities, used laser Doppler velocimetry to measure u', and the turbulent length scales.

Table 1.1.1: Survey of some fan-stirred vessels, including present study.

	Vessel Geometry	Dimensions (mm)	No. of fans	Max. fan speed (rpm)	Max. u' (m/s)
Semenov, (1965)	Spherical	D = 97	4	7,000	10
Andrews et al. (1975)	Cylindrical	D = 305, l = 305	4	5,000	4
Fansler et al., (1990)	Cylindrical	D = 260, l = 260	4	2,500	2.2
Sick et al., (2001)	Spherical	D = 58	4	7,000	1.8
Weiß et al., (2008)	Spherical	D = 118	4	10,000	3.5
Ravi et al., (2013)	Cylindrical	D = 305, l = 356	4	8,300	1.7
Xu et al., (2017)	Cubic	l = 136	2	2,900	1.6
Present study	Spherical	D = 380	4	10,000	12

Hwang and Eaton (2004) created an approximately spherical Plexiglas chamber, with homogeneous, isotropic turbulence, generated by eight synthetic jet actuators. Two-dimensional particle image velocimetry, PIV, measured turbulent rms velocities of 0.87 m/s, corresponding to a Taylor microscale Reynolds number, R_λ, of 218. Bradley et al. (1992, 2003) showed the turbulent burning velocity and flame wrinkling rate to depend on turbulence statistics, such as u', and the turbulent length scales. The consistency of turbulent burning velocity measurements relies on the ability to attain near- isotropic and homogeneous turbulence, with well-defined turbulence statistics. More recently, Weiß et al. (2008) have employed a stainless steel cuboid vessel of 22.28 litres capacity, with eight variable speed fans. Turbulence characteristics were measured by both laser Doppler velocimetry, LDV, and PIV. Values of u' measured by PIV were up to 30% smaller than those measured by LDV. Ravi et al. (2013) employed four impellers, with different geometries, in a cylindrical vessel and measured rms turbulent velocities

between 1.2 and 1.7 m/s, using PIV. The high repetition PIV measurement technique yields more reliable temporal and spatial data. Xu et al. (2017) employed a cubic explosion vessel, with two opposed four bladed fans, giving maximum u' values of 1.6 m/s at 2,900 rpm. Characteristics were measured with PIV, and three sheet velocity fields were measured to reconstruct the 3D boundary of the homogenous region.

In the present work, the PIV was employed in one of the most comprehensive mapping of fan stirred vessels, to generate information about the turbulent velocity maps in the vessel and assess the turbulence data, for dry air in the absence of phase change and chemical reaction. Table 1.1 shows the current vessel to be relatively large, with large u'. So, the purpose was also to ensure the isotropy and homogeneity of the flow in this large vessel. The instantaneous and mean velocities maps are presented at different fan speeds, in the range 1,000-6,000 rpm, in Chapter (4). Temporal and spatial characteristics of the flow are derived from these maps and discussed in Chapter (5).

1.4 Turbulent Burning Velocity

Burners and combustion vessels have been widely employed for investigating turbulent combustion and measuring turbulent burning velocities. For burners, turbulence can be generated with the aid of grids, such as plates with arrays of cross tubes and small holes. It has been possible to measure the turbulent burning velocity, u_{tr}, in this way for a range of hydrocarbon fuels at various conditions (Bédat and Cheng, 1995, Smallwood et al., 1995, Shy et al., 2000, Cheng et al., 2002, Gülder, 2007). A disadvantage of this technique is that u' with which u_{tr} is correlated, decays downstream of the turbulence generators. This can be avoided if measurements are conducted in combustion vessels, where also constant pressure combustion can be achieved for measurements initiated by central ignition. A disadvantage of combustion vessels is that allowance must be made for the transient changes in the effective rms turbulent velocity, to which the flame is exposed. Based on the original study by Abdel-Gayed et al. (1987), Bradley et al. (2009) developed and presented an expression of this rms velocity, called u'_k. It has been derived from one-dimensional cold flow measurements, by integrating the associated power spectral density, PSD, between the limiting wave numbers, as described in Section 2.4.3.

Because of the difficulties in measuring turbulence, and characterising it, ahead of the flame in explosions, the turbulence is often measured prior to explosion. Peters (2000) has shown that the turbulence distribution can be altered significantly by the explosion. In the present work, the PIV technique was employed to directly measure the rms

turbulent velocity ahead of methane/air flames at different experimental conditions (hereafter referred to as u_s'). An empirical expression of u_s' has been developed and presented in Chapter (5), where also the variations of u_{tr} with u_s' are presented and discussed.

1.5 Aims and Objectives

The main aim of the present work is to perform a fundamental study of both laminar and turbulent premixed combustion of a variety of hydrocarbon fuels, using high repetition rate particle image velocimetry (PIV). The objectives may be summarised as follows:

- Installing PIV system, suitable for performing both laminar and turbulent studies.
- Developing a methodology for correcting burning velocities, measured by the flame speed method, due to it not having an adiabatic value of burned gas density.
- Developing a methodology for calculating the strain and curvature Markstein numbers associated to the mass rate of burning.
- Estimate the errors arise in the determination of Markstein numbers, due to using different isotherms.
- Performing measurements of laminar burning velocities and associated Markstein numbers for promising alternative bio-alcohols, ethanol and *n*-butanol.
- Generating information about the turbulent velocity maps in the vessel and assess the turbulence data
- Ensure the isotropy and homogeneity of the flow in the vessel.
- Studying the flame/flow interaction, using methane/air mixtures.
- Developing an empirical expression of the effective rms turbulent velocity, to which the flame is exposed.

1.6 Thesis Outline

This thesis consists of six chapters, Chapter (1) has presented an introduction on the background and motivation of the study, introducing the main aspects of it.

Chapter (2) presents the different techniques used to scrutinise the laminar and turbulent flames as well as the cold flow. Furthermore, a review of the uncertainty in the measurements due to using the conventional methods is presented.

Chapter (3) describes the experimental apparatus, operating techniques and data processing, including the methods used to measure flames radii and the associated image

processing. The adaptive PIV algorithm, used to obtain the flow velocity vector maps, is also described and presented.

Chapter (4) presents the key derived results obtained from the experimental work and an analysis of these results is given in Chapter (5), along with a comparison of these with the literature.

Chapter (6) concludes the main discussions and findings along with recommendations for future work.

Chapter 2 – Laminar and Turbulent Premixed Flames

2.1 Introduction

This chapter is broadly split into three main sections, the first dealing with laminar premixed flames, the second with turbulence characterisation and the third with turbulent premixed flames. The aim of the first section is to introduce the concepts and assumptions surrounding the structure of laminar premixed flames and the determination of the unstretched laminar burning velocity, u_{la}. The study of laminar flames is important, their understanding serves as a vital prerequisite to the study of turbulent combustion, in which stretched laminar flamelets are considered in turbulent flows. The aim of the second and third sections, and indeed this research as a whole, is to discuss how turbulence affects the manner in which flames propagate and vice versa. The reason of this interest is that many real systems, such as internal combustion engines and industrial burners, operate in a turbulence environment. Increasing understanding of this interaction between flame and flow will aid optimisation of the efficiency and functionality of these systems.

2.2 Laminar Premixed Flames

The most simplistic form of flame propagation is that of the premixed laminar flames. A preliminary description of the structure of such flames was first investigated by Mallard and Le Chatelier (1883). They assumed that the controlling mechanism for flame propagation was the conduction of heat from the hot gas to the entrainment

unburned cold mixture. Their analysis concluded that the laminar flame speed was a function of the square root of the product of the unburned mixture thermal diffusivity, the reaction rate and the temperature gradient through the flame. In 1938, Zel'dovich and Frank-Kamenetskii (1938a) highlighted the effect of molecular diffusion of the reactants, alongside thermal conduction, on the laminar burning velocity and further introduced a flame temperature dependent reaction rate. Great attention was then paid to the flame chemistry, especially with the growing understanding of complex chain reactions with the intrinsic formation and consumption of intermediate radicals, as a result of the seminal studies of Semenov (1935) and Hinshelwood (1940). Later, an analytical expression for laminar burning velocity was derived by Zel'dovich and Barenblatt (1959).

Now, laminar burning velocities can be determined either numerically or experimentally. Many numerical methods, with detailed chemical kinetics, have been employed to compute it (Maas and Pope, 1994, Davis et al., 2002, Anupam et al., 2006), especially after the pioneering work of (Dixon-Lewis, 1967, Spalding and Stephenson, 1971 and Warnatz, 1981). Experimentally, several techniques have been employed to measure the laminar burning velocity, such as *spherical combustion vessels* (Aung et al., 1995, Bradley et al., 1998, Gu et al., 2000, Tanoue et al., 2003, Jerzembeck et al., 2009, Eisazadeh et al., 2011, Hinton et al., 2018), *counter flow stagnation burners* (Egolfopoulos et al., 1989, Vagelopoulos and Egolfopoulos, 1998, Dong et al., 2002, Huang et al., 2004) and *flat flame burners* (Maaren et al., 1994, Coppens and Konnov, 2008, Hermanns et al., 2010).

Spherical combustion vessels have a distinct advantage, over counter flow stagnation burners and flat flame burners, which is the potential for the laminar burning velocity measurements at elevated pressures and temperatures close to those encountered in internal combustion engines. Also, igniting a quiescent, premixed, homogenous mixtures in the centre of such vessels creates an outwardly propagating spherical flame, which is very similar to flame propagation in spark ignition engines. This technique was employed in the present work. Detailed description of the vessel and its auxiliary systems can be found in Chapter (3).

The following subsections describe the structure of the laminar premixed flames (Section 2.2.1), laminar flame thickness (Section 2.2.2), laminar flame instabilities (Section 2.2.3) and finally the extraction of the laminar burning velocities from the experimental measurements (Section 2.2.4).

2.2.1 Structure of Laminar Premixed Flames

The structure of premixed laminar flames can be computed numerically for most fuels. This includes the temperature and species concentration profiles, using complete chemical kinetics with knowledge of the associated thermodynamic and molecular transport properties. Figure 2.1 shows an example of a computed composition and temperature profiles through a one dimensional adiabatic premixed CH_4/air laminar flame at 0.1 MPa and 300 K (Turns, 1996). The flame structure consists of four zones: the cold reactants zone, the preheat zone, a reaction zone and finally the products zone. The preheat zone is dominated by heat conduction and mass diffusion of the reactants, whilst, the reaction zone is dominated by chemical reaction and mass diffusion. The reactants are initially at the unburned gas temperature, T_u. This temperature increases in the preheat zone, due to conductive heat transfer from the reaction zone, until the adiabatic burned gas temperature, T_b, is attained in the product zone. The temperature profile is non-linear, due to the nonlinear heat release and transport process. The continuous heating of the reactants eventually leads to their reaction at an increasing rate.

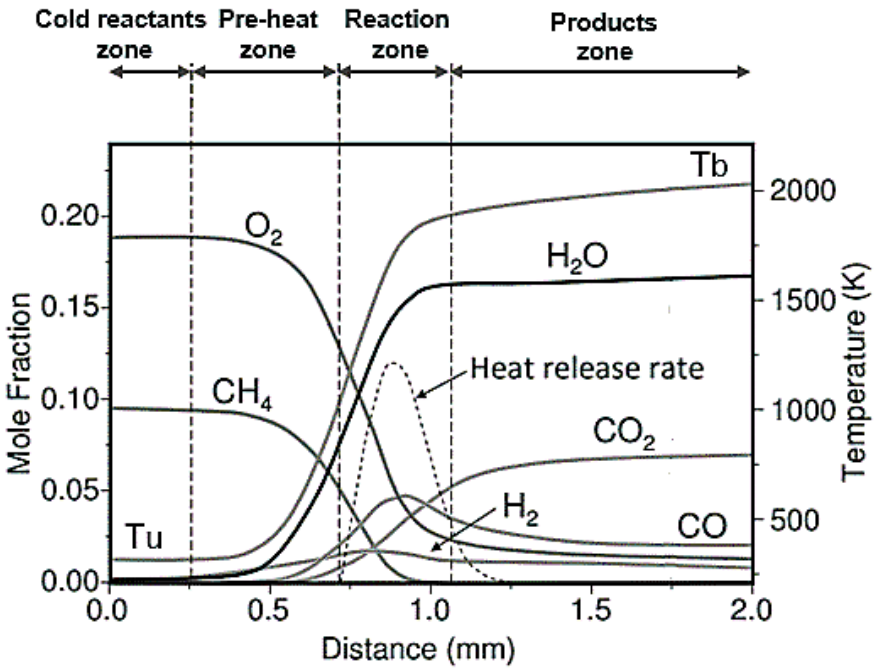

Figure 2.1: Computed composition and temperature profiles for a one dimensional adiabatic premixed laminar flame of a stoichiometric methane/air mixture at 0.1 MPa and 300 K (Turns, 1996).

When looking at premixed laminar flames, the flame thickness, δ_l, is one of the most important quantities to analyse such flames. There are many different definitions of δ_l (Gillespie et al., 2000; Haq, 1998; Poinsot and Veynante, 2005, Palacios and Bradley, 2017). It may be described as the distance between the completely unburned gas, at T_u, and the completely burned gas, at T_b (Gillespie et al., 2000). However, it is difficult to accurately quantify this distance because the change from the unburned gas to the burned gas occurs gradually, often over several millimetres, as shown in Fig. 2.1. Bradley et al. (2018) proposed an accurate expression of δ_l. They defined it as a hydrodynamic length given by:

$$\delta_l = \left(\frac{\nu}{u_l}\right)/Pr. \tag{2.1}$$

Where ν is the mixture kinematic viscosity, u_l is the unstretched laminar burning velocity and Pr the Prandtl number. The values of ν and Pr can be obtained at the unburned gas temperature using the Gaseq code (Morley, 2005).

2.2.2 Flame Stretch Rate

Spherical non-planar flames are subjecting to a transverse and tangential velocity components, together with flame curvature, that "stretch" the flame surface. This affects the species concentration and the gradients of temperature through the flame, and subsequently, the laminar burning velocity (Matalon, 1983, Williams, 1985, Bradley et al., 1992, Aung et al., 1997). The phenomenon of the flame stretch and its effect on flame extinction were first investigated by Karlovitz et al. (1953), followed by a study of Markstein (1964) who investigated the relationship between stretch and flame curvature. Later, the overall stretch rate, α, of a spherical explosion flame was expressed by (Williams, 1985) as:

$$\alpha = \frac{1}{A}\frac{dA}{dt} = \frac{2}{r_u}\frac{dr_u}{dt} = \frac{2}{r_u}\,S_n, \tag{2.2}$$

Where S_n is the stretched flame speed, which can be found from the measured radii of the cold front of the flame, r_u, versus time data as:

$$S_n = \frac{dr_u}{dt}, \tag{2.3}$$

Candel and Poinsot (1990) and Bradley et al. (1996) have shown that it is convenient to split the overall stretch rate, α, into two contributing components, one due to the flow field aerodynamic strain, α_{sr} and the other due to flame curvature, α_{cr}. Figure 2.2 shows a description of normal and tangential straining on a flame, represented as a thin sheet, moving at S_n in the laboratory frame and surrounded by fresh gas at the velocity u_g. From a kinematic perspective, it is possible to express the global parameter, α, as:

$$\alpha = \alpha_{sr} + \alpha_{cr}. \tag{2.4}$$

with

$$\alpha_{sr} = -\vec{n}\vec{n}.\nabla u + \nabla.\vec{u}$$

and

$$\alpha_{cr} = u_n \nabla.\vec{n}.$$

Here u and u_n, are, respectively, the local fluid velocity and the burning velocity normal to the flame surface, with n a unit vector normal to the surface directed from the burned to the unburned side.

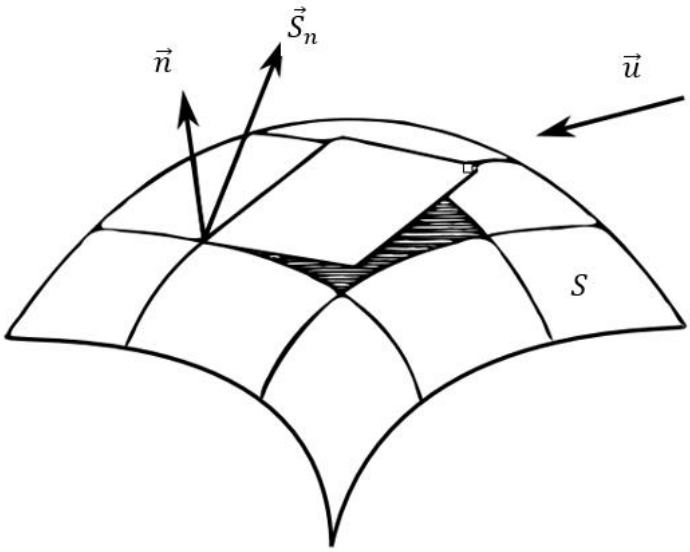

Figure 2.2: Schematic of a surface submitted to strain and curvature.

In spherical coordinates, $(r, \theta, \emptyset)$the components of n and u are written as (n_r, n_θ, $n_\emptyset$) and (u_r, u_θ, $u_\emptyset$), respectively, then

$$\alpha_{sr} = \left[n_r^2 \left(\frac{\partial u_r}{\partial r}\right) + n_\theta^2 \left(\frac{1}{r}\frac{\partial u_\theta}{\partial \theta} + \frac{u_r}{r}\right) + n_\emptyset^2 \left(\frac{1}{r\,sin\,\theta}\frac{\partial u_\emptyset}{\partial \emptyset} + \frac{u_r}{r} + \frac{u_\theta cot\theta}{r}\right) \right.$$
$$+ n_r n_\theta \left(\frac{\partial u_\theta}{\partial r} + \frac{1}{r}\frac{\partial u_r}{\partial \theta} - \frac{u_\theta}{r}\right) + n_r n_\emptyset \left(\frac{\partial u_\emptyset}{\partial r} + \frac{1}{r\,sin\,\theta}\frac{\partial u_r}{\partial \emptyset} - \frac{u_\emptyset}{r}\right)$$
$$+ n_\theta n_\emptyset \left(\frac{1}{r}\frac{\partial u_\emptyset}{\partial \theta} + \frac{1}{r\,sin\,\theta}\frac{\partial u_\theta}{\partial \emptyset} - \frac{cot\,\theta}{r}u_\emptyset\right) + \frac{1}{r^2}\frac{\partial (r^2 u_r)}{\partial r}$$
$$\left. + \frac{1}{r\,sin\,\theta}\frac{\partial (u_\theta\,sin\,\theta)}{\partial \theta} + \frac{1}{r\,sin\,\theta}\frac{\partial u_\emptyset}{\partial \emptyset} \right],$$

$$\alpha_{sr} = u_n \left[\frac{1}{r^2}\frac{\partial (r^2 n_r)}{\partial r} + \frac{1}{r\,sin\,\theta}\frac{\partial (n_\theta\,sin\,\theta)}{\partial \theta} + \frac{1}{r\,sin\,\theta}\frac{\partial n_\emptyset}{\partial \emptyset} \right],$$

For an outward propagating flame, the burning velocity, u_n, is associated with the cold flame front surface and the gas velocity ahead of it is u_g. The flame speed, S_n, is equal to, $u_g + n_r u_n$ (Bradley et al., 1996) with $n_\theta = n_\emptyset = 0$ and $u_r = u_g$, $u_\theta = u_\emptyset = 0$. Hence,

$$\alpha_{sr} = -n_r^2 \left(\frac{\partial u_r}{\partial r}\right) + \frac{1}{r^2}\frac{\partial (r^2 u_r)}{\partial r} = 2\frac{u_g}{r_g}, \tag{2.5}$$

and

$$\alpha_{cr} = u_n \frac{1}{r^2}\frac{\partial (r^2 n_r)}{\partial r} = 2\frac{u_n}{r_u}. \tag{2.6}$$

Here u_g is the maximum outwards gas velocity component, normal to the flame and u_n is the stretched laminar entrainment velocity.

2.2.3 Flame Instabilities

The flame instabilities were first investigated by Darrieus (1938) and later by Landau (1944). They recognized the inevitability of hydrodynamic instability in a planar laminar flame and introduced the seminal framework for analysis of the Darrieus-Landau (D-L) instability. This instability is created by hydrodynamic disturbances, due to the propagation of the flame as a wave of density discontinuity. The interaction between the hot expanding products and the generated vortices within the reaction zone of the flame, are the responsible for creating such disturbance. The disturbance converge and diverge

the streamlines of oncoming cold gases which create a localized pressure changes. The gradients of these pressure changes sustain the original disturbance of the planar front, wrinkling the flame front (Ivashchenko and Rumyantsev, 1978). Figure 2.3 shows the effect of such wave-like disturbance of a planar flame front. The reactants enter the convex flame front section (on the right side), and slow their flow through divergence. Similarly, the reactants enter the concave flame front section (on the left side), causing a contrasting receding effect. Although, the burning velocity remains constant, a dynamic imbalance is induced which increases the protrusion within the flame. This can lead to deforming the flame surface area, such that its area increases and subsequently increases the mean overall burning velocity (Tripathi, 2012).

The hydrodynamic instabilities might be stabilised, or further destabilised, by thermal and mass diffusive mechanisms. The ratio of the thermal and mass fluxes being represented by the Lewis number, ($Le = \lambda_{th}/\rho D_{im} c_p$), which can indicate whether a flame is stable or unstable. For Le < 1, the mass diffusion dominates the flow, which is indicative of an unstable flame. As shown from Fig. 2.3, at the crest convergence of the flame front, the increase in energy is converged into the flame which increase the local enthalpy and burning velocity. In contrast, for Le > 1, the thermal diffusion predominates over the conductive diffusion, which is indicative of a stable flame. At the trough, divergence to the flame front occurs resulting in a reduced burning velocity that stabilises and smoothes the flame surface.

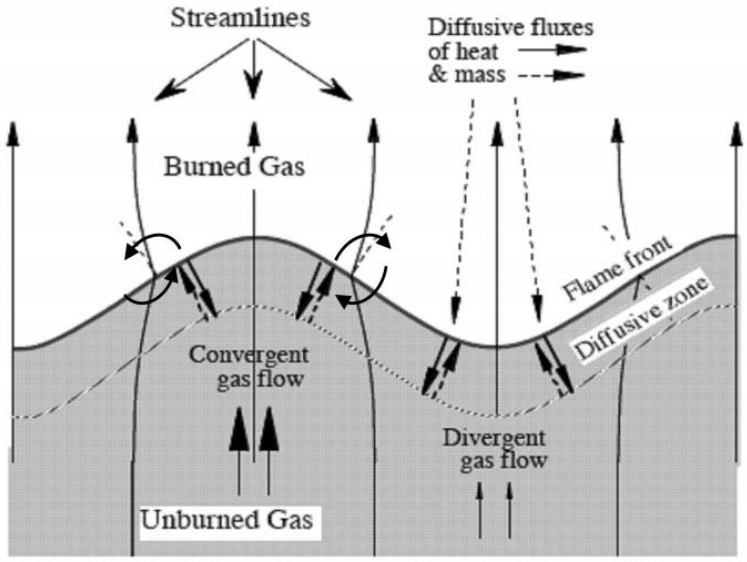

Figure 2.3: Structure of a wrinkled flame front, showing the hydrodynamic streamlines and the diffusive fluxes of heat and mass (Searby, 2004).

At an early stage of flame propagation, the flame is subjected to a high stretch rate due to the relatively low flame surface area and the boost from residual spark energy. This high level of stretch helps in smoothing out any wrinkling of the flame surface up to a critical radius, r_{cl}, where the flame stretch is no longer sufficient to stabilise the flame structure (Gillespie et al. 2000). Beyond this radius, flame instabilities create a cellular flame structure (Bradley and Harper, 1994). An example of schlieren photographs of a stable flame and that of un-stable flame with high cellularity is shown in Fig. 2.4, for stoichiometric *i*-octane/air mixtures at 360 K (Mumby, 2016). The high cellularity increases the flame surface area, resulting in a relative increase in S_n (Bechtold and Matalon, 1987, Beeckmann et al., 2018).

The transition to cellularity can be quantified by the critical Karlovitz number, K_{cl}, as (Bradley et al., 2018):

$$K_{cl} = \alpha_{cl}\delta_l/u_l. \tag{2.7}$$

Here δ_l is the flame thickness, given by Eq. (2.1) and α_{cl}, = $(2/S_n).r_{cl}$, is the critical stretch rate, at which S_n rapidly deviates from its prior response to stretch. Beyond K_{cl}, the burned Markstein length, L_b, is meaningless, because S_n increases due to the flame instabilities. L_b can only be accurately measured in the stable regime, between the minimum un-affected spark radius and the onset of cellularity, at the critical radius, r_{cl}. This stable regime becomes increasingly limited with increasing the equivalence ratio and the initial pressure, as shown from Fig. 2.5 (Bradley et al., 2009). This figure shows the variation of S_n with α for ethanol/air mixture, with φ = 0.9 at 358 K for three different pressures 0.1, 0.7 and 1.0 MPa . Limits of stable, developed flame indicated by # and *. At high pressures ($\geq$ 1.2 MPa), the instability can nearly occur immediately after ignition, hence, the measurement of, L_b and u_l, becomes impossible. This has not been happened during the present study as the maximum pressure was 0.5 MPa.

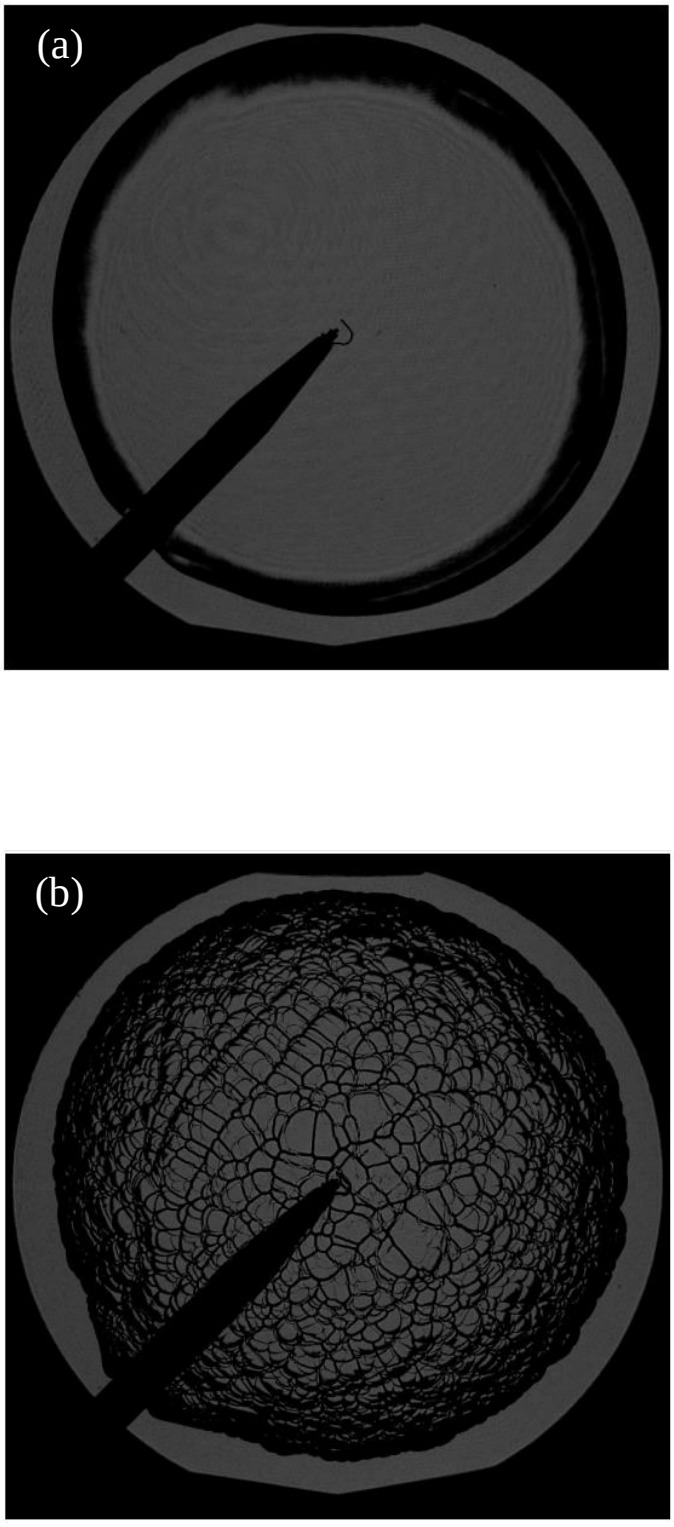

Figure 2.4: Schlieren images of *i*-octane/air mixture, at r_u = 65 mm, φ = 1.0, 360 K and (a) 0.1 MPa, (b) 1.0 MPa (Mumby, 2016).

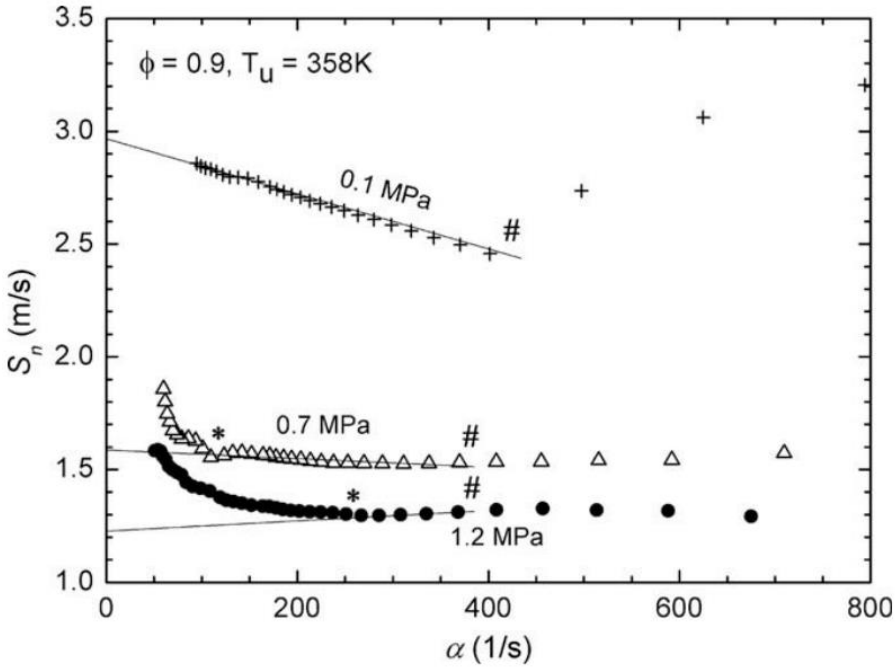

Figure 2.5: Variation of flame speed, S_n, with flame stretch rate, α, for ethanol/air mixture, with φ = 0.9 at 358 K for three different pressures 0.1, 0.7 and 1.0 MPa (Bradley et al., 2009).

2.2.4 Determination of Laminar Burning Velocities

Laminar burning velocity can be calculated by solving governing conservation equations for the overall mass, species, and temperature (Poinsot and Veynante, 2001) assuming:

- Planar unstretched flame (1-D), constant area, steady flow
- Neglect: kinetic and potential energy, viscous shear work, thermal radiation
- Constant pressure (neglect small pressure difference across flame)
- Diffusion of heat governed by Fourier's law
- Diffusion of mass governed by Fick's law (binary diffusion)
- Lewis number unity
- Individual specific heats are equal and constant
- Fuel and oxidizer form products in a single-step exothermic reaction
- Oxidizer is present in stoichiometric or excess proportions; thus, the fuel is completely consumed at the flame.

The following subsections describe two methods for measuring the unstretched laminar burning velocity, namely flame speed method (FSM) and particle image

velocimetry (PIV) method. These methods were employed in the present work, for measuring the laminar burning velocity of some hydrocarbons.

2.2.4.1 Flame Speed Method (FSM)

For all modes of spherical flame propagation, the rate of burning is expressed as the rate of consumption of reactants at an initial unburned gas density ρ_u, and radius r_u, with an associated burning velocity, u_n (Bradley et al., 1996):

$$\frac{dm_u}{dt} = -4\pi r_u^2 \rho_u u_n. \tag{2.8}$$

Where m_u is the mass of unburned gas. For an explosion:

$$\frac{dm_u}{dt} = -\frac{d}{dt}\left(\int_0^{r_u} -4\pi r_u^2 dr\right) \tag{2.9}$$

where ρ is the density at radius, r. From Eqs. (2.8) and (2.9),

$$u_n = \frac{1}{r_u^2 \rho_u}\frac{d}{dt}\left(\int_0^{r_u} r^2 \rho\, dr\right). \tag{2.10}$$

A mean density, $\bar{\rho}_b$, is defined for the gas within the radius r_u as

$$\bar{\rho}_b = \frac{\int_0^{r_u} 4\pi r^2 \rho dr}{\int_0^{r_u} 4\pi r^2 dr} = \frac{3\int_0^{r_u} r^2 \rho dr}{r_u^3} \; and \; u_n = \frac{\bar{\rho}_b}{\rho_u} S_n + \frac{r_u}{3\rho_u}\frac{d\bar{\rho}_b}{dt}. \tag{2.11}$$

In Eq. 2.11 the gas within the sphere of radius r_u might be regarded as comprised of a mixture of burned gas at its adiabatic temperature, with a density of ρ_b, and unburned gas with a density of ρ_u. Thus at a radius r and density ρ, the fraction of burned and unburned gas can be expressed as $(\rho - \rho_u)/(\rho_b - \rho_u)$ and $(\rho_b - \rho)/(\rho_b - \rho_u)$, respectively, enabling Eq. 2.10 to be written as

$$u_n = \frac{1}{r_u^2 \rho_u}\frac{d}{dt}\left(\int_0^{r_u} r^2 \rho_u \left(\frac{(\rho_b - \rho)}{(\rho_b - \rho_u)}\right) dr + \int_0^{r_u} r^2 \rho_b \left(\frac{(\rho - \rho_u)}{(\rho_b - \rho_u)}\right) dr\right). \tag{2.12}$$

The first term on the right represents the rate of entrainment by the flame front of gas that remains unburned, the second the rate of formation of burned gas. Whereas u_n is a burning velocity that expresses the rate of entrainment of cold unburned gas by the flame front, the second term expresses the rate of appearance of completely burned gas behind the front. A burning velocity might thus be defined that is associated solely with the latter. Designated by u_{nr}, it is

$$u_{nr} = \frac{1}{r_u^2 \rho_u} \frac{d}{dt} \left(\int_0^{r_u} r^2 \rho_b \left(\frac{(\rho - \rho_u)}{(\rho_b - \rho_u)} \right) dr \right). \quad (2.13)$$

As stated by Bradley et al. (1996), the mass burning velocity, u_{nr}, excludes the changing amount of unburned gas within the flame thickness. The effect of flame thickness is significant high at the early stages of flame development. As burning velocities u_n and u_{nr} approach the unstretched burning velocity, u_l, the flame spherical surface geometrically approaches the planar one. Geometrically, for a non-planar spherical flame, the previous stretched burning velocities arise because the formation mass rate of burned gas at the inner surface of the flame front differs from the mass of unburned gas entrained into the flame front.

From Eqs. (2.12) and (2.13),

$$u_n = u_{nr} + \frac{1}{r_u^2 \rho_u} \frac{d}{dt} \left(\int_0^{r_u} r^2 \rho_u \left(\frac{(\rho_b - \rho)}{(\rho_b - \rho_u)} \right) dr \right). \quad (2.14)$$

Also invoking Eq. (2.10), it can be shown

$$u_{nr} = (S_n - u_n) \left(\frac{\rho_u}{\rho_b} - 1 \right)^{-1} = u_g \left(\frac{\rho_u}{\rho_b} - 1 \right)^{-1}. \quad (2.15)$$

A stable flame takes time to develop from the initiating spark plasma. Whilst the flame is developing with a small radius, r_u, $\bar{\rho}_b$, is higher than the density of the adiabatically burned equilibrium gas, ρ_b, at a temperature, T_b. Measurements of u_n should be only made, at constant pressure, after a stable flame had become established. With continuing flame growth, the final term in Eq. (2.11) decreases and finally becomes negligible. During this time, this changing condition is expressed by a flame speed factor, S, (Bradley et al., 1996):

$$S = u_n \rho_u / S_n \rho_b \,, \quad (2.16)$$

S starts with a value of about 2 and diminishes towards unity as $\bar{\rho}_b$, in Eq. (2.11), decreases and approaches ρ_b (Bradley et al., 1996). With the flame stretch rate approaching zero, the flame speed approaches a stretch-free value of S_s, with the burning velocity, u_{la}. Neglecting radiative heat transfer from the burned gas, its density at the adiabatic equilibrium temperature of, T_b, in Eq. (216) yields, $S = 1$ and a laminar burning velocity:

$$u_{la} = (\rho_b/\rho_u)S_s, \tag{2.17}$$

Markstein (1964) and Clavin (1985) suggested a linear relationship between S_n and α, with L_b the gradient. They assumed that the flame is planar, has small stretch rate and under adiabatic conditions. Extrapolation of this relationship to $\alpha = 0$, then yields a theoretical stretch-free flame speed, S_s:

$$S_s - S_n = L_b\alpha, \tag{2.18}$$

This linear relationship can be used when the influence of the stretch rate is small, such that the deviation from the measured S_n values to that of S_s is correspondingly small. The deviation between S_n and S_s can be large for flames subjected to high degrees of stretch. In such a case, flames can exhibit nonlinear behaviour between S_n and α, leading to erroneous over estimations of S_s. A relationship was presented by Kelley and Law (2009) from the seminal work of Ronney and Sivashinsky (1989), for flames exhibiting nonlinear S_n and α behaviour. This relationship was expressed as:

$$\left(\frac{S_n}{S_s}\right)^2 ln\left(\frac{S_n}{S_s}\right)^2 = -2\frac{L_b\alpha}{S_s}. \tag{2.19}$$

Giannakopoulos et al. (2015) and Beeckmann et al. (2018) computed the effect of the type of extrapolation on S_s. Figure 2.6 shows such effect on the measurement of S_s for methane/air mixture, at 0.1 MPa and 298 K for three equivalence ratios 0.8, 1.0, and 1.2 (Beeckmann et al., 2018). For flame radii less than 1 cm, the stretch rate effect is high and the flame exhibits a nonlinear behaviour, regardless of the isotherm temperature. In such case, the nonlinear relationship, Eq. (2.19), must be used to obtain S_s. For flame radii higher than 1 cm, the flame exhibits a linear behaviour with no effect of the isotherm temperature. In the present work, flame images were obtained through windows of 150 mm diameter (Chapter 3), enabling flame radii to be measured up to 60 mm, after a stable flame had been established at a radius of about 10 mm. For this range, Fig. 2.6 suggests no effect of the extrapolation type on S_s.

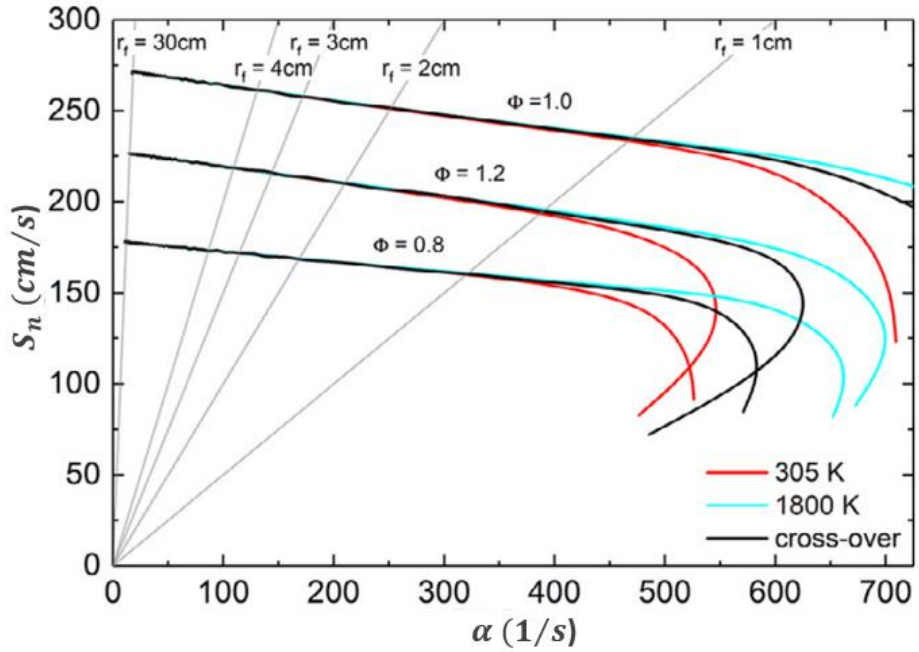

Figure 2.6: Shows the effect of stretch rate, selected flame radii, r_f and extrapolation type on S_s, using methane/air mixture at 0.1 MPa and 298 K for three equivalence ratios 0.8, 1.0, and 1.2. For such case, the crossover temperature from chain-branching to chain-breaking is 1300 K (Peters, 2000)

The influence of the stretch rate upon u_{nr} was expressed by Bradley et al. (1996) in the form of the linearised relationship:

$$u_l - u_{nr} = L_{sr}\alpha_{sr} + L_{cr}\alpha_{cr}, \tag{2.20}$$

Where L_{sr} and L_{cr} are the Markstein lengths, associated to the strain and curvature stretch rates, respectively. Numerical methods were proposed by Bradley et al. (1996) and Giannakopoulos et al. (2015) to calculate L_{sr} and L_{cr}. In recent years, most measurements of u_l have also included measurements of Markstein numbers to express the effect of the stretch. These numbers can be obtained by normalising the Markstein lengths L_{sr} and L_{cr} with the laminar flame thickness, given by Eq. (2.1). Also for the derivation of accurate Markstein numbers, the isotherm upon which α is based in Eq. (2.2) should be closer to the burned gas, than to the unburned gas temperature (Giannakopoulos et al., 2015).

2.2.4.2 Particle Image Velocimetry (PIV) Method

Figure 2.7 shows that, the basic PIV velocities can be kinematically related by:

$$u_n = S_n - u_g, \tag{2.21}$$

Where u_n is the stretched laminar entrainment velocity, S_n, the stretched flame speed given by Eq. (2.3), and u_g the maximum outwards gas velocity component, normal to the flame (Groot and De Goey, 2002, Balusamy et al. 2011). The value of u_g can be obtained directly from the PIV measurements, as explained in Section 4.2.2.

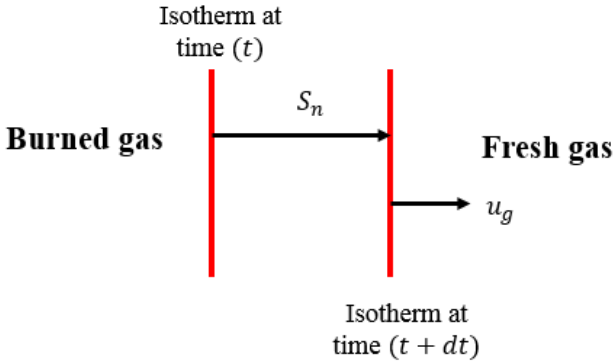

Figure 2.7: Illustration of flame layers and corresponding velocities.

Groot and De Goey, (2002) computed the gas velocity variation throughout a spherically expanding flame and plotted it as a function of the local radius. Figure 2.8 shows such a variation for methane/air mixture at 0.1 MPa and 305 K. The inner reaction layer is located at a flame radius, r, of 10 mm. The unburned gas velocity varies from a minimum close to the reaction zone to a maximum near the preheat zone, identified in (Eq. 2.21) by the term u_g, due to the variation of density through the flame front. Detailed description of the procedures used in the present work to obtain u_g, experimentally from the PIV data, can be found in Sections 3.6.

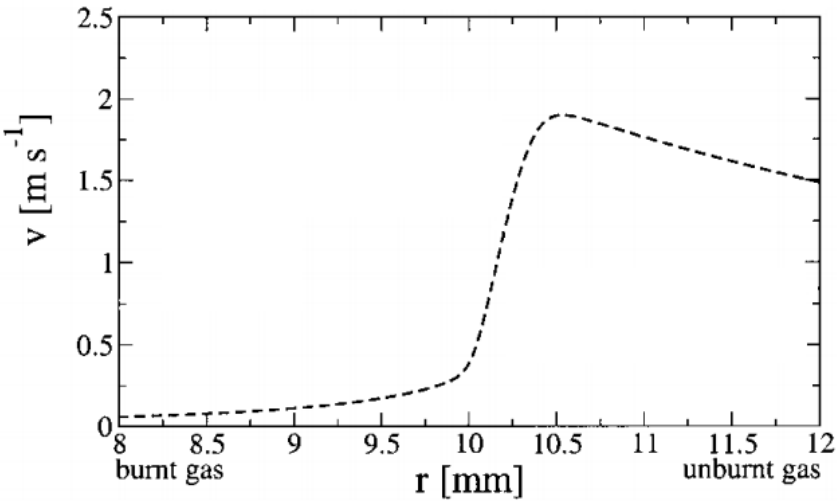

Figure 2.8: The unburned gas velocity profile near flame front, v is gas velocity and r is the local flame radius (Groot and De Goey, 2002).

In the present work, the measurements of r_u enable S_n to be found from Eq. (2.3). The unstretched burning velocity u_{la} can be then calculated, from the flame speed method, using Eq. (2.17). The corresponding PIV value of u_l can be derived from extrapolating u_n, Eq. (2.21), to $\alpha = 0$. Regarding to Markstein numbers, the linear dependency of S_n on α enables L_b to be evaluated from Eq. (2.18). Values of L_{cr} and L_{sr} are derived from Eq. (2.20), using a PIV method which has been developed by the current author. This method is described in Section 4.2.4. Finally, the normalisation of the Markstein lengths by the flame thickness, Eq. (2.1), yields the corresponding Markstein numbers. The results are presented and discussed in Chapter (5). Table 2.1 summarises all the key equations that are used in the present.

Table 2.1: Key questions, used in the present work.

$\delta_l = \left(\frac{\nu}{u_l}\right)/Pr$	Eq. (2.1)
$\alpha = \frac{2}{r_u} S_n$	Eq. (2.2)
$S_n = \frac{dr_u}{dt}$	Eq. (2.3)
$\alpha = \alpha_{sr} + \alpha_{cr}$	Eq. (2.4)
$\alpha_{sr} = 2\frac{u_g}{r_g}$	Eq. (2.5)
$\alpha_{cr} = 2\frac{u_n}{r_u}$	Eq. (2.6)
$K_{cl} = \alpha_{cl}\delta_l/u_l$	Eq. (2.7)
$u_{la} = (\rho_b/\rho_u)S_s$	Eq. (2.17)
$S_s - S_n = L_b\alpha$	Eq. (2.18)
$u_l - u_{nr} = L_{sr}\alpha_{sr} + L_{cr}\alpha_{cr},$	Eq. (2.20)
$u_n = S_n - u_g$	Eq. (2.21)

2.2.5 Possible Sources of Uncertainty in Measuring Laminar Burning Velocity

The unstretched laminar burning velocity, u_{la}, is an important parameter as it determines the fuel burning rate and flame stabilization in practical devices, such as burners and internal combustion (IC) engines. Also, u_{la} is important for developing surrogate fuel models and validating chemical mechanisms (Law et al., 2003; Dooley et al., 2010; Burke et al., 2010; Burke et al., 2011; Ranzi et al., 2012 and Egolfopoulos et al., 2014). Thus, accurate measurement of u_{la} is extremely important.

Recently, substantial attention has been devoted to improving the accuracy of measuring u_{la} of spherically expanding flames (Egolfopoulos et al., 2014, Beeckmann et al., 2018). For large molecular weight fuels (or liquid fuels), the uncertainty in u_{la} measurements is large due to the effects of molecular transport, i.e. differential diffusion of reactants (Jayachandran et al., 2014). For small molecular weight fuels (or gaseous fuels, such as methane and propane, not including hydrogen), the uncertainty in u_{la} measurements is small, especially for measurements at atmospheric conditions (T_u= 298 K, P = 0.1 MPa).

For hydrogen (H_2), the uncertainty in u_{la} measurements is high. The computational study of Varea et al. (2015), found that H_2 diffuses into the stretched flame faster than O_2, changing the equivalence ratio at the position of the flame. This behaviour is shown in Fig. 2.9, for H_2/air mixture with φ = 0.5 at 300K and 0.1MPa. The unburned gases are exactly at φ = 0.5, whereas the φ on the burned side is close to φ = 0.58. The temperature on the burnt side is consequently shifted to the adiabatic temperature at φ = 0.58, which is 1806 K. As a consequence of, the burned gas density takes lower values. It is worth to mention that, this mixture is characterized by Lewis number (*Le*) lower than unity, *Le* = 0.51. Hence, the non-unity Lewis number creates a focusing effect of the reactant species H_2, which causes a reduction in φ. In the present work, the effect of non-unity Lewis number on the burned gas density was experimentally investigated for different types of fuels and a correction method has been developed. This is discussed in Chapter (5).

In order to increase the accuracy of measuring the unstretched laminar burning velocity, u_{la}, the possible sources of uncertainty in u_{la} measurements should be first studied. Table 2.2 summarises the influence of different sources of uncertainty on u_{la}, of methane/air at atmospheric conditions. This fuel has been used in the present work. The table also includes the influence of fuel carbon number on each source of uncertainty. The references cited in this table, give information or details about the influences of each source on u_{la}. Hereafter are conclusions of their findings.

(i). Influence of mixture preparation (i.e. P, T_u and φ)

The small difference in the initial pressure has negligible contribution to the uncertainty of u_{la} (Egolfopoulos et al., 2014, Santner et al., 2015, Li et al., 2015). In contrast to the influence of the initial temperature, T_u. The uncertainty in u_{la} is around

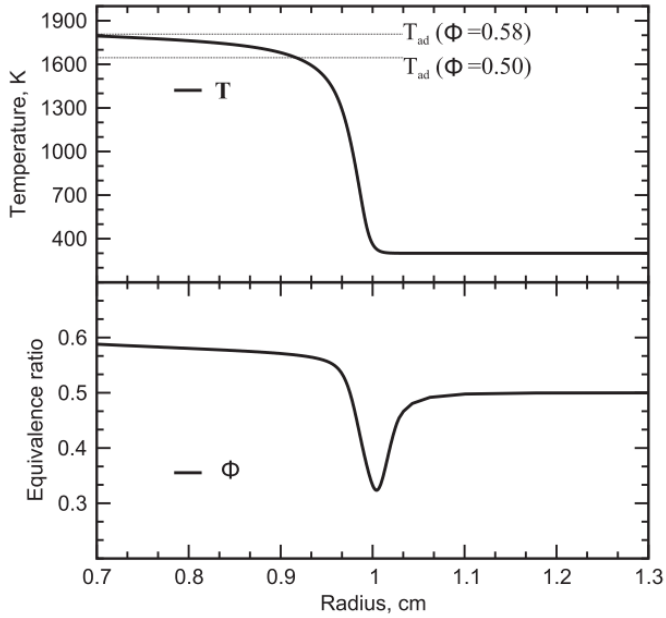

Figure 2.9: Focusing effect of the reactant H_2, due to non-unity Lewis number, for H_2/air flame with φ = 0.50 at 0.1 MPa, 300 K. Flame radius is positioned at r_u = 98 mm (Varea et al., 2015).

±2% when T_u is deviated by ±3 K and it is ±2.5–4% for ΔT = ± 5 K. The uncertainty in φ has much larger contribution to the uncertainty of u_{la}, when its influence is compared to that of P and T_u,especially under lean and rich conditions. A small change of ±0.01 in the value of φ, can change the value of u_{la} by ±4–7% for φ = 0.6 and φ = 1.4. This influence becomes smaller (within ±3%) for 0.8 > φ > 1.2. The uncertainty due to any change in φ depends on the accuracy of pressure gauge used, as a partial pressure method is usually used for preparing mixtures in experiments. The uncertainty due to φ increases when a pressure gauge with normal or low accuracy (≥±0.25%) is used in experiments. For large hydrocarbon fuels, the uncertainty in u_{la} caused by mixture composition is high because the uncertainty in φ is proportional to fuel carbon number. Therefore, a pressure gauge with high accuracy is desirable. In the present work, a pressure gauge with an accuracy of ±0.05% bar is used for preparing mixtures. Thus, the contribution of φ to the uncertainty in u_{la} can be considered negligible in the current study.

(ii).Influence of ignition

The contribution of ignition to the uncertainty in u_{la} can also be considered negligible, when a proper range of extrapolation is used. Flame radius, r_u, above 6 mm should be chosen to eliminate the ignition effect (Bradley et al., 1996).

Table 2.2: Different factors affecting the uncertainty of, u_{la}, measured by the FSM.

No.	Source of uncertainty	Contributions to the uncertainty of u_{la}	References
i	Initial pressure, P, and temperature, T_u Equivalence ratio, φ	Negligible contribution from P; around 2% for ΔT= ±3 K; around 2.5–4% for ΔT = ±5 K, No effect of the fuel carbon number. About 6% for $\varphi = 0.6$ and $\varphi = 1.4$ when pressure gauge with accuracy of $\pm 0.1\%$ is used; significant discrepancy (above 10%) might be caused when pressure gauge with normal or low accuracy of ±0.25% is used. High effect of the fuel carbon number.	(Egolfopoulos et al., 2014, Santner et al., 2015, Li et al., 2015)
ii	Ignition	Negligible contribution when $r_u > 6$ mm. No effect of the fuel carbon number.	(Bradley et al., 1996; Kim et al., 2013; Zhou et al., 2018)
iii	Instability	Negligible contribution, when $r_u < r_{cl}$	(Bradley et al., 2009; Jomaas et al., 2007; Bradley et al., 2018)
iv	Wall confinement	Within $2-3\%$ for (r_u /inner vessel radius, R_i) < 35%; relatively high contribution when R_i is less than 80 mm. No effect of the fuel carbon number.	(Chen et al., 2009; Bonhomme et al., 2013)
v	Extrapolation	Negligible contribution. when $r_{cl} > r_u$ >10 mm.	(Chen, 2015, Beeckmann et al., 2018)
vi	Radiation	Within 3% for $0.7 > \varphi > 1.3$; around 5% for φ = 0.6 and φ = 1.4; above 6% for near lean flammability mixture ($0.5 < \varphi < 0.6$) and increase with P and fuel carbon number.	(Jayachandran et al., 2014; Santner et al., 2014)

(iii). Influence of instability

Regarding to the instability, the constant pressure spherical vessel has the advantage that the instability that might develop over the flame surface during its propagation can be observed either from the $S_n - \alpha$ curve or from the recorded images. As discussed in section 2.2.3, the flame instability contribution to the discrepancies in the uncertainty in u_{la}, can be eliminated when $r_u < r_{cl}$ (Jomaas et al., 2007, Bradley et al., 2018). At high initial pressures (>1.2 MPa), the influence of flame instability becomes stronger (Bradley et al., 2009).

(iv). Influence of confinement

The wall confinement has negligible contribution when a suitable combustion vessel size is used. The maximum radius chosen in extrapolation should be less than 35% of the equivalent vessel radius (Chen et al., 2009), to eliminate the influence of wall confinement.

(v). Influence of extrapolation

Since the flame propagation at small and large radii is affected differently by the three factors discussed above (i.e. ignition, wall confinement and instability), the choice of flame radius range used for extrapolation, is an important source that can cause a high uncertainty in u_{la}. To avoid that, a suitable range of (r_{cl}> r_u>10 mm) should be used for extrapolation (Chen, 2015, Beeckmann et al., 2018).

(vi). Influence of radiation

Although, the flame propagation is affected by radiation, the radiation effect was always neglected in the experimental results in literature. Chen (2010) showed that radiation has thermal effect on flame propagation, by which flame temperature and thus flame speed is reduced. Therefore, radiation can lead to uncertainty in u_{la}. Yu et al. (2014) proposed a method to quantify the reduction in u_{la} due to radiation effect. For methane/air mixture, the radiation reduces u_{la} by about 3% for 0.7 > φ >1.3, and this reduction increases to be around 5% and 4% for φ = 0.6 and φ = 1.4, respectively. The radiation effect increase with increasing the initial pressure, because the flame propagates slower. At high initial temperature, the mixture is more easily to be ignited and the flame propagates faster. Therefore, the radiation effect decreases with the increase of the initial temperature.

As a conclusion, if suitable instruments are used, the influence of P, T_u and φ becomes small. The influence of ignition, instability and extrapolation can be also considered small, if suitable flame radii range is used ($r_{cl} > r_u >$ 10 mm). Some other sources of uncertainty cannot be neglected as it's a nature of the fuel, like the influence of non-unity Lewis number. Each fuel has its own *Le* which is for some fuels higher or lower than unity. This reduces or increases the burned gas density, based on the values of *Le*, and hence alters u_{la}. Another source of uncertainty it that, the flame speed method assumes that the flame propagates adiabatically. Thus, this method is not accurate for measuring u_{la} because of the radiation effect, especially for hydrocarbon mixtures diluted by components like carbon dioxide (CO_2), carbon monoxide (CO), and water vapor (H_2O). These components have strong spectral radiation absorption. Jayachandran et al. (2015) showed that the uncertainty in u_{la} due radiation can be avoided using a high speed PIV technique, which gives a direct measurements of flow and flame propagation velocities. Such technique was employed in the present work, and the laminar burning velocities were measured by the two methods, described in Sections 2.2.4.1 and 2.2.4.2. The difference in the results due to non-unity Lewis number and radiation are discussed in Chapter (5), where a correction method has been also developed and applied to correct u_{la}.

2.3 Characterisation of Turbulence

In research combustion devices, such as Bunsen burners or combustion vessels, the accuracy of the investigation of turbulent flames relies on well-defined turbulence statistics. Thus, the turbulent flow characterisation by means of spatial or temporal spectral analysis is essential, as a first step of a description of turbulent flames.

Three fundamental quantities should be determined to characterise turbulent flow fields. These quantities are the mean velocity, rms turbulent velocity, and the characteristic eddy length and/or time scales. In 1992, the rms turbulent velocity, u', and integral length scale, L, were measured at the centre of the current vessel using Laser Doppler Velocimetry (LDV) technique (Bradley et al., 1992). Such technique can provides a detailed temporal evolution of the flow velocity at the point of measurement as well as information on the mean velocity, higher-order moments and frequency spectra with high accuracy. However, LDV does not provide information on the spatial structure of the flow, unlike PIV measurement technique which is well appropriate for studying the structure of turbulent flows (Galmiche et. al., 2014).

2.3.1 Mean and rms Velocities

The mean velocities and rms turbulent velocity fluctuations in the x- and y-directions, respectively, noted $\bar{u}$, $\bar{v}$, u' and v', can be determined from the temporal evolution of the instantaneous velocities u and v, respectively. In the x-direction, $\bar{u}$ and u' can be calculated at each (x, y) grid node as (Goulier et al,. 2017):

$$\bar{u}(x,y) = \frac{1}{N_{im}} \sum_{i=1}^{N_{im}} u(x,y,i), \tag{2.22}$$

and,

$$u'(x,y) = \sqrt{\frac{1}{N_{im}} \sum_{i=1}^{N_{im}} [u(x,y,i) - \bar{u}(x,y)]^2}, \tag{2.23}$$

Where N_{im} is the total number of vectors, in the i_{th} vector map in time. The corresponding parameters in the y-direction, $\bar{v}$ and v', can be calculated in the same way, by replacing u and $\bar{u}$, in Eqs. (2.22) and (2.23), by v and $\bar{v}$, respectively.

Turbulence is a highly complicated phenomena, hence several simplification assumptions are often employed to simplify it. One of such assumptions is that of isotropic and homogeneous turbulence. According to (Semenov, 1965, Hwang and Eaton, 2004, Ravi et al., 2013, Xu et al., 2017), an area can be considered to be isotropic and homogeneous if ($\bar{u} < 10\%\, u'$ and $\bar{v} < 10\%\, v'$) at all locations within this area. This has been discussed in Section 5.3.

2.3.2 Turbulence Scales

Three commonly used scales can be used to quantify the characteristic size of eddies. The average size of the large eddies which hold most of the turbulent kinetic energy of the flow field, can be defined by the integral length scale, L, and its life time by the integral times scale, τ. While, the average size of the smallest eddies, in which the dissipation of energy takes place by molecular viscosity, can be defined by Kolmogorov length scale, η. The average size of the intermediate eddies in which most of the turbulence shear stresses occurs, can be defined by Taylor length scale, λ (Hinze, 1975).

2.3.2.1 Integral Length/Time Scales

The spatial longitudinal and lateral integral lengths scales L_{ux}, L_{vy} and L_{uy}, L_{vx}, can be determined directly from the integral of the correlation coefficients, R_{ux}, R_{vy} and R_{uy}, R_{vx}, respectively, of the fluctuating velocity values in x-direction and in y-direction. In x-direction, R_{ux} and R_{vx} can be calculated as (Goulier et al,. 2017):

$$R_{ux}(\xi) = \frac{\langle u(x,y)u(x+\xi,y)\rangle}{u'^2}, \qquad L_{ux} = \int_0^{R_0} R_{ux}(\xi)\, d\xi, \tag{2.24}$$

$$R_{vx}(\xi) = \frac{\langle v(x,y)v(x+\xi,y)\rangle}{v'^2}, \qquad L_{vx} = \int_0^{R_0} R_{vx}(\xi)\, d\xi, \tag{2.25}$$

Here R_0 is the first point at which the correlation coefficient equals to zero (De Jong et al, 2009, Ravi et al., 2013, Xu et al., 2017). Equations (2.18) and (2.19) can be employed to calculate R_{uy} and R_{vy}, in y-direction (Goulier et al,. 2017).

The integral time scales, τ_u and $\tau_{v,}$ can be calculated, at a given point, by the integration of the temporal coefficients R_u and R_v (Galmiche et. al., 2014). R_u is given by:

$$R_u(t) = \frac{u(t)u(t+\Delta t)}{u'^2}, \qquad \tau_u = \int_0^{R_0} R_u(t)\, dt. \tag{2.26}$$

R_v can be calculated from Eq. (2.26) by using v and v' instead of u and u', respectively.

2.3.2.2 Taylor and Kolmogorov Scales

According to (McComb, 1990, Pasquier et al., 2007), the Taylor length scale, λ, can be related to the turbulence dissipation rate, ε, by:

$$\lambda = (15\nu\langle u^2\rangle/\langle\varepsilon\rangle)^2. \tag{2.27}$$

where ν is the kinematic viscosity, values of which can be obtained from (Morley, 2005) and $\langle\ \rangle$ denotes time averaging. The corresponding Reynolds number is given by, $R_\lambda = \lambda u'/\nu$ (McComb, 1990). For homogeneous and isotropic flow, the turbulent energy dissipation rate, ε, is defined by (Hinze, 1975) as:

$$\varepsilon = 15\nu\left\langle\left(\frac{\partial u}{\partial x}\right)^2\right\rangle. \tag{2.28}$$

The dissipation rate can be calculated directly from the PIV vector maps by using the velocity spatial derivatives in Eq. (2.28). To account for the error of the finite spatial resolution of PIV measurements, a correction method to the dissipation rate, ε, has been proposed by (Lavoie et al., 2007). The correction includes filtering a known energy spectrum to account for the attenuation of the derivatives in the measured PIV data. The ratio of the measured derivative, denoted by the superscript (m), to the ''corrected'' derivative for the longitudinal measurement is given by (Lavoie et al., 2007) as:

$$\frac{\varepsilon^m}{\varepsilon} = \frac{\langle(\partial u_x/\partial x_x)^2\rangle^m}{\langle(\partial u_x/\partial x_x)^2\rangle} = \frac{\iiint_{-\infty}^{\infty} B^2 \frac{\sin^2(\Delta x_x k_x/2)}{(\Delta x_x/2)^2} \Phi_{xx}(\underline{k}) dk_x dk_y dk_z}{\iiint_{-\infty}^{\infty} k_x^2 \, \Phi_{xx}(\underline{k}) dk_x dk_y dk_z}, \tag{2.29}$$

where B is the spatial spectral filtering function given by:

$$B = \frac{8}{(wk_x)(hk_y)(zk_z)} sin\left(\frac{k_x w}{2}\right) sin\left(\frac{k_y h}{2}\right) sin\left(\frac{k_z z}{2}\right), \tag{2.30}$$

and,

$$\Phi_{xx}(\underline{k}) = \frac{E(k)}{4\pi k^4}(k^2\delta_{xx} - k_x k_x), \tag{2.31}$$

where $\underline{k}$ is the wavenumber vector with a magnitude k and $k_x, k_y$and k_z are the wave vector components in the x, y and z directions. The variable $w, h, s, \Delta x_x$ correspond to the width, height, and depth of the PIV interrogation volume and the separation between PIV vectors respectively. $E(k)$ is the 3D energy spectrum, which is defined by (Lin, 1972) as:

$$E(k) = \alpha_\eta u_\eta^2 \eta\left((k\eta)^{-5/3} + (k\eta)^1\right) \times \exp\left[-\alpha_\eta\left(\frac{3}{2}(k\eta)^{4/3} + (k\eta)^2\right)\right], \tag{2.32}$$

With α_η = 1.8, u_η is the Kolmogorov velocity scale, $= (\nu\varepsilon)^{1/4}$, and η is the Kolmogorov length scale given by (McComb, 1990):

$$\eta = (\nu^3/\varepsilon)^{1/4}. \tag{2.33}$$

An alternative correction method to correct the dissipation rate, based on the average distance between consecutive zero-crossings of $u(x)$, can be found in (Fragner et al., 2015). To calculate Taylor and Kolmogorov length scales, the corrected dissipation rate, ε, should be first computed using Eqs. (2.28) to (2.32) and then substituted into Eqs.

(2.27) and (2.33), respectively. This method was used in the present work to calculate λ and η. The results are presented in Section 4.3 and discussed in Section 5.3.

2.4 Turbulent Premixed Flames

This section presents the turbulent combustion theory relevant to the present study and is split into several subsections. Section 2.4.1 presents the structure of premixed flames. Section 2.4.2 addresses the definitions of turbulent flame radius and the derivation of turbulent burning velocities from the Mie scattering images. Finally, Section 2.4.3 describes the turbulence spectrum and the evolution of the effective root mean square turbulence velocity, by which a flame is affected.

2.4.1 Structure of Turbulent Premixed Flames

Several diagrams have been proposed to indicate different regimes of premixed turbulent combustion (Williams, 1985, Peters, 1986, Abdel-Gayed et al., 1989, Poinsot et al., 1991). One of the most commonly known is that developed by Borghi (1985), who employed the ratios (L/δ_l) and (u'/u_l) as shown in Fig. 2.10, which is often referred to as "Borghi diagram".

Some dimensionless groups have been employed in Fig. 2.10, to identify different regimes. One of these dimensionless groups is the turbulent Reynolds number, for a non-reacting flow, R_L. This group can be defined as:

$$R_L = u'L/\nu. \tag{2.34}$$

Another important dimensionless group is the Damköhler Number, Da. It is defined as the ratio between the characteristic flow time of the turbulent eddies and the characteristic chemical time of the reaction and given by:

$$Da = \frac{\text{Eddy life time}}{\text{Chemical life time}} = \left(\frac{L}{u'}\right)\Big/\left(\frac{\delta_l}{u_l}\right). \tag{2.35}$$

The Karlovitz number, Ka, is closely related to the Damköhler number, essentially describing its inverse, as a characteristic chemical time divided by the characteristic flow time. It is often estimated in terms of the flame characteristics relative to the smallest scales of turbulence, described by the Kolmogorov scale, η, and given by (Bray, 1996, Chakraborty and Cant, 2006) as:

$$Ka = \frac{\text{Chemical life time}}{\text{Eddy life time}} = \left(\frac{\delta_l}{u_l}\right) \Big/ \left(\frac{\eta}{u_\eta}\right). \tag{2.36}$$

where u_η is Kolmogorov turnover velocity.

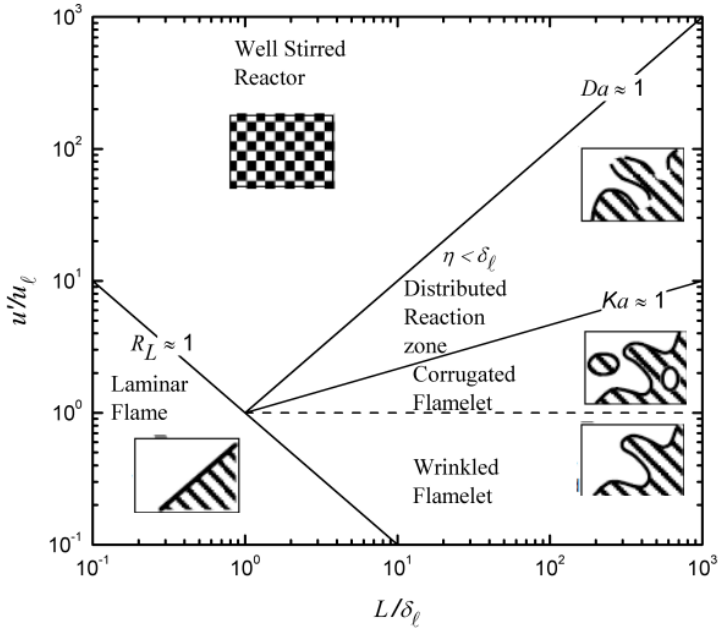

Figure 2.10: Turbulent combustion regimes**,** Borghi (1985).

In Fig. 2.10, different regimes of premixed combustion are identified as:

(i). Laminar flame regime

In this regime (R_L < 1, L/δ_l is small and u'/u_l is weak). The flow is considered laminar with minimum extent of flame wrinkling.

(ii).Wrinkled flamelet regime

Here (R_L > 1, Ka <1, and $u'/u_l < 1$); the flame thickness is less than the Kolmogorov length scale, and the chemical reaction can be completed even within the smallest eddy. Hence, the laminar flame structure remains within the turbulent flow field. The turnover velocity, u', of the eddies is lower than the laminar burning velocity, u_l, implying that the flamelet surface is only slightly wrinkled while passing through these eddies.

(iii). Corrugated flamelet regime

This regime is characterised by (R_L > 1, Ka <1, and $u'/u_l > 1$). The turnover velocity, u', of turbulent eddies is high and the flamelet surface becomes highly convoluted and folded upon traversing the eddies. Wrinkling the flame front up to this

limit leads to the formation of pockets of unburned and burned gases. However, the flame front still conserves its laminar flame characteristics.

(iv). Distributed reaction zones or thickened flame regime

Here $Ka > 1$ and $Da > 1$, the chemical lifetime is longer than the lifetime of the smallest turbulent eddies. Only the smallest eddies can penetrate into the preheat zone, enhancing the heat and mass transfer rates. Therefore, the time of chemical reaction will not be sufficient to burn the smallest eddy before that eddy breaks up, which breaks up the reaction zone. So that, the flame structure is dominated by the turbulent motions of the smallest eddies.

(v). Well-stirred reactor regime

For this regime ($Da \leq 1$ and $Ka >> 1$). The chemical lifetime is longer than the lifetime of the large eddies. Hence, all the turbulent eddies are able to penetrate into the preheat zone and therby enhance the heat and mass transfer rates. This leads to a steep drop in the flame temperature and consequently extinction of the flame. The entire flow behaves like a well-stirred reactor with no distinct local structure.

2.4.2 Turbulent Burning Velocity and Reference Radii

Although our understanding of the turbulent premixed combustion is continually improving, the problem of precise definition of the turbulent burning velocity, u_{tr}, is still one of the most serious challenges in combustion (Ghenai et al., 1998, Shepherd and Cheng, 2001, Lipatnikov and. Chomiak, 2002a, Lipatnikov and. Chomiak, 2002b, Driscoll, 2008).

Several definitions of u_{tr} and the associated surfaces have been proposed by (Beretta et al., 1983; Tabaczynski et al., 1980; Gillespie, 2000, Bradley et al. 2003; Filatyev et al., 2005, Lawn and Schefer, 2006). Beretta et al. (1983) employed the mean flame surface at the leading edge of the flame front. A significant amount of unburned gases reside behind the mean surface and the flow velocity normal to this surface was termed the engulfment or entrainment velocity, u_e. Beretta et al. stated that the velocity, u_e, expresses the rate at which reactants move from the external zone into the leading edge of the flame front and not the rate of burning. Bradley et al., (1994a) estimated the burning rate behind this leading surface by assuming it to be proportional to the concentration of unburned gas.

Later, Bradley et al. (2003) defined and presented different flame radii, along with the associated turbulent burning velocities using simultaneously Mie scattering and schlieren flame imaging techniques. From the mean flame radius, $r_v(=\sqrt{A/\pi})$, where A is the flame surface area, the turbulent flame speed , S_t, and the turbulent burning velocity, u_t, with reference to consumption of cold reactants can be defined respectively as:

$$S_t = \frac{dr_v}{dt} \tag{2.37}$$

and

$$u_{tr} = \frac{\rho_b}{\rho_u} S_t. \tag{2.38}$$

Where ρ_b is the adiabatic burned gas density and ρ_u is unburned gas density, calculated at the initial conditions. Equation (2.32) has been used in the present work, to calculate the turbulent burning velocity using the PIV system described in Section 3.4.

2.4.3 Turbulence Spectrum and Effective rms Velocity

As a flame grows after central ignition, it is initially comprises a small kernel with laminar propagation of the front during bodily convection by the turbulent flow (Abdel Gayed et al., 1987). During this early stage of flame-kernel growth, only the smallest turbulence wavelengths are affecting the surface structure and the effective rms turbulent velocity, u'_k, that acting on the flame is less than the rms velocity, u', that is measured in the vessel in the absence of any flame. As the flame propagates, it becomes more susceptible to the full range of turbulence scales present and u'_k increases until approaches u' (Bradley et al. 2009). As a consequence, the turbulent burning velocity, u_{tr}, approaches its fully developed value (Abdel-Gayed et al. 1987).

The value of, u'_k, can be found from the turbulent kinetic energy, associated with a continuous cascade of eddies, by integrating the associated power spectral density, psd, between the limiting wave numbers, based on one-dimensional cold flow measurements. Abdel-Gayed et al. (1987) calculated the psd between the integral wave number and the minimum wave number, k_n , in the vessel. Such a wave number has been derived by Haq (1998), at a given time in the explosion based on the elapsed time from initiation, t, as:

$$k_n = 2\pi/(s.t), \tag{2.39}$$

here s is the mean cold gas speed. Abdel-Gayed et al. (1987) suggested that s can be estimated from the relationship:

$$s = u'.(8/\pi)^{0.5}, \tag{2.40}$$

More recent, Mandilas (2009) have used an alternative approach to calculate the smallest effective wave number, k_n, based on the kernel diameter, D_k. According to this approach, k_n is given by:

$$k_n = 2\pi/D, \tag{2.41}$$

Based on the original study by Abdel-Gayed (1987), Bradley et al. (2009) developed and presented the ratio of u'_k to u' as:

$$\frac{u'_k}{u'} = \left[\frac{15^{0.5}}{R_\lambda}\int_{\bar{k}_{\eta 1}}^{\bar{k}_{\eta 2}} \bar{S}(\bar{k}_\eta)d\bar{k}_\eta\right]^{1/2}, \tag{2.42}$$

Here R_λ is the Reynolds number, based on the Taylor scale λ, $\bar{S}(\bar{k}_\eta)$ is the non-dimensional power spectral density and is expressed in terms of $\bar{k}_\eta$, which is a dimensionless wavenumber obtained from the wavenumber multiplied by the Kolmogorov length scale, η. $\bar{S}(\bar{k}_\eta)$ is given by:

$$\bar{S}(\bar{k}_\eta) = \frac{0.01668R_\lambda^{2.5} + 3.74R_\lambda^{0.9} - 70R_\lambda^{-0.1}}{1 + \left(0.127R_\lambda^{1.5}\bar{k}_\eta\right)^{5/3} + \left(1.15R_\lambda^{0.622}\bar{k}_\eta\right)^4 + \left(1.27R_\lambda^{0.357}\bar{k}_\eta\right)^7}, \tag{2.43}$$

The limits $\bar{k}_{\eta 1}$ and $\bar{k}_{\eta 2}$, in Eq. (2.42), represent the smallest and largest possible wavelengths and are conveniently expressed by $n_k L$, where n_k is the number of integral length scales, as:

$$\bar{k}_{\eta k} = \frac{2\pi\eta}{n_k L} = \left(\frac{32\pi}{15^{0.25}n_k}\right)R_\lambda^{-1.5}, \tag{2.44}$$

The lower limit $\bar{k}_{\eta 1}$, in Eq. (2.42), is assumed to be the flame diameter, D $(= 2r_v)$, as it is based on the maximum wavelength, $n_k L$, that can wrinkle the flame. In the case of explosions, the upper limit $\bar{k}_{\eta 2}$ depends upon the size of the smallest eddy that can be

chemically acting on the flame during its lifetime. This limiting smallest wavelength is the Gibson scale, l_G, with a value of n_k given by (Bradley et al., 2009) as:

$$n_{kG} = 0.133\left(\frac{u'}{u_l}\right)^{-3}. \tag{2.45}$$

The value of $\bar{k}_{\eta 2}$ is obtained from Eq. (2.44) with $n_k = n_{kG}$. In the present study, the lower limit, $\bar{k}_{\eta 1}$, corresponding to the maximum possible wavelength, which is close to the internal diameter of the vessel, namely 380 mm. The upper limit, $\bar{k}_{\eta 2}$, corresponds to the smallest wavelength, should be the Kolmogorov scale, η. Consequently, $n_k L$ in Eq. (2.44) is η and $\bar{k}_{\eta 2}$ is 2π. Figure 2.11 shows the variation of u'_k/u' with n_k for different values of R_λ. The greatest increase in u'_k occurs between ignition and when the flame has reached a radius four times the integral length scale of turbulence. Thereafter, the value of u'_k increases towards u'.

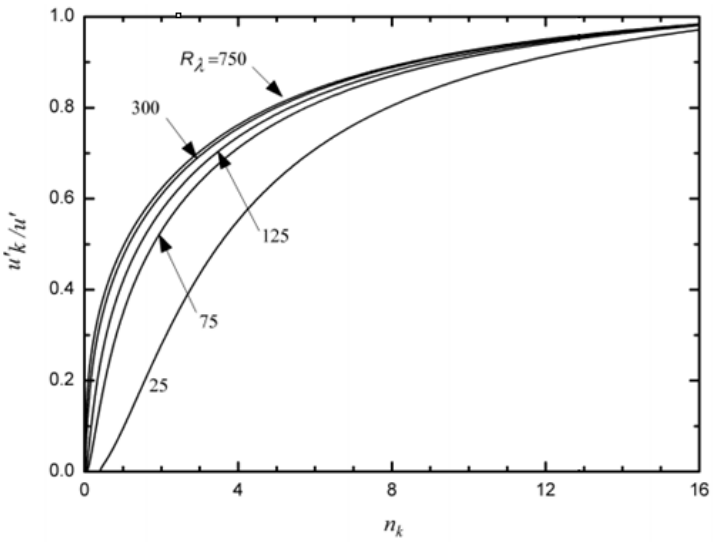

Figure 2.11: Development of $u_k^{'}/u^{'}$ spatially during spherical explosion, for different values of R_λ, Bradley et al. (2009).

Although, u'_k is a useful tool to understand the effect of turbulence on the flame propagation, it is still questionable. This is due to the disparity between the cold flow turbulence, from which u'_k has been deduced, and the turbulence in the presence of combustion. As a part of the present work, u'_k has been calculated and compared with the spatial rms turbulent velocity, here after referred to as u'_s . The later has been deduced directly from the PIV measurements of turbulent premixed flames. The results are presented and discussed in Section 5.4.

Chapter 3 - Experimental Apparatus and Data Processing

3.1 Introduction

Laminar and turbulent burning velocities can be measured using a variety of experimental methods and apparatus (Broustail et al., 2011; Van Lipzig et al., 2011; Saeed and Stone, 2004). These include constant volume combustion vessels (Hu et al., 2009; Jerzembeck et al., 2009; Marshall et al., 2011), adiabatic perforated plate burners (Dirrenberger et al., 2014; Konnov et al., 2011; Sileghem et al., 2013) and the twin counter flame stagnation technique (Egolfopoulos et al., 1992; Yamaoka and Tsuji, 1985).

The experiments reported in this thesis were carried out in a fan-stirred constant volume vessel with optical access. This allows a range of combustion fundamentals to be studied over a wide range of variables: fuel type, temperature, pressure, equivalence ratio, rms turbulent velocity and turbulence length scales. This vessel has also many features that make it suitable for the present work. The flow within the central volume of this vessel is close to homogenous, isotropic, turbulence with no mean flow, as shown in Chapter (5). The equivalence ratio, pressure and temperature can be controlled over a wide range of conditions. Also, only a small amount of fuel is required and the combustion is less affected by complex feedback mechanisms in more complex systems, such as internal combustion (IC) engines. The operating range is also not limited by flashback or blow off and the flame is more stable compared to those of burners.

Furthermore, it allows for various imaging techniques to be used; such as high speed digital schlieren (Mansour, 2010), high-speed 3D laser-sheet imaging (Thorne, 2017) and various flow field imagining techniques, such as particle image velocimetry (PIV) (Jayachandran et al., 2015).

In the present work, high speed digital particle image velocimetry, PIV, is installed, by the current author, and employed to measure the laminar burning velocity of different hydrocarbon fuels. For this a methodology for correcting burning velocities, measured by the flame speed method, was developed and discussed in Section 5.2. It also has been used to generate information about the turbulent velocity field in the vessel and to assess the turbulence data, for dry air in the absence of phase change and chemical reaction, as discussed in Section 5.3. Furthermore, it is used to measure the rms turbulent velocity ahead of methane/air flames, as discussed in Section 5.4.

This chapter is devoted to describing the experimental devices and data processing procedures that have been used in the present work. Sections 3.2 describes the Leeds fan-stirred combustion vessel, whilst, Section 3.3 describes the auxiliary systems that have been used with this vessel, for mixture preparation, ignition, and monitoring the flame during its propagation. Sections 3.4 and 3.5 present the PIV system and experimental procedures, respectively. Finally, Section 3.6 presents the various data processing procedures.

3.2 The Fan-Stirred Vessel

The measurements were made in a spherical stainless steel explosion vessel, with an inner diameter of 380 mm, with a total internal volume of 0.30372 m^3. Figure 3.1 shows a schematic view of the combustion vessel and its auxiliary systems. The vessel has three pairs of optically flat and non-conformal quartz windows of 150 mm diameter, allowing a full visualisation of the centre of the vessel. Four identical fans, each powered by an 8 kW three phase electric motor, were located close to the wall of the vessel. These were arranged in a regular tetrahedron configuration, in an attempt to optimise homogenous, isotropic turbulence, as shown in Fig. 3.2. In laminar studies, these fans were used for mixing the mixture. Each fan had 8 blades, of about 75 mm length, and these are about 72 mm apart at their edges. They were controlled by individual solid state variable frequency convertors, with a speed control range of 200-10,000 rpm (3.3-176 Hz), in increments of 20-30 rpm.

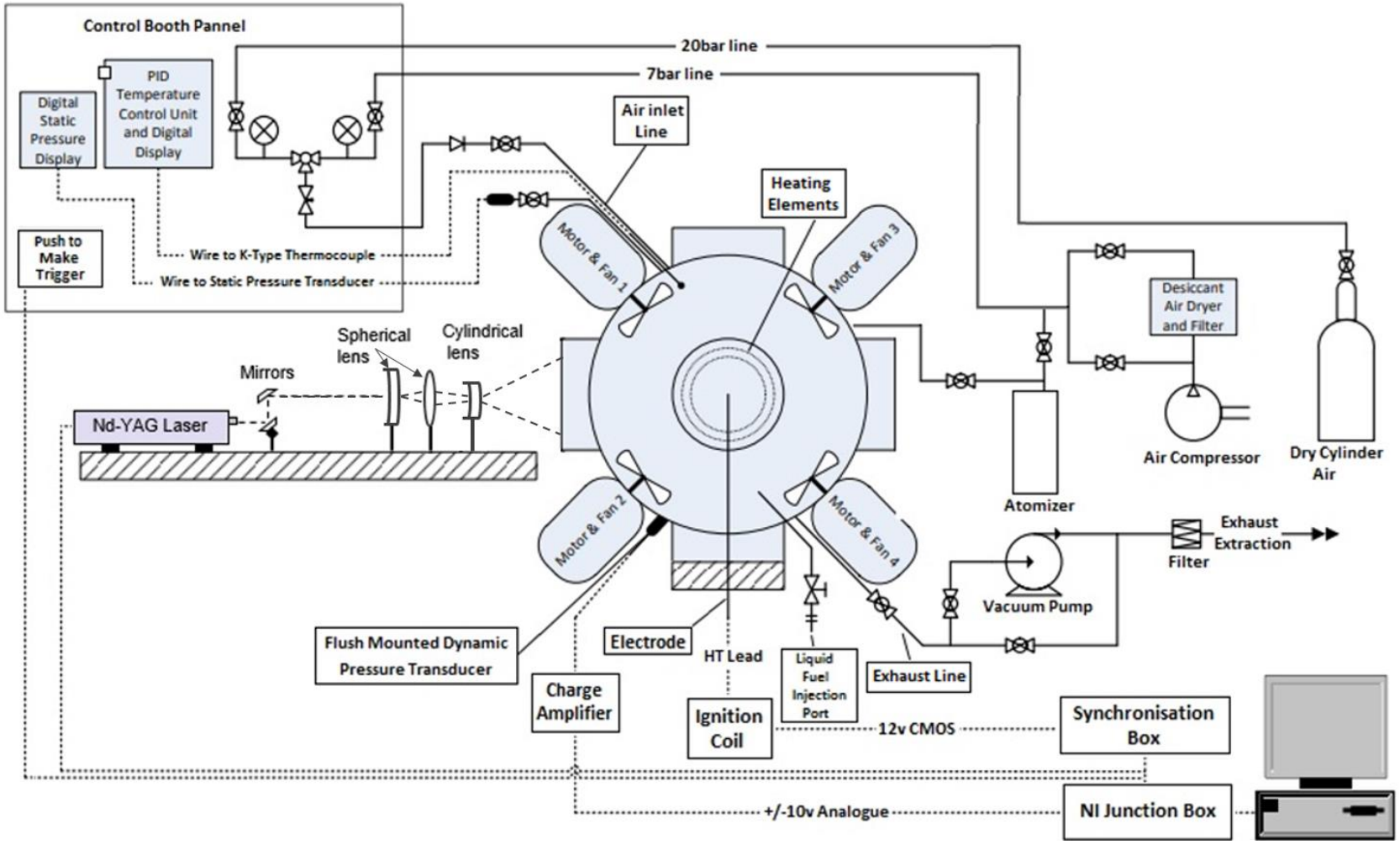

Figure 3.1: Schematic of the vessel and its auxiliary systems (Bradley et al., 2019).

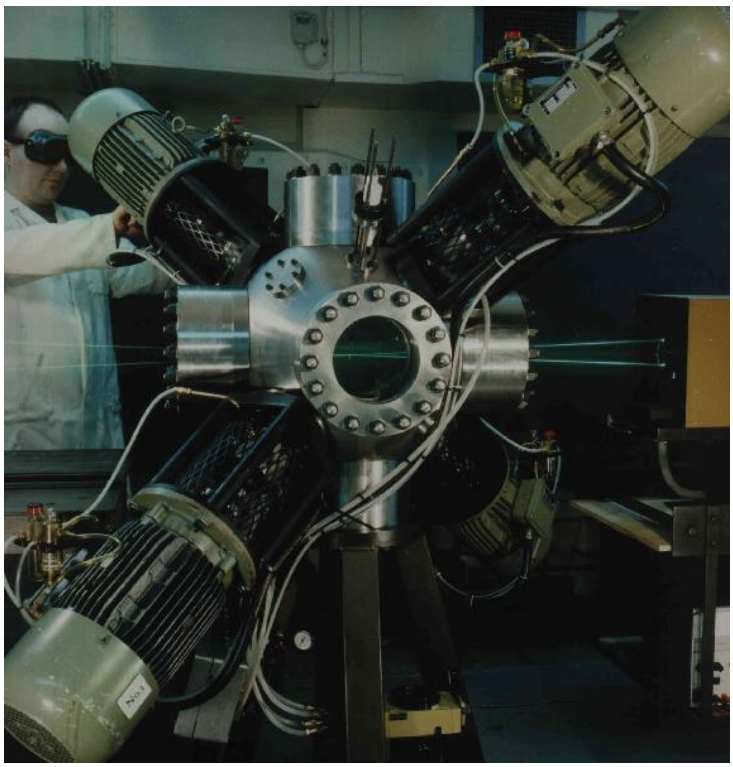

Figure 3.2: Leeds fan-stirred vessel (Tripathi, 2012).

3.3 Auxiliary Systems

Several auxiliary systems were employed on the vessel for mixture preparation ignition, and monitoring the flame during its propagation. These included a heating system, an ignition system, and a pressure measurement system. Further descriptions are given in the following subsections.

3.3.1 Heating Control System

An internal 2 kW coiled heating element was employed to heat the vessel. This element was attached to the inside of the access cover as shown in Fig. 3.3. During the mixture preparation, the initial temperature was measured by a 25 μ Chromel-Alumel wire Type K thermocouple, sheathed in a 1.5 mm diameter stainless steel tube and positioned 75 mm away from the vessel inner surface, to avoid any radiation and conduction effects from the vessel wall. A PID controller (CAL Controls, CAL3200) mounted in the control panel, in the protected area of the laboratory (Tripathi, 2012), was employed to set, control and display the temperature using a feedback from the thermocouple.

The entire vessel was initially preheated by setting the temperature of the PID controller higher than the desired initial mixture temperature, that significantly reduced

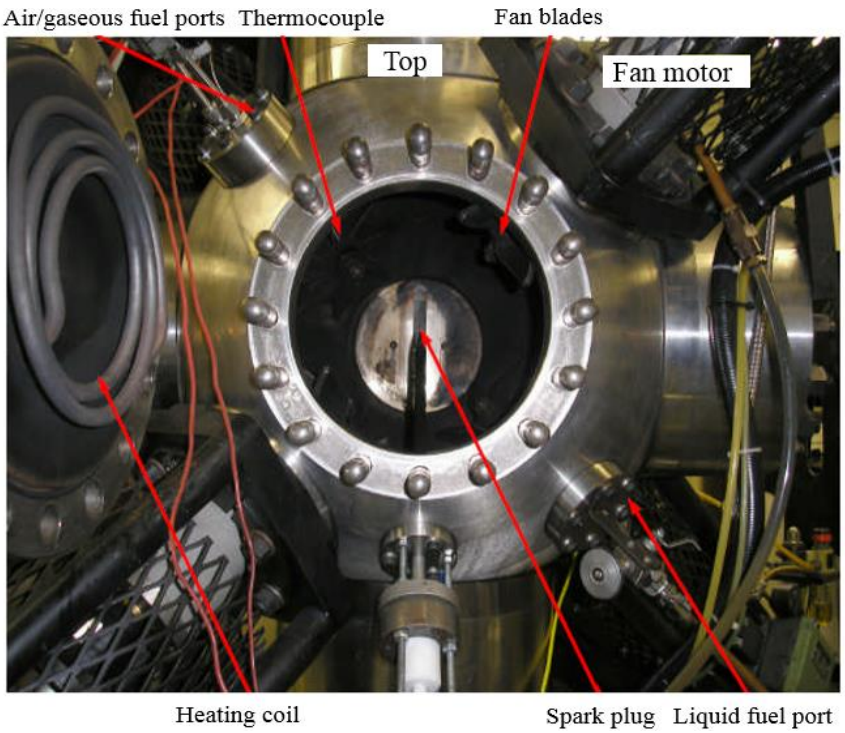

Figure 3.3: Shows the vessel in detail.

the heat up time. The four fans were employed, during the heating, to generate a turbulent flow which aid in enhancing the convective heat process and spread the heat uniformly throughout the vessel. They also protect the heaters from overheating, and reduce the risk of any pre-combustion reactions of the mixture due to hot spots (Mandilas, 2009). After reaching the set temperature, the heating element was turned off automatically and the vessel temperature was then allowed to fall towards the desired temperature. During this time, the thermal conduction ensured a uniform temperature distribution across the vessel wall.

3.3.2 Ignition System

A variable arc discharge ignition system with a centrally positioned spark plug, was used to ignite all reported mixtures. The spark plug was designed and developed, at the University of Leeds, to minimise any aerodynamic interference with the flame. Shown in Fig. 3.4, this consisted of a central 1.5 mm diameter high carbon steel anode, sheathed in a ceramic insulating material and contained within an outer stainless steel tube of 6.35 mm diameter, which acted as the cathode. This tube was mounted through the vessel wall. This grounded the outer stainless steel section to earth for the cathode side of the circuit. The anode electrode was connected to a Lucas 12V transistorized automotive ignition

coil system via a high tension (HT) cable, with the other side earthed to increase the original charge of the unit. Hence, any risk of uncontrolled ignition, due to residual ignition energy, was avoided (Kondo et al. 1997). For all experiments, the spark plug gap was set to 0.6 mm and the spark ignition energy was about 0.4 mJ.

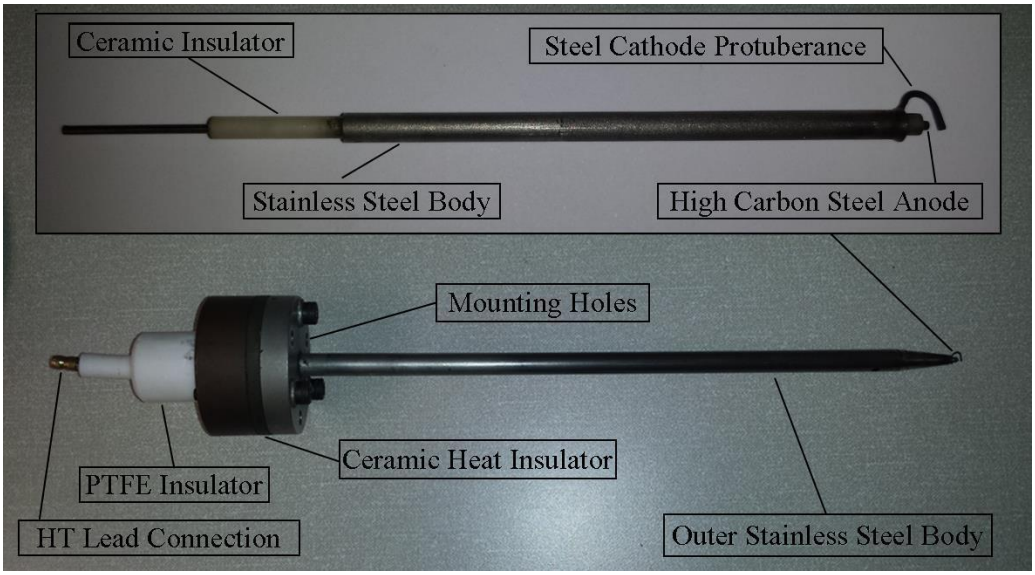

Figure 3.4: Spark plug assembly (Mumby, 2016).

3.3.3 Pressure Measurement System

A static pressure transducer (Druck PDCR 911), with a range of 0-1.5 MPa was connected to an LCD display, employed to measure absolute pressure in the vessel during the mixture preparation. Prior to triggering an explosion, a swage lock ball valve was used to isolate this transducer from the rapid pressure rises experienced during explosions. The dynamic pressure was measured by a piezoelectric dynamic pressure transducer (Kistler 701A), with a range of 0-25 MPa, mounted flush to the inner wall of the vessel. The output charge from this transducer was converted to an analogue signal of (0 -10V) by a Kistler 5007 charge amplifier. To maximise the signal to noise ratio, the charge amplifier range was set at 0.5 v/MPa for initial pressures of 0.1 and 0.5 MPa. An analogue to digital convertor (Microlink 4000), digitised this voltage signal, which was then interpreted by a LabVIEW software.

3.4 Particle Image Velocimetry (PIV) System

3.4.1 Basic Principle

PIV is a well-established technique and its basic operation is fully documented in (Raffel et al., 2018 and Westerweel, 1993). Only brief details are provided here. PIV is a non-intrusive optical technique that can provide a two-dimensional velocity fields and a sectional visualisation of a propagating flame front with relatively high temporal resolution. Figure 3.5 shows a schematic diagram of a basic PIV system. Micron sized tracer particles are introduced into the flow, which assumed to move perfectly with the local flow velocity. These particles are then illuminated twice within a short time interval, in a selected plane, by a thin laser sheet that has been formed using a series of lenses.

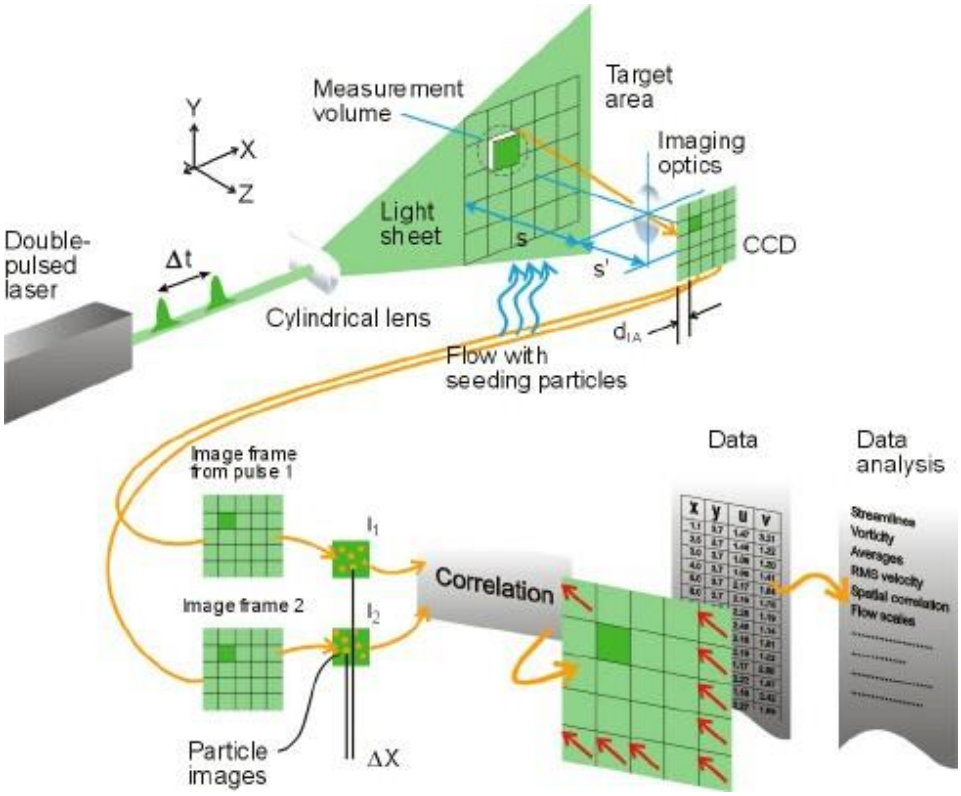

Figure 3.5: A schematic diagram of a PIV system, reproduced from Dantec Dynamics, 2015.

Scattered light from particles is captured by a high-resolution digital camera, which is usually positioned perpendicular to the plane of the laser sheet. In general, two methods are used to capture these images: 1) Single frame, double exposure imaging, and 2) Double frame, double exposure imaging. The latter arrangement is employed for the majority of applications, as it works well with modern digital imaging processes. Discussion is confined to this arrangement (i.e. double frame/double exposure), as it was

adopted throughout this study. More details of the first arrangement (i.e. Single frame/double exposure), and its processing methods, can be found in (Raffel et al., 2018 and Westerweel, 1993).

Subsequently, each pair of PIV images is evaluated by dividing these images into an array of small sub-areas called “interrogation areas”. For each interrogation area (IA), the associated vectors of the particles displacement are then resolved using a numerical correlation algorithm. This takes into consideration the time difference between the two exposures and the images magnification (Raffel et al., 2018). To obtain accurate results, the following aspects must be taken into consideration:

- The size of the IA is such that no significant velocity gradient exists within this size, i.e. all particles are moving homogeneously in the same direction and the same distance. It is also recommended that the number of particles within one IA be about eight (Raffel et al., 2018).
- The laser sheet should have a thickness of between 0.5 and 2 mm (Raffel et al., 2018). Too thin sheet would result in some particles escaping from the interrogation area, due to a velocity component normal to that sheet. Too thick a sheet (>2 mm) would result in the image of the flame edge becoming obscured by remote particles in the flow away from that plane.
- The time interval between the laser illuminations should be adjusted such that particles do not move more than a quarter of the IA. This is to avoid the loses due particles entering or escaping to/from the selected plane of measurement. This also to minimise the uncertainty of measuring particles displacements (Westerweel, 1993).
- In order to avoid blurring of the image, the time of each laser pulse must be short enough to freeze the motion of the particles during exposure.

These aspects were taken into consideration during installing and using the PIV system in the present work. A high repetition rate double pulsed Nd:YAG laser (DM60-DH, Photonics), was employed to generate pulses of 12 mJ at a wavelength of 532 nm at 5 KHz. The laser beam was expanded into a vertical sheet of about 1.0 mm thickness, passing through the centre of the vessel, where it uniformly illuminated the dispersed seeding particles of olive oil. These were < 1 μm diameter, generated by six jet atomisers (9010F0021, DANTEC). The laser pulses, were synchronized with a high-speed camera perpendicular to the laser sheet, to record a 12-bit image pair of 1024×1024 pixels, under

the control of Dantec dynamics studio software. This system was employed to determine the flow characteristics in the absence and presence of combustion.

3.4.2 Laser Sheet Optics

The schematic diagram in Fig. 3.6 shows top and side view layouts of the optics, used to form the laser sheet. These optics consisted of a plano-concave and bi-convex spherical lenses of -300, 650 mm focal lengths, respectively, with a plano-concave cylindrical lens of -20 mm focal length. The beam was expanded in one dimension by the cylindrical lens, while the bi-convex spherical lens focused the beam on the centre of the vessel, resulting in a thin sheet of light being formed across a plane within the middle of the vessel. The thickness of the light sheet could be controlled and adjusted by the separation of the two spherical lenses. This thickness was kept at approximately 1 mm for all experiments, using the arrangement shown in Fig. 3.6. The height of the light sheet, measured at the centre of the vessel was ~170 mm, limited by the aperture angle (20°), the window edge and the available distance next to the vessel. However, this height was more than sufficient to cover the whole area of the access window (D= 150 mm). The laser sheet was positioned 1±0.5 mm away from the spark tip. This was the closest possible distance without causing excessively strong reflections of light from the spark holder to the camera.

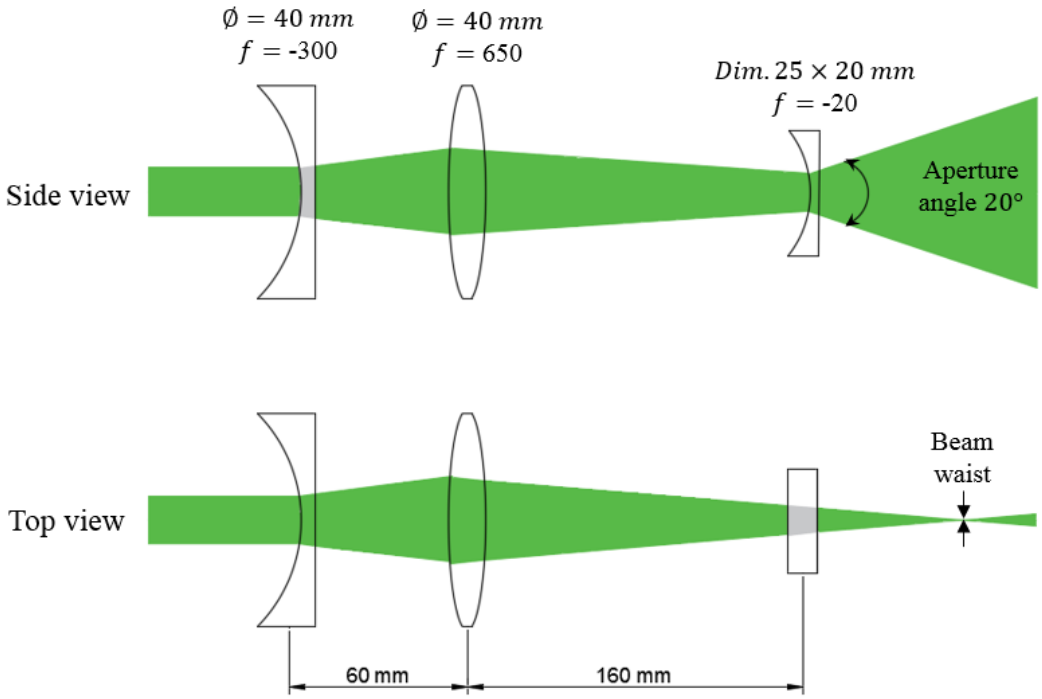

Figure 3.6: Lenses configuration.

3.4.3 Seeding System

The main function of seeding particles is to scatter the laser light, so as to track their motion and determined the flow velocity. These particles must have the following characteristics:

- The particles must be sufficiently small and homogenously distributed, in order to follow the flow and track it accurately. On the other hand, they must be large enough to scatter a reasonable quantity of light, to be detected by the camera (Melling, 1997). Therefore, the choice of the particle size is extremely important.
- In the case of combustion, the seed material must vaporise at the flame front. This helps to distinguish between the burned/unburned regions and identify the flame edge.
- Any combustion of seed must has no effect on the overall combustion of the fuel/air mixture.

In the present work, olive oil droplets of approximately 1 μm diameter were employed, for both the laminar and turbulent studies. This seed satisfied all of the requirements outlined above. The relevant properties of which are listed in Table 3.1.

Table 3.1: Characteristics of seeding particles and air

Particle diameter, d_p	$1x10^{-6}$	m
Density of oil, ρ_p	920	kg/m^3
Boiling temperature of oil	573	K
Density of air, ρ_a, at 300 K and 0.1MPa.	1.2	kg/m^3
Viscosity of air, μ_a, at 300K and 0.1MPa.	18.7×10^{-5}	$N.s/m^2$

To ensure the particles are able to follow the flow and track it accurately, their relaxation time, τ_r, should be short. It also should be less than the characteristic time scale (Raffel et al., 2018). It can be calculated from the expression of (Melling, 1997):

$$\tau_r = \frac{d_b^2}{18} \times \frac{\rho_p}{\mu_a} \times \left(1 - \frac{\rho_a}{\rho_p}\right). \quad (3.1)$$

For an olive oil particle of diameter 1 μm, this time was 2.8 μs which was very short and much less the integral time scale (Chapter 5). With this selected size, the droplets were small and fast enough to follow the current flows. The selected size was also large enough

to scatter sufficient light. The average number of particles for each interrogation window was about 9 particles, for most cases. The optimized number should be around 8-10, as suggested by Melling, (1997) and Reffel et al., (2007). This indicated that the seeding density inside the vessel during PIV measurements was just sufficient and not too much to influence the data processing, nor too small to provide absent velocity.

During investigating the characteristics of premixed flames, it is supposed that the olive oil particles are to be consumed by the flame front. This had been assessed by comparing the boiling temperature of olive oil with the flame temperature gradient within the flame front. The temperature gradient was calculated first assuming a linear temperature profile ranging from the temperature of the unburned gas, T_u, to the temperature of the burned gas, T_b. The lowest T_u , used in the present work, was 300 K for methane/air mixture during the laminar and turbulent studies. Assuming that due to heat losses, Lewis number and dissociation, the burned gas temperature, T_b, would be below the adiabatic flame temperature, about 2226 K (see Fig. 5.1). The thermal flame front thickness, δ, for a stoichiometric methane/air flame has been shown to be approximately 1 mm (Turns, 1996). The temperature gradient can be then calculated using $dT/dx = (T_b - T_u)/\delta$ (Tripathi, 2012). The boiling point temperature of olive oil is presented to be 573 K, comparing this with the temperature gradient was shown that the distance into the flame front required for the consumption of the olive oil seeding was ~0.15 mm. This distance was much less than the thermal flame front thickness, which proves that the olive oil was completely consumed by the flame front.

Any combustion of seeding particles should also not affect that of the mixture. This was examined by comparing the pressure variation of two experiments, with and without of seeding. As shown in Fig. 3.7, there was a negligible difference between the two pressure records, suggesting no significant differences in the combustion.

To exclude any other effects arising from the presence of the seeding, the unstretched laminar burning velocity was measured, for the same conditions of Fig. 3.7, with and without seeding, using the pressure method described in (Hinton et al., 2018). It was found that the unstretched laminar burning velocity remained constant at around 0.5 m/s regardless of the presence of seeding. Therefore, the effect of the presence of the seeding can be considered negligible.

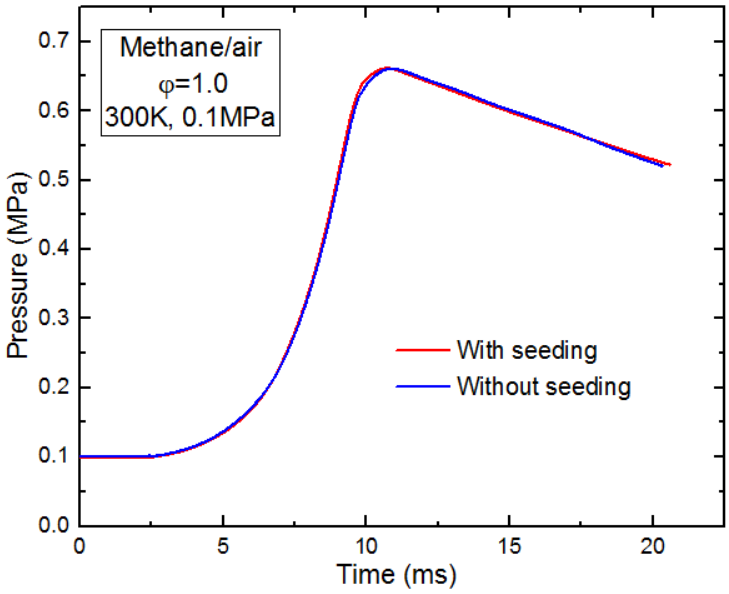

Figure 3.7: Pressure variation in the presence and absence of seeding, for stoichiometric methane/air mixture at 300 K and 0.1 MPa.

To generate the required seeding particles to the vessel, a six jet atomiser (9010F0021, DANTEC) was employed. This was specifically designed and manufactured to provide tracer particles for fluid flow measurement using virtually any liquid. It incorporated a number of special features, such as the ability to introduce particles into a pressurised system using an inbuilt pressure regulator, pressure gauge, a self-contained dilution system, and the ability to select one to six particle generating jets. All these features allow a broad range of control over both the particle number concentration and the total particle output.

This atomiser, shown in Fig. 3.8, was consisted of four main parts:

- The inlet to the atomiser which consisted of a pressure regulator and gauge. The regulator was used to control the input pressure, which was then displayed on the gauge.
- The atomiser incorporated a dilution system, which was used to vary the output concentration.
- A rotameter was mounted adjacent to the regulator, which gave the flow rate of the dilution air.
- Six atomisers were incorporated and located within the liquid reservoir.

The outlet assembly was designed to meet the high particles output demanded when all six atomiser jets were used and/or when high dilution air settings were used.

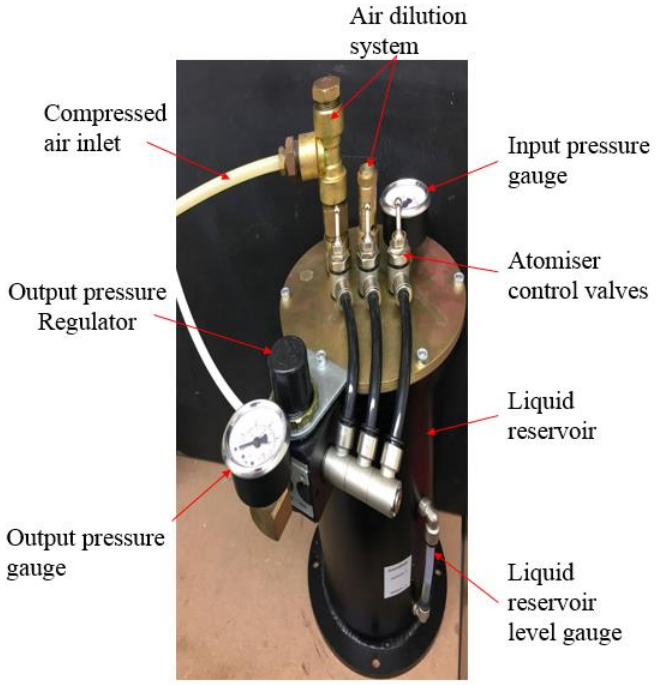

Figure 3.8: Atomiser, model (9010F0021, DANTEC).

3.4.4 Image Recording System

A high-resolution Phantom ultra-high-speed UHS-12, model v2512, CCD camera was positioned perpendicular to the laser sheet, to record the laser light scattered from the particles. The camera operated, with a 12-bit image pair of 1024×1024 pixels, under the control of Dantec dynamics studio software. A Nikon 105 mm lens was attached to the camera. The camera was positioned such that the maximum field of view of 120 × 120 mm^2, with a resolution of ~ 0.117 pixel/mm. This resolution was more than sufficient to capture a defined flame edge and detailed flow structure, whilst allowing the sampling rate of 5000 frames per second (fps).

Prior to the experiments, the camera was calibrated. A circular calibration plate, shown in Fig. 3.9, to which the grid paper with equidistant dots were attached, was used for the calibration. First the camera was focused manually on the measurement plane, using this plate and then using the seeding particles themselves. Figure 3.9b shows an image of the calibration, checking the performance of the camera. The standard deviation of the detected dots was σ = 0.098, calculated by Dantec software. The calibration procedures are outlined in (Dantec, 2015).

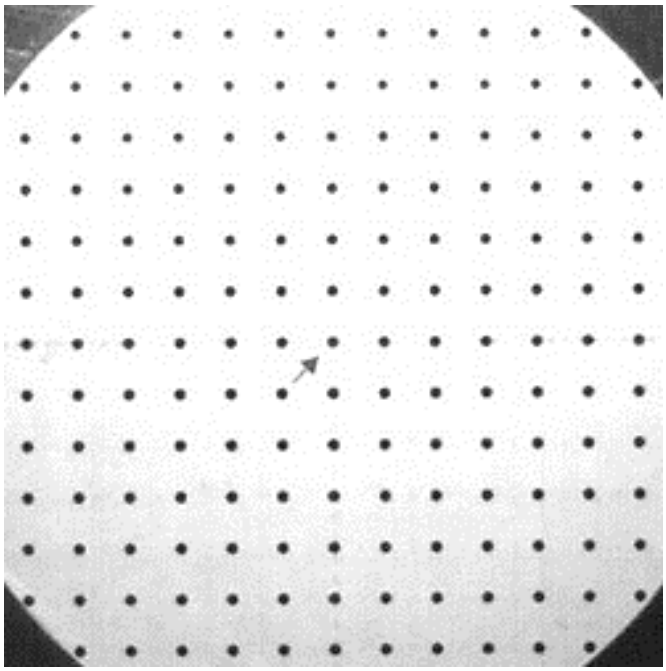

(a)

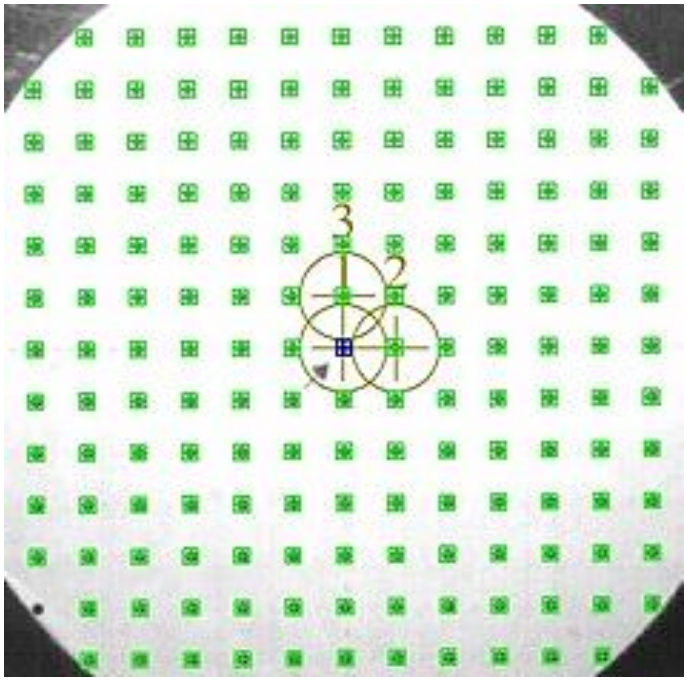

(b)

Figure 3.9: Camera calibration, (a) Image of the calibration plate. (b) Calibration result, taken from Dantec dynamic studio software, for the CCD camera applied in the PIV measurements, σ =0.09802 pixel.

The camera could be adjusted to work in three modes, providing different exposure times: (i) A continuous recording, free-run mode, could be used for long exposure time at low frequencies; (ii) A single exposure mode, in which images could be

acquired for auto-correlation or a single frame cross correlation PIV technique; and, (iii) A double exposure mode that allowed a camera to record a pair of images on separate frames. For the purpose of the work presented in this thesis, the camera was operated in the double exposure mode.

3.4.5 Synchronisation System

To capture images of the flow field and propagating flames with the PIV, the laser pulses, camera and ignition system must be triggered to operate in the correct sequence appropriate to the investigation. A computer-controlled synchroniser, or timer box, (Dantec, model 80N77), achieved this task, operating separate units together as an integrated automated system, following sequential operations as shown by Fig. 3.10. Internal trigger and external trigger modes can be employed, to start the timer box. For safety reasons, the external trigger mode was used through the present work.

Pressing the external trigger button generated a +5v TTL trigger signal. The rising edge of this signal triggered the start of the timer box, which was programmed to control the camera and the Nd: YAG laser pulsing sequence so that the laser pulses are located in the appropriate frames in the camera. The corresponding falling edge of the TTL trigger signal initiated a +12v CMOS pulse to trigger the ignition coil and generating a spark. The first laser pulse was set to fall at the very end of the first frame, and the next pulse at the start of the second frame. This was achieved by adjusting the first pulse delay and the time difference between the laser pulses, based on the velocity of the flow under investigation.

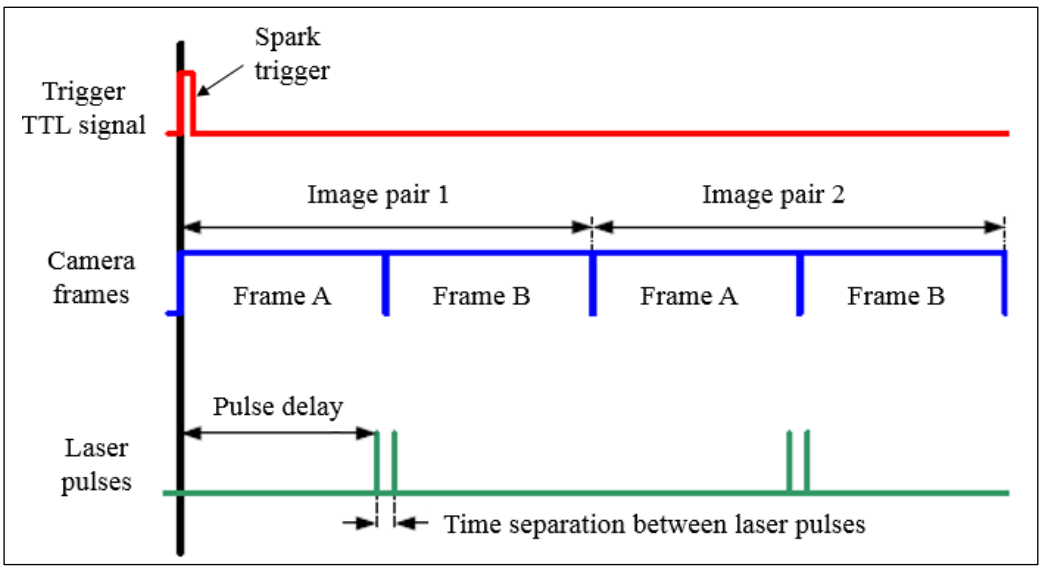

Figure 3.10: Sequence of triggering for camera, ignition system and laser pulses.

3.5 Experimental Procedure

Before an experiment, the vessel was preheated and an initial sealing test performed, in which the vessel was pressurised with dry air to the desired initial mixture pressure and monitored for at least five minutes, to ensure no leakage. The vessel was then evacuated twice down to 1.5 x 10^{-3} MPa, to ensure that the vessel was free from any undesirable residual gases from previous experiments. This ensured any residual gases were kept to a maximum of 0.06%. To charge the vessel, the required amount of seeding was first added, leading to a partial pressure increase of about 90 to 150 mbar, depending on the experimental conditions. This was followed by adding fuel and air, respectively.

To add gaseous fuel, the relevant needle valve was opened until the required partial pressure of fuel had been added, as indicated by the digital static pressure gauge. To add liquid fuel, the liquid volume of fuel required for each mixture was first calculated, using ideal gas laws, known volume of the vessel, fuel composition and density. A Hamilton glass gas tight syringe was then filled with the required amount of fuel and connected to the vessel via a liquid fuel delivery port. This syringe had stated accuracy by the manufactures of 0.5% at full scale. With the vessel under low pressure at 15 x 10^{-3} MPa, the port valve was then opened and the fuel drawn in due to the pressure difference. The valve was then closed and the associated partial pressure from the evaporation of the fuel was confirmed via the digital static pressure gauge.

Air was then added to the desired initial mixture pressure whilst, ensuring the mixture temperature had stabilised to the desired initial mixture temperature. During mixture preparation, the fans were in operation, at 806 rpm (u'=1 m/s), to improve mixing and temperature distribution. During laminar experiments, the fans were switched off prior to ignition and a 15s time period was allowed, to ensure a full decay of turbulence and allow the mixture to equilibrate and become quiescent. Whilst, the fan speed was adjusted to that required, during the turbulent experiments. Once the fans had reached the desired speed, as indicated by the digital fan-speed readout in the controlled area, a minimum of 5s was allowed to ensure full development of turbulence. This also allowed sufficient time to arm the triggering system, perform a final brief visual inspection, and return to the protected area. After ensuring the initial mixture pressure and temperature were as required, the static pressure transducer and inlet air supply were isolated, by remotely closing ball valves, and finally, the trigger button pressed.

After combustion, the burned gases were exhausted via a remotely operated exhaust valve. This ensured the vessel was depressurised to a safe level before leaving the protected area. The fans were then reactivated, the static pressure transducer and inlet air supply isolation valves reopened, and the vessel flushed with dry air for at least one minute to aid the evacuation of burned gases. During this time the acquired data were saved in a database within the Dantec dynamic studio software. Five explosions were performed for each given conditions throughout the current study.

3.6 Data Processing

The present work involved a large number of experiments, including combustion and cold flow measurements, and thus many thousands of images were processed. In the case of combustion, the flame speed and unburned gas velocity were derived, as discussed in Sections 3.6.1 and 3.6.2, respectively. Further analyses, such as determining burning rates, could be applied (see Section 4.2). Whilst, only the air velocity was required for the cold flow study, to measure the turbulence characteristics (see Section 4.3).

3.6.1 Flame Image Processing

A series of MATLAB automated batch processing tools were developed by the present author, to process the flame images. The tools operated directly on the digital images from the PIV measurements. Figure 3.11 illustrates the steps undertaken to process these images, with the use of a sample image for laminar and turbulent stoichiometric methane flames at 300 K and 0.1 MPa. The first stage of processing identified the location of the flame edge, tracking its progression from one image to the next, using a phase boundary detection tool based on Otsu's method (Otsu, 1979). The tool used a combination of global thresholding and local thresholding to determine the flame boundaries. The location of the flame edge was defined by the disappearance of the oil particles, T=573 K, as they evaporate in the preheat zone of the flame front, as discussed in Section 3.4.3. The flame edge was identified from the images by initially enhancing the low level light present in the images, using an image balanced tool. Such tool corrects light sheet non-uniformities that affect the outcome of other analysis routines. The low intensity particles help to distinguish between the burned and unburned regions. The flame edge was then identified from the sharp gradient in light intensity present at the burned/unburned gas interface. The detected flame edges were smoothed

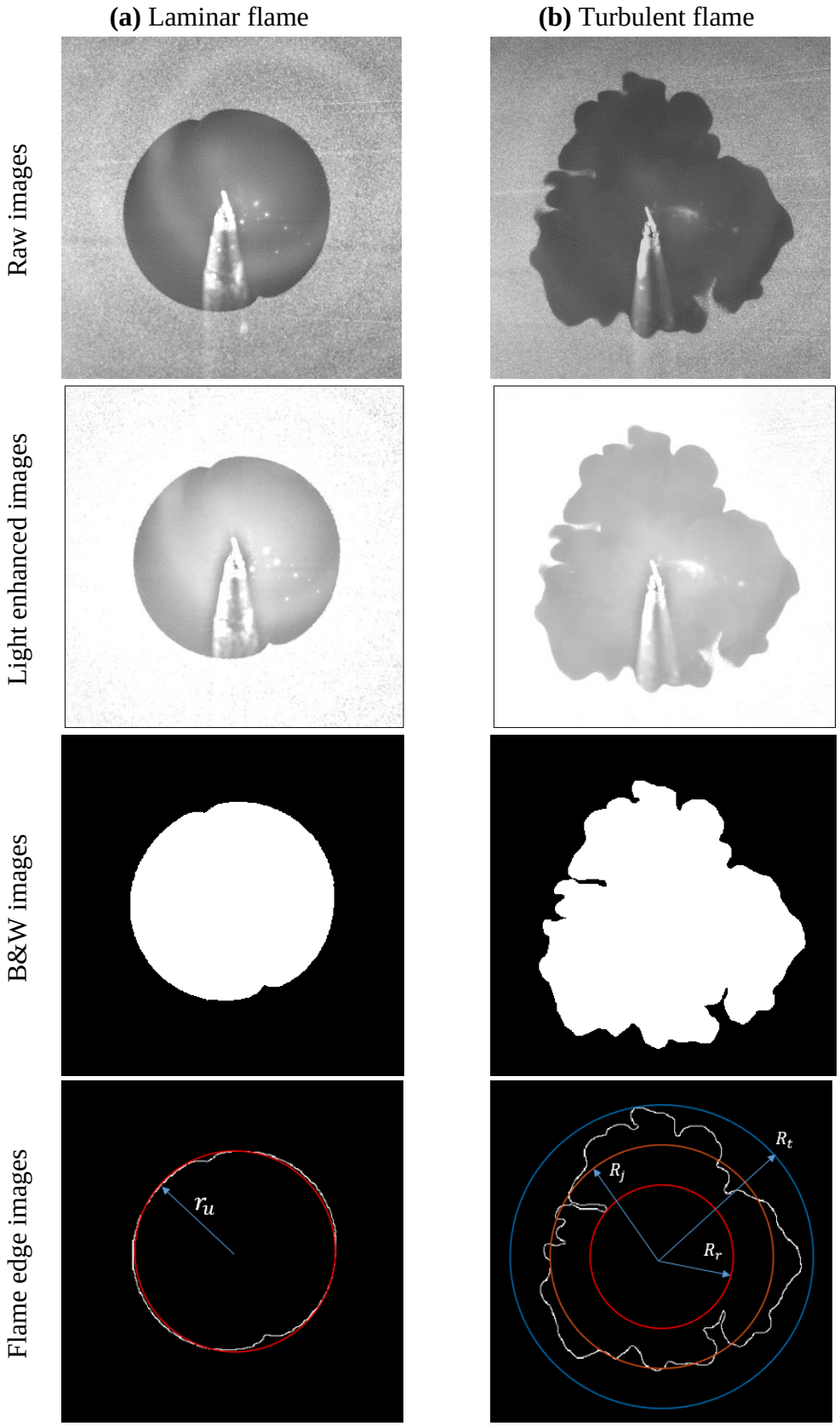

Figure 3.11: Image processing for, (a) laminar flame and (b) Turbulent flame.

by a low pass filter to remove any noise. For laminar flames, a least squares algorithm was used to calculated the best fit circle to the flame edge and the corresponding flame radius, r_u, from which the flame speed was calculated ($S_n = dr_u/dt$), as discussed in Section 2.2. Whilst, the required turbulent flame radius and its flame speed were calculated, as discussed in Section 2.4.

3.6.2 Evaluation of Velocity Vectors

After images of the seeding particles were recorded by the PIV system, an evaluation was made in order to determine the velocities present. As only a double exposure mode, allowed the camera to record a pair of images on separate frames, was employed throughout this work, the evaluation relevant to this form or recording was considered. An adaptive algorithm was employed within the Dantec software, hereafter referred to as the Adaptive PIV method. This was an iterative and automatic way of calculating velocity vectors, based on the seeding particle density and flow gradients. The first step in this method was to divide the recorded image pair into spatially matched interrogation areas, IAs. The orientation, shape, and size of individual IAs were iteratively adjusted to fit the local seeding densities and velocity gradients, as shown in Fig. 3.12.

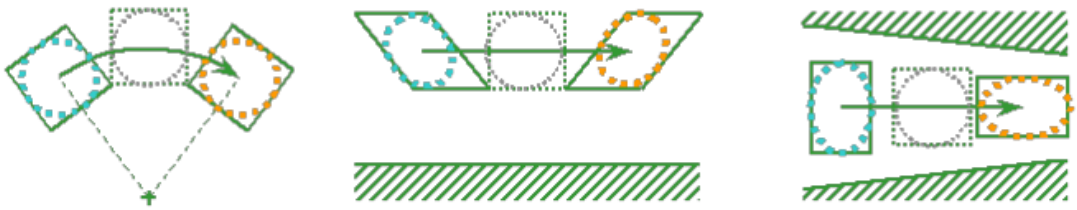

(a) **(b)** **(c)**

Figure 3.12: Shows the variation of the orientation of the shape and size of an IA, with the flow, (a) how it rotates while moving, (b) Short move near the wall and long move with the free flow, (c) Vertical squeeze and horizontal stretch. Reproduced from Dantec dynamic studio 2015.

The appropriate IA size was automatically determined for each individual IA, by specifying maximum and minimum size limits. A first iteration always used the largest IA size, which was reduced in subsequent iterations. This allowed reduction of IA sizes where the particle density was sufficiently high. When the translational part of the IA shape correction was less than the specified convergence limit, the iteration was stopped for the given IA and continued for other IAs. The minimum IA determined the location

and magnitude of vectors. Figure 3.13 shows an example of this iteration process. In Fig. 3.13a the results after the first iteration and in Fig. 3.13b the same area after the second iteration. The blue rectangles illustrate the IAs, scaled down to prevent them from overlapping in the display. In Fig. 3.13a, the red rectangle shows the actual IA size and in Fig. 3.13b the IA translation in yellow. Comparing Fig. 3.13a and Fig. 3.13b, the IA size was clearly reduced from the first to the second iteration. When an iteration was converged, the blue rectangle turned to green.

The second step of the adaptive PIV method was to match and correlate pixel by pixel the intensity field recorded from the light scattered by the particles existing within an IA of the first illumination image with that of the corresponding IA of the second illumination image and then calculate the mean displacement for that area. The matching and correlation process involved spatially shifting one IA with sub-pixel accuracy with respect to its matched IA on the other image, calculating the degree of correlation associated with that position. The correlation was calculated for all possible shifts, resulting in a correlation map which represents the correlations versus the displacement in X and Y plane with many small peaks representing the noise and only one dominant peak, as shown in Fig. 3.14. This dominant peak corresponds to the average particle displacement. Its location was chosen to be associated with the edge of the minimum IA. The peak/noise ratio was ~ 14-18 for the most cases reported in this thesis.

A sample of the PIV raw data collected in the present study and its vector field after processing is shown in Fig. 3.15. The difference in the light intensity between the first frame and second frame in Fig. 3.15a is negligible with less variation of the intensity within each frame that suggests a uniform laser pulses and a homogeneous distribution of the seeding particles. In Fig. 3.15b, there is a velocity vector for each IA in the plane of measurement which suggests a sufficient amount of seeding was used during the experiment. More details about the adaptive PIV method can be found in Appendix A.

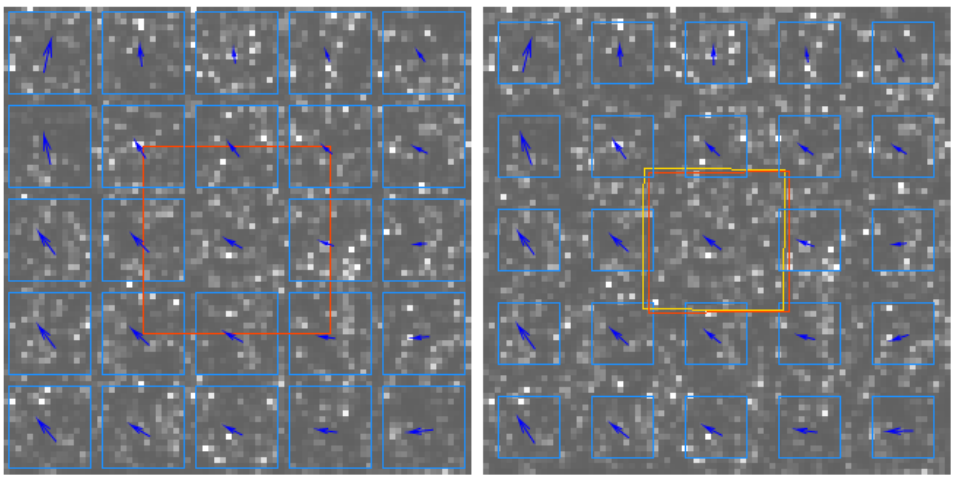

(a) **(b)**

Figure 3.13: Shows an example of the adaptive PIV iteration process, reproduced from Dantec dynamic studio 2015.

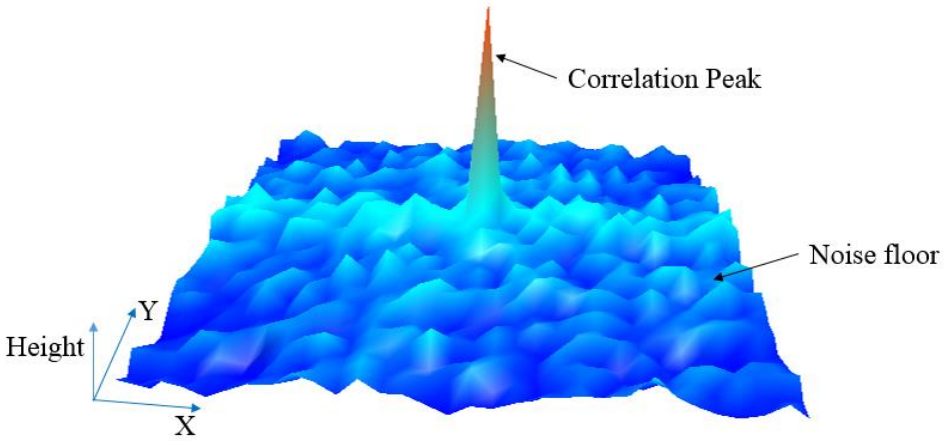

Figure 3.14: Shows the adaptive PIV correlation results, with IA_{min} of (16×16 pixels) and IA_{max} of (32×32 pixels), taken from the present work.

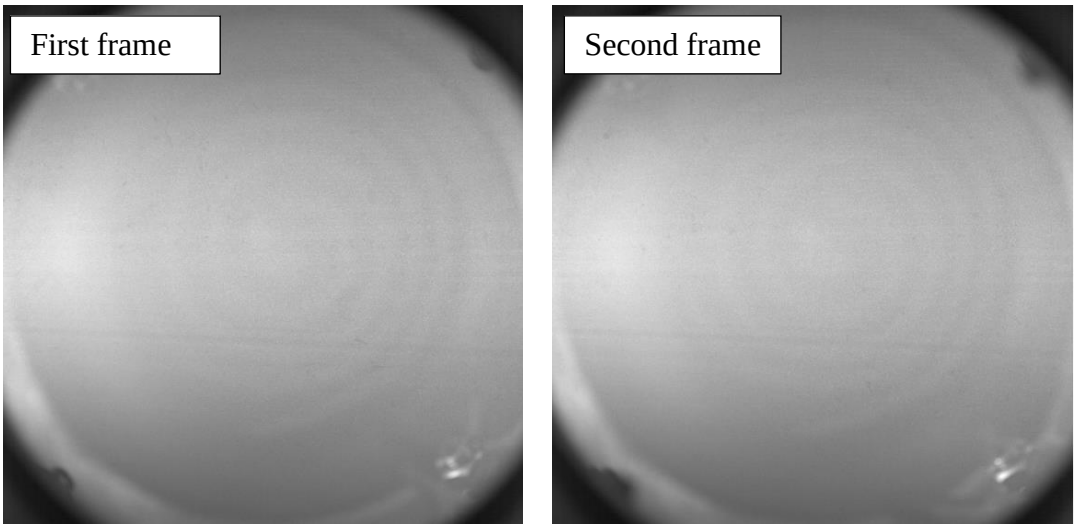

(a)

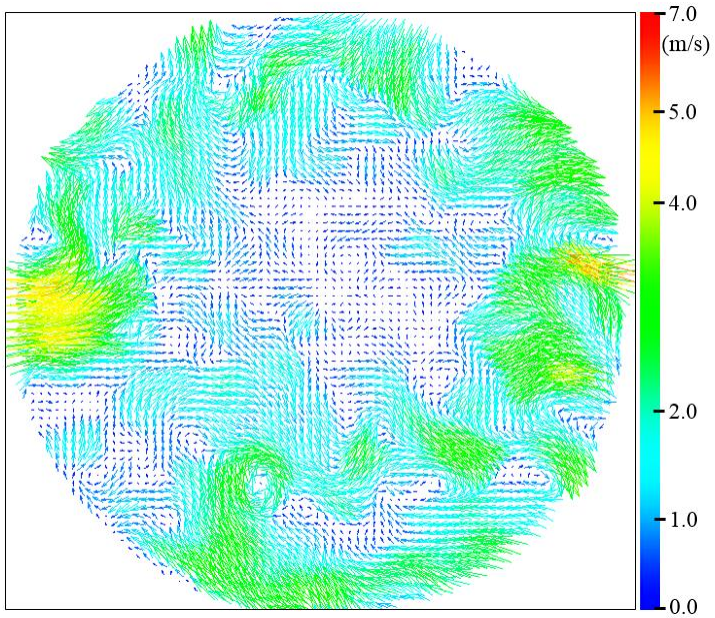

(b)

Figure 3.15: Sample of the PIV raw data collected in this study and its vector field after processing, at fan speed 2,000 rpm (a) First and second frames of PIV raw image, (b) PIV vector field after processing, with IA_{min} of (16×16 pixels) and IA_{max} of (32×32 pixels).

3.7 Error analysis

3.7.1 Random errors

The technique for measuring the burning velocity detailed within this chapter operates by recording the displacement of the flame front over a known time period. The inaccuracies that occur within this process are therefore linked to how precisely those

positions can be ascertained in both time and space. The position of the flame fronts recorded using the PIV system can only be measured to the nearest pixel location due to the analysis routine used and digital nature of the recording, it is therefore dependent on the image area and camera resolution. For the case of the example data shown in section 3.6.1 the image size was 120 mm square, recorded using a high-resolution Phantom ultra-high-speed UHS-12, model v2512, CCD camera which had a resolution of 1024 by 1024 pixels. As a result, the flame leading edge of the flame position, recorded at the isotherm where the oil particles are vaporised, can only be determined to within a tolerance of ±0.11 mm. The curvature of the flame perpendicular to the laser sheet will also induce a bias in flame position. This bias that varies depending on the location of the flame relative the vessel centre. However, as both instances of flame front identification suffer from the same bias and the displacement of the flame between images is small, its effect on flame velocity measurement is very small, 0.1 mm in the worst case. Mean value of burning velocities were used, at each condition, to minimize the error in processing procedures. As a result flame edge locations can only be determined to within an accuracy of ± 0.02 mm.

3.7.2 Systematic Errors

(i). Errors in the amount of fuel

A syringe was used to inject the liquid fuels in the vessel, as described earlier. The maximum expected error in the syringe reading is one division and is corresponding to 0.01 cc, while the full scale is corresponding to 5 cc. Hence, the error in the fuel volume, in the worst case, is ± 0.2%

(ii). Errors in pressure measurement

A pressure gauge with an accuracy of ±0.05% bar is used for preparing mixtures. Hence the error, associate with the pressure measurement, is less than ±0.5 mbar if the experiment was performed under atmospheric conditions.

(iii). Errors in temperature measurement

The maximum error in the thermocouple reading is ±2 K which represent the maximum deviation from the true value obtained during calibration of the thermocouple, while the minimum temperature employed in the present work was 300 K. Hence, the error in the temperature measurement, in the worst case, is ± 0.7%.

Chapter 4 - Results

4.1 Introduction

The PIV technique was employed for measuring laminar burning velocities of some hydrocarbons, characterising the cold flow turbulence, and later observing the flow fields induced by turbulent flames. Details of the experimental procedures and the associated readings appear in Chapter (3). The current chapter presents the key derived results.

Flame speeds, S_n, and unburned gas velocities, u_g, from which the laminar burning velocities were calculated, are presented first in Section 4.2, for methane, *i*-octane, ethanol, and *n*-butanol over a range of equivalence ratios at atmospheric pressure and, in the case of *n*-butanol, also over a range of pressures. The PIV technique allows a direct measurement of the laminar burning velocity, by the measurement of the flame speed and gas velocity just ahead of the flame, as described in Chapter (2). Measurements made in this way were compared with those obtained from the flame speed method, which is based on the flame front propagation speed and the ratio of unburned to burned gas densities. Different values arise between the two methods, and the principal reason is the common assumption in the flame speed method that the burned gas density is at the equilibrium, burned gas, adiabatic temperature, as discussed in Chapter (5).

The PIV technique also enables direct measurements of turbulence statistics. A knowledge of these statistics and the aerodynamic characteristics of the turbulent flow enables a better analysis of flame/turbulence interactions. Also, the consistency of turbulent burning velocity measurements relies on the ability to attain near- isotropic and

homogeneous turbulence, with well-defined turbulence statistics. Thus, the turbulent flow characterization by means of spatial or temporal spectral analysis was essential. Section 4.3 presents the instantaneous velocity maps of the turbulent flow inside the vessel, from which the turbulence statistics were derived, using dry air in the absence of phase change and chemical reaction, for fan speed range, 1,000-6,000 rpm.

Finally, the spherical expanding turbulent premixed flames were investigated, to define and quantify the turbulent burning velocity, u_{tr} and the effective rms turbulent velocity, affecting the spherical flame wrinkling. Three equivalence ratios, φ = 0.8, 1.0 and 1.3, of methane/air have been employed at 300 K and 400 K, over range of pressures. Flame radii, flame speeds and the associated turbulent burning velocities, u_{tr} are presented in Section 4.4. Subsequent discussions of the experimental data within this Chapter are presented in Chapter (5).

4.2 Laminar Burning

Stretched laminar flame speeds, S_n, together with the unburned gas velocities, u_g, were measured at different conditions, for a variety of fuel/air mixtures, listed in Table 4.1.

Table 4.1: Laminar experimental conditions

Fuel	φ	P (MPa)	T (K)
(Methane) CH_4	0.6 – 1.3	0.1	300
(*i*-octane) *i*- C_8H_{18}	0.8 – 1.3	0.1	358
(Ethanol) C_2H_5OH	0.8 – 1.3	0.1	360
(*n*-butanol) *n*-C_4H_9OH	0.7 – 1.3	0.1 – 0.5	383

In the early stage of laminar flame propagation, the flame is subjected to a high stretch rate due to the relatively low flame surface area and the boost from residual spark energy. This high level of stretch helps in smoothing out any wrinkling of the flame surface and makes the flame stable, up to a critical radius, r_{cl} (Bradley and Harper, 1994). Beyond r_{cl}, where the flame stretch is no longer sufficient to stabilise the flame structure due to the hydrodynamic instabilities, the flame becomes cellular and some cracks propagate across the flame surface as described by Kuznetsov and Minaev (1996). This phenomenon can be clearly seen from Figs. 4.1 to 4.4, which show the development of stoichiometric *n*-butanol/air laminar flame, at 0.1 MPa and 0.5 MPa, respectively. Shown in the column (a) is a selection of flame Mie scattering raw images and in column (b) the corresponding velocity vector maps, with colouring to show the magnitude of the two

component velocity vectors. The time on all figures represents the elapsed time from ignition. At 0.1 MPa, Figs. 4.1 and 4.2, the raw images show the flame surface to be smooth with only two cracks, caused when the flame passed through the spark earth electrode. This has been observed for all lean fuel/air mixtures, listed in Table 4.1, at 0.1 MPa. As the equivalence ratio became richer, some cracks due to flame instability were formed, especially at φ = 1.2 and 1.3. At 0.5 MPa, these cracks were formed and propagated earlier, as shown from Figs. 4.3 and 4.4. As a consequence of this, the stable regime was reduced.

On the other hand, the vector maps show that the unburned gases to be pushed ahead of the flame front by the rapidly expanding burned gases. The velocity of these gases is maximum a head of the flame front and fall quickly with a distance away from the flame, satisfying mass conservation. At 0.5 MPa, the unstable flames causes disturbances in the flow ahead of the flame. However, there was no any sign of vortices generated in the flow a head of the flame front.

4.2.1 Flame Speed

The stretched flame speed, S_n, was calculated from the temporal evolution of the flame front, using the procedure described in Section 3.6.1. Figures 4.5 to 4.9 show S_n variation with flame radii, r_u, and corresponding S_n variation with stretch rate, α, given by Eq. (2.2), for all fuel/air mixtures, listed in Table 4.1. A single representative explosion was chosen of five experiments performed at each condition. In all cases, as equivalence ratio increases, the stable regime in which the burned Markstein length, L_b, can accurately be measured becomes increasingly limited, between the minimum unaffected spark radius of about 10 mm (Beeckmann et al. 2018) and the onset of cellularity, at the critical radius, r_{cl} (Bradley et al., 1996). As described in Chapter (2), r_{cl} is defined as the radius, at which S_n rapidly deviates from its prior response to stretch. The instability effect became considerably high at high pressure, as shown from Fig. 4.9b, where the critical radius is indicated by, *, for all φ.

From the plots of $S_n - \alpha$, using linear extrapolation within the stable regime of the flame, values of unstretched flame speed, S_s, were obtained as described in Chapter (2), from which the unstretched laminar burning velocity, u_{la}, was calculated using Eq. (2.17) and the flame speed Markstein length, L_b, was found using Eq. (2.18).

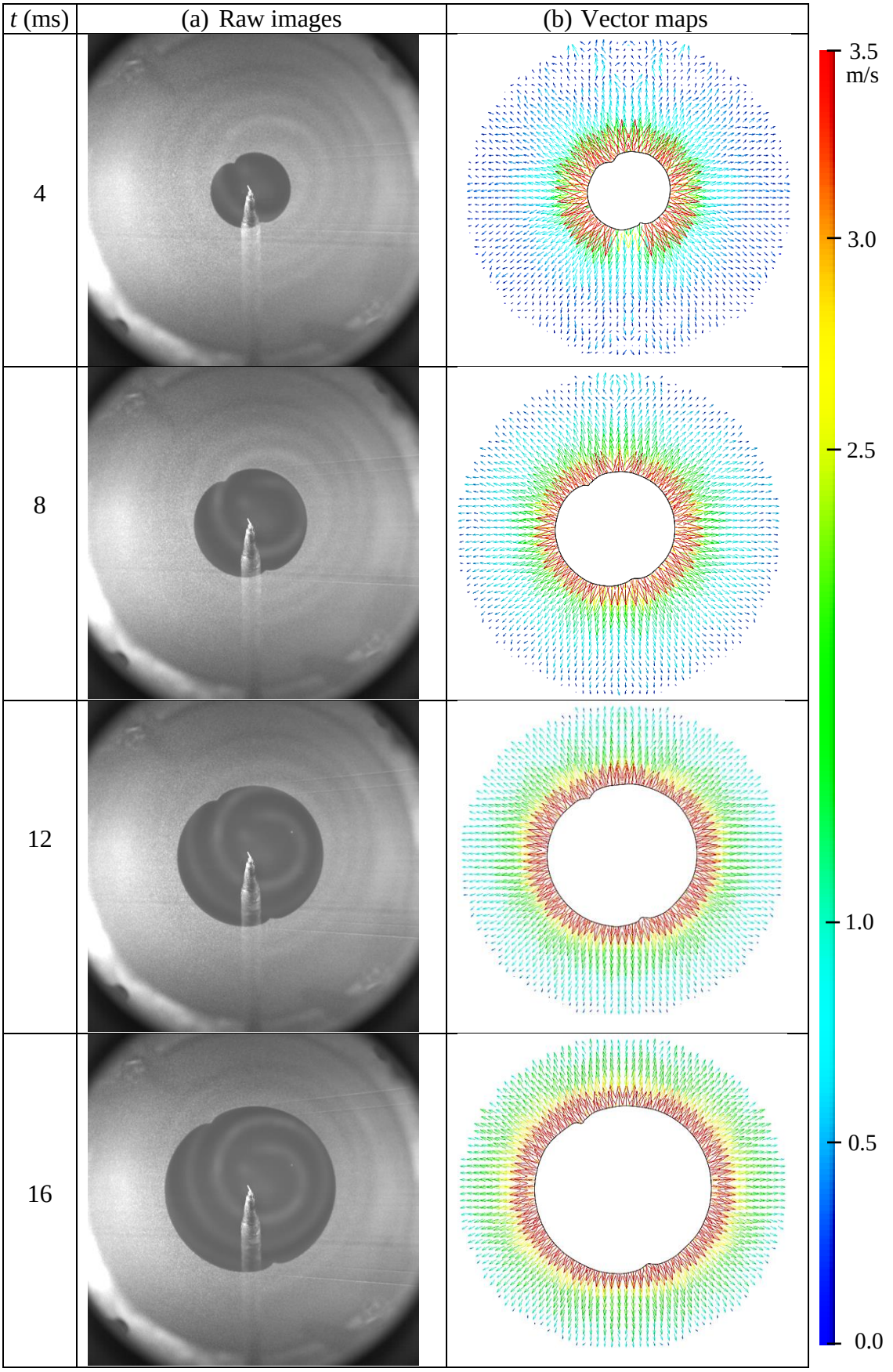

Figure 4.1: Development of *n*-butanol/air laminar flame, φ =1.0 at 0.1 MPa and 383 K, from *t* = 4 to 16 ms. (a) Raw images, and (b) Vector maps.

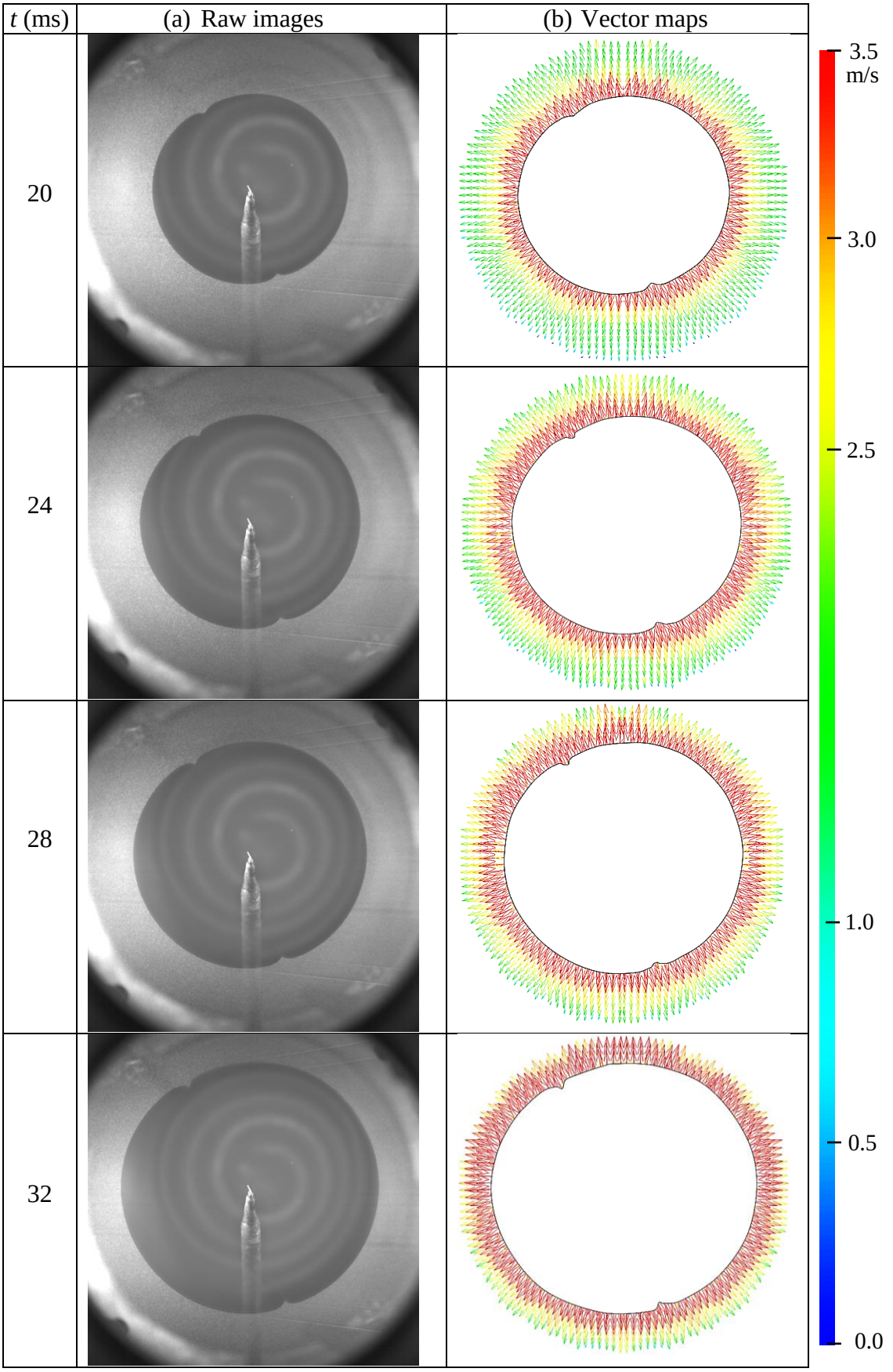

Figure 4.2: Development of *n*-butanol/air laminar flame, φ =1.0 at 0.1 MPa and 383 K, from *t* = 20 to 32 ms. (a) Raw images, and (b) Vector maps.

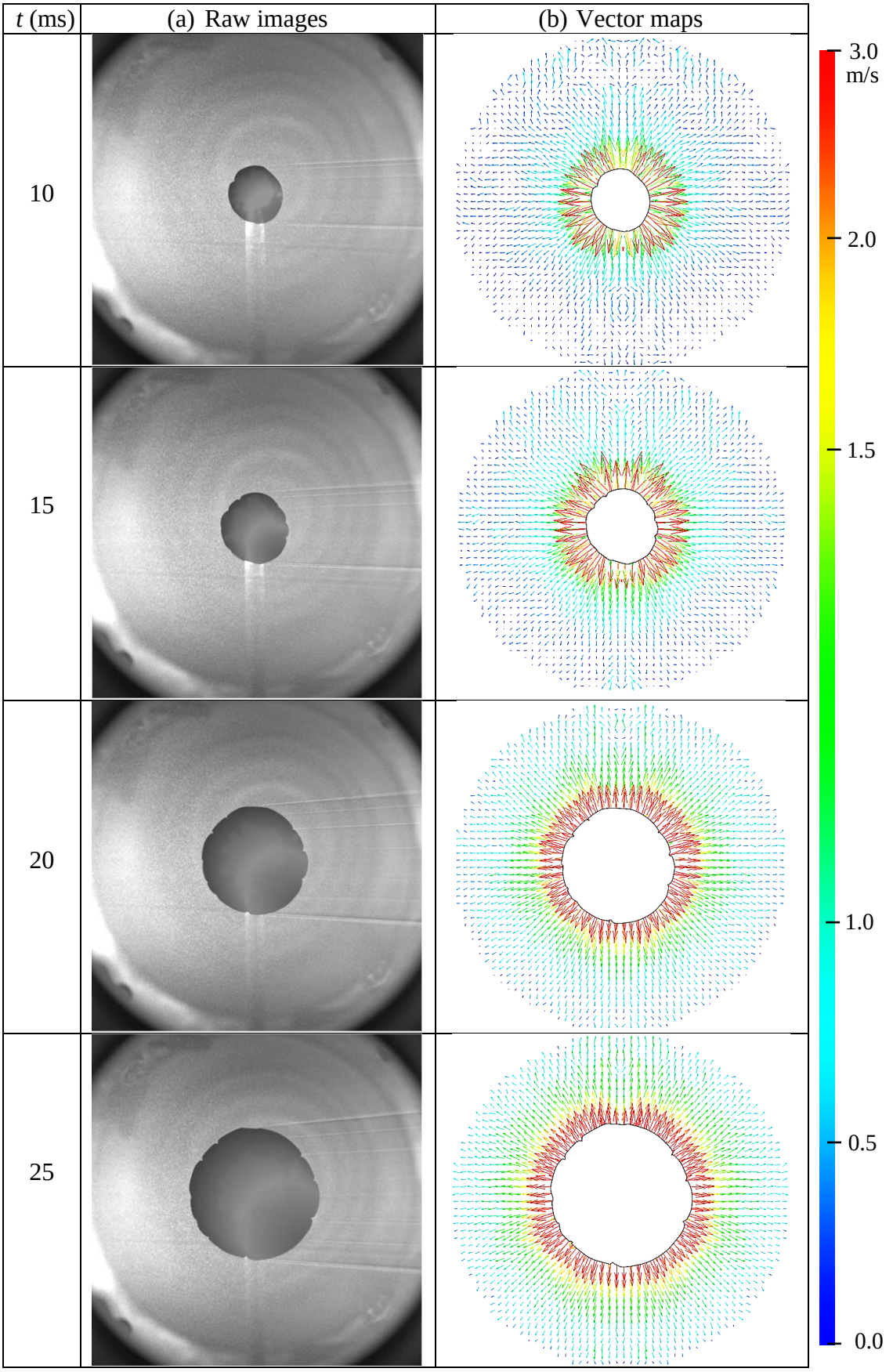

Figure 4.3: Development of *n*-butanol/air laminar flame, φ =1.0 at 0.5 MPa and 383 K, from *t* = 10 to 25 ms. (a) Raw images, and (b) Vector maps.

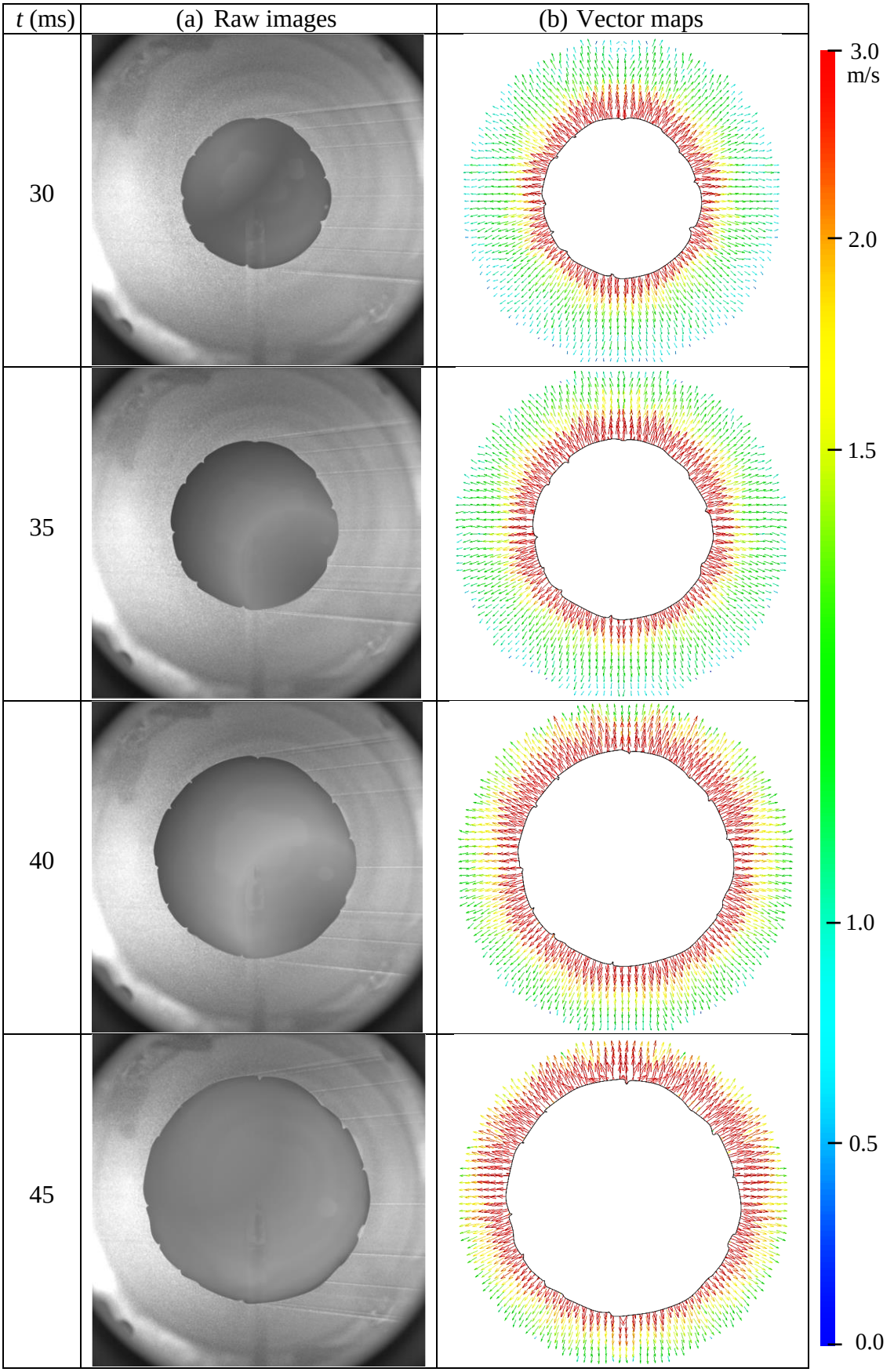

Figure 4.4: Development of *n*-butanol/air laminar flame, φ =1.0 at 0.5 MPa and 383 K, from *t* = 30 to 45 ms. (a) Raw images, and (b) Vector maps.

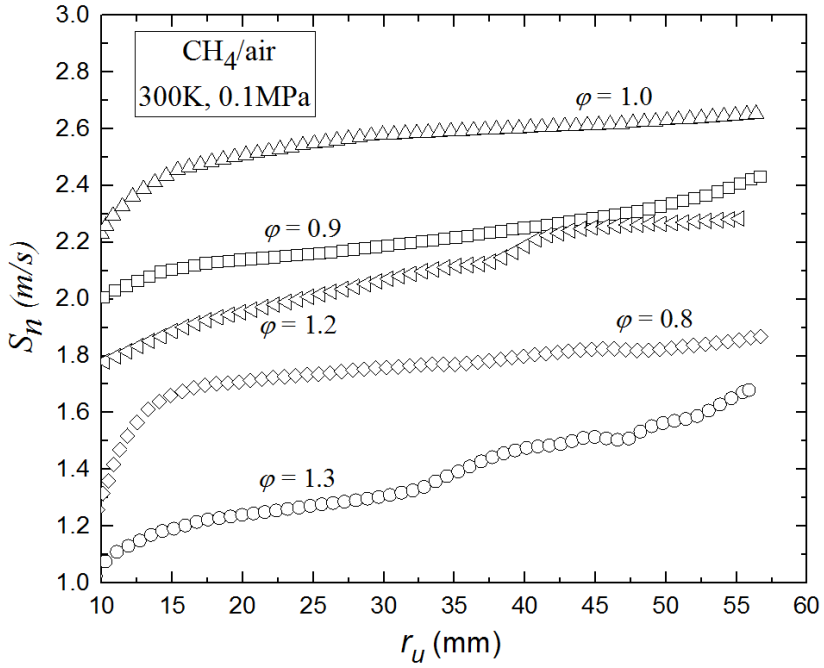

(a)

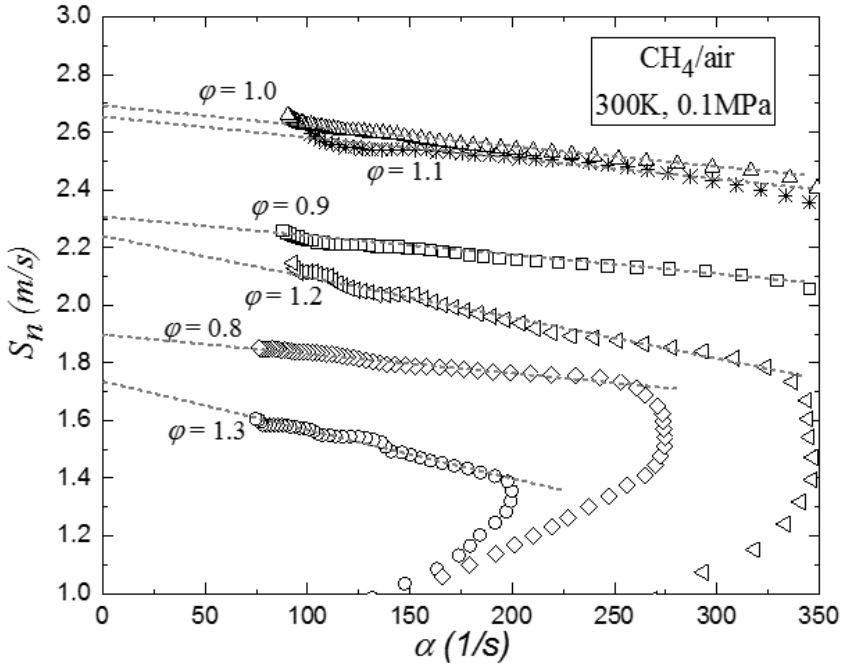

(b)

Figure 4.5: a) S_n variation with r_u, b) S_n variation with α, for methane/air mixtures at 0.1 MPa, 300 K and φ = 0.8-1.3.Dashed lines denote linear relationship extrapolation to zero stretch rate for L_b through data points.

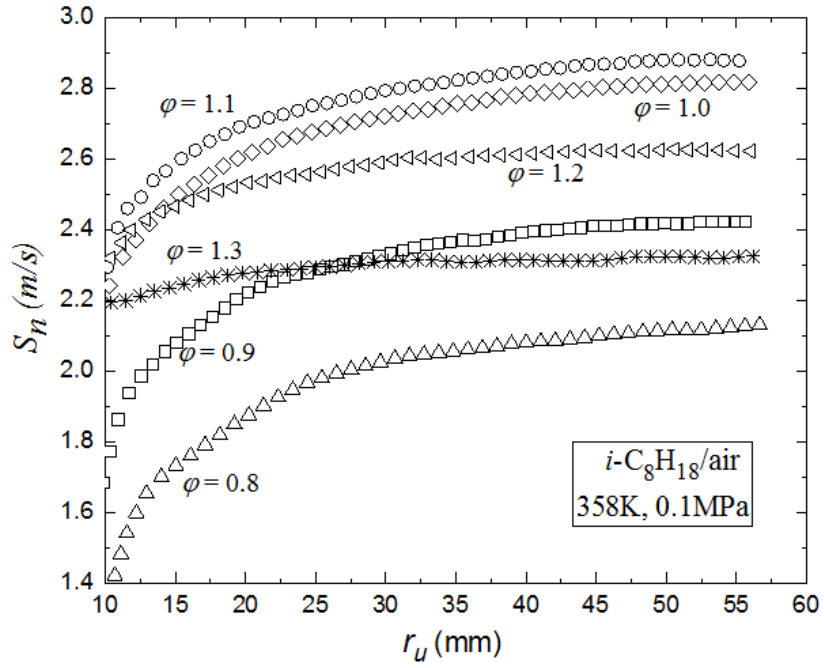

(a)

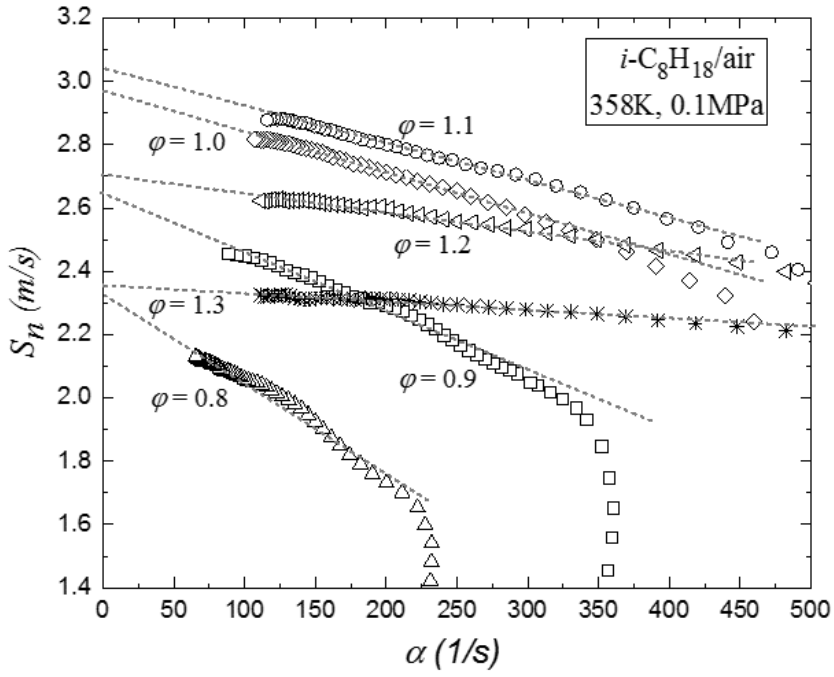

(b)

Figure 4.6: a) S_n variation with r_u, b) S_n variation with α, for *i*- octane/air mixtures at 0.1 MPa, 358 K and φ = 0.8-1.3.Dashed lines denote linear relationship extrapolation to zero stretch rate for L_b through data points.

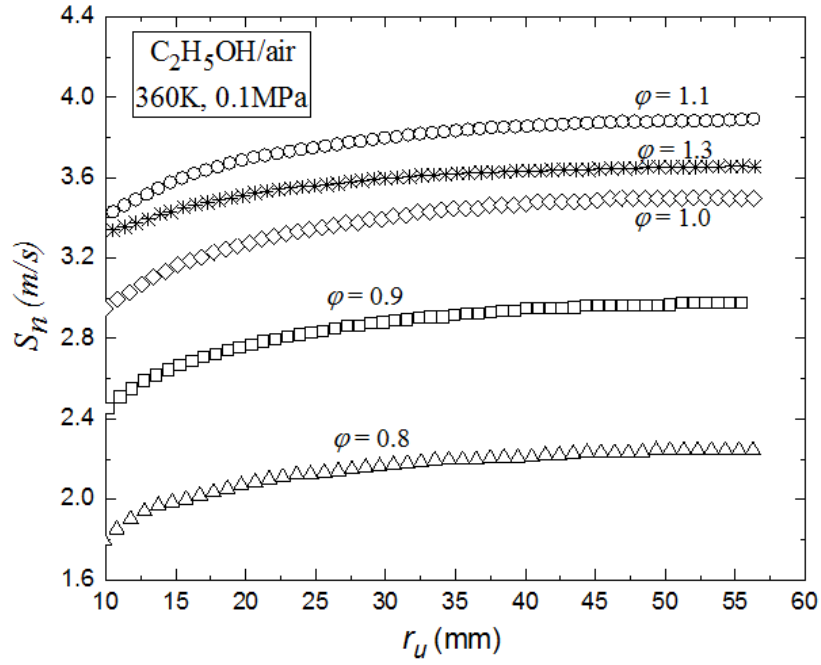

(a)

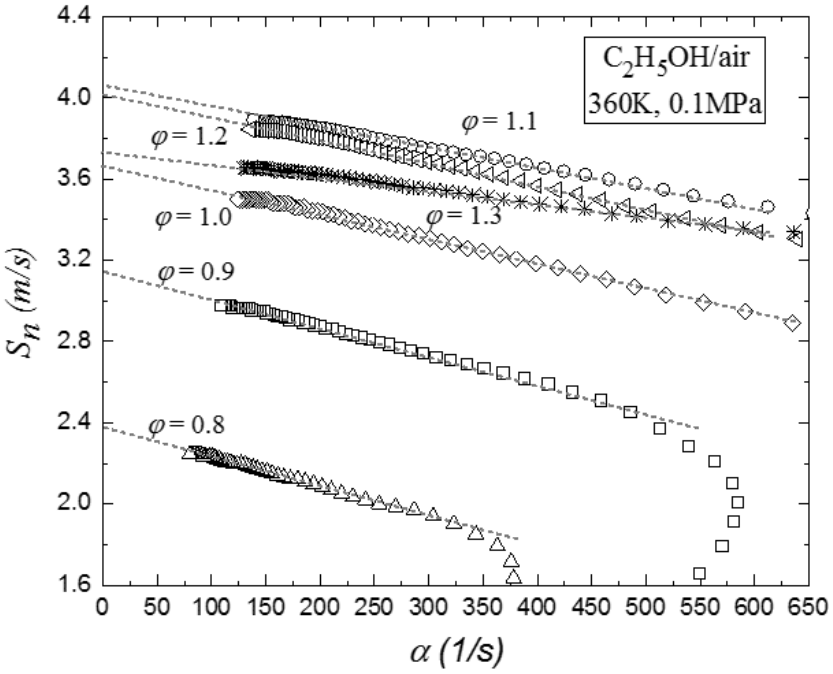

(b)

Figure 4.7: a) S_n variation with r_u, b) S_n variation with α, for ethanol/air mixtures at 0.1 MPa, 360 K and φ = 0.8-1.3.Dashed lines denote linear relationship extrapolation to zero stretch rate for L_b through data points.

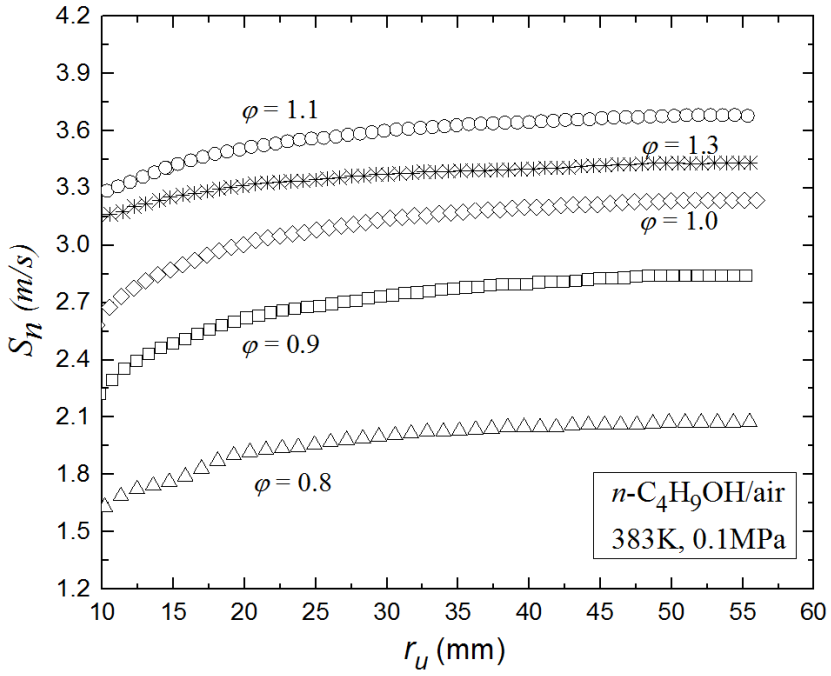

(a)

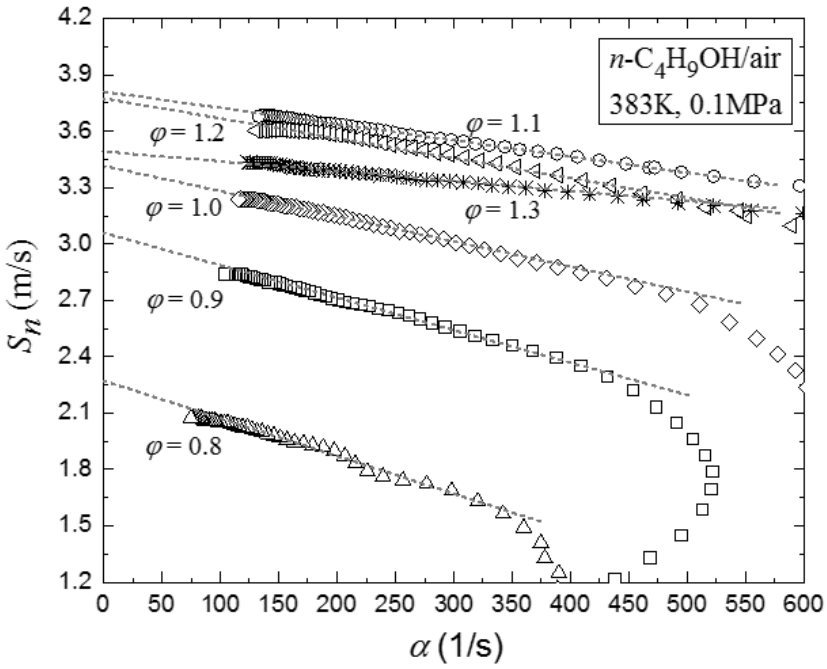

(b)

Figure 4.8: a) S_n variation with r_u, b) S_n variation with α, for *n*-butanol/air mixtures at 0.1 MPa, 383 K and φ = 0.8-1.3.Dashed lines denote linear relationship extrapolation to zero stretch rate for L_b through data points.

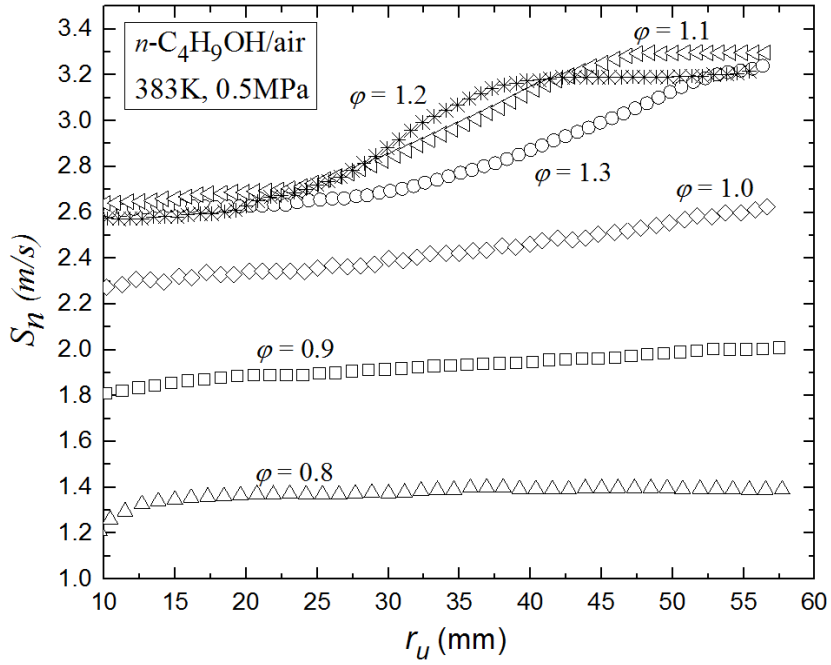

(a)

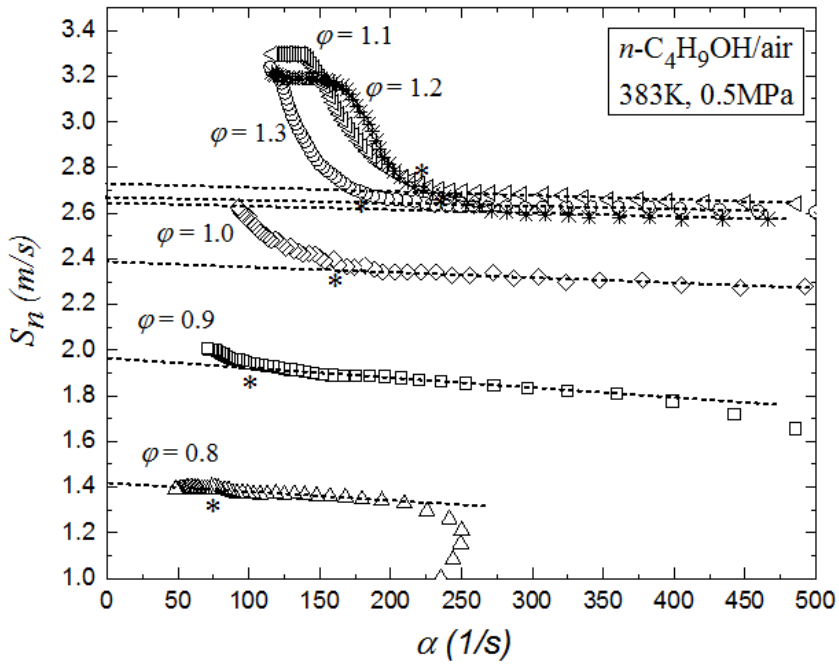

(b)

Figure 4.9: a) S_n variation with r_u, b) S_n variation with α, for *n*-butanol/air mixtures at 0.5 MPa, 383 K and ϕ = 0.8-1.3. Dashed lines denote linear relationship extrapolation to zero stretch rate for L_b through data points.

4.2.2 Unburned Gas Velocity

To characterise the velocity profile ahead of the laminar flame front, a sub-pixel tool was developed by the current author, and linked to the Dantec software to achieve the value of the minimum IA with one pixel step, after processing the Mie scattering images, using the procedure described in Section 3.6.2. The minimum IA employed 8 pixels along the flame front and 2 pixels in the normal direction to the flame (0.94 mm × 0.23 mm), while the maximum was (8 × 8 pixels ~ 0.94 × 0.94 mm). The radial velocity component was then calculated. An example of an instantaneous radial outward gas velocity profile for a methane/air flame is presented in Fig. 4.10, in which zero distance locates the evaporation isotherm. The maximum gas velocity, u_g, is obtained by fitting the velocity profile to a 6th order polynomial, which gives the highest value of R^2. This maximum value is located about 2–8 pixels (0.23–0.94 mm) ahead of the evaporation isotherm. Computational studies show a sharp change in gas velocity within the flame zone, with a much smaller variation ahead of the flame (Bradley and Mitcheson, 1976), as indicated by the profile of measured values, with the maximum value arrowed, in Fig. 4.10. The average value of the maximum unburned gas velocities around the flame front, indicated hereafter (u_g), was then calculated and used in Eqs. (2.21) and (2.15) to determine both the stretched laminar burning velocity, u_n and the mass burning rate velocity, u_{nr}, respectively. Figures 4.11 to 4.15 show u_g variation with flame radius, r_u, for all fuel/air mixtures.

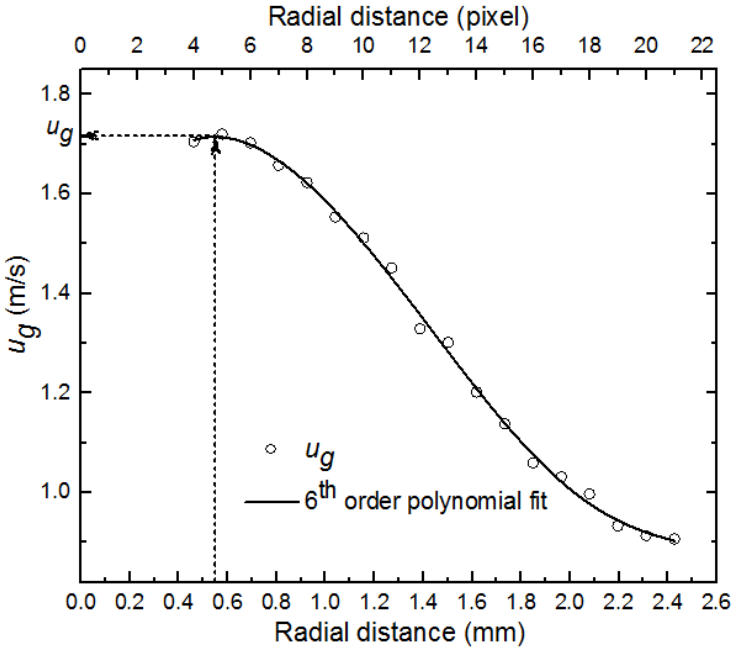

Figure 4.10: Gas velocity ahead of flame, methane/air, φ = 1.0, at 0.1 MPa, 300 K.

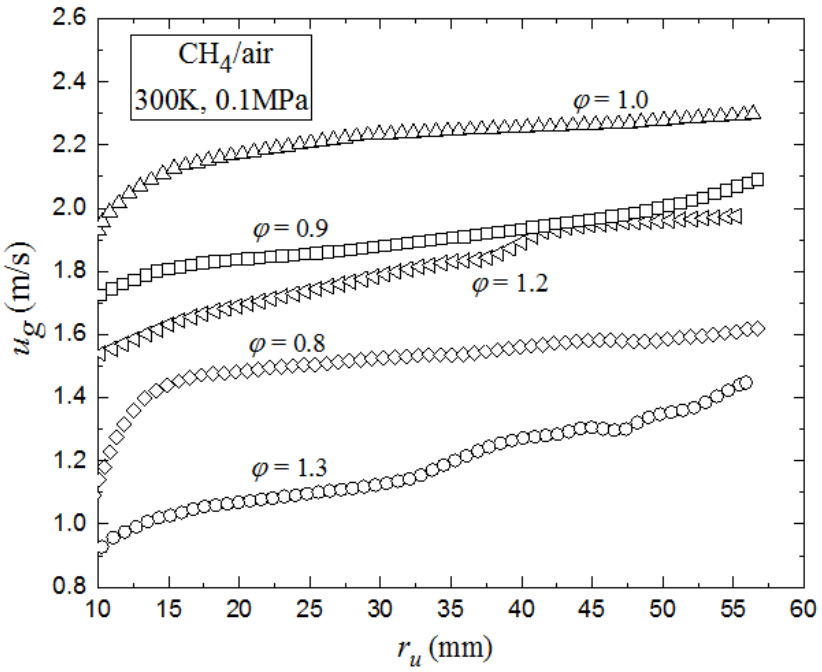

Figure 4.11: Variation of u_g with r_u, for methane/air mixtures at 0.1 MPa, 300 K and φ = 0.8-1.3.

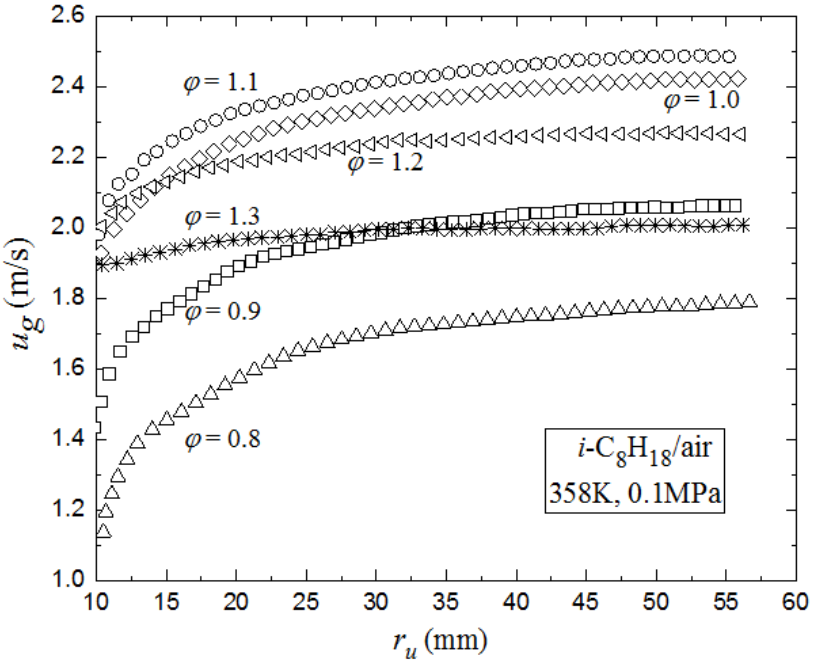

Figure 4.12: Variation of u_g with r_u, for *i*-octane/air mixtures at 0.1 MPa, 358 K and φ = 0.8-1.3.

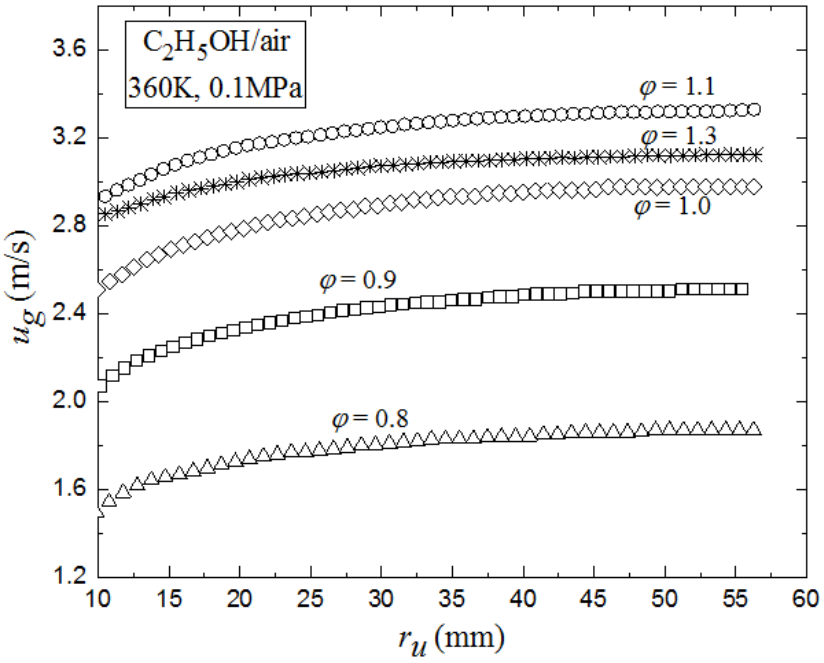

Figure 4.13: Variation of u_g with r_u, for ethanol/air mixtures at 0.1 MPa, 360 K and φ = 0.8-1.3.

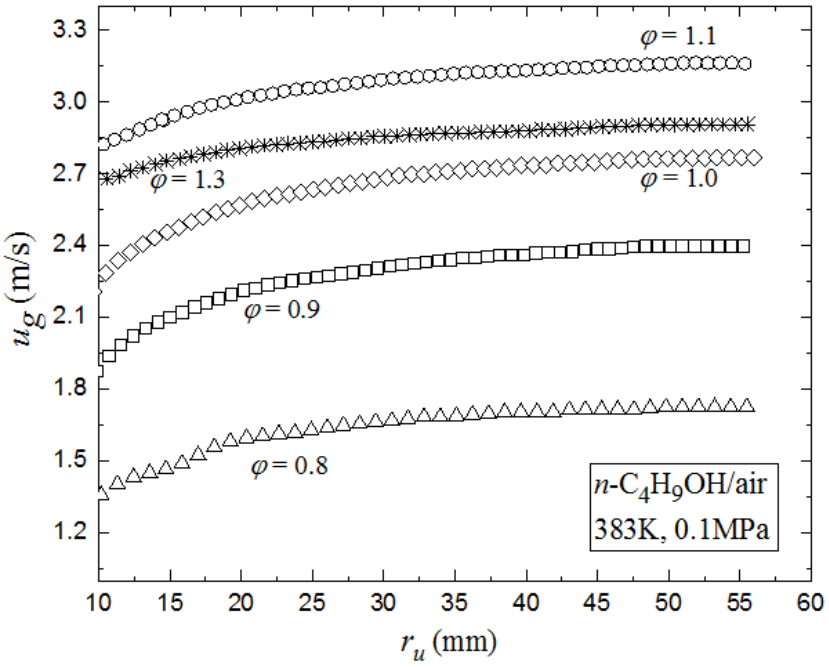

Figure 4.14: Variation of u_g with r_u, for *n*-butanol/air mixtures at 0.1 MPa, 383 K and φ = 0.8-1.3.

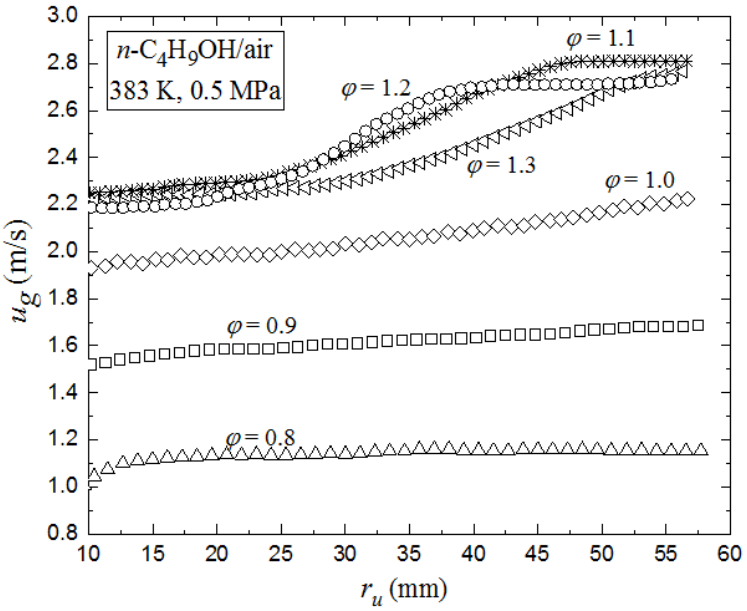

Figure 4.15: Variation of u_g with r_u, for *n*-butanol/air mixtures at 0.5 MPa, 383 K and φ = 0.8-1.3.

4.2.3 Laminar Burning Velocities

As discussed in Chapter (2), the flame speed method of determining u_{la} employs Eq. (2.17), with S_n plotted against α, given by Eq. (2.2); S_n is extrapolated to zero stretch rate, where $S_n = S_s$, and $u_{la} = (\rho_b/\rho_u)S_s$. Figure 4.16 shows such a plot for methane/air, φ = 1.0, at 0.1 MPa and 300 K. Values on the *y* axes are so chosen that the horizontal dashed line in the figure shows S_s on the secondary S_n axis and u_{la} from Eq. (2.17) on the burning velocity axis, with ρ_b/ρ_u calculated from the Gaseq code (Morley, 2005). Also plotted are PIV values of u_n from Eq. (2.21). Because the flame speed factor, S, and hence u_n/S_n, always decrease in an explosion, as S_n increases, u_n must decrease, as in the figure, and, from Eq. (2.15), u_{nr} must increase, also as shown.

The experimental values of S_n and u_n, plotted in Fig. 4.16, cover the entire stable regime between the minimum unaffected flame radius by the spark plasma, ~10 mm (Lawes et al., 2016, Beeckmann et al. 2018), and the critical radius, r_{cl}. At r_{cl}, the Karlovitz stretch factor, K, = $\alpha\delta_l/u_l$ attains a critical condition, with $\alpha = \alpha_{cl}$. The corresponding stability limit, in terms of α, is indicated by the short vertical line, K_{cl} = 0.016 in Fig. 4.16. In some instances, just prior to the rapid increase in flame speed, values of S_n became oscillatory.

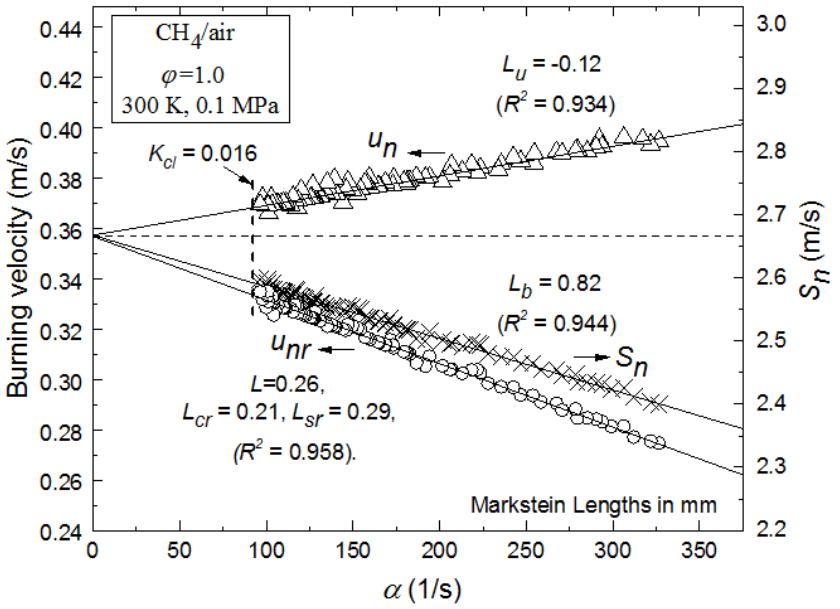

Figure 4.16: Variations of S_n, u_n and u_{nr} with α for methane/air mixtures, φ = 1.0, at 0.1 MPa and 300 K. Dashed horizontal line links u_n $(= u_l)$ and S_n $(= S_s)$ in Eq. (2.17).

In Fig. 4.16, the validity of the two experimental lines of S_n and u_n is confined to the markers. This suggests the flame speed method for measuring u_{la} is satisfactory. In contrast, for the stoichiometric *n*-butanol/air mixture in Fig. 4.17, the values of S_n and u_n do not converge on the same value of $u_n = u_l$ at $\alpha = 0$. Equation (2.10) is not satisfied, and clearly, from Fig. 4.17, $u_n/S_s > (\rho_b/\rho_u)$. The adiabatic equilibrium burned gas density, $\rho_{b,}$ is not attained and the actual density, $\bar{\rho}_b$, is higher than ρ_b. Derivation of u_{la} using the flame speed method with Eq. (2.17) at $\alpha = 0$ results in a value of u_{la} that is 8% lower than the extrapolated PIV value of u_l, suggesting ρ_b is too low.

4.2.4 Markstein Lengths

Values of u_{nr} were found from PIV data using Eq. (2.15) and L_{sr} and L_{cr} by numerical iteration of the u_{nr} data. In a first iteration, L_{sr} and L_{cr} in Eq. (2.20) were assumed equal. This yielded an optimal value of L= 0.26 mm, for this mixture in Fig. 4.16. Further iterations with separate values of L_{sr} and L_{cr} yielded the values given on the figure. The second iteration step plotted u_{nr} against α_{sr} and α_{cr} separately. This gave initial values of the corresponding L_{sr} and L_{cr}. The third step inserted these initial values into a Matlab code, developed by the current author, in which a series of iterations comp-

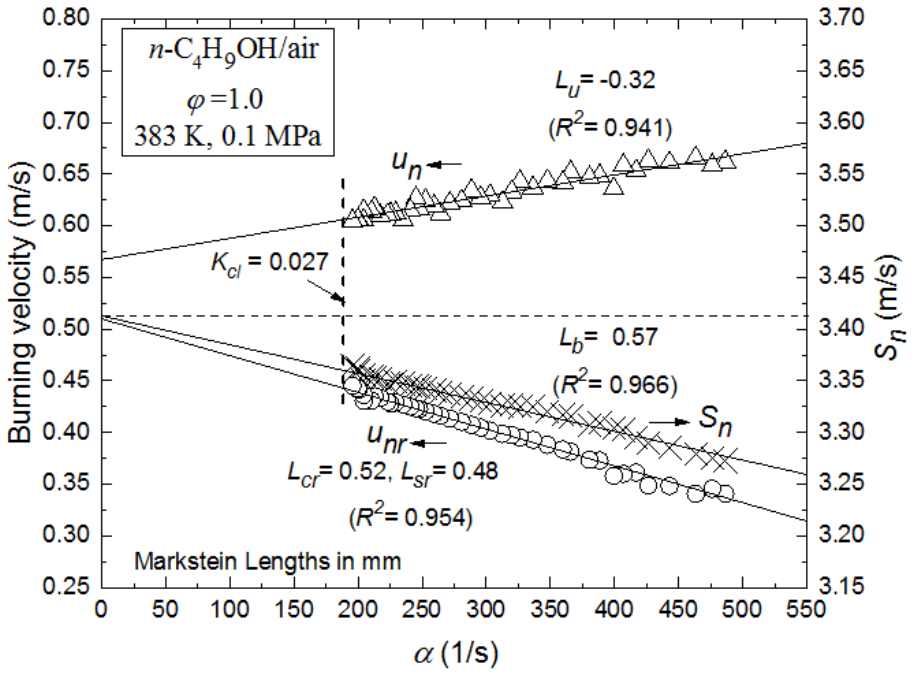

Figure 4.17: Variations of S_n, u_n and u_{nr} with α for *n*-butanol/air mixture, φ = 1.0, at 0.1 MPa and 383 K. Dashed line links $u_n\ (= u_l)$ and $S_n\ (= S_s)$ in Eq. (2.17).

-uted the associated values of u_{nr} from Eq. (2.15). These were sensitive to the combination of L_{sr} and L_{cr}. Those that gave the highest value of R^2 were adopted. These were L_{sr}= 0.29 mm and L_{cr} = 0.21 mm for methane/air mixtures, φ = 1.0, at 0.1 MPa and 300 K. This procedure was followed for all mixtures, listed in Table 4.1. Values of L_b, L_{sr} and L_{cr} for all the other mixtures are tabulated in Appendix B.

Although a value of unburned Markstein length, L_u, in, $u_l - u_n = L_u\alpha$ (Varea et al., 2012), is given in Figs. 4.16 and 4.17, Eq. (2.11) shows u_n, is not a sole variable with α, but depends upon other factors. Only in the later stages does it become a true burning velocity. Because L_u lacks the consistency of a Markstein length, no attempt is made to feature it or evaluate its two components.

4.2.5 Error Analysis of Linear S_n - α Methodology

In deducing the notional u_l of a spherically expanding flame, the methodology of linearly extrapolating the stable regime of the flame on a $S_n - \alpha$ plot to zero stretch became convention for many years. However, it is becoming widely accepted that in the case of strong nonlinear $S_n - \alpha$ behaviour, a nonlinear extrapolation methodology is necessary as to avoid over estimation errors that the traditional methodology would likely

incur. As mentioned in Section 2.2.4, the Markstein length is the gradient of $S_n - \alpha$ curve within the stable regime.

To increase the certainty of Markstein lengths measurements, average values from sets of five experiments were used. The variance of these five measurements was calculated by calculating the difference between each of the five measurements and the average. Then the squares of these differences were added and divided by five. Finally, the standard deviation was calculated by simply calculating the square root of the variance. Typically, this had a value of between 0.005 and 0.016 mm, in most cases.

Further discussion about the measurement of both laminar burning velocity and Markstein lengths can be found in Chapter (5).

4.3 Characterisation of Turbulence

As mentioned in Section 4.1, the accuracy of investigating turbulent flames relies on well-defined turbulence statistics. In the case of spherically expanding flames, the initial small flame front is not exposed to the full spectrum of turbulence. It is initially affected only by small length scale. As it propagates, the flame is wrinkled by the energy-containing small to progressively larger length scales of turbulence. Thus, the turbulent flow characterization by means of spatial and temporal spectral analysis is essential to for an understanding of flame/turbulence interaction.

The PIV system, described in Section 3.4, was employed to characterise the turbulence inside the vessel, using dry air, in the absence of phase change and chemical reaction, for fan speed range of 1,000-6,000 rpm, temperature range 300-400 K, and pressure range of 0.1-1.0 MPa. Each experiment was undertaken during about 2.5s, with the collection of an average of 12,500 images, at a frequency of 5 KHz. Larrson (2009) has shown no effect of the sampling time on the turbulence statistics. The adaptive algorithm within the Dantec software, described in Section 3.6.2, was employed to process the recorded images, with a minimum interrogation area of (16×16 pixels) and a maximum of (32×32 pixels), with a magnification ratio of ~ 0.117 mm/pixel.

The ways in which the instantaneous change with increasing fan speeds of 1,000, 3,000, and 6,000 rpm are shown in Figs. 4.18 to 4.20. For clarity, only half the vectors are displayed. The same colour code was used for all fan speeds, to allow comparison between different speeds. The time in all figures represents the instantaneous time, at which the image has been captured. The corresponding time averaged local mean velocity

vectors obtained, from 12,500 images are shown in Fig. 4.21. Both instantaneous and mean velocities increase with fan speed and radius, most markedly in the outer regions closest to the fans. Within the centralised circled regions in Fig. 4.21, the local mean velocity is less than 10% of the local rms velocity. Outside the circles mean velocities reach up to ± 0.4, ± 1.2 and ± 1.4 m/s at 1,000, 3,000 and 6,000 rpm, respectively. However, there is a similarity in flow patterns at all fan speeds, and the mean velocities are generally low. Further discussion about the homogeneity of the flow in the vessel, turbulence scales and the influence of P and T on theses scales can be found in Chapter (5).

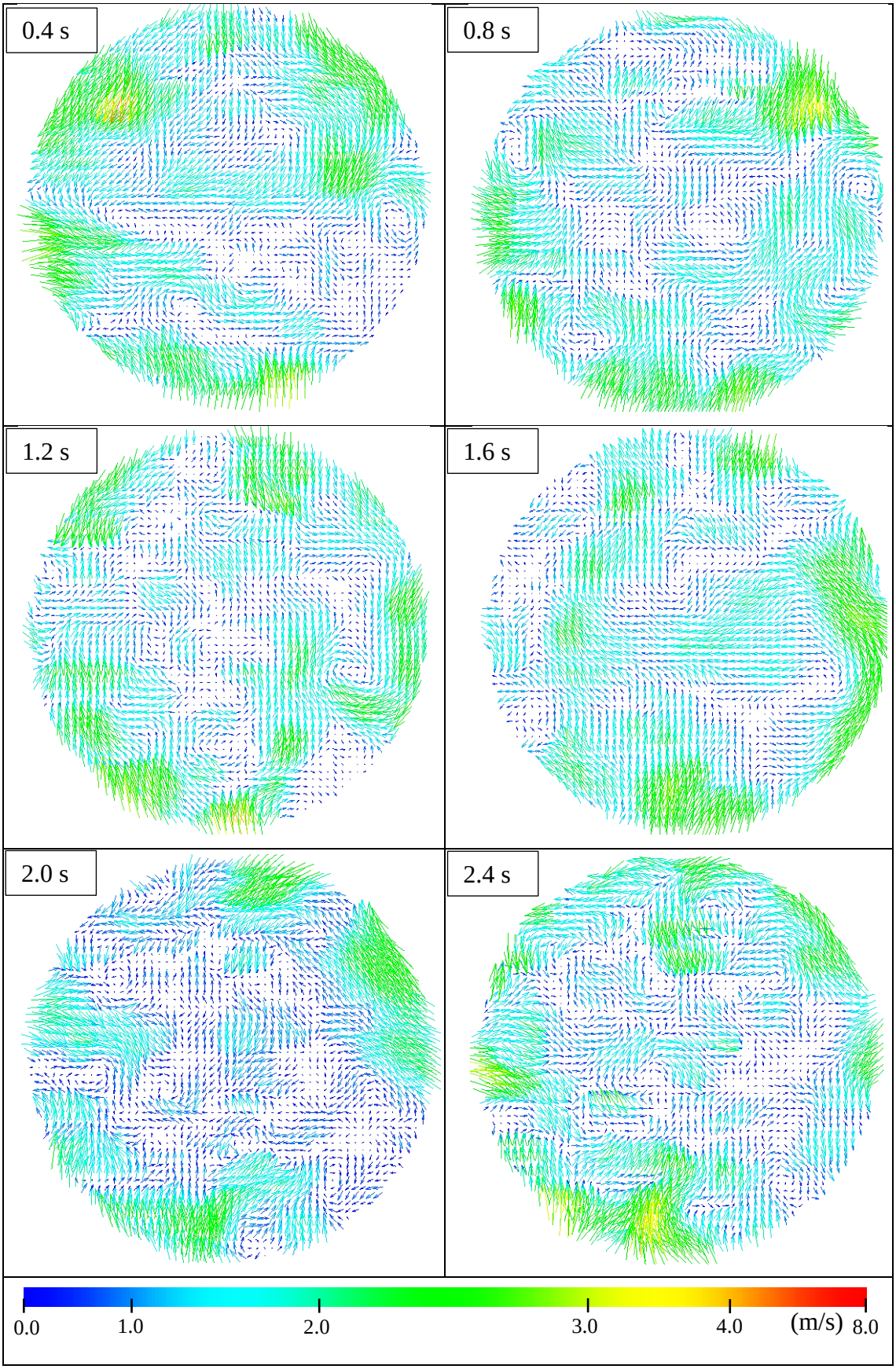

Figure 4.18: Instantaneous velocity vector maps, at different times, for fan speed 1,000 rpm.

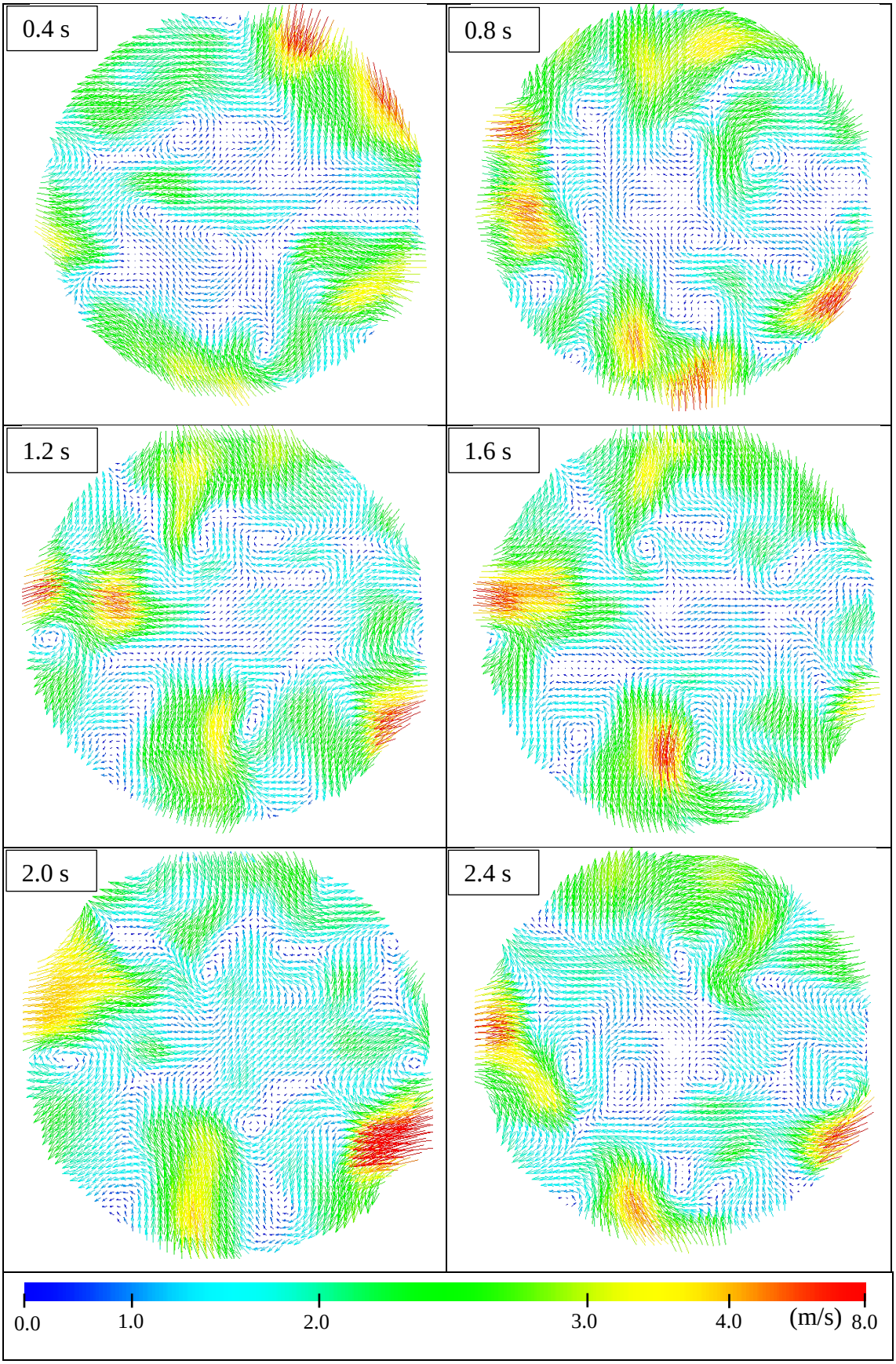

Figure 4.19: Instantaneous velocity vector maps, at different times, for fan speed 3,000 rpm.

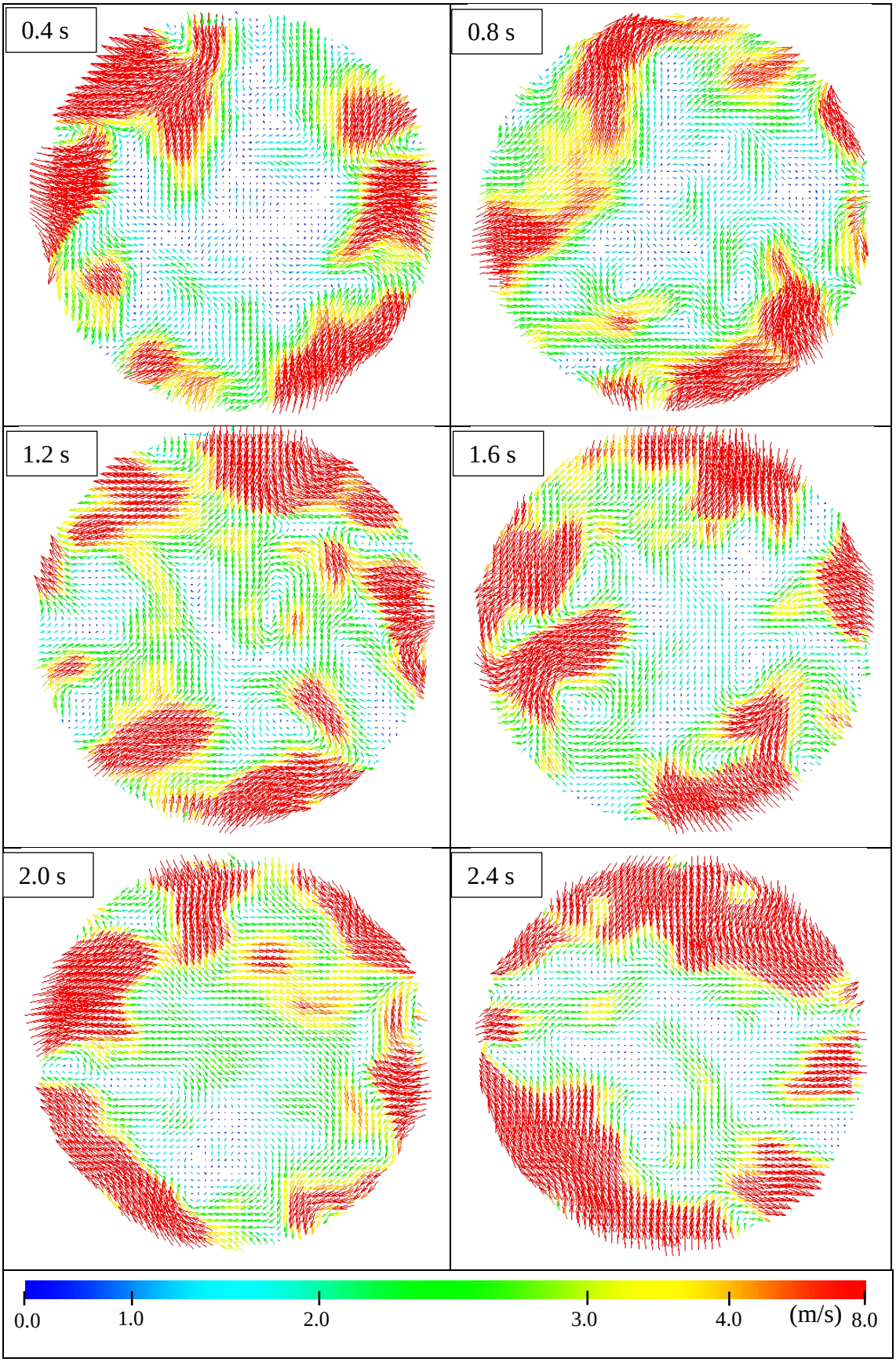

Figure 4.20: Instantaneous velocity vector maps, at different times, for fan speed 6,000 rpm.

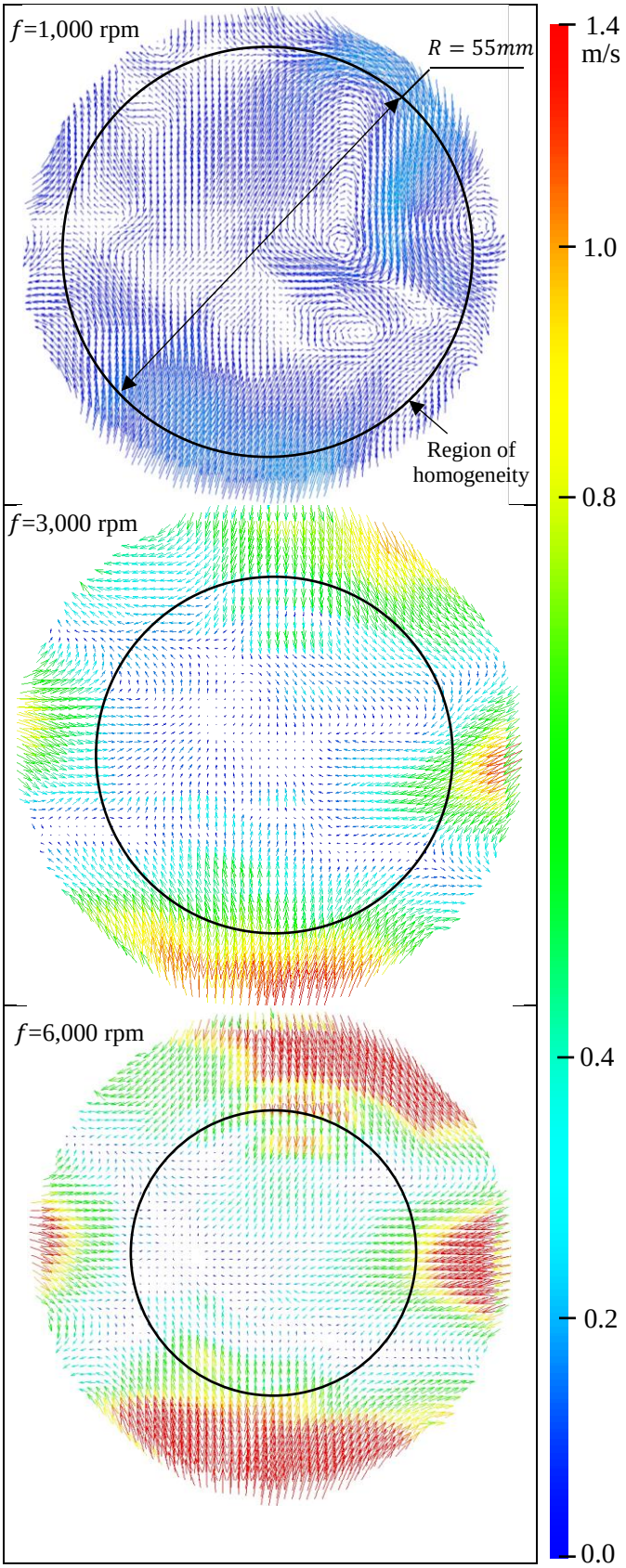

Figure 4.21: Examples of 2D mean velocity fields for fan speeds of 1,000, 3,000 and 6,000 rpm.

4.4 Turbulent Burning

This section presents the measured values of turbulent burning velocity, u_{tr}, of methane/air mixtures measured during spherical explosions in the fan-stirred vessel, with rms turbulent velocities, u', up to 4 m/s (~3226 rpm) and, φ= 0.8, 1.0 and 1.3. Initial pressures are 0.1 and 0.5 MPa, at initial temperatures of 300 and 400 K. Values were obtained as described in Chapter (2). At least, five explosions were conducted at each operating condition, in an attempt to minimize the irregularities associated with turbulence behaviour and the errors arising from capturing Mie scattering images in two dimensions only.

4.4.1 PIV Arrangements

It is useful to image as large an area as possible in order to investigate how the flame front propagation develops through its interaction with the turbulent flow field. With the available distance next to the vessel, window size and the capture angle of the lens, the maximum area that could be physically imaged at the central plane of the vessel was a region of 150 mm square, as discussed in Chapter (3). However, due to the finite resolution of the camera (1024×1024 pixels), this would result in poor spatial resolution of the measured velocity fields. Therefore, it was necessary to establish the maximum spatial resolution possible that ensures sufficient spatial resolution of the turbulent structures.

As the objective of this work is to investigate the relationship between flame and flow, the turbulent flow structures that have a strong influence must be resolved, while also preserving information of any bulk-flow behaviour. The integral scale of turbulence, L, within the vessel has been measured, by the current author, to be about 20 mm (see Section 5.2), indicating a relatively large scale flow structure, relative to the flame brush thickness. The Taylor microscale, λ, at atmospheric conditions, was about 2.24 mm, 1.53 mm and 0.71 mm, respectively, for u' of 1, 2 and 4 m/s. The Kolmogorov length scale, η, was calculated to be between 0.18 mm and 0.07 mm for the range u' =1- 4 m/s. The minimum interrogation area size, which can be used in conjunction with the PIV adaptive method without excessive loss in accuracy, is 8 (~0.94 mm) pixels square. This is 5-12 larger than η. Clearly, it is not possible to capture the velocity fluctuations associated with η, while also recording the larger scales of turbulence, between L and λ. Therefore, a compromise needs to be made.

Given an integral scale, L, of 20 mm, value of, u_l, of 0.358 m/s (Section 4.2), an inner reaction zone thickness of 0.75 mm (Section 2.3.2.1) and an rms turbulent velocity u', between 1 and 4 m/s, combustion occurs in the corrugated flamelet region on the Borghi diagram (Chapter 2). In this region, the influence of the scales of turbulence larger than the flame thickness is more important, as these are the most active in wrinkling and distorting the flame structure. For this reason, an area of interest larger than the integral length scale is supposed to be used, in conjunction with an interrogation area size around the same size as λ. Based on that, a square area of 120 mm was selected. The adaptive algorithm within the Dantec software, described in Section 3.6.2, was employed again to process the recorded images, with a minimum interrogation area of (8×8 pixels) and a maximum of (32×32 pixels), with a magnification ratio of 0.117 mm/pixel. Each experiment was undertaken during about 30 ms, at a frequency of 5 kHz. This arrangement would therefore capture the turbulent motion between λ and L that are most active in controlling the flame shape.

It would be of interest to investigate the impact of the small scales between the Kolmogorov and Taylor scales. However, due the limitations of the equipment, this is beyond the limits of the presented study.

4.4.2 Observations of Turbulent Flame Propagation

Figures 4.22 to 4.26 show a selection of Mie scattering raw images and the corresponding vectors maps of stoichiometric methane/air flames at an initial pressure of 0.1 MPa and initial temperature of 300 K for u' = 1, 2 and 4 m/s, respectively. The time, t, is the elapsed time after ignition. One representative experiment of five is shown here, at each u'.

It is clear that the interaction between the unburned flow field and the flame front changes significantly with u'. As u' increases, the propagation of the flame changes from something that is loosely spherical in nature (at u' = 1 m/s) to something highly deformed and convoluted (at u' = 4 m/s). It is clear also from that the flow structures exist before ignition are different at each u' and the flame front responds to these structures from an early stage of the flame propagation. Some sections of the flow are initially moving away from the point of ignition. These sections drag the flame front along with the flow, making it appear that the flame propagates aggressively in that direction. This phenomenon is somewhat clear in Fig. 4.26 at u' = 4 m/s. In contrast, where the flow is moving in towards

the flame, the distance the flame travels noticeably arrested. Clearly, the response of the flame to the flow movement, is due to the relative difference between the burning velocity of the mixture and the flow velocity ahead of the flame. The laminar burning velocity, u_l, for an outwardly propagating flame through stoichiometric methane/air, at an initial pressure of 0.1 MPa, is 0.358 m/s (Section 4.2).

If this burning velocity is compared with the flow velocity at each u', it is clear that the local change in flow velocity is significantly higher than the burning velocity. As a result of this difference, the flow is able to wrinkle and displace the flame front before a particular flow structure is consumed by the flame. For the case of u' = 1.0 m/s, the flow velocity is not substantial enough to seriously distort the flame front and convolute it significantly from its spherical nature and the flame front is only slightly wrinkled. As u' increases, the velocity fluctuations are also increase and become significantly higher. As a result, the flame is distorted and moved by the flow, wrinkling and stretching the flame front beyond recognition from its spherical natures. It is important to note that the relevant Lewis numbers are all close to unity. This diminishes any chances of diffusional thermal instability, see Section 4.2.

For all u', as the flame propagates, the velocity of unburned gas ahead of the flame being pushed by outwards by the expanding burned gases. This phenomenon are most noticeable at u' = 1.0 m/s, due to the relatively slow moving structures, but it is still evident even for u' = 4.0 m/s. This indicates that there is a symbiotic relationship between the flow structures contained within the reactants and the propagating flame front. The flame is affecting the structure of the flow, and the flow is affecting the structure of the flame.

4.4.3 Turbulent Flame Speed

As mentioned above, five explosions were conducted at each experimental condition. For each explosion, the flame radii, r_v, was obtained from measurements of the area of the Mie scattering images, as described in Section 3.6.1. Figure 4.27 shows the variations of the radii of methane/air expanding flames with time, after ignition, at φ = 1.0 for u' = 0.5, 1.0, 2.0 and 4.0 m/s at initial temperature and pressure 300 K and 0.5 MPa, respectively.

In the early stage of flame propagation, the variation of flame radii at different u'changes gently, as long as the flame is significantly less than the integral length scale of the

turbulence, 20 mm. Then, the rate of turbulent flames growth increase, with a change in the radius of the flame from 20 to 50 mm. This trend is very obvious at u'= 4 m/s. These curves were differentiated to yield the turbulent flame speeds, S_t (= dr_v/dt). Shown in Fig. 4.28 are typical turbulent flame speeds, S_t , plotted against r_v, for φ = 1.0 and for different u' at 0.5 MPa. Results of five explosions are displayed at each of four values of u'. For a given value of u', S_t increased with increasing r_v during an explosion, this is due to the turbulent flame development (Abdel-Gayed et al., 1984).

Variations of S_t with r_v , are shown in Figs. 4.29 and 4.30 for most of the remaining conditions. Each curve is the mean of five identical explosions. Error bars indicate the standard deviation from the mean values at each set of experimental condition. For a given value of u', S_t increased with flame radius. The increase was particularly rapid in the late stages, a consequence of the rapid increase in the effective spatial rms velocity, u'_s (see Chapter 5). The equivalence ratio, φ, has slight effect on S_t. The stoichiometric flames exhibited the maximum flame speeds. At φ = 1.3, the flames exhibit quantitatively the same flame speeds as flames at φ = 0.8. These results are might be attributed to the dependency of u_l and Ma_{sr} of these flames on φ, illustrated in Figs. 5.5 and 5.10, respectively, in Chapter (5). Also, comparison of the variations of S_t of lean, φ = 0.8, flames with rich, φ = 1.3, at u'= 1 m/s and 0.1 MPa, plotted in Fig. 4.29 (a and c), shows that the variation of Ma_{sr} causes the slight decrease in S_t. Figure 4.30 shows the variations of S_t with r_v at 0.5 MPa. As the pressure rises, so does S_t. That can be seen clearly when flames of 0.1 MPa at φ = 1.0 and u'= 2 m/s, shown in Fig. 4.29 (b), are compared with those of Fig. 4.30 (b) at 0.5 MPa. Conversely, comparison the flames of φ = 1.3 and u'= 1 m/s shown in Fig. 4.29 (c) at 0.1 MPa and Fig. 4.30 (b) at 0.5 MPa shows negligible variations in S_t. In general, S_t seems to be mainly dependent on r_v, affected drastically by u', and slightly by φ and P.

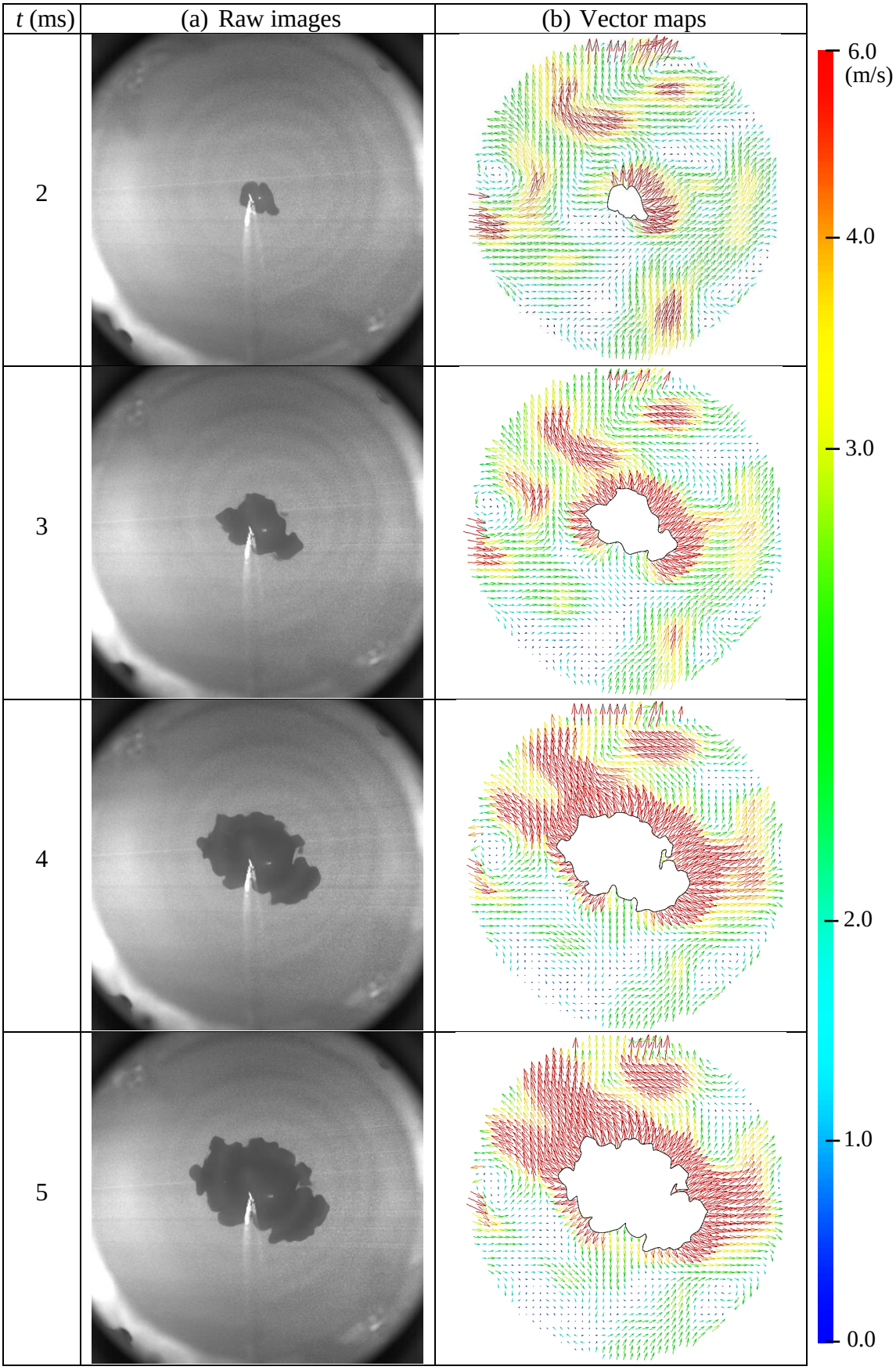

Figure 4.22: Development of CH_4/air turbulent flame, u' = 1 m/s, φ =1.0 at 0.1 MPa and 300 K, from t = 2 to 5 ms. (a) Raw images, and (b) Vector maps.

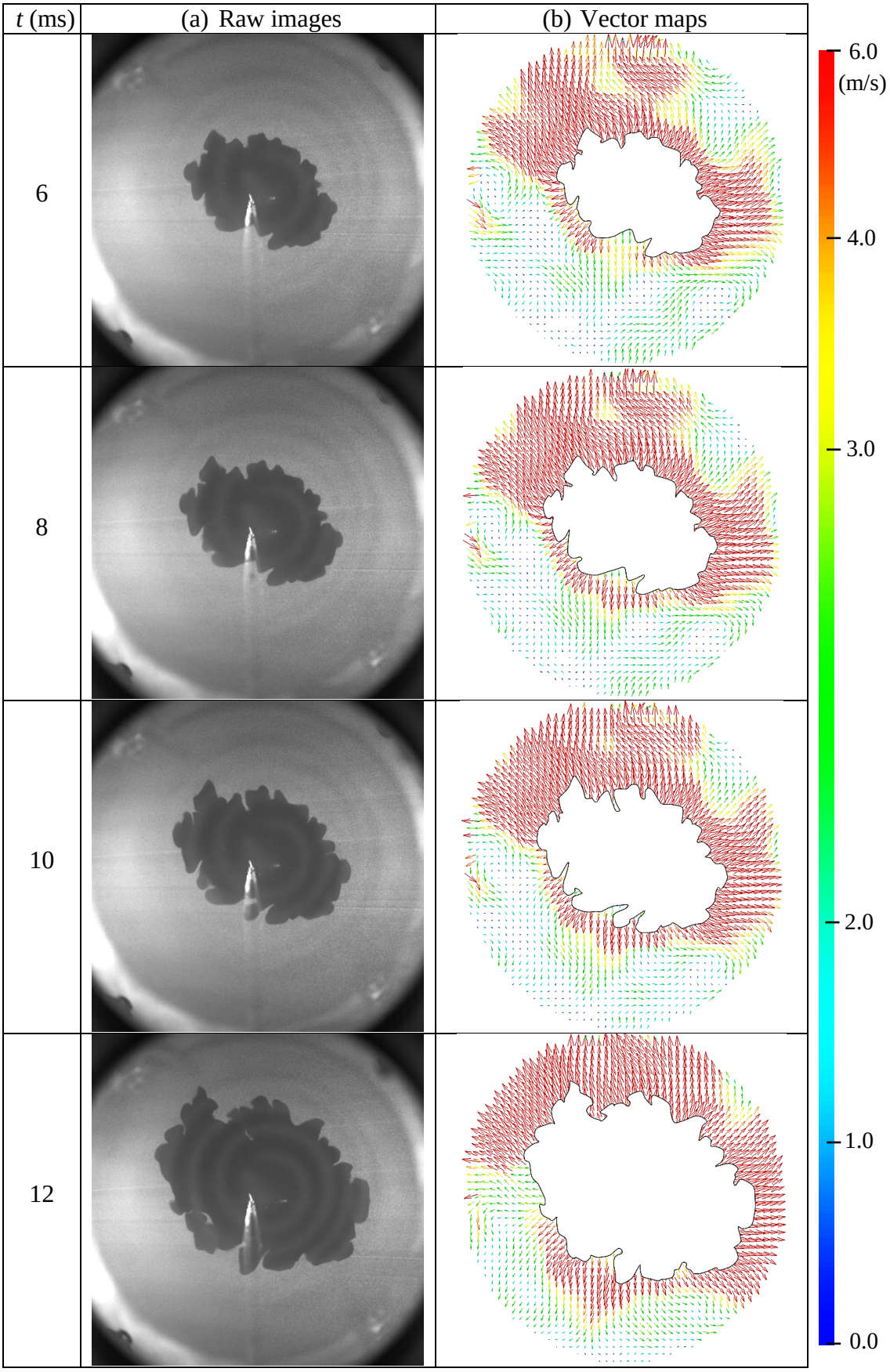

Figure 4.23: Development of CH_4/air turbulent flame, u' = 1 m/s, φ =1.0 at 0.1 MPa and 300 K, from t = 6 to 12 ms. (a) Raw images, and (b) Vector maps.

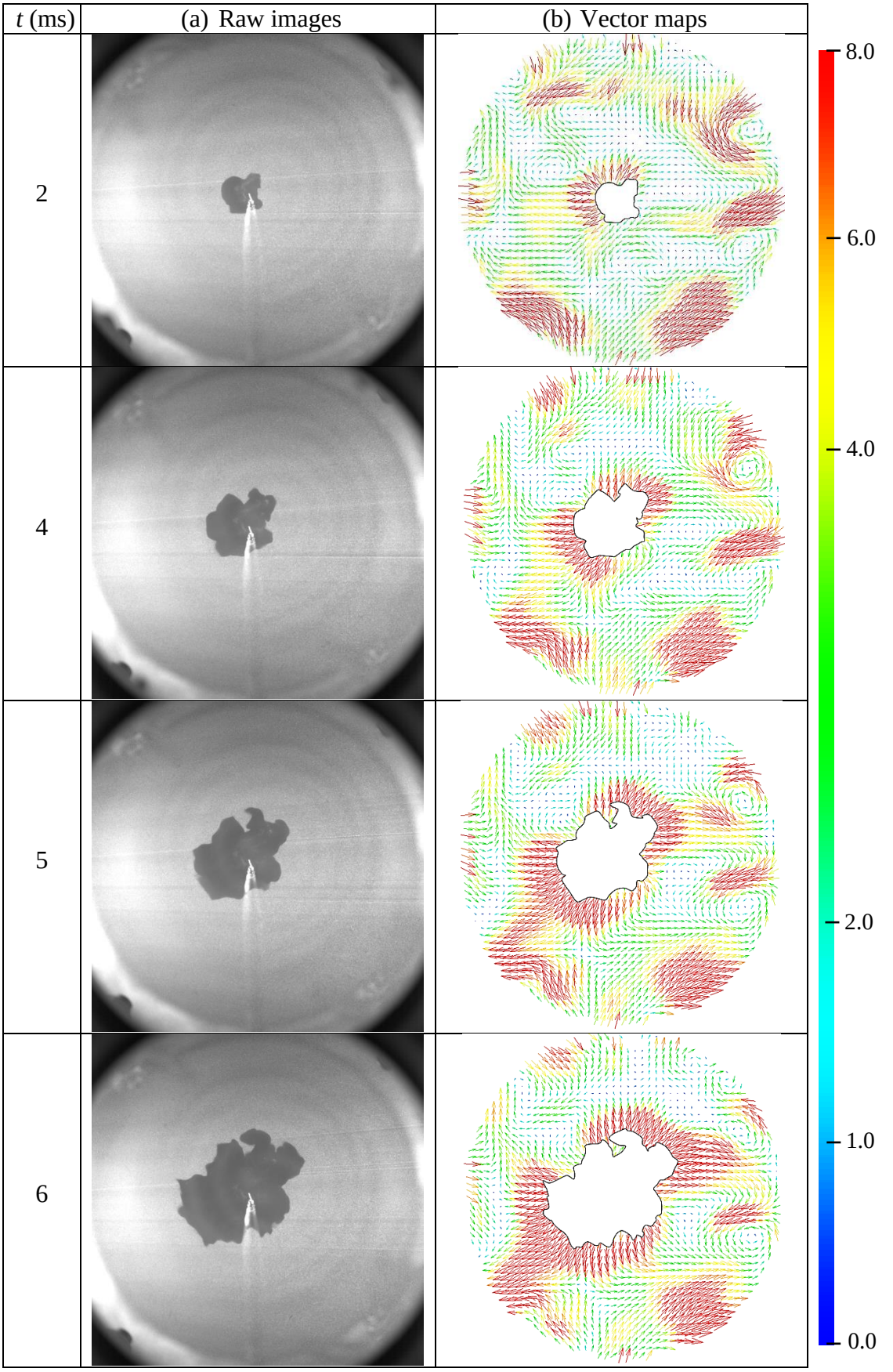

Figure 4.24: Development of CH_4/air turbulent flame, u' = 2 m/s, φ =1.0 at 0.1 MPa and 300 K, from t = 2 to 6 ms. (a) Raw images, and (b) Vector maps.

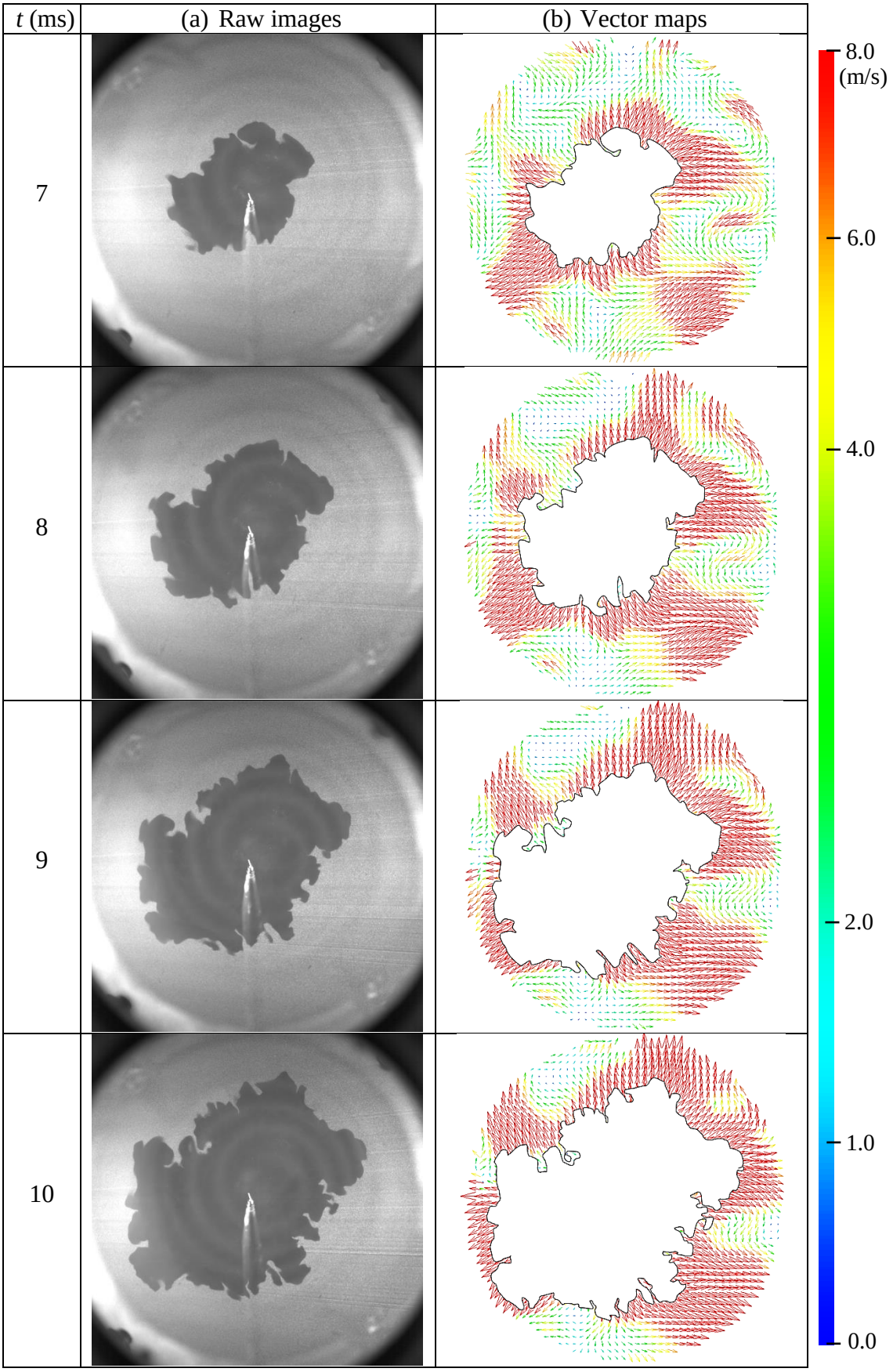

Figure 4.25: Development of CH_4/air turbulent flame, u' = 2 m/s, φ =1.0 at 0.1 MPa and 300 K, from t = 7 to 10 ms. (a) Raw images, and (b) Vector maps.

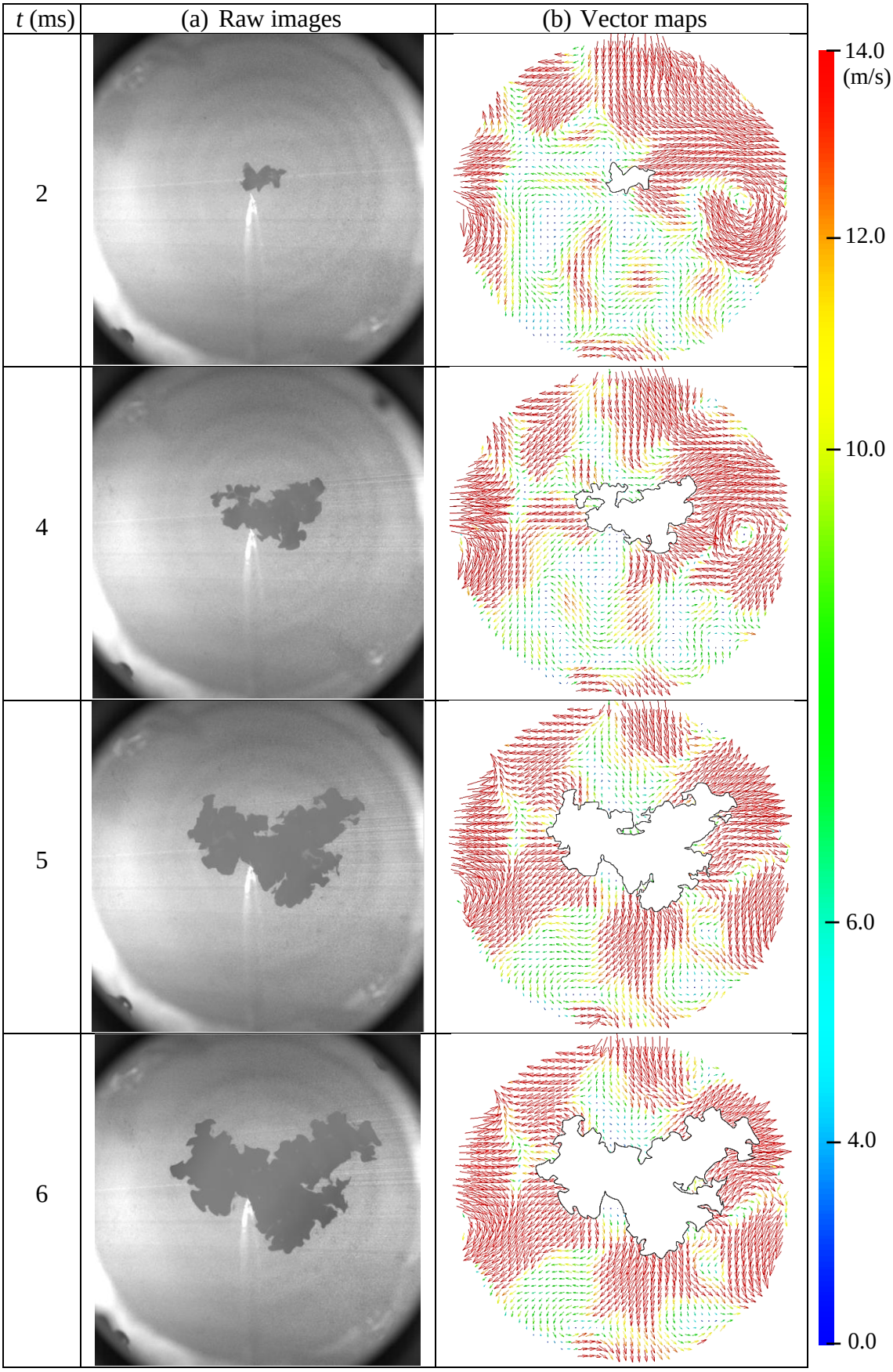

Figure 4.26: Development of CH_4/air turbulent flame, u' = 4 m/s, φ =1.0 at 0.1 MPa and 300 K, from t = 2 to 6 ms. (a) Raw images, and (b) Vector maps.

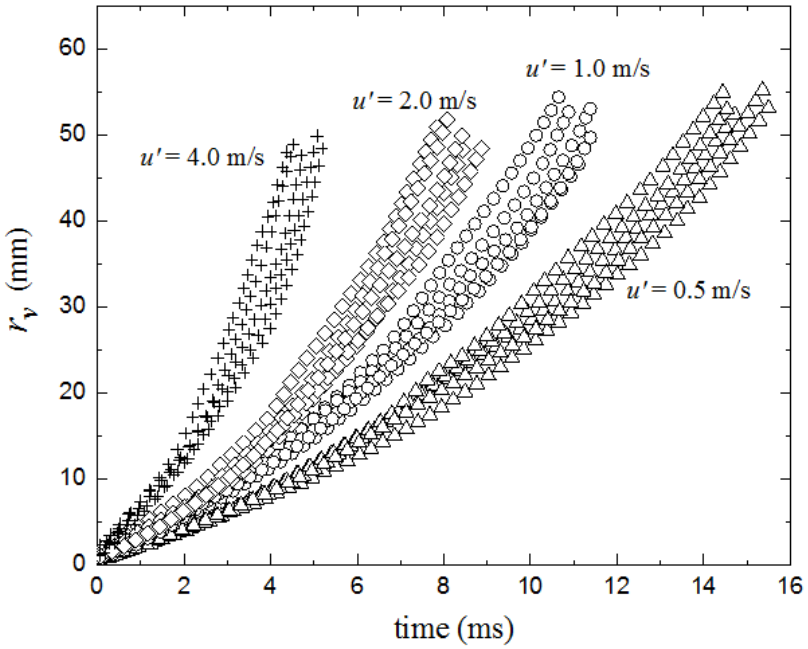

Figure 4.27: Flame radius, r_v, against time, in five explosions, with increasing u', methane/air mixture, φ = 1.0 at 0.5 MPa and 300 K.

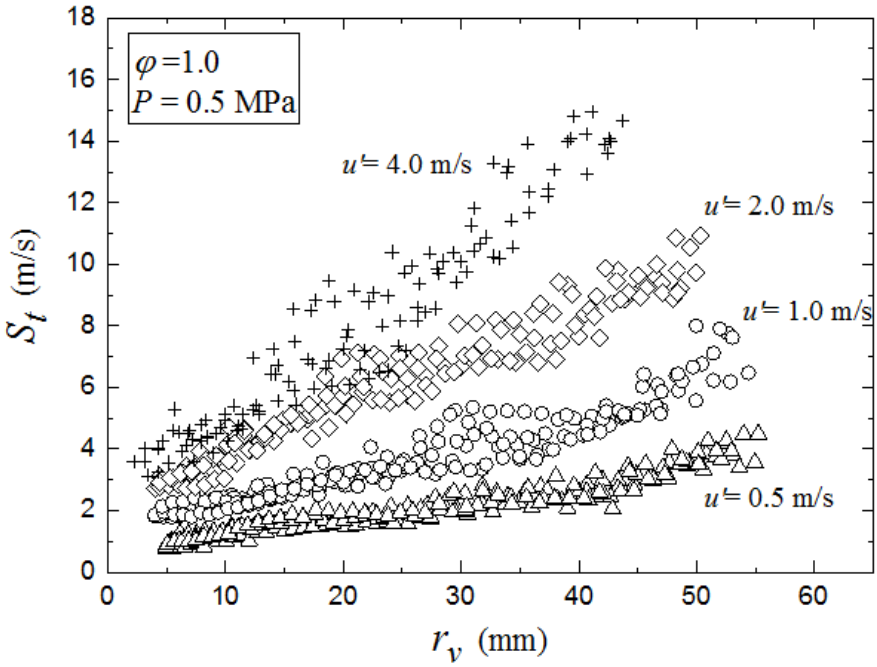

Figure 4.28: Variations of flame speed, S_t, with flame radius, r_v, in five explosions, with increasing u', methane/air mixture ,φ = 1.0 at 0.5 MPa and 300 K.

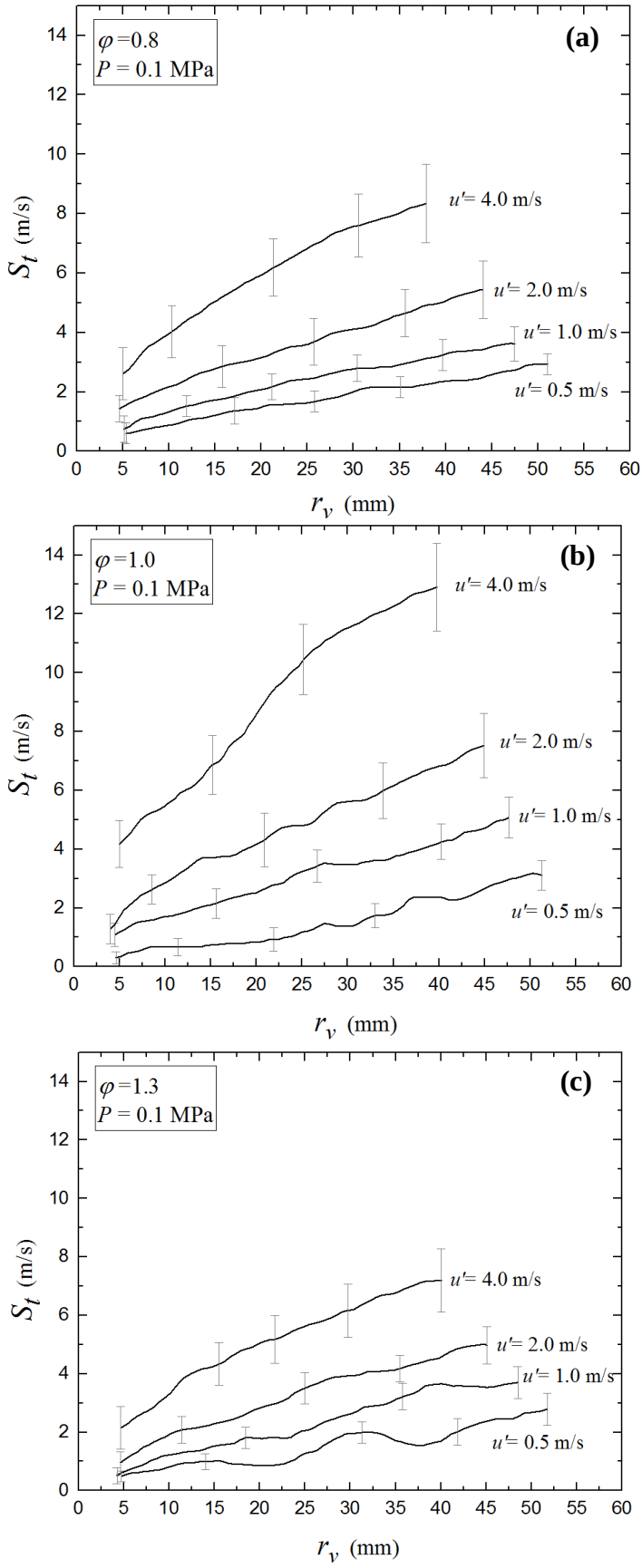

Figure 4.29: Variations of flame speed, S_t, with flame radius, r_v, for different u', at 0.1 MPa and 300 K, for (a) φ = 0.8, (b) φ = 1.0 and (c) φ = 1.3.

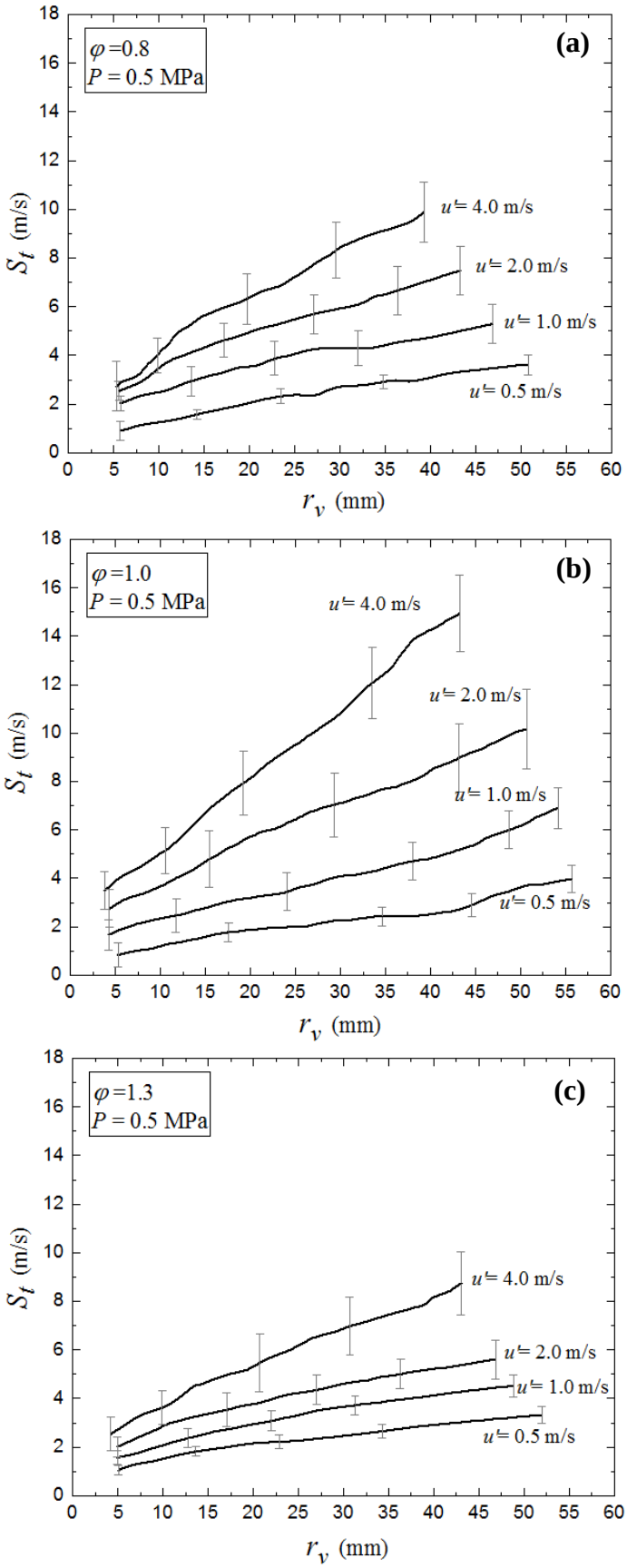

Figure 4.30: Variations of flame speed, S_t, with flame radius, r_v, for different u', at 0.5 MPa and 300 K, for (a) φ = 0.8, (b) φ =1.0 and (c) φ =1.3.

4.4.4 Turbulent Burning Rate

Values of u_{tr} were found from Eq. (2.38) with S_t obtained from r_v, as described in Chapter (2), and ρ_b/ρ_u from the Gaseq code (Morley, 2005). For the flame speeds, S_t, shown in Figs. 4.29 and 4.30, the corresponding values of u_{tr} derived in this way are shown in Figs. 4.31 and 4.32 for different φ and u' at an initial pressures of 0.1 MPa and 0.5 MPa, respectively. The most effective parameter is the rms turbulent velocity, u', as it has a significant influence on the wrinkling and stretching flame characteristics (Steinberg and Driscoll, 2009). As it can be seen from Figs. 4.31 and 4.32, the higher the u' the higher the turbulent burning velocity, u_{tr}.

These figures show the turbulent burning velocity, u_{tr}, is increasing with P, even though the laminar burning velocity u_l, presented in Chapter (5), exhibit the opposite trend. Also, it is observed that the effect of P on u_{tr} depends on the equivalence ratio, φ. At φ = 1.3, there was a slight increase in the values of u_{tr} with P, whilst at φ = 0.8 there was a considerable increase. Maximum values of u_{tr} were observed at φ =1.0 and u'= 4.0 m/s, at 0.5 MPa.

Figures 4.33 and 4.34 show the values of u_{tr} plotted against φ, at a flame radius of 40 mm and pressures of 0.1 and 0.5 MPa, respectively. Symbols represents the mean value of five explosions and the error bars show the standard deviation from this mean at each condition. Solid curves show the best fit curve for the experimental values. It is suggested in (Lawes et al., 2012) that, comparison of u_{tr} at a fixed radius is the easiest way to elucidate the effect of different parameters, i.e. φ, u' and P. Large scatter of u_{tr} values were observed at u' = 4.0 m/s, irrespective of φ and P. At 0.1 MPa and 0.5 MPa, the values of u_{tr} are maximum for u' = 4.0 m/s and decreases with u'. The effect of φ is negliglable at u' = 0.5 and 1.0 m/s and becomes considerable at 4.0 m/s. For all u' and P, the maximum values of u_{tr} were found for the stoichiometric mixtures.

As mentioned in Chapter (2), global measurement of u_{tr} is a highly useful tool for understanding the impact of turbulence on flame propagation. However, it does not provide the information required to know how a flame front affects the flow field it is propagating through. It is important to assess how much the flame and flow affect each other and whether the rate of charge consumption is impacted. Further discussion about that is presented in Chapter (5), where a novel expression of the spatial effective rms velocity, u'_s, to which the flame is exposed, is also developed and presented.

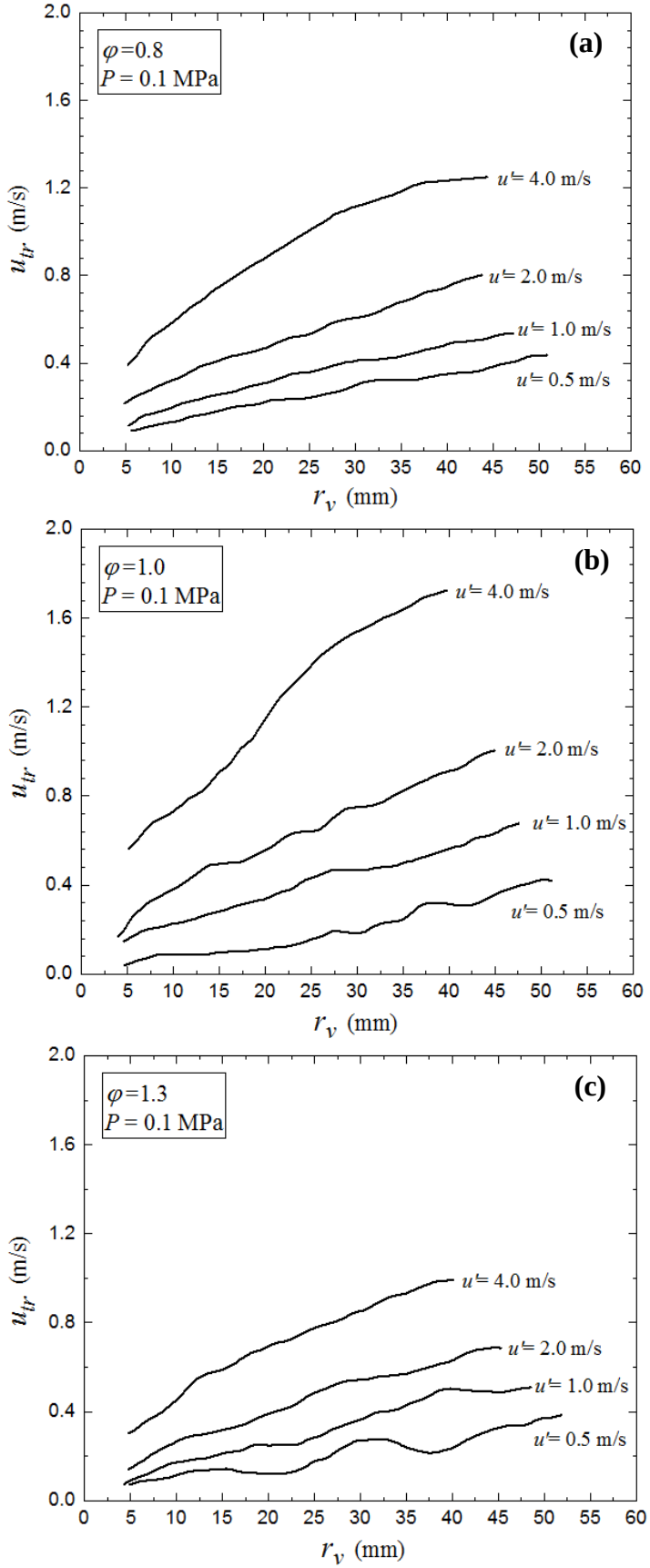

Figure 4.31: Variations of turbulent burning velocity, u_{tr}, with flame radius, r_v, for different u', at 0.1 MPa and 300 K, at (a) φ = 0.8, (b) φ = 1.0 and (c) φ = 1.3.

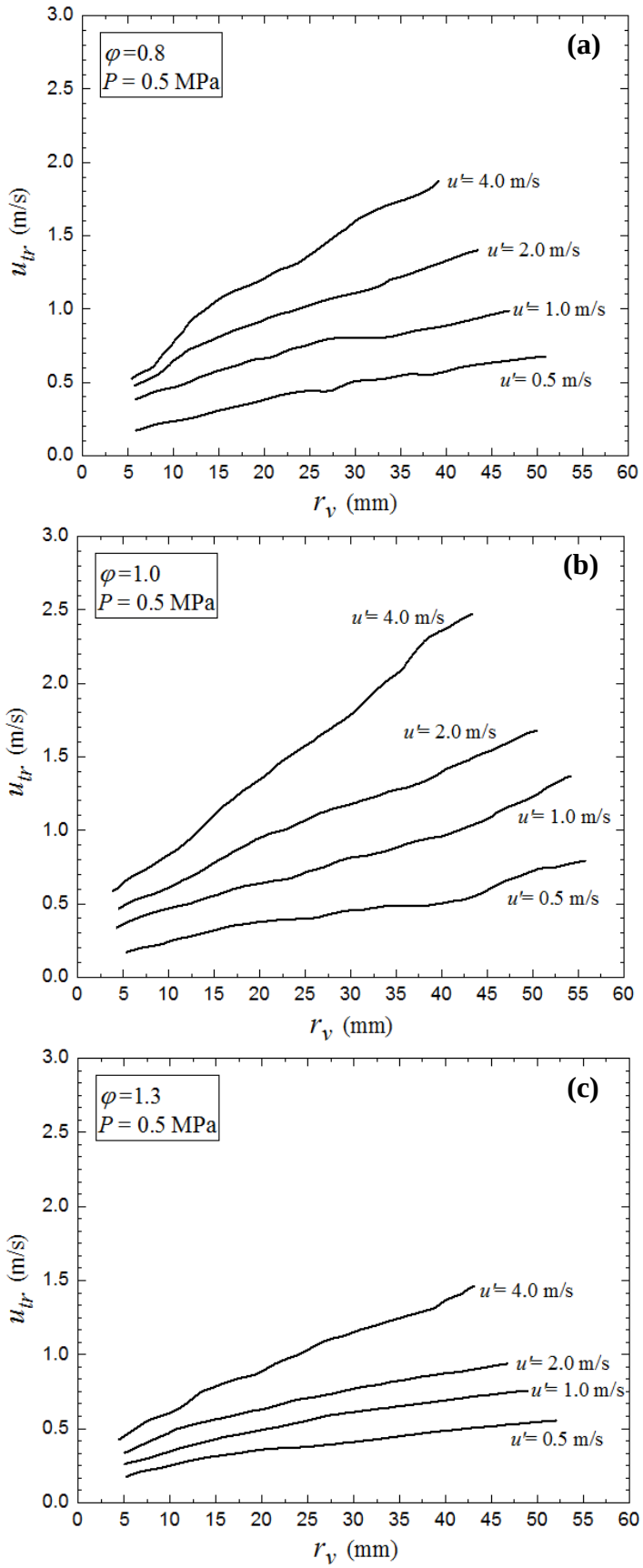

Figure 4.32: Variations of turbulent burning velocity, u_{tr}, with flame radius, r_v, for different u', at 0.5 MPa and 300 K, at (a) φ = 0.8, (b) φ = 1.0 and (c) φ = 1.3.

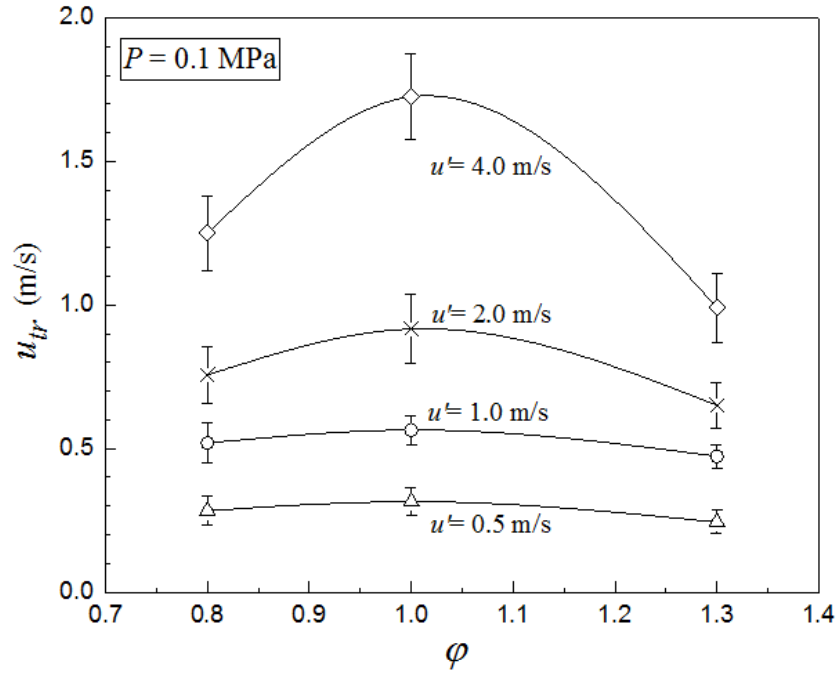

Figure 4.33: Influence of φ on $u_{tr,}$ at flame radius r_v = 40 mm, for different u', at 0.1 MPa and 300 K.

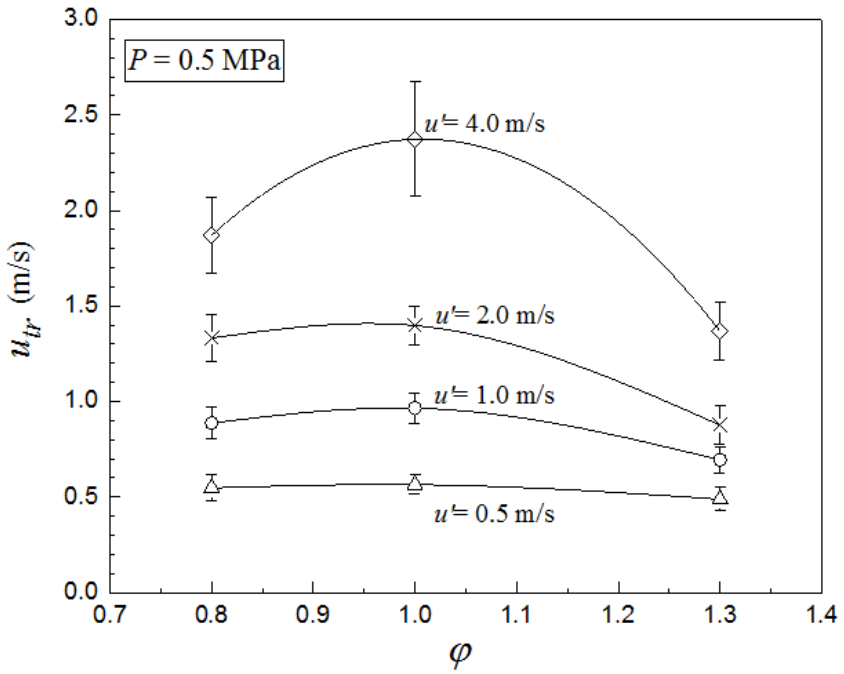

Figure 4.34: Influence of φ on $u_{tr,}$ at flame radius r_v = 40 mm, for different u', at 0.5 MPa and 300 K.

Chapter 5 - Discussion

5.1 Introduction

This Chapter presents various discussions on the measured data for laminar burning, cold flow turbulence and turbulent burning, presented in Chapter (4).

The laminar burning results have been discussed in Section 5.2, where burning velocities are presented from both of the flame speed methods, as well as the PIV-derived values for methane, *n*-butanol, *i*-octane and ethanol mixtures with air. A methodology has been developed for correcting burning velocities, measured by the flame speed method, due to it not having an adiabatic value for the burned gas density. Errors arise in the determination of Markstein numbers, if the temperature of the associated isotherm is too low, are also discussed and quantified.

Section 5.3 discusses the cold flow turbulence results, where evaluation of the extent of the central homogenous volume of isotropic turbulence at different fan speeds is performed. Spatial and temporal distributions of mean and root mean square, rms, velocity fluctuations are investigated, as well as integral length scales, L, Taylor microscales, λ, and Kolmogorov length scales, η. A relationship between the autocorrelation function and integral length scale was developed, for when Taylor's hypothesis is invalid.

Lastly, Section 5.4 discusses the turbulent burning results, where the influences of pressure, temperature and equivalence ratio on, the root mean square (rms) velocity ahead

of the flame front, u_s', are investigated and discussed. Correlation of u_s' as a function of such parameters has been developed. Comparison between u_s' and u_k' is also presented and discussed.

5.2 Laminar Burning

PIV measurements were made in spherical explosions, from which burning velocities can be derived from the flame speed measurements. The unburned gases velocity measurements also enable entrainment and mass rate of burning velocities to be found, along with flame stretch rates and associated Markstein numbers. In the flame speed method of measuring burning velocity, it is often assumed that the burned gas density at zero stretch rate is that of an adiabatic flame under equilibrium conditions, ρ_b. This tends to be an under-estimation, giving burning velocities that are shown to be about 4-11 % low. A modification of this approach is developed, involving the burned gas density of the stretched flame, entirely in the regime of stable propagation, prior to the development of unstable flames at low stretch rate. In the stable regime, the mean burned gas density, $\bar{\rho}_b$, is larger than ρ_b, and depends on the stretch rate, α, and Lewis number, Le. There is little change in $\bar{\rho}_b$ before the instability develops. Values of $\bar{\rho}_b$ yield values of burning velocities that are closer to those determined by PIV. Detailed discussions are given in the following subsections.

5.2.1 Burned Gas Density

Only if reaction has been completed adiabatically, is Eq. (2.17) valid. Clavin and Williams (1982) show the value of burned gas density to be dependent upon α and the Lewis number, Le. The deviation of the mean burned gas temperature, $\bar{T}_b$, from the adiabatic burned gas temperature, T_b, is given by (Law et al., 1986 and Bonhomme et al., 2013):

$$\frac{\bar{T}_b - T_b}{T_b} = \frac{D}{(u_{la})^2}\left(\frac{1}{Le} - 1\right)\alpha\,. \tag{5.1}$$

Here, D, is the thermal diffusivity of the mixture, obtained, like T_b, from (Morley, 2005), for the initial conditions of T_u and P. Measurements of temperature distributions have confirmed the general validity of this equation (Law et al., 1986 and Bonhomme et al., 2013). It shows that high α and Le values can, under some circumstances, create mean temperatures significantly below adiabatic values. As α decreases the temperature slowly

recovers, but only with Le = 1.0 can $\bar{T}_b = T_b$. The changes in α are known, as the flame radius increases during the period of flame stability. Figures 5.1 and 5.2, derived from this equation, show $\bar{T}_b$ and $\bar{\rho}_b$ plotted against flame radius, r_u. For the stoichiometric methane mixture of Fig. 5.1 with Le = 0.99 (Tahtouh et al., 2009 and Lowry et al., 2010) and D = $2.01 \times 10^{-5}\ m^2/s$ (Morley, 2005), the figure shows the near unity value of Le ensures early attainment of the adiabatic equilibrium values, T_b and ρ_b, in accordance with Eq. (2.17). This explains the good convergence of the S_n and u_n straight lines at α = 0 in Fig. 4.16, giving $u_l = u_{la}$ = 0.358 ± 0.005 m/s.

In sharp contrast, is the stoichiometric *n*-butanol mixture at 383 K and 0.1 MPa, with Le = 1.58 (Li et al., 2015) and $D = 2.72 \times 10^{-5}\ m^2/s$ (Morley, 2005). Here the high Le ensures $\bar{T}_b$ does not attain T_b in Fig. 5.2, and $\bar{\rho}_b > \rho_b$. Figure 5.3 shows data for the same mixture, but with $\bar{T}_b$ and $\bar{\rho}_b$ at 0.5 MPa, $Le = 1.12$ and $D = 5.6 \times 10^{-6}\ m^2/s$ (Morley, 2005). The figure shows the increase in pressure to lead to a rather more rapid attainment of adiabatic equilibrium, attributable to the decreases in both Le and D.

Mean values, $\bar{\rho}_b$, within the stable extrapolation range of S_n, were found in this manner during explosions. There is little change in $\bar{\rho}_b$ during the developed stable flame propagation. To find the stretch-free value of burning velocity with this modified the flame speed method, S_n is plotted against α down to zero, and the mean value of $\bar{\rho}_b$ evaluated throughout the period of developed, stretched, stable propagation. Equation (2.17) is then applied to the value of u_{la}, except that now the relevant density becomes $\bar{\rho}_b$. Flame speed values of, u_{la}, determined in this way, designated u_{ls}, are closer to those of the PIV values of u_l at zero stretch rate than those based on ρ_b.

The values of the critical Karlovitz number, K_{cl}, Eq. (2.7), below which the flame becomes unstable, are shown for *n*-butanol/air at different φ, at 0.1 MPa and 383 K in Fig. 5.4. The associated PIV based limiting stable values of u_{nr} at this stretch rate are also shown. At higher values of K_{cl}, flames become unstable and faster burning. The filled square symbols and dotted curve shows the stretch-free values, u_{ls}, derived from this modified flame speed method, allowing for $\bar{\rho}_b$ and Le. These are higher than those of u_{nr}. The lower values of Markstein numbers on the rich side, see Section 5.2.4, contribute to higher u_{nr} values there.

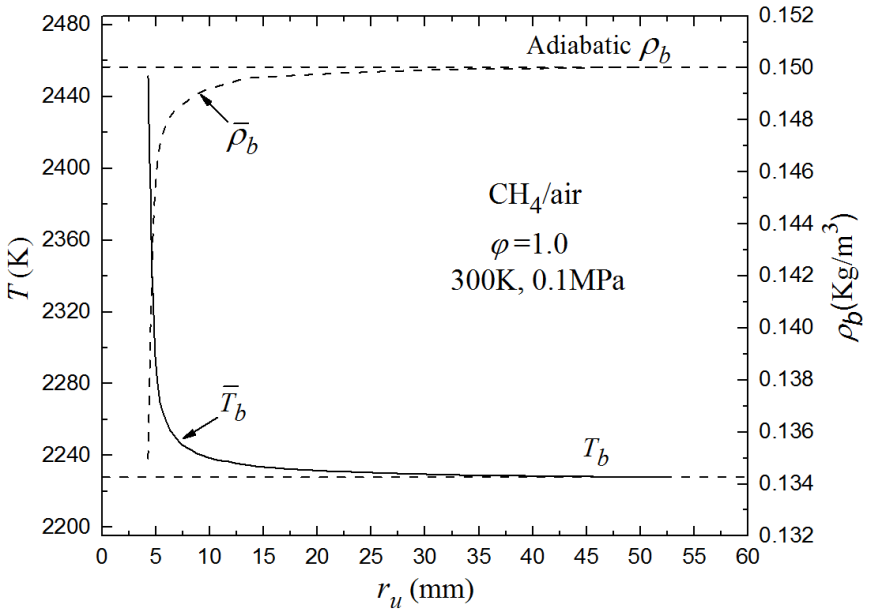

Figure 5.1: Computed burned gas temperature and density methane/air, φ = 1.0, at 300 K and 0.1 MPa, *Le* = 0.991.

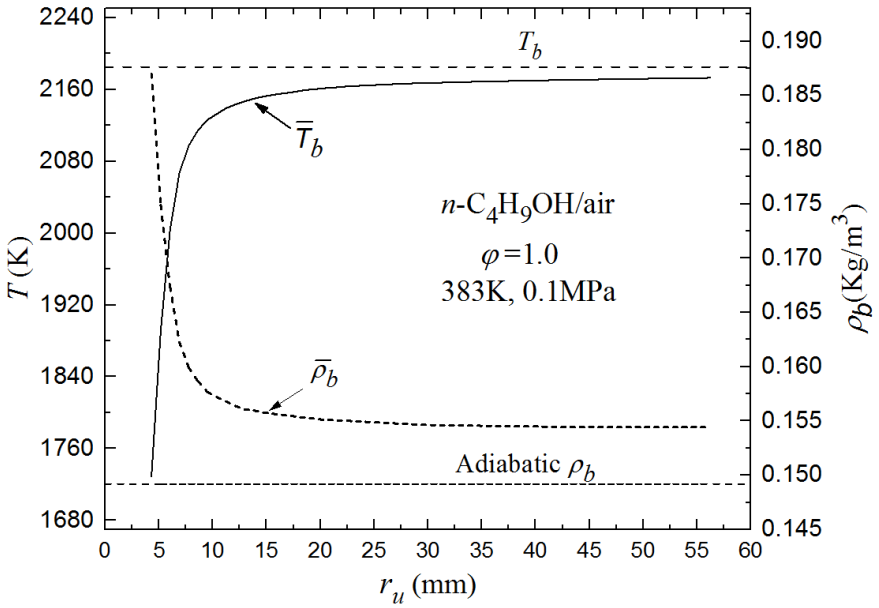

Figure 5.2: Computed burned gas temperature and density for *n*-butanol/air, φ = 1.0 at 383 K and 0.1 MPa, *Le* = 1.58.

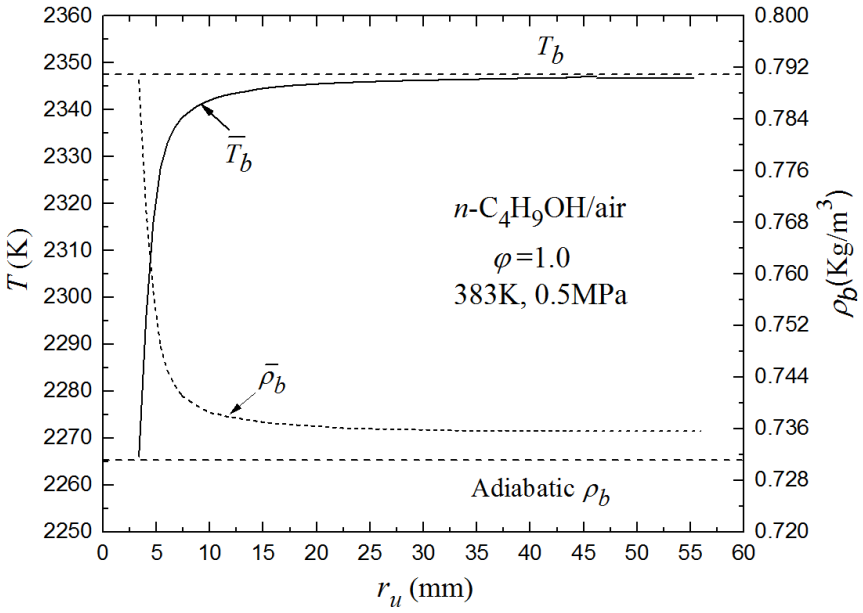

Figure 5.3: Computed burned gas temperature and density for *n*-butanol/air, φ = 1.0 at 383 K and 0.5 MPa, *Le* = 1.12.

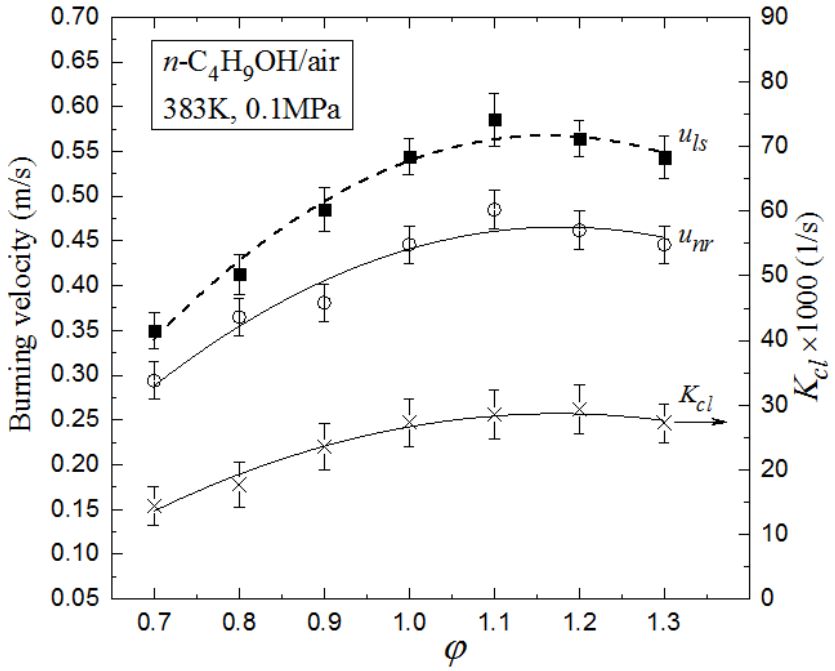

Figure 5.4: PIV values of u_{nr} at the boundary values of critical Karlovitz number, K_{cl}, and values of u_{ls} for *n*-butanol/air at 0.1 MPa and 383 K.

5.2.2 Radiative Heat Loss

The flame speed method of measuring u_{la} employs the adiabatic values of both density, ρ_b, and temperature, T_b, with no inherent allowance for either strain rate changes in $\bar{\rho}_{b,}$ or those due to radiative energy loss. Radiative heat loss in laminar flames has been computed by several researchers. Chen et al. (2015), found u_{la} for methane/air mixtures, to be reduced by the radiation, and decreased by up to 5% and 4% for φ = 0.6 and 1.4, respectively. For completeness, mathematical modeling of laminar flames requires the effects of flame stretching and radiative energy loss or gain to be included, along with the detailed chemical kinetics and flow patterns. Such modelling shows radiative heat loss to decrease the burning velocity. The decrease in temperature slows the propagation rate, and the burned gas cooling generates an inwards flow (Chen, 2010). Santner et al. (2014) have shown that in an atmospheric heptane/air flame, reductions in burning velocities due to radiative energy loss are less than 1% between φ = 0.9 and 1.5. Reductions increase as the lean and rich flammability limits are approached.

Based on their chemical kinetic modelling, Yu et al. (2014) have presented generalised empirical expressions for the reductions in burning velocities of hydrocarbon /air mixtures, as a result of this energy loss under a variety of conditions. The measured burning velocities were subjected to radiative loss. In (Yu et al., 2014) these losses were calculated for seven different fuels, at different temperatures and pressures. The authors mentioned that this empirical correlation could be used with other fuel/air mixtures, except diluted mixtures. This approach was adopted in the present work and losses were calculated as in (Yu et al., 2014), and added to the PIV values of u_l at α = 0 for the different mixtures. To demonstrate what the hypothetical value of burning velocity would be like in the absence of radiative loss, the calculated loss in burning velocity was added to u_l to give u_{lr} .

5.2.3 Laminar Burning Velocities

The increases in values of u_l to u_{lr}, in the absence of radiative ĺoss, are shown by the filled triangles on the ensuing Figs. 5.5 - 5.8. These are expressed as % increases in the first column of Table 5.1. This Table covers three different aspects of the full range of mixtures, at atmospheric pressure. The second column shows the K_{cl} values, marking the onset of instability, whilst the third shows the increases in u_{la} to u_{ls} that occur with the revised flame speed method of processing.

Table 5.1: Extent of radiative loss, critical Karlovitz numbers, and strain rate/Le flame speed corrections at atmospheric pressure.

	Radiative loss % Increase in PIV u_l with no radiative loss				Critical Karlovitz number ($K_{cl} \times 10^3$)				Flame Speed Method % Increase in u_{la} to u_{ls} due to strain/Le			
φ	CH_4	i-C_8H_{18}	C_2H_5OH	n-C_4H_9OH	CH_4	i-C_8H_{18}	C_2H_5OH	n-C_4H_9OH	CH_4	i-C_8H_{18}	C_2H_5OH	n-C_4H_9OH
0.7	3.1			1.8	43.7			14.4	-0.9			3.1
0.8	2.0	1.5	1.1	1.5	26.7	11.9	8.1	17.7	-0.9	1.8	1.1	5.0
0.9	1.6	1.4	1.0	1.2	18.5	14.0	8.7	23.5	-0.9	1.6	1.1	4.2
1.0	1.4	1.3	0.9	1.1	16.0	16.2	8.6	27.3	-0.5	1.4	1.8	6.2
1.1	1.4	1.3	0.9	1.0	16.1	17.5	10.0	28.5	1.1	2.7	1.4	5.0
1.2	1.6	1.4	0.9	1.0	19.4	17.7	10.5	29.3	1.0	2.3	1.3	4.3
1.3	2.1	1.7	1.0	1.1	32.3	23.0	13.1	27.2	1.1	3.2	3.6	7.3

Although a stable, un-stretched, flame is an unrealistic concept, the complementary values of u_l provide a useful datum which, along with, Markstein numbers, provides realistic mass burning velocities within the stable flame regime. Such stretch-free values of laminar burning velocities are shown as a function of φ for different fuels in Figs. 5.5 – 5.8. Full line curves, and cross symbols, show PIV values of u_l, based on u_n. Broken curves, and circle symbols, show flame speed method values, u_{la}, based on S_n values from the PIV measurements, extrapolated to $\alpha = 0$, and employing ρ_b in Eq. (2.17). Values of u_{ls} at α =0, derived from the alternative flame speed method, based on $\bar{\rho}_b$ and Le, are shown by the filled square symbols. These values are higher than those of u_{la}, values of the original, broken curve, flame speed method. They are almost equal to the u_l values of the PIV method. These increases are given in the final column of Table 5.1. Some of the highest values of u_l are given by the u_{lr}, filled triangles, with no radiative loss.

Figure 5.5 for methane/air mixtures, over a wide range of equivalence ratios at 300 K and 0.1 MPa, presents PIV values of u_l and ρ_b-based flame speeds values of u_{la}. Points for u_{ls} and u_{lr} also are shown. Values of Le for lean mixtures range from 0.96 to 0.99, and values of Le are close to unity, the u_{ls} correction is small. The closeness of the u_l and u_{ls} curves indicates the near equality of $\bar{\rho}_b$ from the former and ρ_b from the latter. The increases in PIV values due to the elimination of radiative loss, indicated by u_{lr}, also

are rather small. There is close agreement between the two methods, although the u_l values, are always higher. This is because the strain rate correction is small, and there is negligible correction for an increase in the value of $\bar{\rho}_b$ due to the small radiative cooling. Allowance for this could bring the values of u_l and u_{la} closer together. Values of u_{la} from other workers also are shown. The values from (Tanoue et al., 2003) are noticeably higher. This might be due to the pressure being recorded, in the absence of flame photographs, and a lack of coordination in flame front imaging and pressure measurement (Hinton et al., 2018).

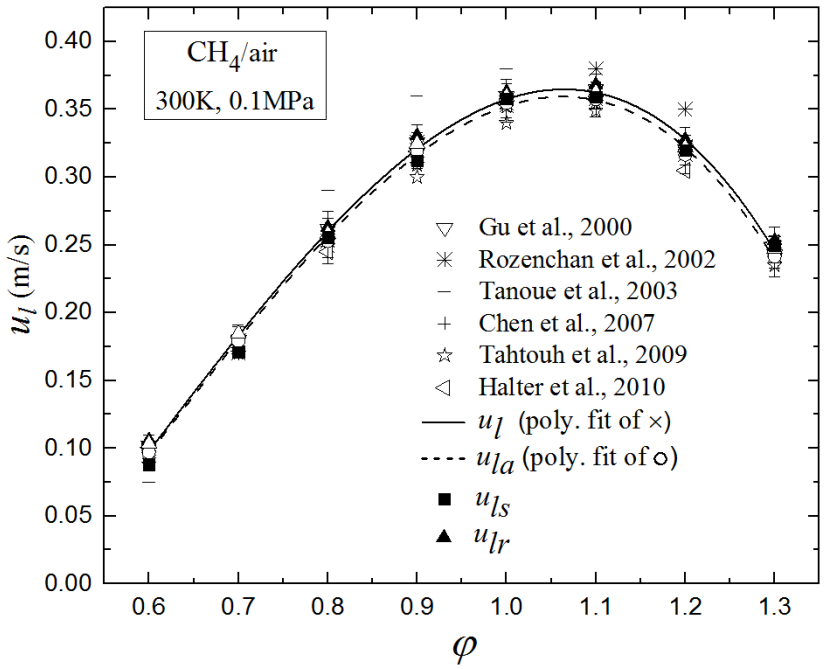

Figure 5.5: Unstretched laminar burning velocities, u_l, u_{la}, u_{ls} and u_{lr} for methane/air mixtures at 0.1 MPa and 300 K. Shown also data from literature.

Figure 5.6 shows unstretched burning velocities for *n*-butanol, the fuel chosen to study the effects of pressure changes. Values of Le ranged from 1.35 to 2.1 (Li et al., 2015), at 0.1 MPa. The high values of Le create the largest strain rate corrections. Here, the flame speed values, u_{la}, at 0.1 MPa are 4-11% lower than the PIV values, u_l, with greater differences for the rich mixtures. Values of all the burning velocities fall with increasing pressure, but always the u_l values are higher. At 0.1 MPa when the, u_{la}, values are corrected for strain rate and Le, the, u_{ls}, values are closer to the u_l values as shown by the filled square points. Allowance for the radiative loss, at 0.1 MPa, results in the u_{lr} values being the highest. Of particular interest is the narrowing of the difference between the PIV values of u_l and flame speed values of u_{la} with increasing pressure.

This can be attributed to values of $\bar{\rho}_b$ approaching those of ρ_b with increasing pressure, as a result of both the more rapid attainment of equilibrium, and the decreasing values of Le with increasing pressure, see Fig. 5.3.

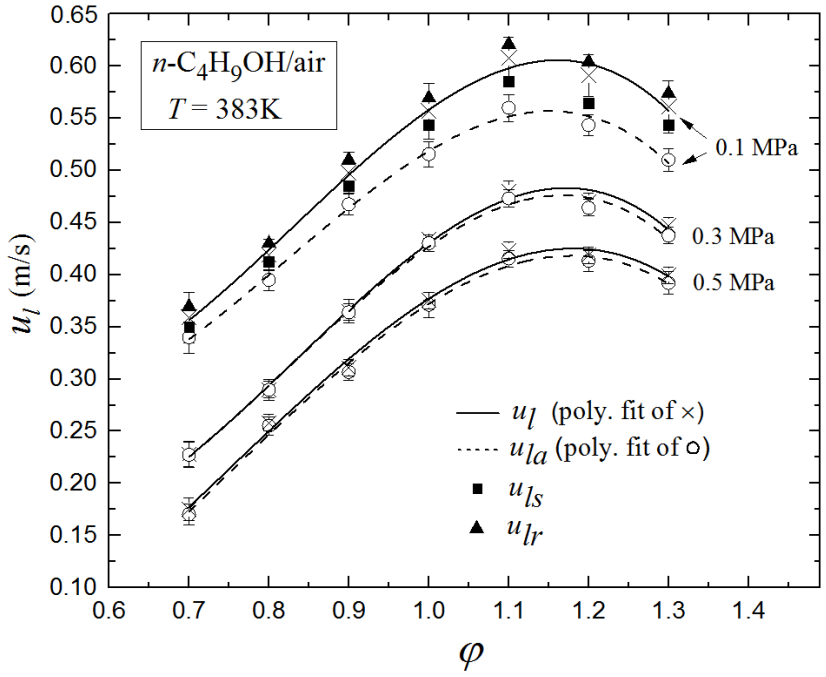

Figure 5.6: Unstretched laminar burning velocities, u_l, u_{la}, u_{ls} and u_{lr} for *n*-butanol/air mixtures at 383 K and different pressures.

Figure 5.7 shows the unstretched burning velocities u_l and u_{la} for *i*-octane/air mixtures at 0.1 MPa and 358 K. The u_{la} values are underestimated, with a maximum difference of 6.5% below the u_l values. There is rather more consistency in the atmospheric data for ethanol/air values in Fig. 5.8. Again, the present results follow a decreasing trend from u_{lr} down to the u_{la} flame speed method based on ρ_b. Table 5.1 shows ethanol to have the lowest radiative energy loss, and its influence is clearly shown by the filled triangles. The original flame speed method underestimates u_{la}, with a maximum difference of 4.5% with PIV values of u_l.

5.2.4 Markstein Numbers

5.2.4.1 Stretch Rate Isotherms

Flame speed, S_n, is plotted against the stretch rate, α, given by Eq. (2.2), from which the flame speed Markstein length, L_b, is found using Eq. (2.18). The flame speed is almost independent of the chosen isotherm, but the flame stretch rate also depends on the changing radius of the isotherm, see Eq. (2.2). An isotherm close to the temperature of the burned gas might be regarded as closest to expressing the rate of formation of

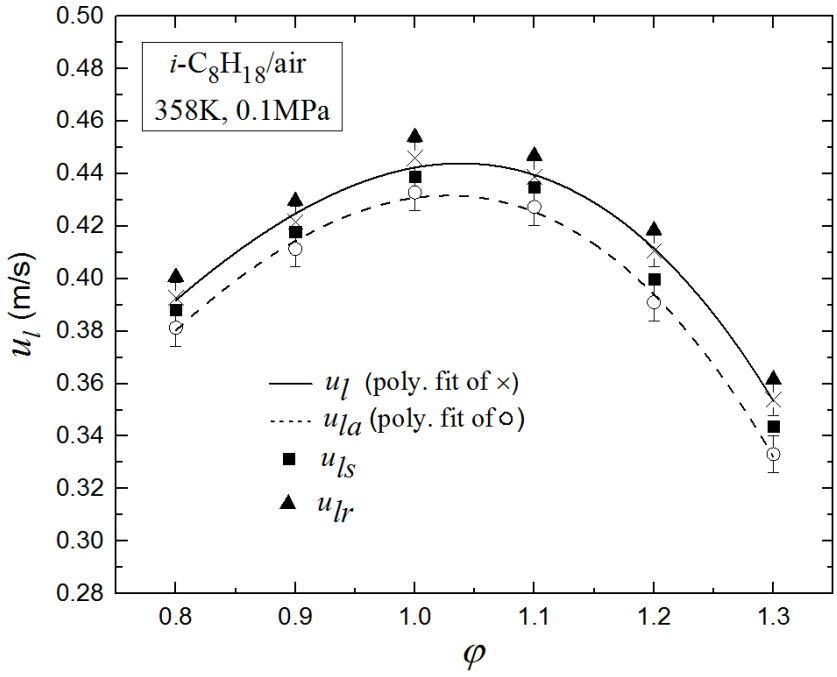

Figure 5.7: Unstretched laminar burning velocities, u_l, u_{la}, u_{ls} and u_{lr} for *i*-octane/air mixtures at 0.1 MPa and 358 K.

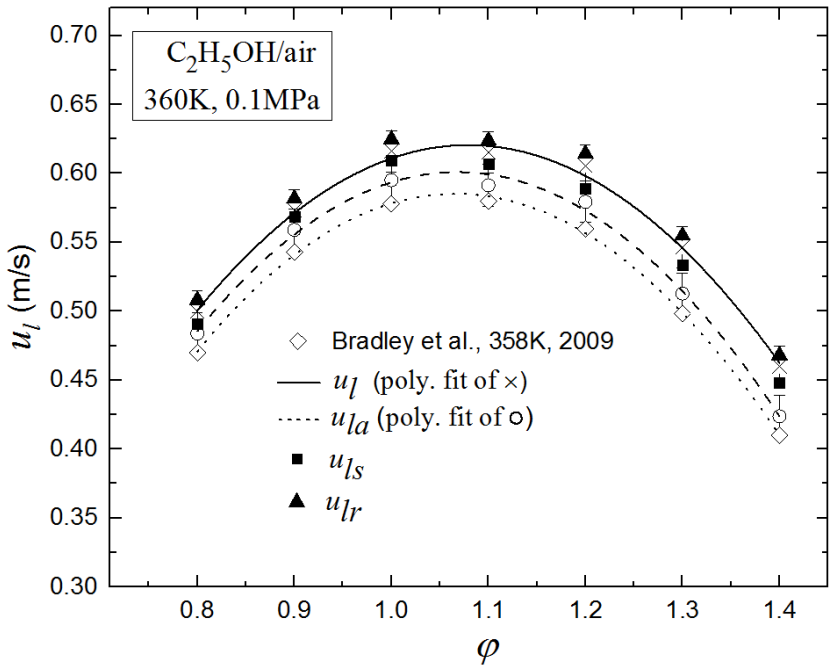

Figure 5.8: Unstretched laminar burning velocities, u_l, u_{la}, u_{ls} and u_{lr} for ethanol/air mixtures at 0.1 MPa and 360 K. Shown also data from literature.

burned gas, akin to u_{nr}, Ma_{sr} and Ma_{cr} (Bradley et al., 1996). Beeckmann et al. (2018) showed that PIV and schlieren techniques yield nearly identical Markstein lengths, for a methane/air mixture, φ =1.1 at 0.25 MPa and 298 K. Giannakopoulos et al. (2015) showed isotherms in the reaction zone to be more reliable than those in the preheat zone for measuring Markstein numbers.

Measured flame speeds from both the PIV and schlieren images, plotted against α, are compared in Fig. 5.9, for ethanol/air flames at different equivalence ratios, φ, at 0.1 MPa, and an initial temperature of 360 K. Those based on PIV Mie scattering images, shown by the full lines, are close to isotherms in the region of 573 K, in contrast to the schlieren images, shown by the broken lines, corresponding to isotherms at about 860 K (Dunn-Rankin and Weinberg, 1998). Detailed description of the schlieren system can be found in (Mansour, 2010, Mumby, 2017). As in (Giannakopoulos et al., 2015), the higher temperatures gives the higher L_b, between 4-12 % higher than the lower temperatures. For the same two temperatures, but using the theoretical propane/air data in (Giannakopoulos et al., 2015) the Markstein numbers would be 50-90% higher at the higher temperature.

In (Giannakopoulos et al., 2015) plateau temperatures are evaluated, at which there is no further change in Markstein number with isotherm temperature. For the conditions in Fig. 5.9, a suitable plateau isotherm would be that at least 1440 K, (4×T_u). When extrapolated to this temperature, values of L_b at 573 and 860 K give values of L_b between 7 and 18 % higher than those measured at the seed disappearance isotherm, and 3-6% higher than those at the schlieren front. Throughout the present study L_b is measured at the PIV droplet disappearance isotherm, and the underestimation is in the higher of the two ranges.

5.2.4.2 Values of Markstein Numbers

With regard to Markstein numbers, all Markstein lengths, based on both S_n and u_{nr}, were found and normalised by the flame thickness, δ. The link between Le and Ma is provided by the early expression of Clavin (1985):

$$Ma = \frac{1}{\gamma} ln \frac{1}{1-\gamma} + \frac{\beta(Le-1)}{2}\left(\frac{1-\gamma}{\gamma}\right) x \int_0^{\gamma/1-\gamma} dx \frac{ln(1+x)}{x} \tag{5.2}$$

With K_s and K_c expressing Karlovitz strain, $\delta\alpha_{sr}/u_l$ and curvature, $\delta\alpha_{cr}/u_l$, numbers, a practical form of Eq. (2.20) is:

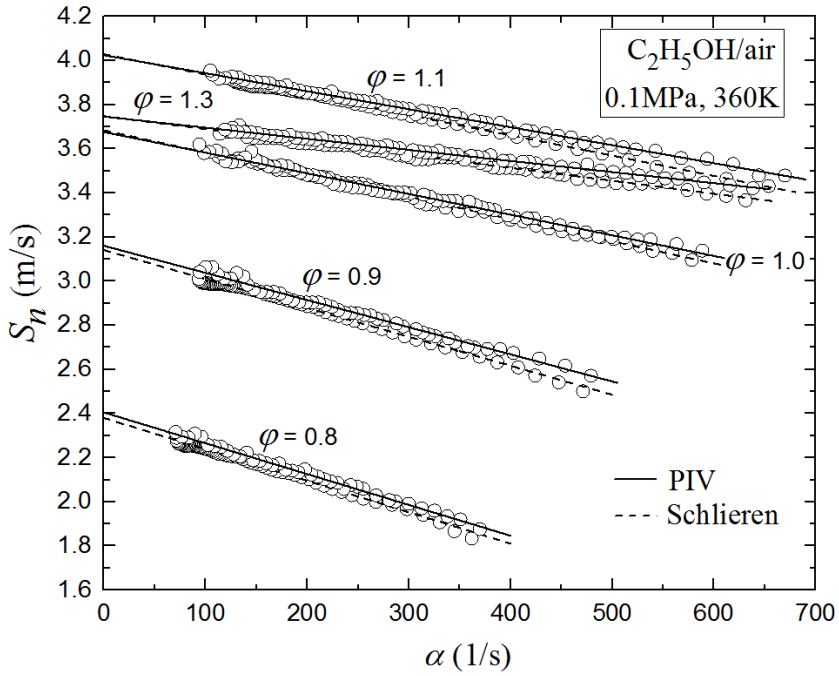

Figure 5.9: Variations of PIV and schlieren S_n values with α for ethanol/air mixtures at 0.1 MPa and 360 K. Full and dashed lines denote linear relationship for L_b through PIV and schlieren points, respectively.

$$\frac{u_l - u_{nr}}{u_l} = K_s\, Ma_{sr} + K_c Ma_{cr} \tag{5.3}$$

The method of deriving the Markstein lengths from the PIV data is given in Section 4.2.4. Contrasting Markstein numbers are shown for different φ in Fig. 5.10 for methane/air at 0.1 MPa and in Fig. 5.11 for *n*-butanol/air at 0.1, 0.3 and 0.5 MPa. For methane/air the influence of small values of *Le* close to unity has been discussed in Section 5.2.1. With lean mixtures, values of *Le* are less than unity, leading to the low Markstein numbers in Fig. 5.10. In contrast, for *n*-butanol/air, with richer mixtures, and O_2 as the minority species, the resulting higher diffusion coefficients creates smaller Lewis numbers, leading to the lower Markstein numbers of Fig. 5.11. With regard to the influence of pressure, *Le* decreases with increasing pressure, and this leads to the associated decreasing values of both Ma_{sr} and Ma_{cr} in Fig. 5.11.

Values of Markstein numbers for all the other mixtures studied are tabulated in Appendix B. There is a significantly greater spread in the reported values of Markstein numbers than in those of burning velocities. This is probably inevitable, due to the problem of evaluating a flame thickness, which is defined by asymptotic end values. Also

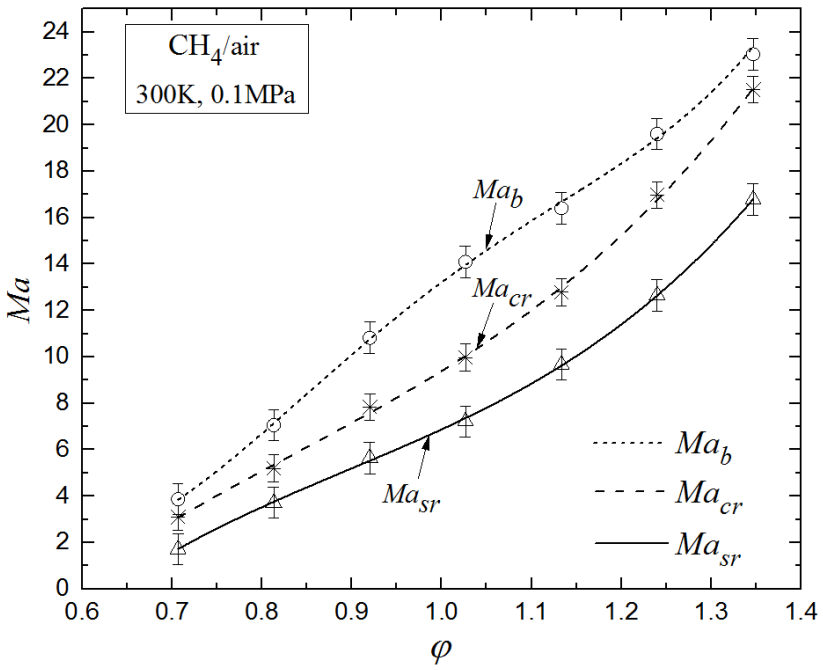

Figure 5.10: Variations of Ma_b, Ma_{sr} and Ma_{cr} with φ for methane/air mixtures at 300 K and 0.1 MPa.

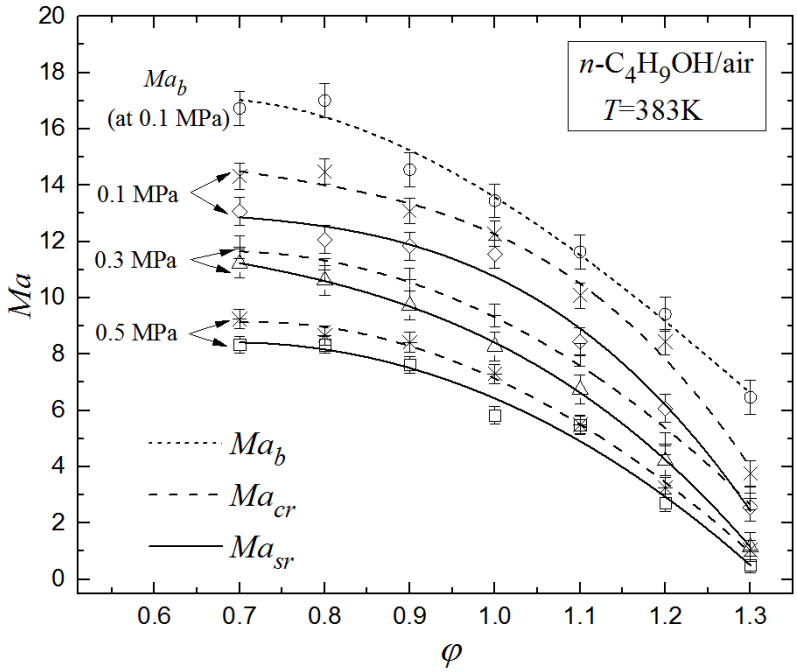

Figure 5.11: Variations of Ma_{sr} and Ma_{cr} with φ for *n*-butanol/air mixtures at different pressures and 383 K.

there are at least three algebraic expressions for flame thickness (Palacios and Bradley, 2017). In addition, see Section 5.2.4.1, there is a probability of up 4-12% underestimation, depending upon the mixture, in the values of L_b. In the present study this is a consequence of the low temperature, 573 K, for the stretch rate isotherm. This degree of underestimation would extend to the different Markstein numbers. Figure 5.12 shows the measured values of L_b for methane/air at 300 K and 0.1 MPa that are referenced in the present work. These were predominantly determined from the uncorrected flame speed method.

As a summary of this section, different values of burning velocities arise between the flame speed method and PIV method, and the principal reason is the common assumption in the flame speed method that the burned gas density is at the equilibrium, burned gas, adiabatic temperature. When allowance is made for the effects of flame stretch rate and Lewis number on the adiabatic density, the differences in burning velocities are significantly decreased. Burning velocities and Markstein numbers are presented for methane, *i*-octane, ethanol, and *n*-butanol over a range of equivalence ratios at atmospheric pressure and, in the case of *n*-butanol, also over a range of pressures. All principle findings and conclusions of this work are outlined in Section 6.1.1.

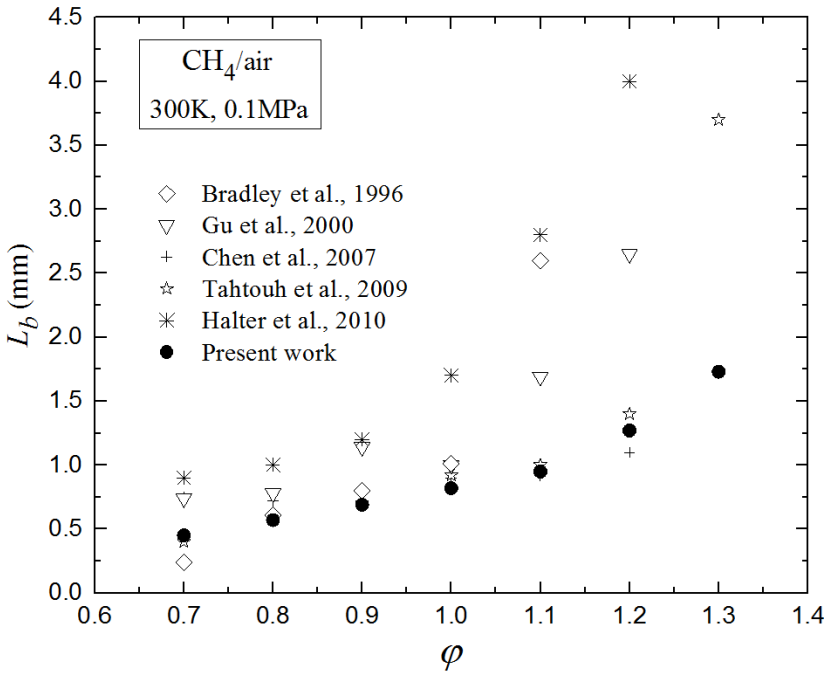

Figure 5.12: Flame speed Markstein length, L_b, for methane/air mixtures at 300 K and 0.1 MPa.

5.3 Characterisation of Turbulence

This section is devoted to assess the turbulence data, for dry air in the absence of phase change and chemical reaction. As mentioned in Chapter (4), the turbulent flow characterisation by means of spatial and temporal spectral analysis is essential to get better understanding of flame/turbulence interaction, which is one of the aims of the present work. The sequential detailed coverage in this section is:

(i). Determination of the extent of the central homogenous volume of isotropic turbulence.

(ii). Derivation of the probability density function of velocity fluctuations normalised by the local rms value.

(iii). Measurement of turbulent length scales.

(iv). Effects of pressure and temperature changes of the air on rms velocities and turbulent length scales.

5.3.1 Homogeneity and Isotropy

For Homogeneous and isotropic flow, the mean flow should be minimal, with spatial and temporal uniformity of the rms turbulent velocity, u', and turbulent length scale, with near-Gaussian turbulent velocity probability density functions, pdfs, all with good control, quantification, and repeatability. This is discussed in the following subsections.

5.3.1.1 Mean and rms Velocity Fluctuations

Figure 5.13 shows the radial distributions of mean velocities, $\bar{u}_x$, $\bar{u}_y$, $\bar{v}_x$ and $\bar{v}_y$ for fan speeds of 1,000 and 6,000 rpm. Data were obtained from 12,500 frames during a time of 2.5s. The velocity components $\bar{u}_x$ and $\bar{v}_x$ were calculated along the x- axis for $y = 0$, whilst, $\bar{u}_y$ and $\bar{v}_y$, were calculated along the y-axis for $x = 0$. The variations of the four components are small and their fluctuations are almost uniform, for x and y distances of $\pm$ 60 mm, indicative of a high level of isotropy. At the higher fan speed of 6,000 rpm, Fig. 5.13b, slight increases and decreases in velocities, of less than 0.95 m/s, are observed beyond a radius of $\pm$ 40 mm. Nevertheless, the values of the four components are small when compared with those of u' and v'.

Figure 5.14 compares the spatial fluctuations of both mean and rms velocities, $\bar{u}$, $\bar{v}$, u' and v' along *x*- and *y*-axes at fan speeds of 1,000, 3,000 and 6,000 rpm. For both mean and rms velocities, *x* and *y* components are similar and isotropic, with $\bar{u}$ and $\bar{v}$ small and less than $0.1u'$. Isotropy and homogeneity are particularly good in the central region at radii up to about 50 mm. However, closer to the fans, at the higher speed of 6,000 rpm and radii greater than 40 mm, isotropy and homogeneity are less good. Average values of $\bar{u}$, $\bar{v}$, u' and v' were computed up to a radius of 60 mm for all fan speeds and these are summarised in Table 5.2.

All measurements geometrically involved the same plane, passing through the centre of the vessel, and the tetrahedral positioning of the fans was intended to maximise the isotropy and homogeneity over other orthogonal planes. According to (Hwang and Eaton, 2004, Ravi et al. 2013, Fansler and Groff, 1990, Xu et al., 2017), an area can be considered to be homogeneous area if ($\bar{u} < 10\%\, u'$ and $\bar{v} < 10\%\, v'$). Such parameters have been calculated at each interrogation area and the corresponding area which satisfy these condition has been assigned. The radial limit, within which there is homogeneity and isotropy is R_H and this is shown, for different fan speeds in Fig. 5.15. Values of u' were estimated for each interrogation window and then averaged over all the interrogation windows within the area of interest. These values also are plotted on the same figure. A linear fit applied to these measurements yields:

$$u' = 0.00124 f(rpm) \quad (m/s). \tag{5.4}$$

These values are up to 5% higher than earlier single point measurements using laser Doppler velocimetry, LDV. This slight difference might be because of the difference in technique, and because the PIV data were averaged over a larger area, with a diameter of 120 mm, whereas the LDV data in (Bradley et al., 1992) were obtained only at the vessel centre.

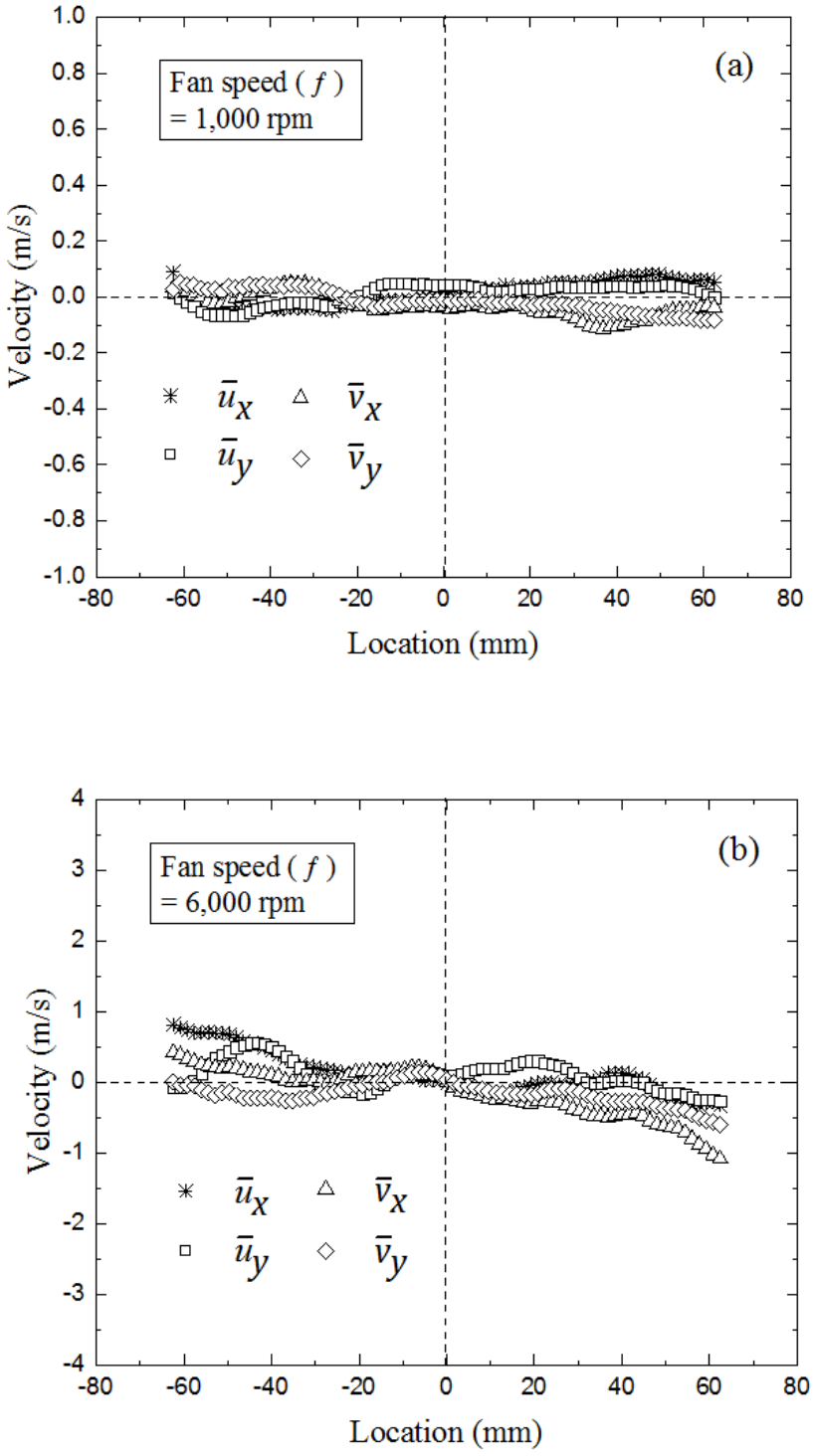

Figure 5.13: Spatial variations of mean velocities of $\bar{u}_x$, $\bar{u}_y$, $\bar{v}_x$ and $\bar{v}_y$ along *x*- and *y*-axes at fan speeds of (a) 1,000 rpm and (b) 6,000 rpm.

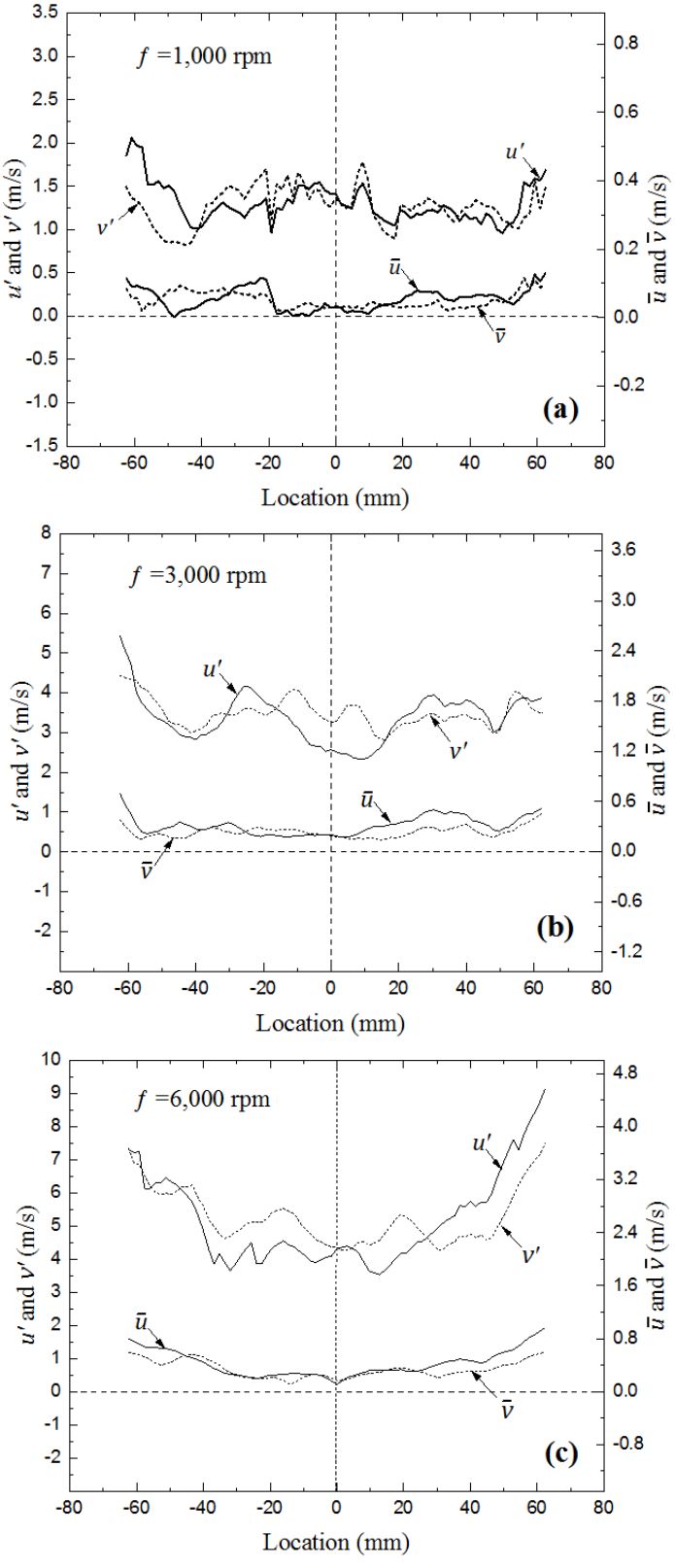

Figure 5.14: Spatial variations $\overline{u}$ and u' along *x*-axis and of $\overline{v}$ and v' along *y*-axis, at fan speeds of (a) 1,000, (b) 3,000 and (c) 6,000 rpm.

Table 5.2: Mean, rms velocities, skewness and kurtosis factors for all fan speeds.

Fan speed (rpm)	1,000	2,000	3,000	4,000	5,000	6,000
$\bar{u}$ (m/s)	0.04 ±0.02	0.22 ±0.04	0.14 ±0.02	0.25 ±0.04	0.51 ±0.04	0.71 ±0.04
$\bar{v}$ (m/s)	0.08 ±0.01	0.17 ±0.02	0.34 ±0.05	0.27 ±0.02	0.63 ±0.03	0.60 ±0.03
u' (m/s)	1.18 ±0.02	2.43 ±0.03	3.62 ±0.03	4.84 ±0.02	6.08 ±0.03	7.23 ±0.05
v' (m/s)	1.22 ±0.02	2.37 ±0.02	3.65 ±0.03	4.81 ±0.03	5.98 ±0.04	7.18 ±0.04
$S_{k,u}$	0.104	0.132	0.105	-0.212	0.282	-0.355
$S_{k,v}$	0.142	0.110	0.151	-0.264	0.232	-0.339
K_u	2.95	2.94	3.01	2.98	2.91	2.86
K_v	2.97	2.96	3.02	3.17	3.12	3.22

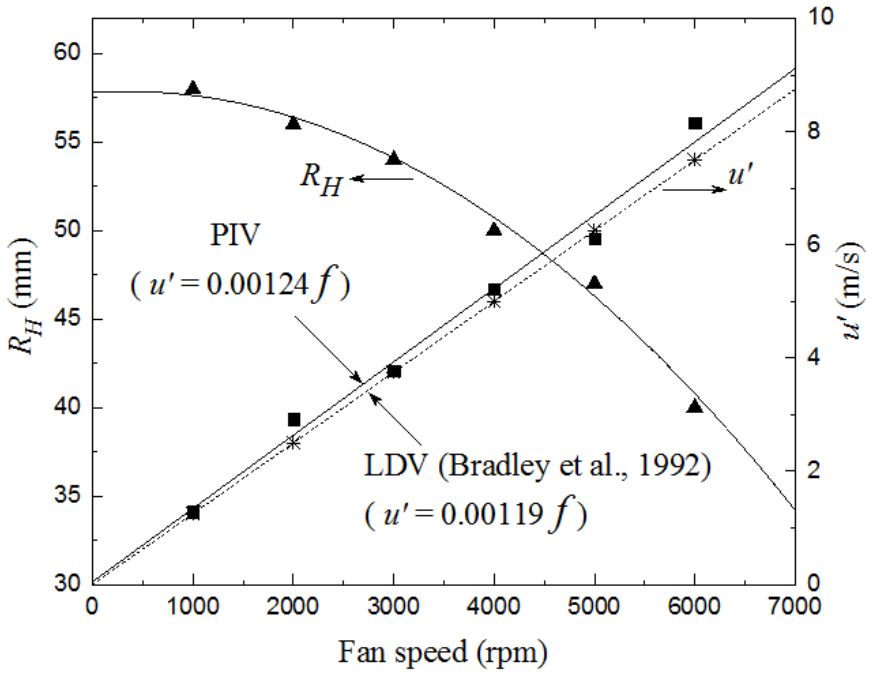

Figure 5.15: Effect of fan speed on the radial extent of homogenous, isotropic turbulence.

5.3.1.2 Pdfs of Turbulent Velocity

Turbulent velocity fluctuations u_N and v_N about the mean, normalised by the local rms value, are calculated as in (Galmiche et al., 2014). u_N is given by:

$$u_N(x,y) = [u(x,y) - \bar{u}(x,y)]/u'(x,y). \tag{5.5}$$

v_N can be calculated using Eq. (5.5), by replacing u, $\bar{u}$ and u' by v, $\bar{v}$ and v', respectively. Figure 5.16 shows the pdfs of u_N and v_N for fan speeds of 1,000 rpm and 6,000 rpm. The results of all pdfs appear to be consistent with normal Gaussian distributions. To quantify more precisely the symmetry of the pdfs and whether the data are heavy-tailed or light-tailed relative to a normal distribution, the Skewness and Kurtosis were evaluated. The Skewness factor is the third moment of u' or v' normalised by the variance. With a symmetric distribution, the skewness factor, S_k, is equal to zero. For S_k> 0, positive fluctuations are dominant. For $S_k < 0$ negative fluctuations dominate. S_k measures the asymmetry of the distribution. In x-direction, S_k and K are given by (Goulier et al., 2017):

$$S_{k,u} = \frac{1}{n}\sum_{j=1}^{n}\left(\frac{\frac{1}{N_{im}}\sqrt{\sum_{i=1}^{N_{im}}[u(x,y,i) - \bar{u}(x,y)]^3}}{[u'(x,y)]^3}\right), \tag{5.6}$$

and,

$$K_u = \frac{1}{n}\sum_{j=1}^{n}\left(\frac{\frac{1}{N_{im}}\sqrt{\sum_{i=1}^{N_{im}}[u(x,y,i) - \bar{u}(x,y)]^4}}{[u'(x,y)]^4}\right). \tag{5.7}$$

Here n is the total number of grid nodes in the i_{th} vector map. The corresponding skewness and kurtosis in the y-direction respectively, noted $S_{k,v}$ and K_v, are calculated in the same way, by using v, $\bar{v}$ and v', in Eqs. (5.6) and (5.7), instead of u, $\bar{u}$ and u', respectivly. Figure 5.17 shows the variations of S_u, S_v, K_u and $K_v$with fan speed. The skewness factors S_u and S_v are very close to zero, indicating a symmetric pdf. Also, the Kurtosis factors, K_u and K_v, are very close to the Kurtosis factor, $K = 3$, of a normal Gaussian curve. These results support the assumption in (Sick et al., 2001) for calculating the integral length scale, that the Kurtosis and Skewness factors are independent of the fan speed. The results of Sections 5.3.1.1 and 5.3.1.2 confirm these features of homogenous and isotropic flow, within the defined regions.

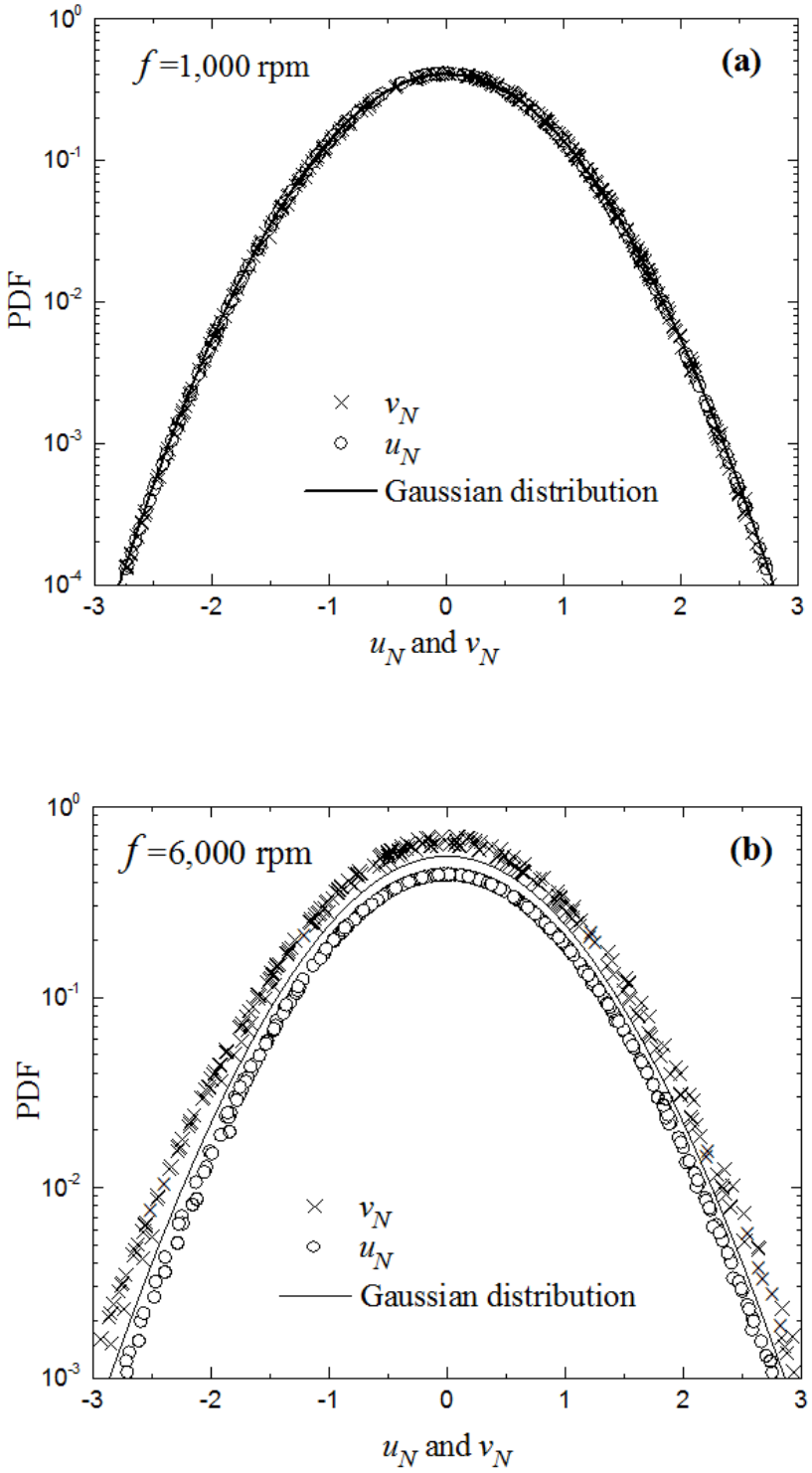

Figure 5.16: Pdfs of u_N and v_N at fan speeds, (a) 1,000 rpm and (b) 6,000 rpm.

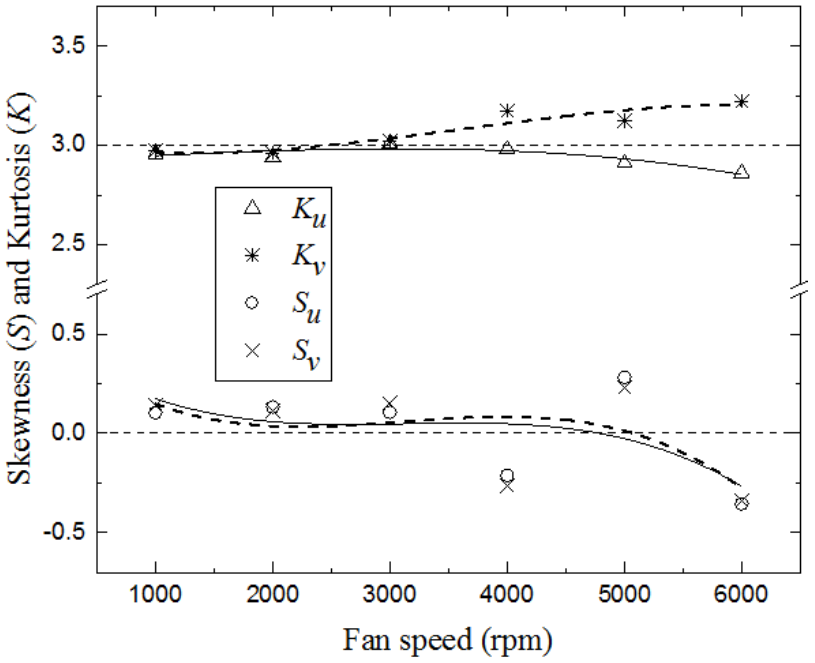

Figure 5.17: Effect of fan speed on skewness and kurtosis factors.

5.3.2 Turbulence Scales

5.3.2.1 Integral Length Scale

A sufficiently large area, 90×90 mm^2, was used to calculate the integral length scales. For all fan speeds, this area was large enough for the correlation coefficient to become zero, R_0 (Ravi et al., 203, Jong et al., 2009). Figure 5.18 shows such an evolution of the longitudinal and lateral correlation coefficients with the spatial lag at a fan speed of 5,000 rpm. The very slight differences between the two longitudinal correlation coefficients R_{ux} and R_{vy} are similar to the differences between the lateral coefficients R_{uy} and R_{vx}, confirming the near isotropic nature of the flow field within the central area.

Figure 5.19 shows the variations of longitudinal and lateral integral length scales, L_{ux}, L_{vy} and L_{uy}, L_{vx} with fan speed, giving mean longitudinal and lateral length scales of 20.4 and 10.5 mm, respectively. Such independence of fan speed has been commonly observed (McComb, 1990, Pasquier et al., 2007).

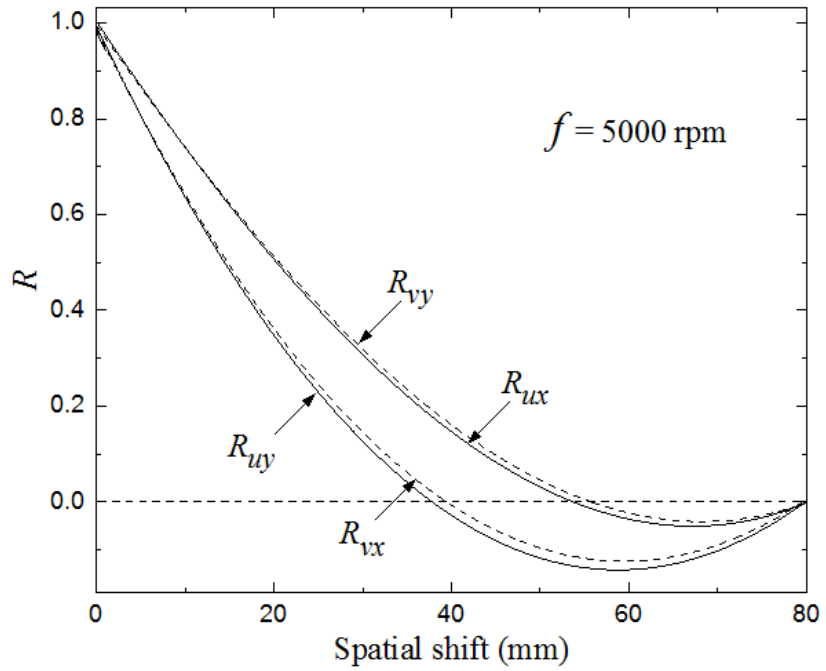

Figure 5.18: Spatial correlation curves of R_{ux}, R_{vy}, R_{uy} and R_{vx} for a fan speed of 5,000 rpm.

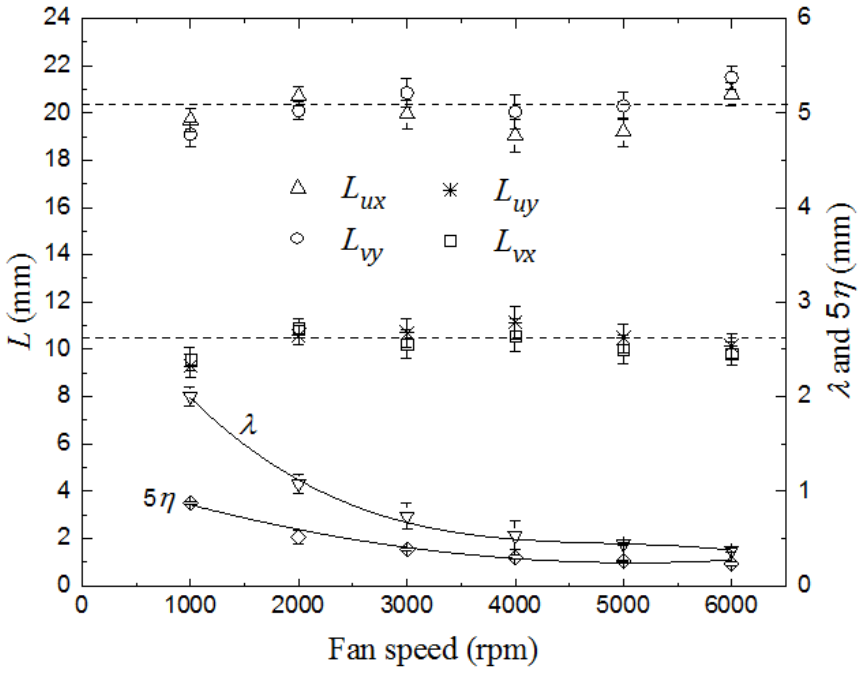

Figure 5.19: Variations of length scales with fan speed.

5.3.2.2 Taylor and Kolmogorov Scales

To calculate Taylor and Kolmogorov length scales, the corrected dissipation rate, ε, was first computed using Eqs. (2.28) to (2.32) and then substituted into Eqs. (2.27) and (2.33), respectively. As shown in Fig. 5.19, λ and η decrease with increasing fan speed. Since L is fixed by the vessel dimensions, increasing Reynolds number $R_L, = Lu'/\nu$ (Tennekes and Lumley, 1972), with the fan speed increases the dissipation rate and leads to finer length scales. Values of the different length scales are tabulated in Table 5.3 for the fan speed range 1,000 to 6,000 rpm, for dry atmospheric air temperatures and pressures. In practice, integral length scales are predominantly determined by the vessel size. In the present case, the diameter of 380 mm is about 19 times larger than L_{ux}, L_{vy}. Clearly, this will be modified by the locations and sizes of the fans and their blades.

Table 5.3: Average values of the lengths scales for all fan speeds, at atmospheric temperature and pressure.

Fan speed (rpm)	R_L	R_λ	L_{ux} (mm)	L_{vy} (mm)	L_{uy} (mm)	L_{vx} (mm)	λ (mm)	5η (mm)
1,000	1,615	220.2	19.7	19.1	9.4	9.1	2.01	0.88
2,000	3,360	317.4	20.7	20.1	10.8	10.6	1.08	0.51
3,000	4,943	385.0	19.9	20.8	10.2	10.7	0.73	0.38
4,000	6,300	434.9	19.1	20.1	10.6	11.1	0.53	0.30
5,000	7,956	488.7	19.2	20.1	10.1	10.5	0.44	0.26
6,000	10,274	555.4	20.8	21.5	9.8	10.1	0.38	0.23

5.3.2.3 Integral Time Scale

The temporal coefficients R_u and R_v coefficients, Eq. (2.26), are plotted in Fig. 5.20, for a fan speed of 1,000 rpm. They are calculated for each interrogation area and then averaged over all interrogation areas within the velocity map. They are closely matched, again indicative of isotropy. The integral length scale L is usually related to the integral timescale τ by Taylor's temporal hypothesis: $L = \bar{u}\tau$, where $\bar{u}$, here, is the advection mean velocity. This is clearly inapplicable when $\bar{u}$ is close to zero, as in the current case. To overcome this, Abdel-Gayed et al. (1984) employed $L = \bar{S}\tau$, with $\bar{S}$, the

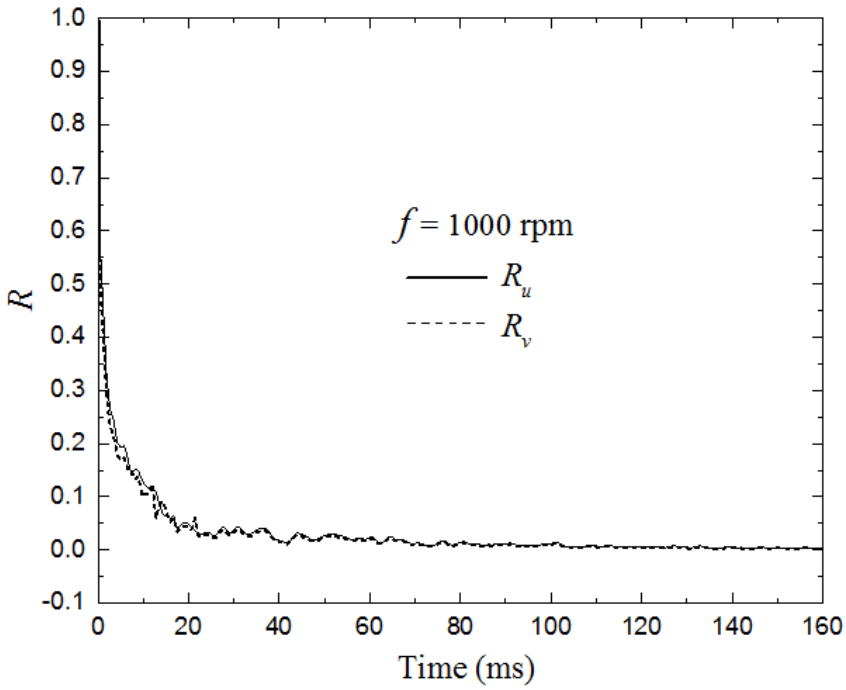

Figure 5.20: Temporal correlation curves R_u and R_v for fan speed 1,000 rpm.

average speed with a three-dimensional Gaussian velocity pdf in isotropic, homogeneous turbulence, given by $\bar{S} = (8/\pi)^{0.5}\, u'$. Hence L could be found from:

$$L = (8/\pi)^{0.5} u'\, \tau. \tag{5.8}$$

Advances in measuring techniques have enabled both L and τ to be measured directly, and the validity of Eq. (5.8) to be assessed. Both L/τ and τ are plotted against u' in Fig. 5.21. Five experiments were employed for each condition. A linear fit to the data yielded $L = 0.88\, u'\tau$. Figure 5.22 shows the mean longitudinal correlation coefficient $R(\xi)$ as a function of the spatial shift (ξ), the mean temporal correlation coefficient $R(L/\tau.t)$ as a function of the product of PIV values of $(L/\tau.t)$ and the mean temporal correlation coefficient $R(\bar{s}.t)$ as a function of the product of $(\bar{s}.t)$. Such of figure shows $R(\bar{s}.t)$ does not coincide with $R(\xi)$. This suggests that the proportionality constant of 0.88, is more acceptable, compared to 1.6 in Eq. (5.8). This result is of practical importance, because optical access often is limited to single point LDV.

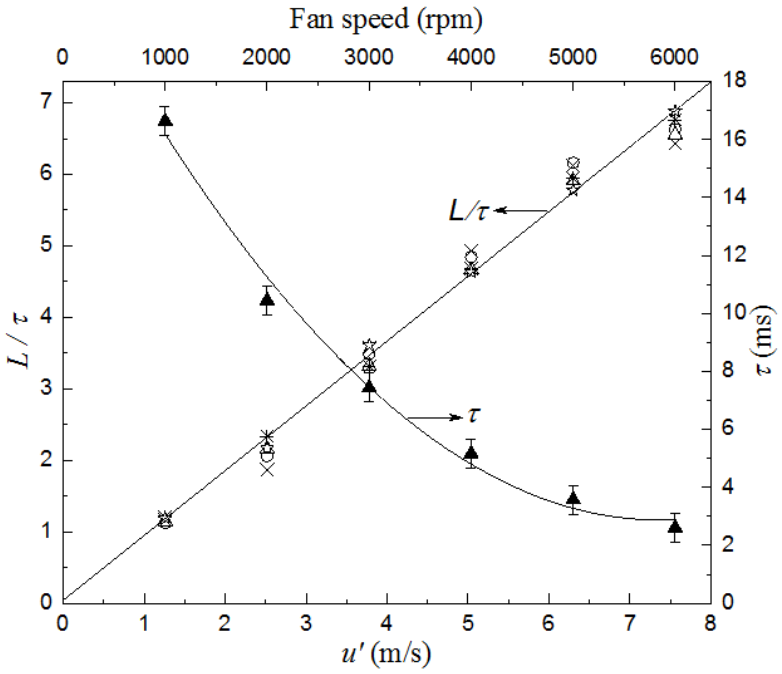

Figure 5.21: Ratio of turbulence integral length scale to integral time scale, L/τ, versus u'.

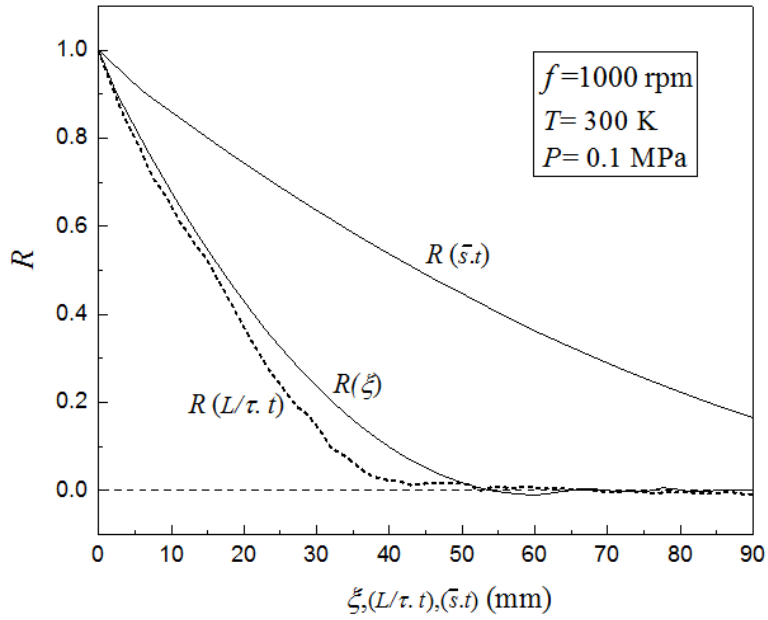

Figure 5.22: Mean temporal and longitudinal correlation curves for a fan speed of 1,000 rpm.

5.3.2.4 Energy Spectra

The one-dimension temporal energy spectra, E_{ux} and E_{vy}, of the velocity fluctuations u and v were computed, using a procedure similar to that outlined in (Doron et al., 2001). They were first computed for each interrogation area, IA, and then averaged over all the IAs, within the velocity map. Figure 5.23 shows average values of energy spectra, E, of the two components E_{Ux} and E_{Vy}, for three rotational speeds of 1,000, 3,000 and 6,000 rpm. The corresponding Reynolds numbers, R_L, are reported in Table 5.3. This figure highlights the inertial subrange, characterised by a (-5/3) scaling law exponent, is extending with R_L, as predicated by the Kolmogorov theory.

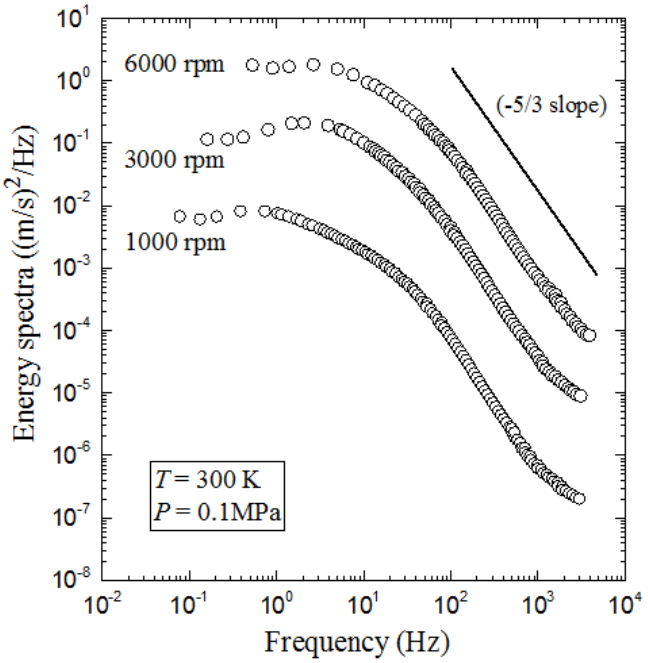

Figure 5.23: Experimental energy spectra at three fan speeds 1,000, 3,000 and 6,000 rpm.

5.3.3 Influence of Temperature and Pressure

Shown, by solid curves, in Fig. 5.24 are the effects of temperature on the temporal rms velocities u' and v' at fan speeds of 1,000, 3,000 and 6,000 rpm at 0.1 MPa. Regardless of the increasing temperature, the values of both u' and v' are very close, at the different fan speeds, suggesting the maintenance of a homogenous isotropic structure of the flow. At fan speeds of 1,000 and 3,000 rpm, there is only a small effect of temperature on the values of u' and v'. At a fan speed 6,000 rpm, the increase in temperature decreases values of u' and v' by up to 12% of the value at 300 K. This might

be associated with increases in kinematic viscosity with increasing *T*. In the same Fig. 5.24, the effect of pressure on the temporal rms velocities u' and v' at fan speeds 1,000, 3,000 and 6,000 rpm at 300 K is shown by broken curves. Increasing pressure showed even smaller changes in the values u' and v' with increasing *P*, which, in this case, slightly increased. The largest effect was at the highest fan speed, possibly associated with a small decrease in kinematic viscosity with increasing *P*.

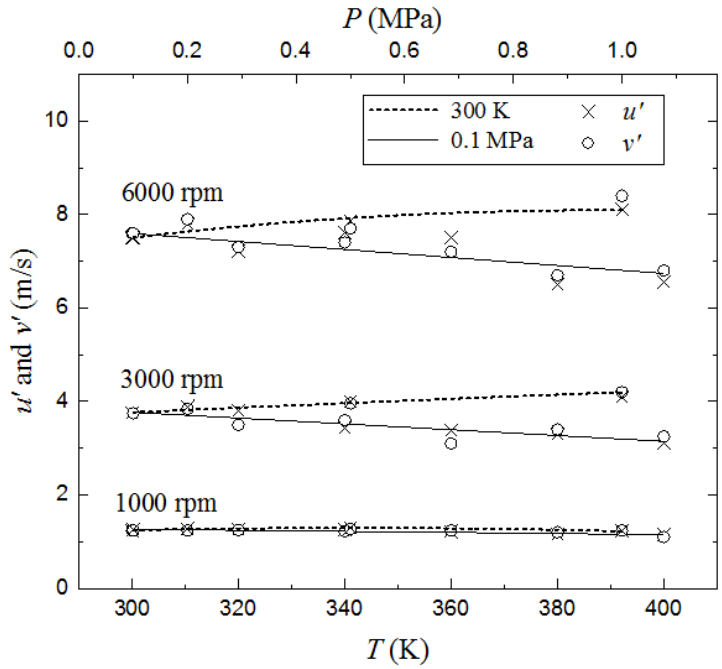

Figure 5.24: Shows, by solid curves, the effect of temperature on u' and v' at 0.1 MPa and, by broken curves, the effect of temperature on u' and v' at 300 K.

The effects of increasing temperatures and pressures on the integral length scale, and the smaller Taylor and Kolmogorov scales are shown in Figs. 5.25 and 5.26, all for a fan speed of 1,000 rpm. Figure 5.25 shows the effect of temperature on length scales at a pressure of 0.1 MPa. This shows the integral length scale, *L*, Taylor length scale, λ, and Kolmogorov length scale, η, are increased by up to 10 %, 36.5% and 47 %, respectively, of their values at 300 K. Such increases can be related to the increase in the kinematic viscosity with temperature in Eqs. (2.27) and (2.33). Figure 5.26 shows the effect of pressure on *L*, λ, and η at 300 K. Increasing the pressure has no effect on the integral length scales, it generates smaller eddies and consequently smaller lengths scales. Both values of λ and η decrease, with increasing the pressure, which agrees with the trend in (Fansler and Groff, 1990). As shown in (Lachaux et al., 2005), for isotropic and homogenous flow, the Taylor length scale varies as $P^{-1/2}$, and the Kolmogorov varies as

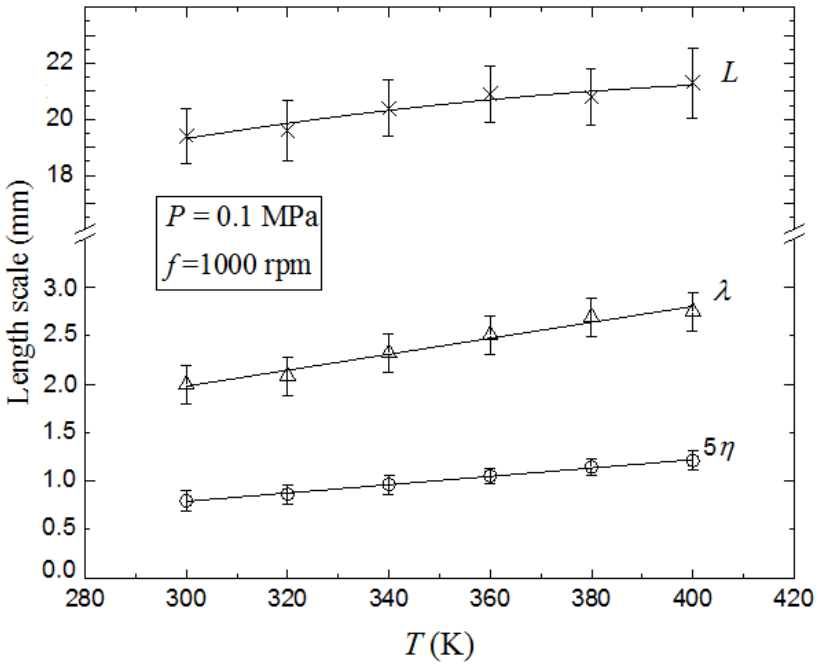

Figure 5.25: Effect of temperature on length scales at a fan speed of 1,000 rpm.

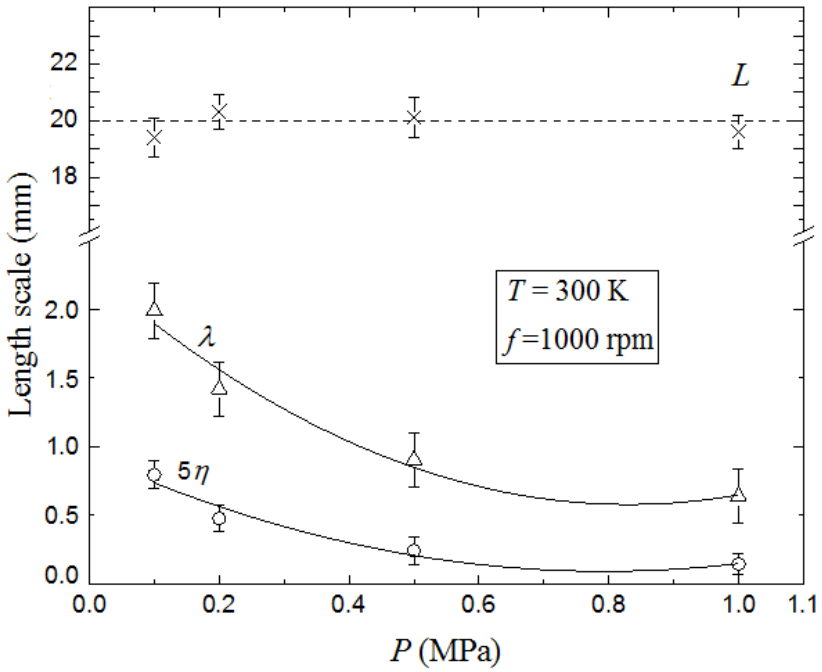

Figure 5.26: Effect of pressure on length scales at a fan speed of 1,000 rpm.

$P^{-3/4}$. These trends have been observed in the present results at different fan speed. These results are summarised in Appendix B, Tables B.5 and B.6, for different temperatures and pressures.

Here ends the discussion of the cold flow turbulence characterisation. As a summary of this work, spatial and temporal distributions of mean and root mean square, rms, velocity fluctuations are investigated, as well as integral length scales, L, Taylor microscales, λ, and Kolmogorov length scales, η, in the fan speed range, 1,000-6,000 rpm. The turbulence is close to homogeneous and isotropic in the central volume. This volume decreases with increasing fan speed. Further conclusions of this work are summarized in Section 6.1.2.

5.4 Turbulent Burning

The presented turbulent burning results in Chapter (4), clearly demonstrated a complex interaction between the turbulence and flame during combustion. Not only the flow has a considerable effect on combustion (i.e. u_{tr}), but also the flame propagation influences the motion of the reactants. This symbiotic evolution of the flow and flame means that both must be examined when analysing turbulent combustion.

For the first time, to the author's knowledge, the rms turbulent velocity, to which the flame is actually exposed during the flame propagation, is calculated directly without any assumptions concerning the cold flow one-dimensional PSD function (Abdel-Gayed et al., 1987, Bradley et al., 2009). This has been discussed in the following subsections.

5.4.1 Radial and rms Velocities

To calculate the rms turbulent velocity, a zone of specified thickness, ~ 0.94 mm, ahead of the flame front was defined, as shown in Fig. 5.27. More analytical details can be found in Appendix C. Within this zone, the radial velocity profile, surrounding the flame front, was deduced and divided into a number of sectors N_i. The spatial rms turbulent velocity, u'_s, was then calculated for each sector and then averaged over all the velocity profile around the flame front as:

$$u'_s(x,y) = \frac{1}{N_i}\sum_{i=1}^{N_i}\left[\sqrt{\left(\frac{1}{N_p}\sum_{p=1}^{N_p}\left[U_r(x,y,p) - \bar{u}_g(x,y)\right]^2\right)}\right]. \quad (5.9)$$

where U_r is the radial velocity component at each (x, y) grid node (see Appendix C), $\bar{u}_g$ is the mean gas velocity within each sector. N_p is the total number of velocity vectors in each sector.

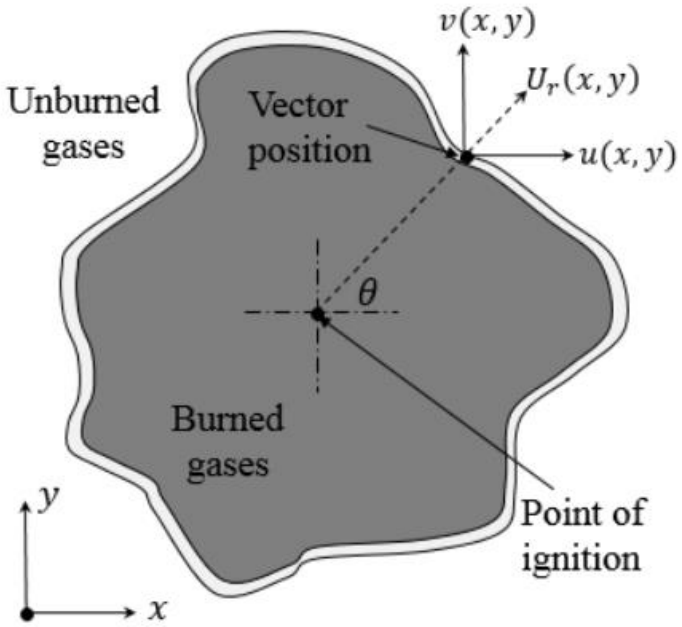

Figure 5.27: Location of measurements.

Figure 5.28 shows the local radial velocity around flame front at two different times, *t* = 2.4 and *t* = 8.6 ms, after ignition. In Fig. 5.28a, at *t* = 2.4 ms, the small flame front has a small number of wrinkles because it is not exposed to the full spectrum of turbulence, as stated by (Ivashchenko and Rumyantsev, 1972). It is only affected by the higher frequencies, while the lower frequencies convect the flame bodily without affecting the flame front significantly. This phenomenon can be clearly seen from the velocity vectors fields, shown in Figs. 4.22 to 4.26 in Chapter (4). Such figures show also that small wrinkles move faster and increase the unburned gas significantly. This has been confirmed by the radial velocity profile, shown in Fig. 5.28. As time passes, the flame front grows and the front becomes affected by small to progressively larger scales causes an increase in the number of wrinkles. This increases the fluctuation of the radial velocity around the flame front, as shown in Fig. 5.28b, and a consequently u_s' is expected to increase with time.

The variation of u_s' was measured during explosions, for three mixtures of methane/air flames, with φ = 0.8, 1.0 and 1.2 at temperatures of 300 and 400 K, and pressures of 0.1 and 0.5 MPa. Firstly, the vectors around the flame front was detected at

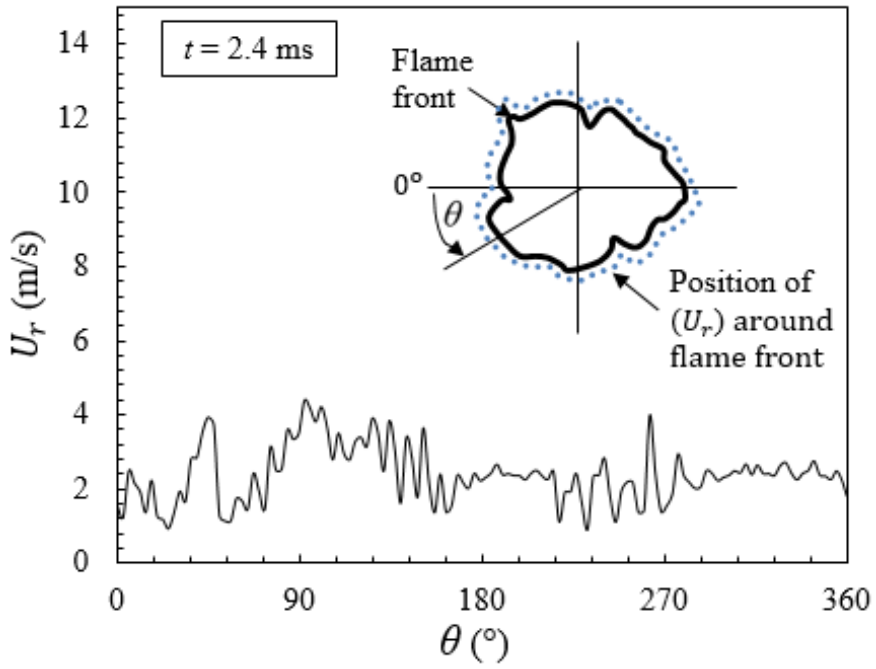

(a)

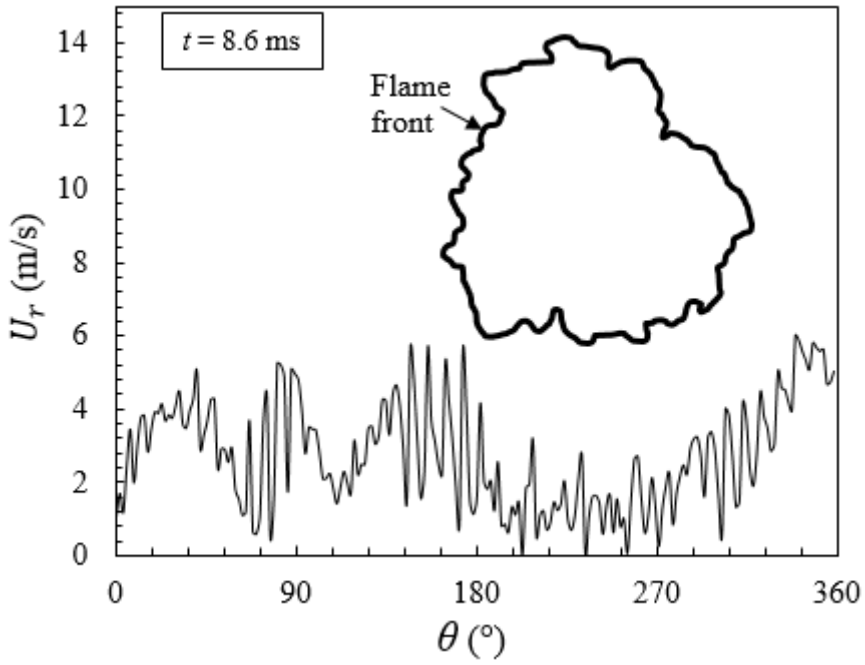

(b)

Figure 5.28: Local radial velocity, U_r, around flame front, for stoichiometric methane/air mixture, u' = 1.0 m/s, 300 K and 0.1 MPa , at (a) t = 2.4 ms (r_v = 14 mm), and (b) t = 8.6 ms (r_v = 30 mm)

each instant during the evolution of the flame and then u_s' is calculated using Eq. (5.9). This calculation was repeated for four levels of turbulence, u'= 0.5, 1.0, 2.0 and 4 m/s. The variation of u_s' with r_v is shown in Fig. 5.29, for stoichiometric methane/air mixture at 300K and 0.1 MPa. Each curve represents the mean of five explosions. For all u', the value of u_s' increases with r_v. Also, as u' increases, so does u_s'.

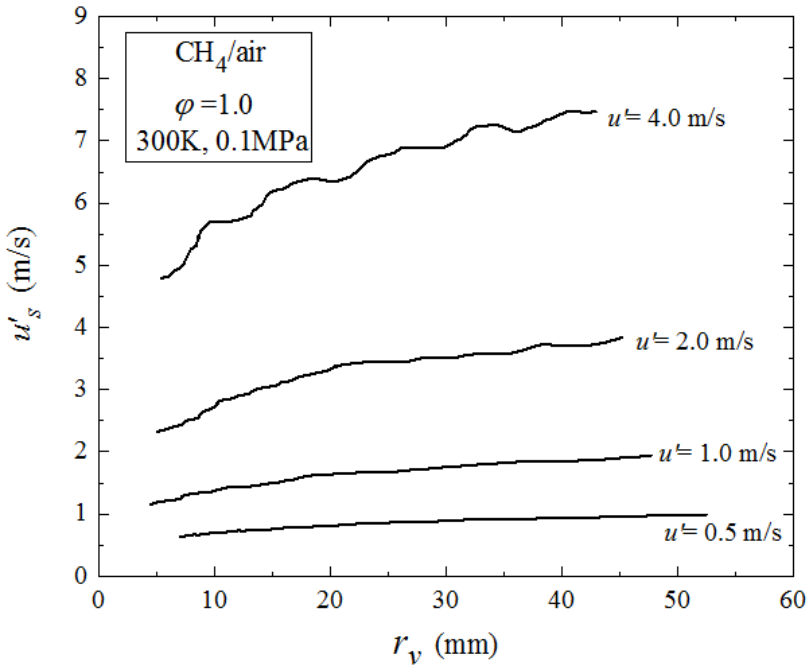

Figure 5.29: Variation of u_s' with flame radius, for stoichiometric methane/air flame at 300 K, 0.1 MPa, u' = 0.5, 1.0, 2.0 and 4.0 m/s.

5.4.1.1 Influence of Temperature and Pressure

The influence of temperature, T_u, on u_s' is shown in Fig. 5.30, for stoichiometric methane/air flame at 0.1 MPa for u'= 0.5, 1.0, 2.0 and 4.0 m/s. Solid curves show the results at 300 K and dotted curves show that of 400 K. For all values u', and flame radius < 20 mm, the influence of T_u is small. As flame grows, the values of u_s' at 400 K become higher than that at 300 K. This might be associated with with the increase in flame speed with increasing T_u.

The influence of initial pressure, P, on u_s' is shown in Fig. 5.31, for stoichiometric methane/air flame at 300 K. Solid curves show the results at 0.1 MPa and dotted curves show that of 0.5 MPa. The effect of P on u_s' is small for u'= 0.5, 1.0 and 2.0 m/s. The

largest effect was at the highest fan speed, u'= 4 m/s, possibly associated with the small increase in flame speed with increasing P (see Section 4.4.3).

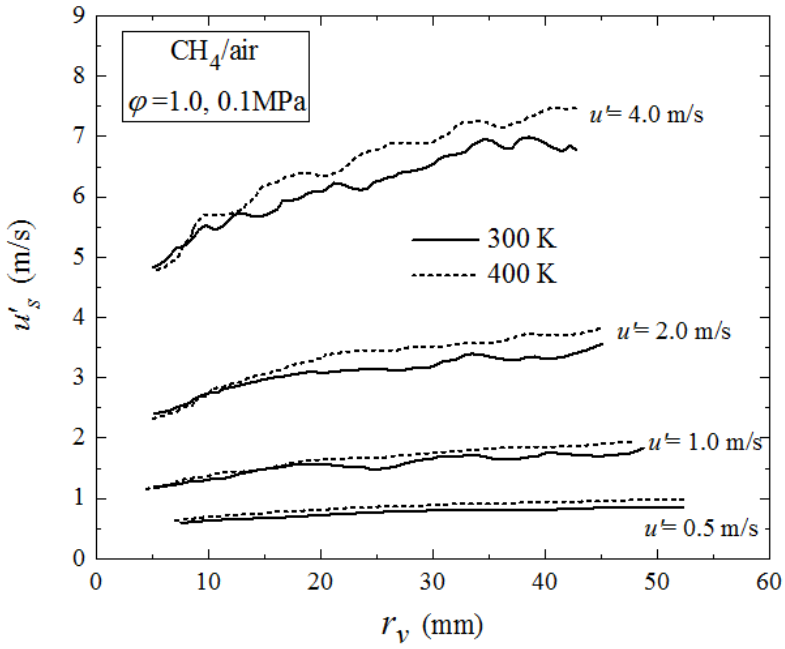

Figure 5.30: Influence of temperature on u'_s.

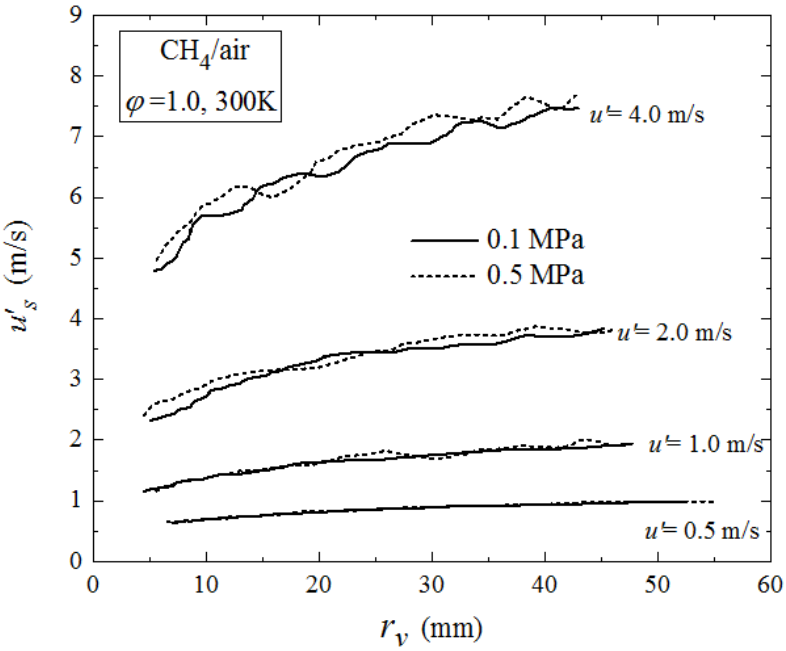

Figure 5.31: Influence of pressure on u'_s.

5.4.1.2 Influence of Equivalence Ratio

The effect of equivalence ratio on the u_s' was investigated, using three mixtures of methane/air (φ= 0.8, 1.0 and 1.3) for u'= 0.5, 1.0, 2.0 and 4.0 m/s at 300 K and 0.1MPa. Figure 5.32 shows an example for such effect at u' = 1.0 m/s. The values of u_s' increases with increasing φ from 0.8 to 1.0. The lowest values of u_s' were at φ =1.3. This can be attributed to the rate of change in flame speed with time (see Section 4.4). At φ =1.3, the flame propagates slower than that for φ = 0.8 and 1.0. This means less wrinkling and consequently less fluctuation in the velocity ahead of the flame which explains the low values of u_s' at φ =1.3.

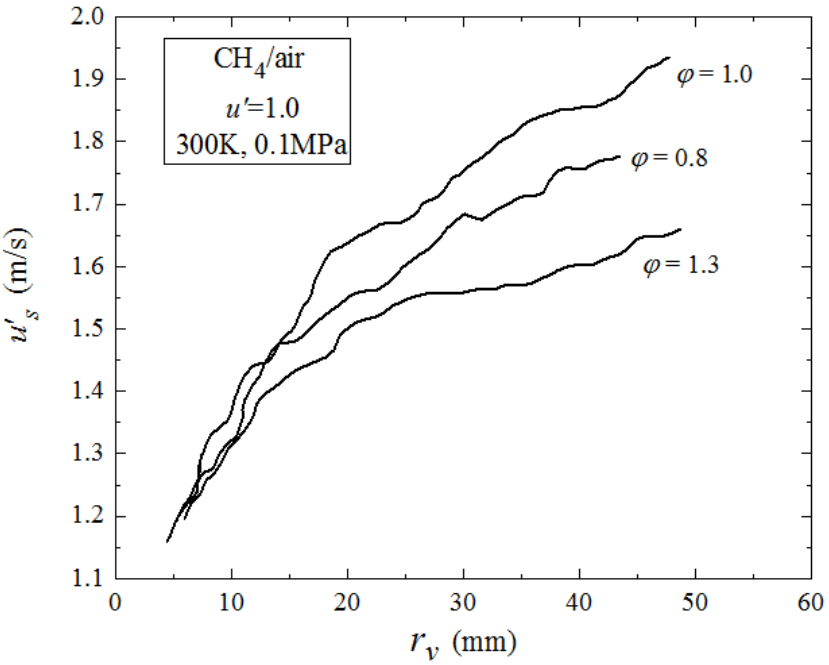

Figure 5.32: Influence of equivalence ratio on u_s'.

5.4.1.3 Correlation of the spatial rms Turbulent Velocity

The results in Figs. 5.29 to 5.32 can be empirically correlated by the following relationship:

$$u_s' = \left[\frac{1 + 0.12\ ln(r_v)}{280}\right].f.\left(\frac{T_u}{T_0}\right)^a\left(\frac{P}{P_0}\right)^b\left(\frac{\varphi}{\varphi_0}\right)^c. \quad (5.10)$$

Where r_v is the flame radius, f is the fan speed in (rpm), T_u and P are the initial temperature and pressure, respectively, φ is the equivalence ratio, $T_0 = 300\ K$, $P_0 = 0.1\ MPa$, φ_0=1.0, $a = 0.81$, $b = 0.01$, $c = 0.36$ for $\varphi < 1.0$ and $c = -0.55$ for $\varphi >$

1. Equation (5.10) can be used to quantify the spatial rms velocity ahead of turbulent methane flames at normal and high pressures up to 0.5 MPa.

5.4.2 Turbulent Burning Velocity

Measurement of turbulent burning velocity, u_{tr}, in a fan-stirred vessel has several advantages, like that the entire spherical flame front is exposed to turbulence that is homogeneous and close to isotropic. Also, constant pressure combustion can be achieved with relatively small fuel samples. The disadvantage is that allowance must be made for the transient changes in rms velocity, to which the flame is exposed (Bradley, 2011).

Figures 5.33 and 5.34 show such variation of u_{tr} with u_s' for different u', covering different initial pressures and equivalence ratios at 300 K. Values of u_{tr} were found from Eq. (2.38) with (ρ_b/ρ_u) obtained from Gaseq (Morley, 2005) and u_s' from Eq. (5.10). During the early stage of the flames propagation at low u', the rate of reactants burning is close to, or slightly higher than, u_l until the turbulent eddies become more energetic to wrinkle the kernel. However, at higher u' and low pressure (i.e. 0.1 MPa), the smaller turbulent scales are more effective and immediately wrinkling the flame front from its onset, as shown in Fig. 5.33. Conversely, at high u' and high pressure (i.e. 0.5 MPa), the flow convect the flame kernels bodily without wrinkling the flame front significantly. This can be seen clearly from the flame images in Chapter (4). After such initial stage, the burning rate turns out to be dependent linearly on u_s', for both low and high pressures.

Shown in Fig. 5.35 is comparison between the variation of u_{tr} with u_s' and its variation with the effective rms turbulent velocity, u_k', described in Chapter (2). The later was measured from the turbulence spectrum, in the absence of any flames. At the same values of u_{tr}, the values u_s' are higher than that of u_k'. Although, the values of u_k' are low, the burning rate increases immediately from the inception of the flame propagation. In contrast, the values of u_s' are high and the burning rate is increasing gradually at the early stage until the turbulent eddies become more effective to wrinkle the kernel as discussed above. One of the possible reasons of this difference between u_s' and u_k' is that u_k' was measured based on one-dimensional energy spectrum results, whilst, u_s' based on two-dimensional measurements. Due to the disparity between these measurements and the highly three-dimensional nature of the flame, these one and two-dimensional measurements cannot provide the complete information required to accurately analyse the complex flame/flow interaction. Inclusion of the third spatial dimension within the

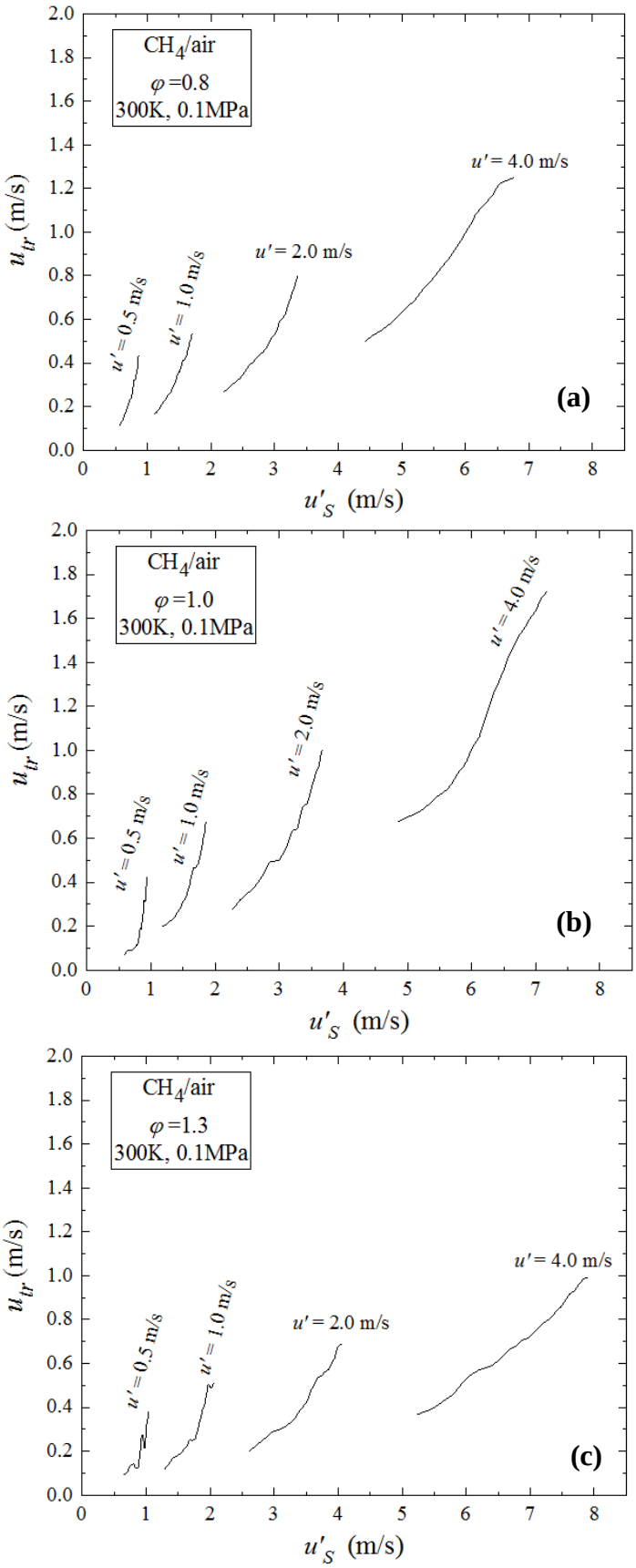

Figure 5.33: Variation of u_{tr} with u'_s for different u' at 300 K and 0.1 MPa for (a) φ = 0.8, (b) φ = 1.0 and (c) φ = 1.3.

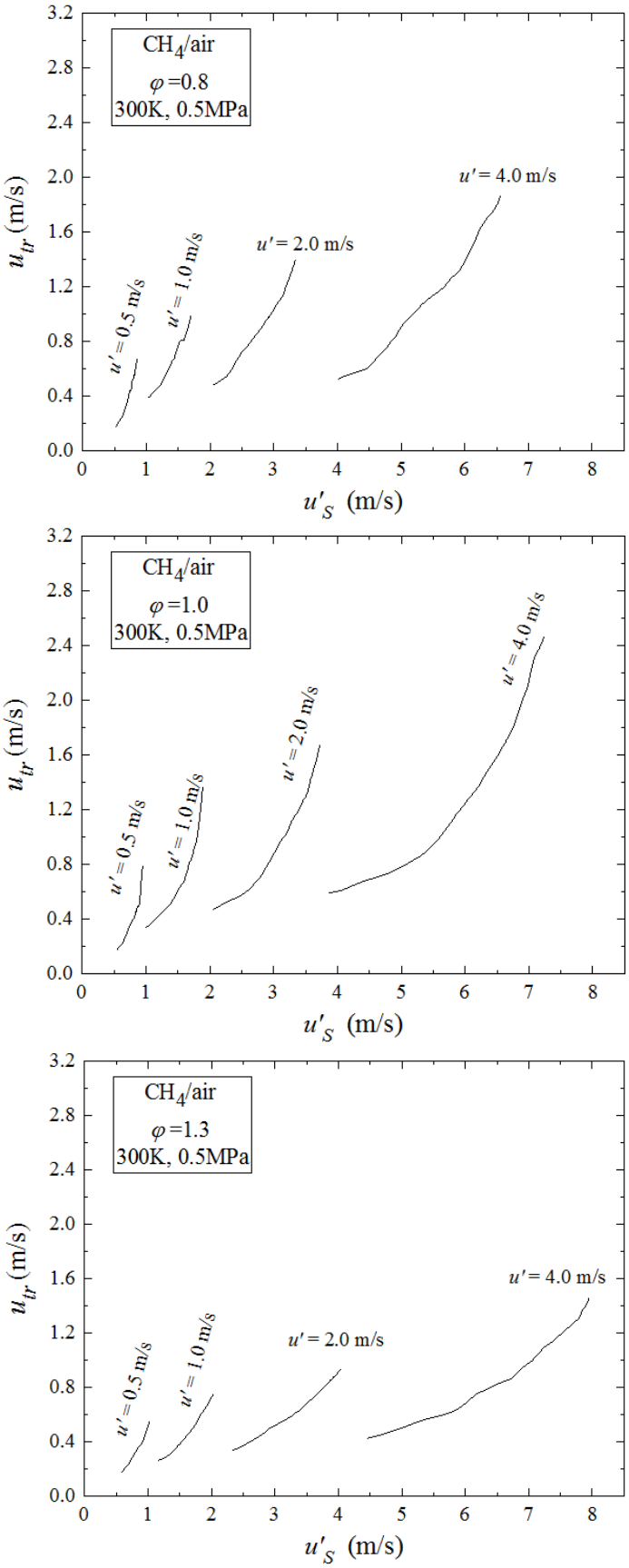

Figure 5.34: Variation of u_{tr} with u'_s for different u' at 300 K and 0.5 MPa for (a) φ = 0.8, (b) φ = 1.0 and (c) φ = 1.3.

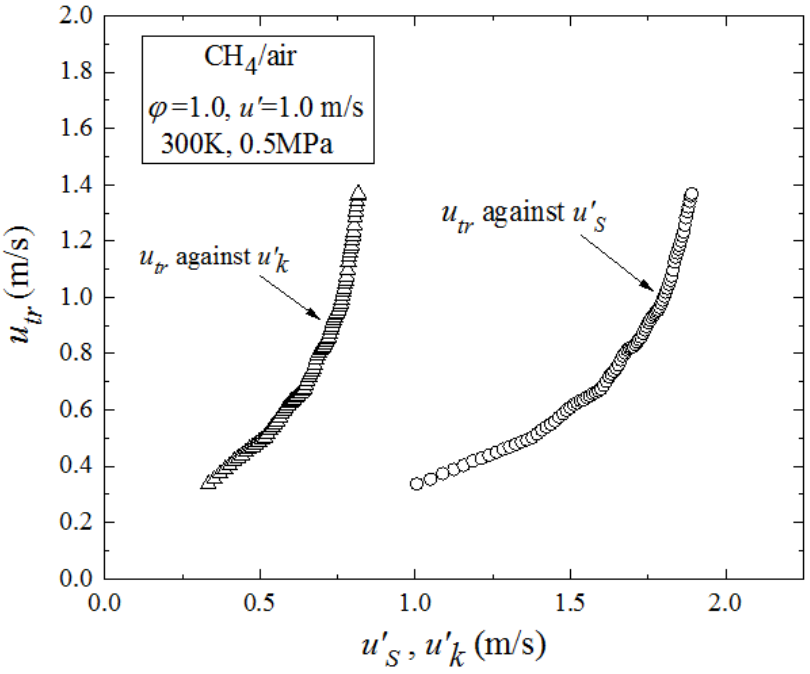

Figure 5.35: Variation of u_{tr} with u'_s and u'_k.

measurements of flame displacement and flow is necessary to get better understanding of this interaction. Disappointingly, the equipment necessary for this is not available. High Speed Stereoscopic PIV would provide information on the third component of flow velocity but cannot give the third component of the flame front displacement. Likewise, high resolution holographic PIV would provide the necessary flow information, but another technique would be required to capture the flame displacement. Perhaps the best hope for this kind of measurement is three-dimensional tomographic PIV where multiple cameras can be used to identify particle locations in time and space. However, the low particle density required would lead to blurring flame front location. It will be also difficult to somewhat to set up multiple cameras using the current vessel. Fully transparent vessel would be more suitable.

As a summary of this work, the rms velocity, u'_s, ahead of the flame front was calculated and presented for methane/air flames. The influence of T_u, P and φ on u'_s has been discussed and relationship for the latter was obtained. Further conclusions and suggestions for future work are outlined in Chapter (6).

Chapter 6 - Conclusions and Future Work

6.1 Conclusions

Particle Image Velocimetry, PIV, introduced to the combustion group was subsequently employed for measuring laminar burning velocities during flame propagation in spherical explosions, characterising the near-homogeneous, isotropic, cold flow turbulence in the fan-stirred vessel and, finally, measuring the changes in rms turbulent velocity during explosion. The principle findings and conclusions of the present work can be summarised as following:

(i). A methodology has been developed for correcting burning velocities, measured by the flame speed method, due to it not having an adiabatic value of burned gas density Laminar Burning.

(ii). Values of burning velocities and Markstein numbers, have been measured over a full range of φ for methane, *n*-butanol, *i*-octane and ethanol mixtures with air. Effects of pressure have been studied for *n*-butanol/air mixtures. These results extend the presented results in the literature, especial for *n*-butanol fuel.

(iii). Greater errors and general variability arise in the measurement of Markstein lengths, due to stretch rate measurements at different isotherms, with higher temperatures preferred. It is estimated that, on this account, the present values of L_b should possibly be increased by between 4 and 12%.

(iv). Spatial and temporal fluctuations of mean and rms velocities have been presented at different fan speeds between 1,000 and 6,000 rpm, using air in the vessel. The

mean velocity within each interrogation area has been shown to be negligible, compared with the rms turbulent velocity indicating the near homogeneity and isotropy of the flow in the vessel.

(v). The length and temporal integral scales are related by a novel expression, $L = 0.88\,u'\tau$, somewhat more direct than an earlier expression, Eq. (5.8).

(vi). The region of homogeneity and isotropy decreases with increasing fan speed. The maximum radius, R_H, of this region is given in terms of the fan speed and u' in Fig. 5.15

(vii). Longitudinal and lateral integral length scales of the turbulence were obtained by integration of the respective correlation coefficients. Values of the length scales L_{ux} and L_{vy} are similar, as are those of L_{uy} and L_{vx}. These differ for the two sets, but are independent of the fan speed. Taylor and Kolmogorov length scales, obtained directly from the PIV correction method, are also presented.

(viii). At low fan speeds and 0.1 MPa, there is little effect of temperature upon u' and v', whereas, at f = 6,000 rpm these values decrease with increasing temperature. At low fan speeds and 300 K, there is but small effect of pressure change, but at 6,000 rpm there is a slight increase in velocities with increasing pressures. With regard to the integral length scales, at 1,000 rpm, the integral length scales are unchanged with pressure, but increase slightly with temperature.

(ix). The turbulent burning velocity, u_{tr}, and turbulent flow fields a head of methane flames have been investigated at different u', P and T_u for φ = 0.8, 1.0 and 1.3. The values of u_{tr} were found to be mainly dependent on r_v, affected drastically by u', and slightly by φ and P.

(x). In terms of influence of flame on flow, the results have shown that the flame propagation alters the bulk flow of the unburned gases ahead of the flame front. As flame grows, the unburned gases are pushed outwards along with the flame front. The fluctuation of the unburned gases velocity ahead of the flame was found to be increasing with u'.

(xi). The variation of the rms turbulent velocity, u_s', ahead of flame, to which the flame is exposed, has been estimated and presented at different conditions. An empirical equation of u_s' has been developed. As flame grows, u_s' increases indicating the increase in the flame wrinkling. After the initial stage of the flame propagation, the burning rate turns out to be dependent linearly on u_s'. The

increase in u_s' is affected drastically by u', and slightly by φ and T_u. The influence of P on u_s' was found to be small.

6.2 Future Work

This section give recommendations based on the results and conclusions presented, in terms of further research paths and the experimental apparatus used.

(i). The underestimation of Markstein lengths using PIV was related to the lower temperature of the flame image isotherm, which is associated to the droplet evaporation temperature. Further study is recommended using different seed materials, with different evaporation temperatures. This will allow studying the isotherms effect on Markstein lengths. The results can be also used to amend the PIV correlations, to provide Markstein lengths close to that are calculated at the burned gases temperature.

(ii). Because no assumptions are needed to extract u_l from the PIV technique, it could be very interesting to apply this technique on highly diluted fuels/air mixtures diluted by gases like carbon dioxide (CO_2), carbon monoxide (CO), and water vapor (H_2O). These gases have strong spectral radiation absorption. Because of the thermal and chemical effects of these gases on the combustion mechanism, real flame temperatures clearly differ from the adiabatic temperature. It is therefore erroneous to calculate unstretched burning velocity using the flame speed method under its adiabatic assumptions.

(iii). The challenges of the PIV technique for measuring u_l relies on the accurate determination of the maximum unburned gas velocity, u_g, ahead of the flame front. Increasing the spatial resolution of the imaging would allow better determination of not only u_g but also for S_n and consequently more accurate determination of u_l. It would be interesting to see to what extent the spatial resolution would affect the PIV measurement of u_l. High resolution camera is required for this study.

(iv). It could be of interest to compute for a simple case (like methane/air flame, for instance), a full 3D DNS of a spherically laminar expanding flame with detailed chemistry and transport. A comparison between both PIV experimental results and numerical results could be a starting point to clearly identify more sources of uncertainties.

(v). Dry air has been used during the characterisation of turbulence inside the vessel. Whilst, this vessel has been specially designed to do several investigations in turbulent combustion, using fuels/air mixtures. Hence, It would be useful to study the effect of using fuels/air mixtures, in absence of phase change and chemical reaction, on the turbulent flow characteristics.

(vi). Fan speed range of 1,000-6,000 has been used, whilst the fan can be run up to 10,000 rpm. Further study is required to extend the presented results. Solid seeding material is recommended, to avoid the rapid dissipation of liquid particles due high velocities. The seeding system must be modified to use such type of particles.

(vii). The resolution of current measurements is finite for a direct computation of the small-scales (i.e. Taylor and Kolmogorov scales). Therefore, a correction method has been applied to calculate these scales. It is recommended to measure these scales with a very high resolution camera, if possible, and compare both results.

(viii). Only methane/air mixtures have been employed in the present study for measuring the turbulent flame/flow interaction. These are characterized by Lewis number close to unity. It would be interesting to study the influence using different fuels/air mixtures on the value of u_s', under different experimental codtions. The results can be used to generalize the current equation of u_s'.

(ix). As a long terms goal, work should be devoted to develop the PIV technique to operate in all three dimensions of space. This would enable more accurate turbulent flame/flow interactions to be investigated. One approach to this could be the use of tomographic PIV where multiple cameras can be used to identify particle locations in time and space. A “new vessel” with more access windows or a “fully transparent vessel” would be more useful for this study.

References

Abdel-Gayed, R. G., Al-Khishali, K. J., Bradley, D., 1984. Turbulent burning velocities and flame straining in explosions. Proceedings of the Royal Society of London. A. Mathematical and Physical Sciences, 391(1801), 393-414.

Abdel-Gayed, R. G., Bradley, D., Lawes, M., 1987. Turbulent burning velocities: a general correlation in terms of straining rates. Proceedings of the Royal Society of London. A. Mathematical and Physical Sciences, 414(1847), 389-413.

Abdel-Gayed, R. G., Bradley, D., Lung, F. K., 1989. Combustion regimes and the straining of turbulent premixed flames. Combustion and Flame, 76(2), 213-218.

Addabbo, R., Bechtold, J. K., Matalon, M., 2002. Wrinkling of spherically expanding flames. Proceedings of the Combustion Institute, 29(2), 1527-1535.

Andrews, G. E., Bradley, D., 1972. Determination of burning velocities: a critical review. Combustion and Flame, 18(1), 133-153.

Andrews, G. E., Bradley, D., Lwakabamba, S. B., 1975. Measurement of turbulent burning velocity for large turbulent Reynolds numbers. In Symposium (International) on Combustion, 15(1), 655-664.

Anupam, D., Ting, D. S.-K. and Checkel, M. D. (2006), "The Effects of Temperature and Pressure on Stretched, Freely Propagating, Premixed, Laminar Methane-Air Flame", SAE Paper 2006-01-0494.

Aung, K. T., Hassan, M. I., Faeth, G. M., 1997. Flame stretch interactions of laminar premixed hydrogen/air flames at normal temperature and pressure. Combustion and flame, 109(1-2), 1-24.

Aung, K. T., Tseng, L. K., Ismail, M. A., Faeth, G. M., 1995. Laminar burning velocities and Markstein numbers of hydrocarbon/air flames. Combustion and Flame, 102(4), 526-530.

Balusamy, S., Cessou, A., Lecordier, B., 2011. Direct measurement of local instantaneous laminar burning velocity by a new PIV algorithm. Experiments in fluids, 50(4), 1109-1121.

Batur, İ., Bayram, I. S., Koc, M., 2019. Impact assessment of supply-side and demand-side policies on energy consumption and CO_2 emissions from urban passenger transportation: The case of Istanbul. Journal of Cleaner Production, 219, 391-410.

Bechtold, J. K., Matalon, M., 1987. Hydrodynamic and diffusion effects on the stability of spherically expanding flames. Combustion and Flame, 67(1), 77-90.

Bedat, B., Cheng, R. K., 1995. Experimental study of premixed flames in intense isotropic turbulence. Combustion and Flame, 100(3), 485-494.

Beeckmann, J., Hesse, R., Schaback, J., Pitsch, H., Varea, E., Chaumeix, N., 2019. Flame propagation speed and Markstein length of spherically expanding flames: Assessment of extrapolation and measurement techniques. Proceedings of the Combustion Institute, 37(2), 1521-1528.

Beretta, G. P., Rashidi, M., Keck, J. C., 1983. Turbulent flame propagation and combustion in spark ignition engines. Combustion and flame, 52, 217-245.

Bonhomme, A., Selle, L., Poinsot, T., 2013. Curvature and confinement effects for flame speed measurements in laminar spherical and cylindrical flames. Combustion and Flame, 160(7), 1208-1214.

Borghi, R., 1985. On the structure and morphology of turbulent premixed flames. In Recent advances in the Aerospace Sciences, Plenum Press, New York.

Bouvet, N., Halter, F., Chauveau, C., Yoon, Y., 2013. On the effective Lewis number formulations for lean hydrogen/hydrocarbon/air mixtures. International journal of hydrogen energy, 38(14), 5949-5960.

Bradley, D., Gaskell, P. H., Gu, X. J., 1996. Burning velocities, Markstein lengths, and flame quenching for spherical methane-air flames: a computational study. Combustion and flame, 104(1-2), 176-198.

Bradley, D., Harper, C. M., 1994. The development of instabilities in laminar explosion flames. Combustion and Flame, 99(3-4), 562-572.

Bradley, D., Haq, M. Z., Hicks, R. A., Kitagawa, T., Lawes, M., Sheppard, C. G. W., Woolley, R., 2003. Turbulent burning velocity, burned gas distribution, and associated flame surface definition. Combustion and Flame, 133(4), 415-430.

Bradley, D., Hicks, R. A., Lawes, M., Sheppard, C. G. W., Woolley, R., 1998. The measurement of laminar burning velocities and Markstein numbers for *iso*-octane/air and *iso*-octane–*n*-heptane/air mixtures at elevated temperatures and pressures in an explosion bomb. Combustion and flame, 115(1-2), 126-144.

Bradley, D., Hundy, G. F., 1971. Burning velocities of methane-air mixtures using hot wire anemometers in closed vessel explosions. Proceedings of the Combustion Institute, 13(1) 575-583.

Bradley, D., Lau, A. K. C., Lawes, M., Smith, F. T., 1992. Flame stretch rate as a determinant of turbulent burning velocity. Philosophical Transactions of the Royal Society of London. Series A: Physical and Engineering Sciences, 338(1650), 359-387.

Bradley, D., Lawes, M., Liu, K., Verhelst, S., Woolley, R., 2007. Laminar burning velocities of lean hydrogen–air mixtures at pressures up to 1.0 MPa. Combustion and Flame, 149(1-2), 162-172.

Bradley, D., Lawes, M., Morsy, M. E., 2019. Measurement of Turbulence Characteristics in a Large Scale Fan-Stirred Spherical Vessel. Journal of Turbulence, 20(3), 195-213.

Bradley, D., Lawes, M., Mansour, M. S., 2009. Flame surface densities during spherical turbulent flame explosions. Proceedings of the Combustion Institute, 32(1), 1587-1593.

Bradley, D., Lawes, M., Mansour, M. S., 2009. Explosion bomb measurements of ethanol–air laminar gaseous flame characteristics at pressures up to 1.4 MPa. Combustion and Flame, 156(7), 1462-1470.

Bradley, D., Lawes, M., Mansour, M. S., 2011. Correlation of turbulent burning velocities of ethanol–air, measured in a fan-stirred bomb up to 1.2 MPa. Combustion and Flame, 158(1), 123-138.

Bradley, D., Lawes, M., Mumby, R., Ahmed, P., 2018. The stability of laminar explosion flames. Proceedings of the Combustion Institute, 37(2), 1807-1813.

Bradley, D., Mitcheson, A., 1976. Mathematical solutions for explosions in spherical vessels. Combustion and Flame, 26, 201-217.

Bradley, D., Lawes, M., Scott, M. J., Mushi, E. M. J., 1994a. Afterburning in spherical premixed turbulent explosions. Combustion and Flame, 99(3-4), 581-590.

Bradley, D., Sheppard, C. G. W., Suardjaja, I. M., Woolley, R., 2004. Fundamentals of high-energy spark ignition with lasers. Combustion and Flame, 138(1-2), 55-77.

Bray, K. N. C., 1996. The challenge of turbulent combustion. In Symposium (International) on Combustion, 26(1), 1-26).

Burke, M. P., Chaos, M., Dryer, F. L., Ju, Y. 2010. Negative pressure dependence of mass burning rates of H_2/CO/O_2/diluent flames at low flame temperatures. Combustion and Flame, 157(4), 618-631.

Burke, M. P., Dryer, F. L., Ju, Y., 2011. Assessment of kinetic modeling for lean H_2/CH_4/O_2/diluent flames at high pressures. Proceedings of the Combustion Institute, 33(1), 905-912.

Burke, M. P., Chaos, M., Ju, Y., Dryer, F. L., Klippenstein, S. J., 2012. Comprehensive H_2/O_2 kinetic model for high-pressure combustion. International Journal of Chemical Kinetics, 44(7), 444-474.

Burleson, E., 2016. Paris agreement and consensus to address climate challenge. ASIL Insight, Forthcoming.

Candel, S. M. and Poinsot, T. J., 1990. Flame Stretch and the Balance Equation for the Flame Area. Combust. Sci. and Tech., 70: 1, 1 – 15.

Chakraborty, N., Cant, R. S., 2006. Influence of Lewis number on strain rate effects in turbulent premixed flame propagation. International journal of heat and mass transfer, 49(13-14), 2158-2172.

Chen, Z., 2009. Effects of hydrogen addition on the propagation of spherical methane/air flames: a computational study. International journal of hydrogen energy, 34(15), 6558-6567.

Chen, Z., 2010. Effects of radiation and compression on propagating spherical flames of methane/air mixtures near the lean flammability limit. Combustion and Flame, 157(12), 2267-2276.

Chen, Z., 2015. On the accuracy of laminar flame speeds measured from outwardly propagating spherical flames: methane/air at normal temperature and pressure. Combustion and Flame, 162(6), 2442-2453.

Chen, Z., 2017. Effects of radiation on large-scale spherical flame propagation. Combustion and Flame, 183, 66-74.

Cheng, R. K., Shepherd, I. G., Bedat, B., Talbot, L., 2002. Premixed turbulent flame structures in moderate and intense isotropic turbulence. Combustion Science and Technology, 174(1), 29-59.

Clavin, P., 1985. Dynamic behavior of premixed flame fronts in laminar and turbulent flows. Progress in energy and combustion science, 11(1), 1-59.

Clavin, P., Williams, F. A., 1982. Effects of molecular diffusion and of thermal expansion on the structure and dynamics of premixed flames in turbulent flows of large scale and low intensity. Journal of fluid mechanics, 116, 251-282.

Coppens, F. H., Konnov, A. A., 2008. The effects of enrichment by H_2 on propagation speeds in adiabatic flat and cellular premixed flames of CH_4+ O_2+ CO_2. Fuel, 87(13-14), 2866-2870.

Dantec, 2015. Dantec dynamic studio. https://www.dantecdynamics.com/.

Davis, S. J., Caldeira, K., Matthews, H. D., 2010. Future CO_2 emissions and climate change from existing energy infrastructure. Science, 329(5997), 1330-1333.

Davis, S. G., Quinard, J. and Searby, G. (2002), "Markstein Numbers in Counterflow, Methane-and Propane-Air Flames: A Computational Study", Combust. Flame, 130:123–136.

De Jong, J., Cao, L., Woodward, S. H., Salazar, J. P. L. C., Collins, L. R., Meng, H., 2009. Dissipation rate estimation from PIV in zero-mean isotropic turbulence. Experiments in fluids, 46(3), 499.

Dixon-Lewis, G. (1967), "Flame Structure and Flame Reaction Kinetics. I. Solution of Conservation Equations and Application to Rich Hydrogen-Oxygen Flames", Proc. Roy. Soc. Lond., A298: 495-513.

Dong, Y., Vagelopoulos, C. M., Spedding, G. R., Egolfopoulos, F. N., 2002. Measurement of laminar flame speeds through digital particle image velocimetry: mixtures of methane and ethane with hydrogen, oxygen, nitrogen, and helium. Proceedings of the combustion institute, 29(2), 1419-1426.

Dooley, S., Won, S. H., Chaos, M., Heyne, J., Ju, Y., Dryer, F. L., Santoro, R. J., 2010. A jet fuel surrogate formulated by real fuel properties. Combustion and flame, 157(12), 2333-2339.

Driscoll, J. F., 2008. Turbulent premixed combustion: Flamelet structure and its effect on turbulent burning velocities. Progress in energy and Combustion Science, 34(1), 91-134.

Dunn-Rankin, D., Weinberg, F., 1998. Location of the schlieren image in premixed flames: axially symmetrical refractive index fields. Combustion and flame, 113(3), 303-311.

Egolfopoulos, F. N., Cho, P., Law, C. K., 1989. Laminar flame speeds of methane-air mixtures under reduced and elevated pressures. Combustion and flame, 76(3-4), 375-391.

Egolfopoulos, F. N., Hansen, N., Ju, Y., Kohse-Höinghaus, K., Law, C. K., Qi, F., 2014. Advances and challenges in laminar flame experiments and implications for combustion chemistry. Progress in Energy and Combustion Science, 43, 36-67.

Eisazadeh-Far, K., Moghaddas, A., Al-Mulki, J., Metghalchi, H., 2011. Laminar burning speeds of ethanol/air/diluent mixtures. Proceedings of the Combustion Institute, 33(1), 1021-1027.

Filatyev, S. A., Driscoll, J. F., Carter, C. D., Donbar, J. M., 2005. Measured properties of turbulent premixed flames for model assessment, including burning velocities, stretch rates, and surface densities. Combustion and Flame, 141(1-2), 1-21.

Fragner, R., Mazellier, N., Halter, F., Chauveau, C., Gökalp, I., 2015. Multi-scale high intensity turbulence generator applied to a high pressure turbulent burner. Flow, Turbulence and Combustion, 94(1), 263-283.

Galmiche, B., Mazellier, N., Halter, F., Foucher, F., 2014. Turbulence characterization of a high-pressure high-temperature fan-stirred combustion vessel using LDV, PIV and TR-PIV measurements. Experiments in fluids, 55(1), 1636.

Ghenai, C., Gouldin, F. C., Gökalp, I., 1998. Mass flux measurements for burning rate determination of premixed turbulent flames. In Symposium (International) on Combustion, 27(1) 979-987).

Gillespie, L., Lawes, M., Sheppard, C. G. W., Woolley, R., 2000. Aspects of laminar and turbulent burning velocity relevant to SI engines. SAE transactions, 13-33.

Giannakopoulos, G. K., Gatzoulis, A., Frouzakis, C. E., Matalon, M., Tomboulides, A. G., 2015. Consistent definitions of "Flame Displacement Speed" and "Markstein Length" for premixed flame propagation. Combustion and Flame, 162(4), 1249-1264.

Goulier, J., Chaumeix, N., Halter, F., Meynet, N., Bentaïb, A., 2017. Experimental study of laminar and turbulent flame speed of a spherical flame in a fan-stirred closed vessel for hydrogen safety application. Nuclear Engineering and Design, 312, 214-227.

Groot, G. R. A., De Goey, L. P. H., 2002. A computational study on propagating spherical and cylindrical premixed flames. Proceedings of the Combustion Institute, 29(2), 1445-1451.

Gu, X. J., Haq, M. Z., Lawes, M., Woolley, R., 2000. Laminar burning velocity and Markstein lengths of methane–air mixtures. Combustion and flame, 121(1-2), 41-58.

Gülder, Ö. L., Smallwood, G. J., 2007. Flame surface densities in premixed combustion at medium to high turbulence intensities. Combustion science and technology, 179(1-2), 191-206.

Haq, Z., 1998. Fundamental Studies of Premixed combustion. PhD Thesis, University of Leeds.

Herman, S. R., 2019. The Paris Climate Agreement: Harbinger of a New Global Order. Swarthmore International Relations Journal, 1(3), 1.

Hermanns, R. T. E., Konnov, A. A., Bastiaans, R. J. M., De Goey, L. P. H., Lucka, K., Köhne, H., 2010. Effects of temperature and composition on the laminar burning velocity of CH_4+ H_2+ O_2+ N_2 flames. Fuel, 89(1), 114-121.

Hinton, N., Stone, R., Cracknell, R., 2018. Laminar burning velocity measurements in constant volume vessels–reconciliation of flame front imaging and pressure rise methods. Fuel, 211, 446-457.

Hinshelwood, C. N., 1940. Kinetics of chemical change.

Hinze, J. O., 1975. Turbulence McGraw-Hill. New York, 218, 457.

Huang, Y., Sung, C. J., Eng, J. A., 2004. Laminar flame speeds of primary reference fuels and reformer gas mixtures. Combustion and Flame, 139(3), 239-251.

Hwang, W., Eaton, J. K., 2004. Creating homogeneous and isotropic turbulence without a mean flow. Experiments in Fluids, 36(3), 444-454.

Ivashchenko, P. F., Rumyantsev, V. S., 1978. Convective rise and propagation velocity of a large flame focus. Combustion, Explosion, and Shock Waves, 14(3), 338-341.

Jayachandran, J., Zhao, R., Egolfopoulos, F. N., 2014. Determination of laminar flame speeds using stagnation and spherically expanding flames: molecular transport and radiation effects. Combustion and Flame, 161(9), 2305-2316.

Jerzembeck, S., Peters, N., Pepiot-Desjardins, P., Pitsch, H., 2009. Laminar burning velocities at high pressure for primary reference fuels and gasoline: Experimental and numerical investigation. Combustion and Flame, 156(2), 292-301.

Jomaas, G., Law, C. K., Bechtold, J. K., 2007. On transition to cellularity in expanding spherical flames. Journal of fluid mechanics, 583, 1-26.

Karlovitz, B., Denniston Jr, D. W., Knapschaefer, D. H., Wells, F. E., 1953. Studies on Turbulent flames: A. Flame Propagation Across velocity gradients B. turbulence Measurement in flames. In Symposium (international) on combustion, 4(1), 613-620).

Kelley, A. P., Law, C. K., 2009. Nonlinear effects in the extraction of laminar flame speeds from expanding spherical flames. Combustion and Flame, 156(9), 1844-1851.

Kim, H. H., Won, S. H., Santner, J., Chen, Z., Ju, Y., 2013. Measurements of the critical initiation radius and unsteady propagation of *n*-decane/air premixed flames. Proceedings of the Combustion Institute, 34(1), 929-936.

Kuznetsov, E. A., Minaev, S. S., 1996. Formation and propagation of cracks on the flame surface. Physics Letters A, 221(3-4), 187-192.

Larrson, 2009. Turbulence related cyclic variation in combustion. PhD thesis, University of Leeds, UK.

Lavoie, P., Avallone, G., De Gregorio, F., Romano, G. P., Antonia, R. A., 2007. Spatial resolution of PIV for the measurement of turbulence. Experiments in Fluids, 43(1), 39-51.

Law, C. K., Cho, P., Mizomoto, M., Yoshida, H., 1988. Flame curvature and preferential diffusion in the burning intensity of Bunsen flames. In Symposium (International) on Combustion 21(1), 1803-1809.

Law, C. K., Sung, C. J., Wang, H., Lu, T. F., 2003. Development of comprehensive detailed and reduced reaction mechanisms for combustion modeling. AIAA journal, 41(9), 1629-1646.

Lawes, M., Ormsby, M. P., Sheppard, C. G., Woolley, R., 2012. The turbulent burning velocity of iso-octane/air mixtures. Combustion and Flame, 159(5), 1949-1959.

Lawes, M., Sharpe, G. J., Tripathi, N., Cracknell, R. F., 2016. Influence of spark ignition in the determination of Markstein lengths using spherically expanding flames. Fuel, 186, 579-586.

Lawn, C. J., Schefer, R. W., 2006. Scaling of premixed turbulent flames in the corrugated regime. Combustion and flame, 146(1-2), 180-199.

Li, Q., Cheng, Y., Jin, W., Chen, Z., Huang, Z., 2015. Study on the laminar characteristics of ethanol, *n*-butanol and *n*-pentanol flames. SAE Technical Paper.

Li, X., You, X., Wu, F., & Law, C. K., 2015. Uncertainty analysis of the kinetic model prediction for high-pressure H_2/CO combustion. Proceedings of the Combustion Institute, 35(1), 617-624.

Lin, J. T., 1972. Velocity spectrum of locally isotropic turbulence in the inertial and dissipation ranges. The Physics of Fluids, 15(1), 205-207.

Lindow, R., 1968. An improved burner method for determining laminar flame velocity of fuel gas/air mixtures. Brenst- Warme-Kraft 20(1), 8.

Lipatnikov, A. N., Chomiak, J., 2002a. Turbulent flame speed and thickness: phenomenology, evaluation, and application in multi-dimensional simulations. Progress in energy and combustion science, 28(1), 1-74.

Lipatnikov, A., Chomiak, J., 2002b. Turbulent burning velocity and speed of developing, curved, and strained flames. Proceedings of the Combustion Institute, 29(2), 2113-2121.

Lowry, W., de Vries, J., Krejci, M., Petersen, E., Serinyel, Z., Metcalfe, W., Bourque, G. 2010. Laminar flame speed measurements and modeling of pure alkanes and alkane blends at elevated pressures. In ASME Turbo Expo 2010: Power for Land, Sea, and Air, 855-873.

Maas, U., Pope, S. B., 1994. Laminar flame calculations using simplified chemical kinetics based on intrinsic low-dimensional manifolds. In Symposium (International) on Combustion (Vol. 25, No. 1, pp. 1349-1356). Elsevier.

Mallard, E., Le Chatelier, H. L., 1883. Thermal model for flame propagation. In Annales des mines (Vol. 4, No. 18, pp. 379-568).

Mandilas, H., 2009. Laminar and Turbulent Burning Characteristics of Hydrocarbon Fuels. PhD Thesis, University of Leeds.

Markstein G. H., 1964. Non-Steady Flame Propagation. New York.

Matalon, M., 1983. On flame stretch. Combustion Science and Technology, 31(3-4), 169-181.

McComb, W. D., 1990. The Physics of Fluid Turbulence Oxford University Press.
Morley, C., 2005. Gaseq: a chemical equilibrium program for Windows. Ver. 0.79.

Mumby, R., 2017. Experimental Characterisation of Fuel Blends. PhD Thesis, University of Leeds.

Ortiz, M., Gayán, P., Luis, F., García-Labiano, F., Abad, A., Pans, M. A., Adánez, J., 2011. Hydrogen production with CO_2 capture by coupling steam reforming of methane and chemical-looping combustion: Use of an iron-based waste product as oxygen carrier burning a PSA tail gas. Journal of Power Sources, 196(9), 4370-4381.

Palacios, A., Bradley, D., 2017. Generalised correlations of blow-off and flame quenching for sub-sonic and choked jet flames. Combustion and Flame, 185, 309-318.

Pasquier, N., Lecordier, B., Trinite, M., Cessou, A., 2007. An experimental investigation of flame propagation through a turbulent stratified mixture. Proceedings of the Combustion Institute, 31(1), 1567-1574.
Peters, N., 2000. Turbulent combustion. Cambridge university press.

Poinsot, T., Veynante, D., 2005. Theoretical and numerical combustion. R.T. Edwards.

Poinsot, T., Veynante, D., Candel, S., 1991. Quenching processes and premixed turbulent combustion diagrams. Journal of Fluid Mechanics, 228, 561-606.

Poinsot, T., Veynante, D., 2001. Theoretical and numerical combustion, RT Edwards Inc. Philadelphia, PA.

Ranzi, E. L. I. S. E. O., Frassoldati, A., Grana, R., Cuoci, A., Faravelli, T., Kelley, A. P., Law, C. K., 2012. Hierarchical and comparative kinetic modeling of laminar flame speeds of hydrocarbon and oxygenated fuels. Progress in Energy and Combustion Science, 38(4), 468-501.

Ravi, S., Peltier, S. J., Petersen, E. L., 2013. Analysis of the impact of impeller geometry on the turbulent statistics inside a fan-stirred, cylindrical flame speed vessel using PIV. Experiments in fluids, 54(1), 1424.

Ronney, P. D., Sivashinsky, G. I., 1989. A theoretical study of propagation and extinction of nonsteady spherical flame fronts. SIAM Journal on Applied Mathematics, 49(4), 1029-1046.

Santner, J., Haas, F. M., Ju, Y., Dryer, F. L., 2014. Uncertainties in interpretation of high pressure spherical flame propagation rates due to thermal radiation. Combustion and Flame, 161(1), 147-153.

Santner, J., Haas, F. M., Dryer, F. L., Ju, Y., 2015. High temperature oxidation of formaldehyde and formyl radical: A study of 1, 3, 5-trioxane laminar burning velocities. Proceedings of the Combustion Institute, 35(1), 687-694.

Searby, G., 2004. Experimental Studies of Instabilities of Laminar Premixed Flames. Proceedings of International Conference on Combustion and Detonation.

Semenov, E. S., 1965. Measurement of turbulence characteristics in a closed volume with artificial turbulence. Combustion, Explosion, and Shock Waves, 1(2), 57-62.

Semenov, N. N., 1935. Chemical kinetics and chain reactions.

Shepherd, I. G., Cheng, R. K., 2001. The burning rate of premixed flames in moderate and intense turbulence. Combustion and Flame, 127(3), 2066-2075.

Shukman, D., 2013. Carbon dioxide passes symbolic mark, British Broadcasting Corporation.

Shy, S. S., Lin, W. J., Peng, K. Z., 2000. High-intensity turbulent premixed combustion: General correlations of turbulent burning velocities in a new cruciform burner. Proceedings of the Combustion Institute, 28(1), 561-568.

Singh, B., Rajendran, L. K., Giarra, M., Vlachos, P. P., Bane, S. P., 2018. Measurement of the flow field induced by a spark plasma using particle image velocimetry. Experiments in Fluids, 59(12), 179.

Smallwood, G. J., Gülder, Ö. L., Snelling, D. R., Deschamps, B. M., Gökalp, I., 1995. Characterization of flame front surfaces in turbulent premixed methane/air combustion. Combustion and Flame, 101(4), 461-470.

Sokolik, A. S., Karpov, V. P., Semenov, E. S., 1967. Turbulent combustion of gases. Combustion, Explosion, and Shock Waves, 3(1), 36-45.

Spalding, D. B. and Stephenson, P. L. 1971. Laminar Flame Propagation in Hydrogen+Bromine Mixtures. Proc. Roy. Soc. Lond., A324: 315-337.

Stellingwerf, H. M., Kanellopoulos, A., van der Vorst, J. G., Bloemhof, J. M., 2018. Reducing CO_2 emissions in temperature-controlled road transportation using the LDVRP model. Transportation Research Part D: Transport and Environment, 58, 80-93.

Tabaczynski, R. J., Trinker, F. H., Shannon, B. A., 1980. Further refinement and validation of a turbulent flame propagation model for spark-ignition engines. Combustion and Flame, 39(2), 111-121.

Tahtouh, T., Halter, F., Mounaïm-Rousselle, C., 2009. Measurement of laminar burning speeds and Markstein lengths using a novel methodology. Combustion and Flame, 156(9), 1735-1743.

Tanoue, K., Shimada, F., Hamatake, T., 2003. The effects of flame stretch on outwardly propagating flames. JSME International Journal Series B Fluids and Thermal Engineering, 46(3), 416-424.

Tripathi, N., 2012. Dynamics of Confined Premixed Laminar Explosion Flames, PhD Thesis, University of Leeds.

Turns, S. R., 1996. An introduction to combustion (Vol. 499). New York: McGraw-Hill.

Vagelopoulos, C. M., Egolfopoulos, F. N., 1998. Direct experimental determination of laminar flame speeds. In Symposium (international) on combustion, 27 (1) (1998) 513–519.

UNFCCC, 2015. Unitied Nations, Paris Agreement. http://unfccc.int/2860.php.

Van Maaren, A., Thung, D. S., DE GOEY, L. R. H., 1994. Measurement of flame temperature and adiabatic burning velocity of methane/air mixtures. Combustion Science and Technology, 96(4-6), 327-344.

Varea, E., Beeckmann, J., Pitsch, H., Chen, Z., Renou, B., 2015. Determination of burning velocities from spherically expanding H_2/air flames. Proceedings of the Combustion Institute, 35(1), 711-719.

Varea, E., Modica, V., Vandel, A., Renou, B., 2012. Measurement of laminar burning velocity and Markstein length relative to fresh gases using a new postprocessing procedure: Application to laminar spherical flames for methane, ethanol and isooctane/air mixtures. Combustion and Flame, 159(2), 577-590.

Warnatz, J. (1981), "The Structure of Laminar Alkane-, Alkene-, and Acetylene Flames", Eighteenth Symposium (International) on Combustion, pp. 369-384.

Weiß, M., Zarzalis, N., Suntz, R., 2008. Experimental study of Markstein number effects on laminar flamelet velocity in turbulent premixed flames. Combustion and Flame, 154(4), 671-691.

Williams, F. A., 1985. Combustion Theory. 2nd Edition, Addison-Wesley, California.

Xu, S., Huang, S., Huang, R., Wei, W., Cheng, X., Ma, Y., Zhang, Y., 2017. Estimation of turbulence characteristics from PIV in a high-pressure fan-stirred constant volume combustion chamber. Applied Thermal Engineering, 110, 346-355.

Yu, H., Han, W., Santner, J., Gou, X., Sohn, C. H., Ju, Y., Chen, Z., 2014. Radiation-induced uncertainty in laminar flame speed measured from propagating spherical flames. Combustion and Flame, 161(11), 2815-2824.

Zel'dovich, Y. B., Barenblatt, G. I., 1959. Theory of flame propagation. Combustion and Flame, 3, 61-74.

Zel'dovich, Y. B., Frank-Kamenetskii, D. A., 1938a. The theory of thermal propagation of flames. Zh. Fiz. Khim, 12, 100-105.

Zhou, M., Li, G., Liang, J., Ding, H., Zhang, Z., 2018. Effect of ignition energy on the uncertainty in the determination of laminar flame speed using outwardly propagating spherical flames. Proceedings of the Combustion Institute, 37(2), 1615-1622.

Appendix A

A.1 Introduction

This Appendix provides more details about the adaptive PIV method, used for processing and evaluating the velocity vectors. The Adaptive PIV method is an automatic and adaptive method for calculating velocity vectors based on particle images. The method is iteratively adjust the orientation of the individual interrogation areas (IA) in order to adapt to local seeding densities and flow gradients. The method also includes options to apply window functions, frequency filtering as well as validation in the form of Universal Outlier Detection. Figure A.1 shows the recipe dialog for the Adaptive PIV tool.

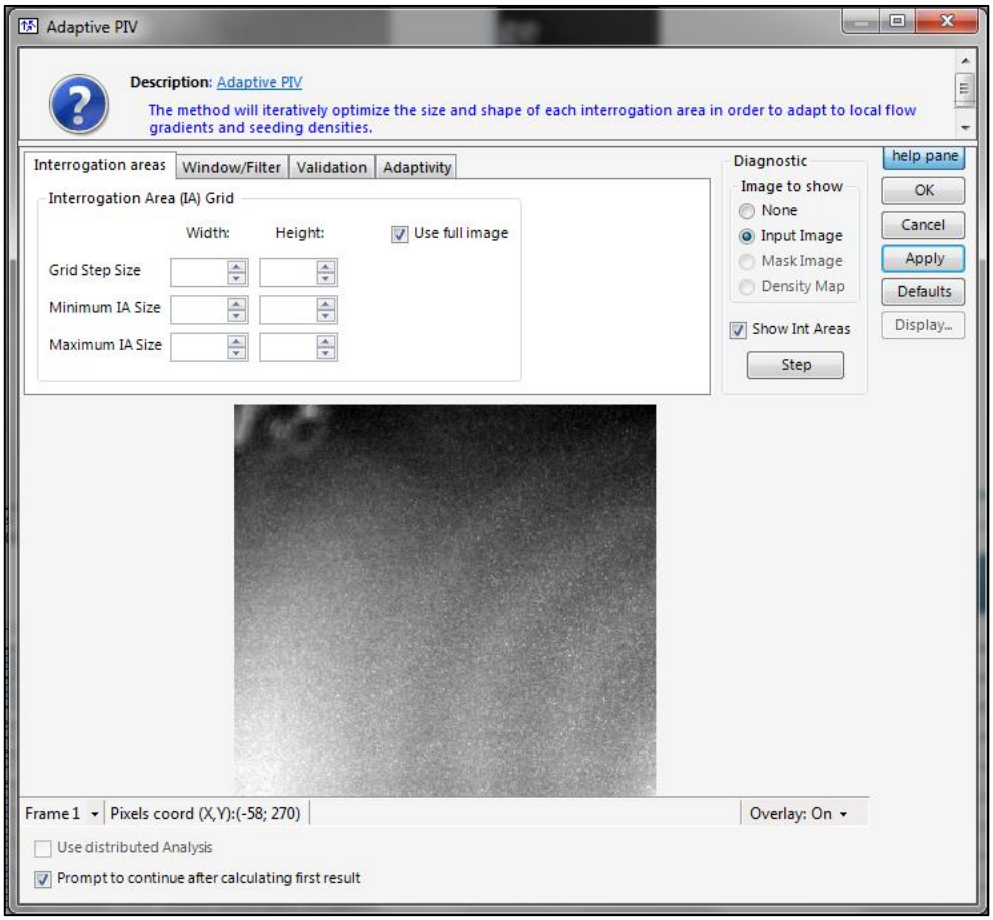

Figure A.1: Picture shows the recipe dialog for the Adaptive PIV tool.

The number of IAs and the spacing between their edges positions are determined by the parameter ‘Grid Step Size’. The grid step is specified as number of pixels from one IA to its neighbor. If grid step is small, the IAs will be packed closer thereby resulting in more IAs inside the calculation area. The Adaptive PIV method can automatically determine an appropriate IA size to use for each individual IA, but specified minimum and/or maximum IA sizes limits the range. The first iteration is always using the largest IA size allowed, while subsequent iterations is allowed to reduce IA sizes where particle density is high enough to justify it. Minimum IA size is also used to determine the location of vectors; Both horizontally and vertically there are as many vectors as possible within the area covered (full image or ROI); Grid Step Size determines the distance between neighbor vectors, while Minimum IA Size determine how close to the borders a vector may be located.

A.2 Windowing and Filtering

The tab ‘Window/Filter’, in the previous front panel, is used to apply a spatial windowing and/or frequency filtering function.

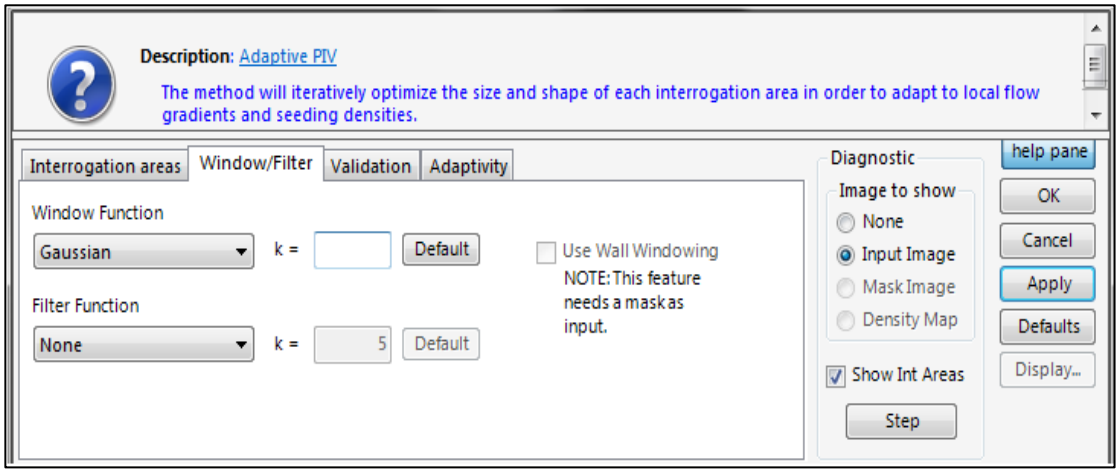

Figure A.2: Shows the recipe dialog for filters.

The purpose of windowing is to mitigate wall bias; Correlation measures the average displacement/velocity of particles within the interrogation area (IA). There are (normally) no particles inside walls, so when an IA extends into a wall resulting displacements/velocities may be biased by particles far from the wall, that generally move faster than particles close to the wall. Windowing attempts to mitigate this effect by masking also the particles far from the wall, so remaining particles are symmetrically distributed around the centre of the IA.

A.3 Validation

The validation is used to prevent outliers from disturbing the iterations and thus the velocity measurements. The validation is done by first applying peak validation on the image correlation and secondly by comparing each vector to its neighbors using the Universal outlier detection algorithm.

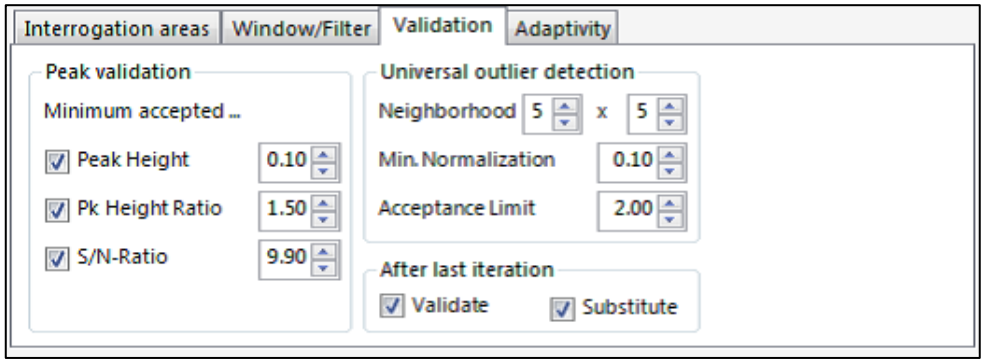

Figure A.3: Shows the recipe dialog for validation.

Three peak validation schemes are proposed in order to invalidate vectors based on the image correlation peaks:

- **Peak Height**

  If the Peak Height validation is enabled, then only the correlation peaks above the specified value will be retained as valid.

- **Peak Height Ratio**

  If the Peak Height validation is enabled, then the ratio between the two highest correlation peaks is calculated. This ratio must be higher than the specified value in order to validate the calculated displacement.

- **S/N-Ratio**

  If S/N ratio is enabled, first the noise level in the correlation plane is evaluated by the root mean square of the negative correlation values. If the ratio between the correlation peak and the noise level is above the specified value, then the calculated displacement is considered valid.

Using Peak Height or S/N-Ratio validation criterion is recommended. Indeed, if the interrogation area only contains noise the ratio between the two highest peaks may still be quite high, as shown in Fig. A.4.

If either peak validation fails the corresponding vector will be rejected. Later when the Universal Outlier detection is performed, and substitution is enabled, the rejected vector may be replaced with the median of valid neighbour vectors. After the first and intermediate iterations validation and substitution is mandatory, but after the last iteration the user may choose not to validate at all, to validate, but not substitute rejected vectors or to both validate and substitute. The figure below shows the correlation peak height as a function of the interrogation displacement.

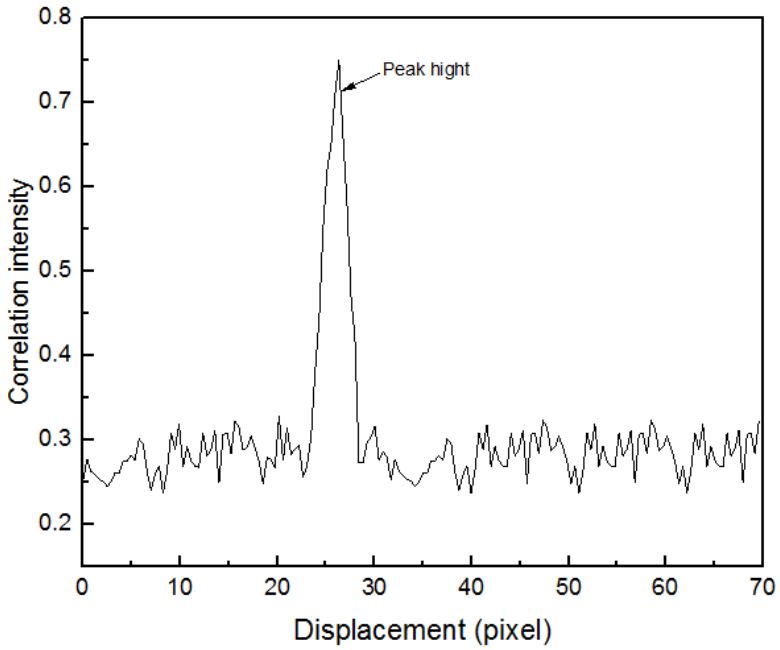

Figure A.4: Shows the correlation intensity.

A.4 Adaptivity

The ‘Adaptivity’ tab contains settings that will affect the adaptive adjustment that is iteratively applied to each IA. It is possible to enable/disable adaptivity of the size of the IA based on the particle density. If adaptivity to particle density is switched off the first iteration will use the maximum IA size allowed (as normal), while in each of the following iterations the IA size is divided by two until the specified minimum IA size is reached. If adaptivity to particle density is switched on the initial correlation will still use the maximum IA size allowed, while in each of the following iterations the IA size is determined from an estimated particle density.

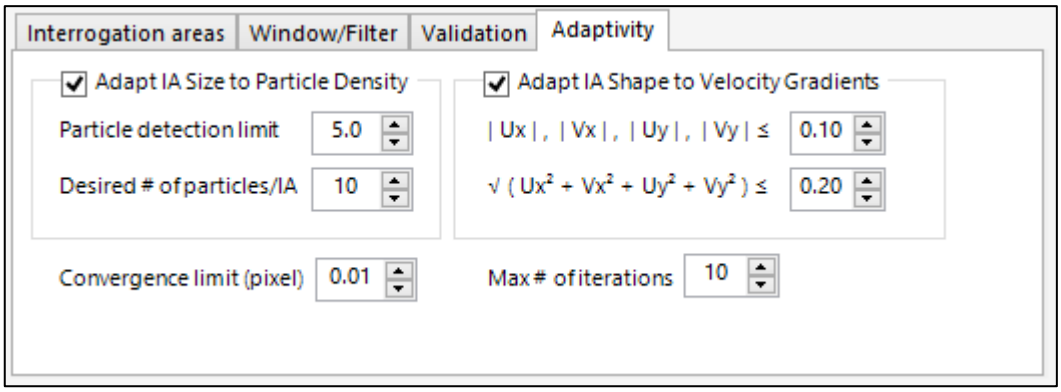

Figure A.5: Shows the recipe dialog for adaptivity.

Two parameters adjust how the particle density adaptivity works:

1. Particle detection limit:

Determines how a particle is detected. A gray scale peak must rise this many times above the noise floor to be counted as a particle.

2. Desired number of particles/IA:

Will affect the size of the interrogation areas by specifying how many particles an IA should nominally contain. Regardless of particle density IA Size will always be in the Minimum - Maximum range specified on the 'Interrogation areas' Tab.

Two different limits can be set, to ensure that the shape of the interrogation area is not changed to something way out. First the absolute magnitude of each of the four gradients can be limited. Second the combined effect of all four gradients can be limited as well. When the translational part of the IA shape correction is less than the specified convergence limit, the iteration is stopped for the given IA. It may continue for other interrogation areas. The analysis is stopping after the specified number of iteration, no matter if the analysis of the IA has converged or not.

A.5 Image Balancing

The Image balancing process corrects light sheet non-uniformities that affect the outcome of other analysis routines. Figure A.6 shows the sequence of image balancing. Image balancing is a two-step process. The first step is to create an image balance map that consists of factors determined from an ensemble of input images. The map is then applied onto individual image maps, correcting for any strong variations in laser intensity.

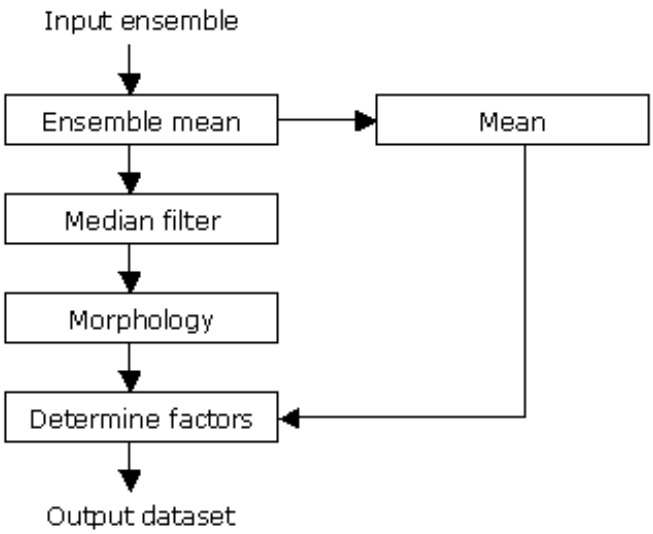

Figure A.6: Sequence of image balancing processing.

A.5.1 Image Balance Map (Step 1)

An ensemble of image maps is selected. There should be enough images in the ensemble so that a mean image generated would show relatively soft variations in light and limited noise activity. The “Image Balance Map” tool is then selected from the list of analysis methods. This tool is then used to process the data and produces a correction map.

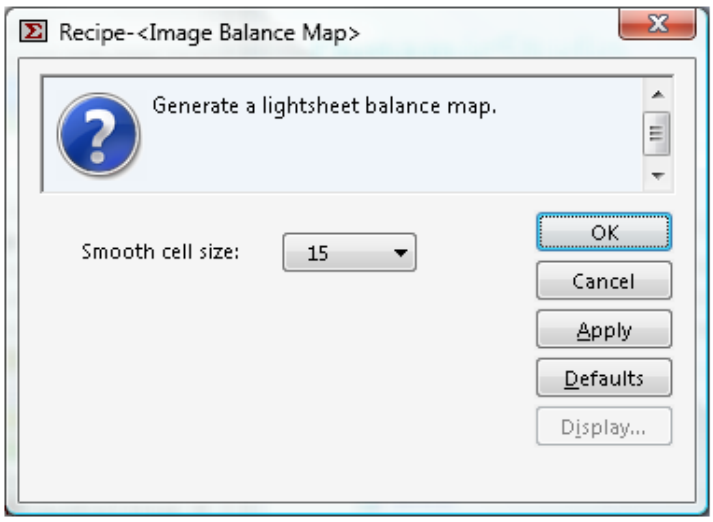

Figure A.7: Shows the recipe dialog for image balance map.

A.5.2 Balance Mapping (Step 2)

The second step is to select an image balance map as fixed input and then selecting the required input dataset to process. Figure A.8 shows an example of the image balancing processing.

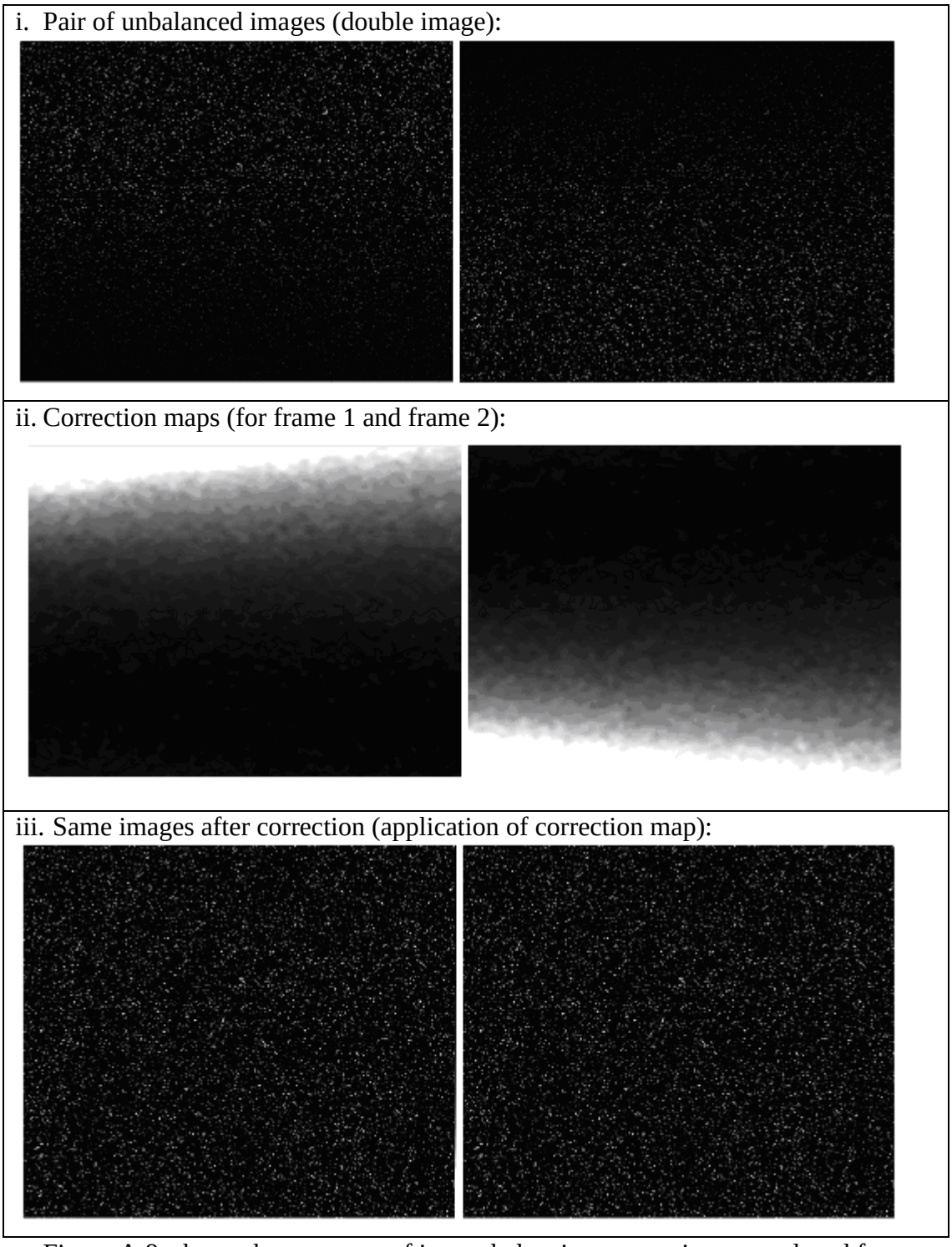

Figure A.8: shows the sequence of image balancing processing, reproduced from (Dantec, 2015).

Appendix B

B.1 Burning Velocities and Markstein Numbers

Table B.1: Burning velocities and Markstein numbers of methane/air mixtures at 300 K and 0.1 MPa, using PIV method and flame speed method.

φ	u_l (m/s)	u_{la} (m/s)	u_{lr} (m/s)	u_{ls} (m/s)	L_{sr} (mm)	L_{cr} (mm)	L_b (mm)
0.7	0.179	0.179	0.185	0.171	0.18	0.1	0.45
0.8	0.258	0.253	0.263	0.256	0.21	0.15	0.57
0.9	0.325	0.320	0.331	0.312	0.25	0.18	0.69
1.0	0.358	0.355	0.363	0.358	0.29	0.21	0.82
1.1	0.363	0.357	0.368	0.359	0.37	0.28	0.95
1.2	0.322	0.317	0.328	0.320	0.55	0.41	1.27
1.3	0.248	0.242	0.253	0.250	0.91	0.71	1.73

Table B.2: Burning velocities and Markstein numbers of *i*-octane/air mixtures at 358 K and 0.1 MPa, using PIV method and flame speed method.

φ	u_l (m/s)	u_{la} (m/s)	u_{lr} (m/s)	u_{ls} (m/s)	L_{sr} (mm)	L_{cr} (mm)	L_b (mm)
0.8	0.392	0.381	0.401	0.388	0.92	1.01	2.8
0.9	0.421	0.411	0.430	0.418	0.65	0.8	1.9
1.0	0.445	0.433	0.454	0.439	0.42	0.55	1.32
1.1	0.438	0.427	0.447	0.439	0.29	0.34	0.95
1.2	0.41	0.391	0.419	0.400	0.21	0.3	0.54
1.3	0.353	0.333	0.362	0.344	0.12	0.24	0.28

Table B.3: Burning velocities and Markstein numbers of ethanol/air mixtures at 360 K and 0.1 MPa, using PIV method and flame speed method.

φ	u_l (m/s)	u_{la} (m/s)	u_{lr} (m/s)	u_{ls} (m/s)	L_{sr} (mm)	L_{cr} (mm)	L_b (mm)
0.8	0.501	0.484	0.508	0.491	0.45	0.48	1.36
0.9	0.573	0.559	0.582	0.569	0.32	0.36	1.2
1.0	0.616	0.595	0.625	0.610	0.24	0.27	0.92
1.1	0.615	0.591	0.624	0.607	0.17	0.21	0.81
1.2	0.605	0.579	0.614	0.589	0.11	0.16	0.66
1.3	0.546	0.513	0.555	0.534	0.1	0.13	0.52
1.4	0.46	0.424	0.468	0.448	0.07	0.12	0.21

Table B.4: Burning velocities and Markstein numbers of *n*-butanol/air mixtures at different pressures and 383K, using PIV method and flame speed method.

φ	P (MPa)	u_l (m/s)	u_{la} (m/s)	u_{lr} (m/s)	u_{ls} (m/s)	L_{sr} (mm)	L_{cr} (mm)	L_b (mm)
0.7	0.1	0.358	0.340	0.364	0.349	0.85	0.95	1.12
0.7	0.3	0.228	0.227	0.232	0.229	0.39	0.41	0.69
0.7	0.5	0.175	0.170	0.179	0.172	0.37	0.41	0.65
0.8	0.1	0.418	0.395	0.424	0.413	0.67	0.82	0.98
0.8	0.3	0.289	0.290	0.294	0.295	0.29	0.3	0.52
0.8	0.5	0.258	0.255	0.263	0.258	0.25	0.26	0.41
0.9	0.1	0.497	0.468	0.503	0.485	0.55	0.62	0.69
0.9	0.3	0.364	0.364	0.369	0.370	0.21	0.23	0.3
0.9	0.5	0.310	0.307	0.315	0.310	0.19	0.21	0.28
1.0	0.1	0.556	0.516	0.562	0.544	0.48	0.52	0.57
1.0	0.3	0.433	0.430	0.438	0.438	0.15	0.17	0.21
1.0	0.5	0.375	0.371	0.381	0.375	0.12	0.15	0.17
1.1	0.1	0.607	0.560	0.613	0.585	0.32	0.39	0.45
1.1	0.3	0.479	0.473	0.485	0.485	0.11	0.13	0.12
1.1	0.5	0.423	0.416	0.430	0.421	0.1	0.1	0.1
1.2	0.1	0.582	0.544	0.588	0.565	0.24	0.34	0.38
1.2	0.3	0.470	0.464	0.476	0.475	0.07	0.08	0.08
1.2	0.5	0.418	0.413	0.424	0.418	0.05	0.06	0.07
1.3	0.1	0.570	0.510	0.576	0.543	0.12	0.18	0.31
1.3	0.3	0.447	0.438	0.454	0.449	0.02	0.05	0.03
1.3	0.5	0.399	0.392	0.406	0.399	0.01	0.02	-0.04

B.2 Lengths Scales

Table B.5: Average values of the lengths scales for all fan speeds of this study, at 0.1 MPa and different temperatures.

Fan speed (rpm)	$T\ (K)$	L_{uy} (mm)	L_{vy} (mm)	L_{uy} (mm)	L_{vx} (mm)	λ (mm)	$\eta \times 5$ (mm)
1,000	300	19.7	19.1	9.4	9.1	2.21	0.88
1,000	340	20.5	19.6	10.2	10.8	1.69	0.84
1,000	360	19.8	20.5	9.8	11.4	1.79	0.93
1,000	400	20.9	19.2	10.9	9.8	1.98	1.08
2,000	300	20.7	20.1	10.8	10.6	1.08	0.51
2,000	340	19.2	20.9	10.6	10.8	0.83	0.50
2,000	360	19.7	20.7	9.7	11.9	0.89	0.55
2,000	400	20.7	19.1	10.9	10.1	1.00	0.64
3,000	300	20.0	20.9	10.2	10.7	0.73	0.38
3,000	340	19.9	20.9	11.1	9.7	0.56	0.37
3,000	360	19.2	20.5	10.5	10.5	0.59	0.41
3,000	400	21.1	19.2	9.8	11.2	0.66	0.47
4,000	300	19.1	20.1	10.6	11.1	0.53	0.30
4,000	340	20.8	19.1	9.8	11.5	0.42	0.30
4,000	360	20.3	19.5	10.9	10.1	0.45	0.33
4,000	400	20.4	19.8	9.4	12.0	0.49	0.38
5,000	300	19.2	20.1	10.1	10.5	0.44	0.26
5,000	340	20.3	19.7	11.2	9.8	0.34	0.25
5,000	360	19.5	20.9	10.6	10.4	0.36	0.28
5,000	400	20.6	19.2	10.3	10.7	0.39	0.32
6,000	300	20.8	21.5	9.8	10.1	0.38	0.23
6,000	340	20.5	19.1	10.8	10.2	0.28	0.22
6,000	360	19.8	20.7	9.8	11.4	0.30	0.24
6,000	400	20.9	20.1	10.2	10.9	0.34	0.28

Table B.6: Average values of the lengths scales for all fan speeds of this study, at 300 K and different pressures.

Fan speed (rpm)	P (MPa)	L_{ux} (mm)	L_{vy} (mm)	L_{uy} (mm)	L_{vx} (mm)	λ (mm)	$\eta \times 5$ (mm)
1,000	0.1	19.7	19.1	9.4	9.1	2.21	0.88
1,000	0.2	20.3	19.8	9.7	10.3	1.11	0.68
1,000	0.5	20.1	19.8	9.8	10.2	0.71	0.22
1,000	1.0	19.4	20.5	8.9	9.7	0.49	0.13
2,000	0.1	20.7	20.1	10.8	10.6	1.08	0.51
2,000	0.2	19.5	19.8	9.8	10.2	0.54	0.40
2,000	0.5	20.2	19.9	9.7	9.8	0.35	0.13
2,000	1.0	19.7	19.4	9.3	9.4	0.24	0.24
3,000	0.1	20.0	20.9	10.2	10.7	0.73	0.38
3,000	0.2	19.7	20.3	10.3	10.4	0.37	0.30
3,000	0.5	20.4	20.2	9.8	9.4	0.23	0.10
3,000	1.0	19.8	19.6	9.9	9.2	0.17	0.18
4,000	0.1	19.1	20.1	10.6	11.1	0.53	0.30
4,000	0.2	20.4	20.1	10.2	10.8	0.28	0.24
4,000	0.5	19.8	20.4	10.3	9.8	0.17	0.08
4,000	1.0	20.3	19.7	9.7	9.9	0.12	0.15
5,000	0.1	19.2	20.1	10.1	10.5	0.44	0.26
5,000	0.2	19.7	20.3	9.9	10.3	0.22	0.20
5,000	0.5	20.4	20.7	9.7	9.5	0.14	0.07
5,000	1.0	19.4	19.2	9.3	9.4	0.10	0.12
6,000	0.1	20.8	21.5	9.8	10.1	0.38	0.23
6,000	0.2	19.7	19.4	10.4	9.7	0.18	0.18
6,000	0.5	19.3	19.8	9.5	9.2	0.11	0.06
6,000	1.0	19.1	19.4	9.6	9.4	0.08	0.11

Appendix C

C.1 Measurement of the Radial Velocity

After processing the Mie scattering images using the adaptive PIV method, described in Section 3.6.2, the velocity of each interrogation window was extracted from the Dantec software and stored in a Cartesian coordinate system. To calculate the radial velocity component, $U_r(x_i, y_i)$, these velocities were converted in to a polar coordinate, which is more appropriate to the propagation of spherical flames. The calculation of $U_r(x_i, y_i)$ was executed in three steps, using a series of MATLAB scripts developed by the current author. The first step was to detect the flame front, as described in Section 3.6.1, and convert it into points, (x_i, y_i), in a Cartesian coordinate. The second step was to match the flame front coordinates with the nearest unburned gas velocity. The last step was to calculate the radial velocity component, $U_r(x_i, y_i)$, from which the spatial rms turbulent velocity, u_s', was calculated, as explained in Section 5.4.1.

The polar transformation of the velocities starts from the determination of the global centre (x_c, y_c), which indicates the spark position. The local angle of each velocity, around the flame front, was then calculated as:

$$\theta_i = \arctan\{(y_i - y_c)/(x_i - x_c)\}, \tag{C.1}$$

and the radial velocity was calculate from the velocity components as:

$$U_r(x_i, y_i) = u(x_i, y_i)\cos(\theta_i) + v(x_i, y_i)\sin(\theta_i). \tag{C.2}$$

where positive value of $U_r(x_i, y_i)$ means the outward direction, $u(x_i, y_i)$ is the velocity component in the x-direction and $v(x_i, y_i)$ is the velocity component in the y-direction.

C.2 Thickness of Measurement

Measurement of the spatial rms turbulent velocity, u_s', was based on the measurement of the unburned gas velocity, surrounding the flame front, within a zone of specified thickness ahead of the flame front. The effect of the measurement thickness on U_r and u_s' were investigated at different u'. An example of such effect on U_r surrounding a stoichiometric methane/air flame front at 300 K, 0.1 MPa and u'= 0.5 m/s is shown in Fig. C.1. Three different values of the measurement thickness were used. These are 0.94, 1.88 and 2.82 mm. Figure C.1 shows that the measurement thickness has a significant

effect on the fluctuation of U_r and hence on u_s'. As the thickness of measurement increases, the velocity fluctuation decreases. That is because of the decay of U_r in the radial direction away from the flame, as described in Chapter (4). The corresponding values of u_s', for each thickness, are 0.95, 0.91 and 0.85 m/s. These results show that u_s' is decreasing with increasing the thickness of measurement. In order to minimise the influence of U_r decay along the radial direction and keep the sufficient amount of data samples in the thickness of measurement, this thickness was chosen to be ~ 0.94 mm. This was the minimum thickness can be used with the adaptive PIV thickness method, described in Section 3.6.2.

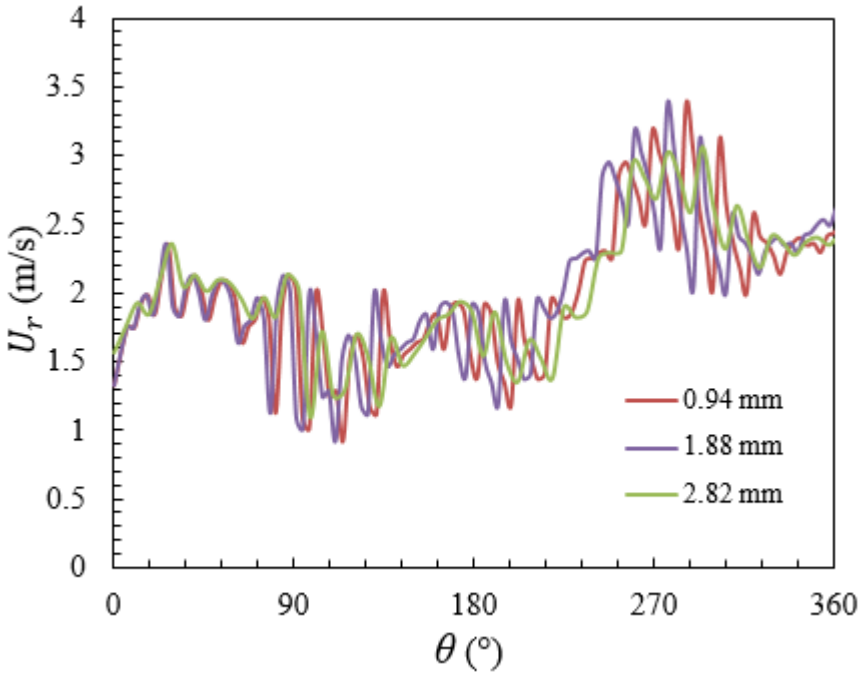

Figure C.1: Radial velocity profiles for stoichiometric methane/air mixture, u' = 0.5 m/s, 300 K and 0.1 MPa , r_v = 35 mm, using different measurement thickness of 0.94, 1.88 and 2.82 mm.

C.3 Length of Sectors

To calculate, u_s', the radial velocity profile, surrounding the flame front, was divided into equal sectors, with an angle of 5 degrees. Figure C.2 shows the influence of using different angles on u_s'. For θ < 15°, the influence of θ on u_s' can be consider negligible. At θ = 20°, the values of u_s' becomes very small. So that, an angle of 5 degrees was chosen.

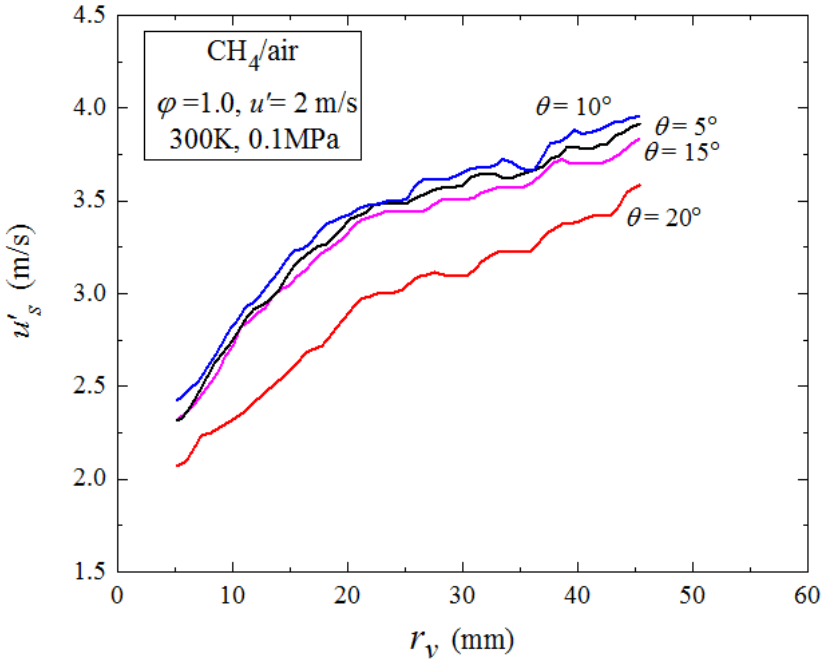

Figure C.2: Effect of sector length on the rms turbulent velocity

C.4 Radial Variation of the rms Turbulent Velocity

To extract the influence of flame propagation on the flow ahead of it, at a given time, the mean radial unburned gas velocity, u_g, was calculated ahead of the flame front. The radial gas velocity, U_r, was first detected and estimated at each grid node within an annulus area of (dR ~ 1 mm) around the flame front and then averaged over all the entire annulus area. The calculation started from the tip of the flame front, as shown in Fig. C.3. This process was repeated with increasing the annulus inner radius, moving from the tip of the flame front towards the inner surface of the vessel. Figure C.4 shows an example of such variation of u_g with the radial distance at three times 4, 8 and 12 ms, for stoichiometric methane/air flame at 300 K, 0.1 MPa and u'= 1 m/s. The velocity profile before ignition is also shown in the same figure. When a turbulent flame develops from a point ignition source, the flame propagation is laminar-like, as shown from the velocity profile at t = 4 ms. As time passes and the flame grows, the turbulent flame speed increases and consequently u_g increases. The corresponding profiles of u_s' are shown in Fig. C.5, for the same conditions of Fig. C.4. The value of, u_s', was calculated, using Eq. (5.9). As flame propagates, the flame front is exposed to an increasing range of turbulent wave lengths. As a result, u_s' that acting on the growing flame front is increasing as shown from Fig. C.5.

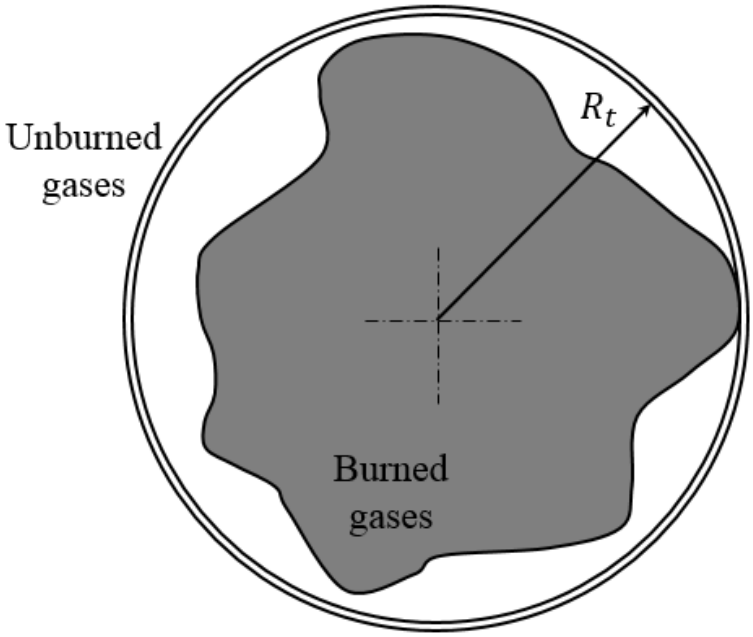

Figure C.3: Measurement of the spatial variation of u'_s.

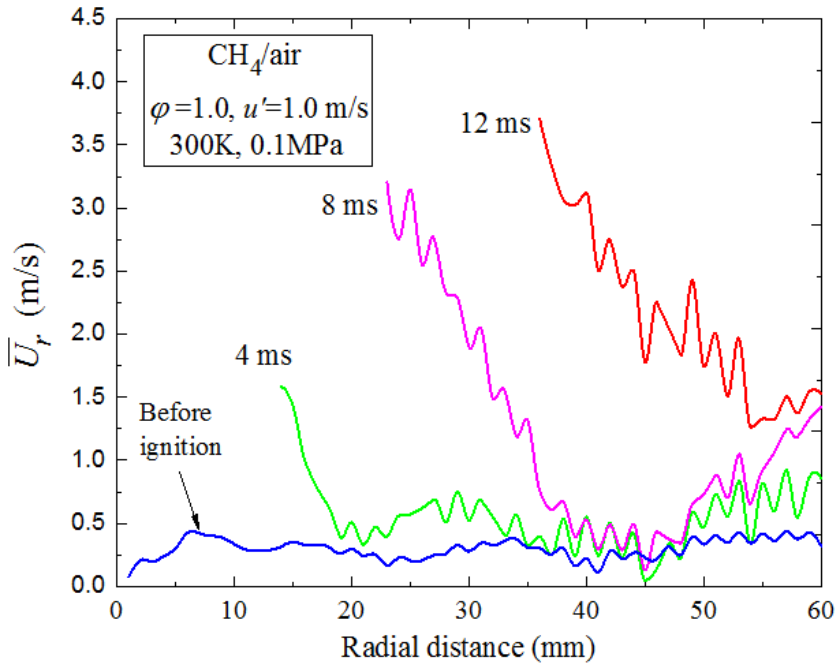

Figure C.4: Variation of mean radial gas velocity with the radial distance, using stoichiometric methane/air flame at 300 K, 0.1 MPa and u' = 1m/s.

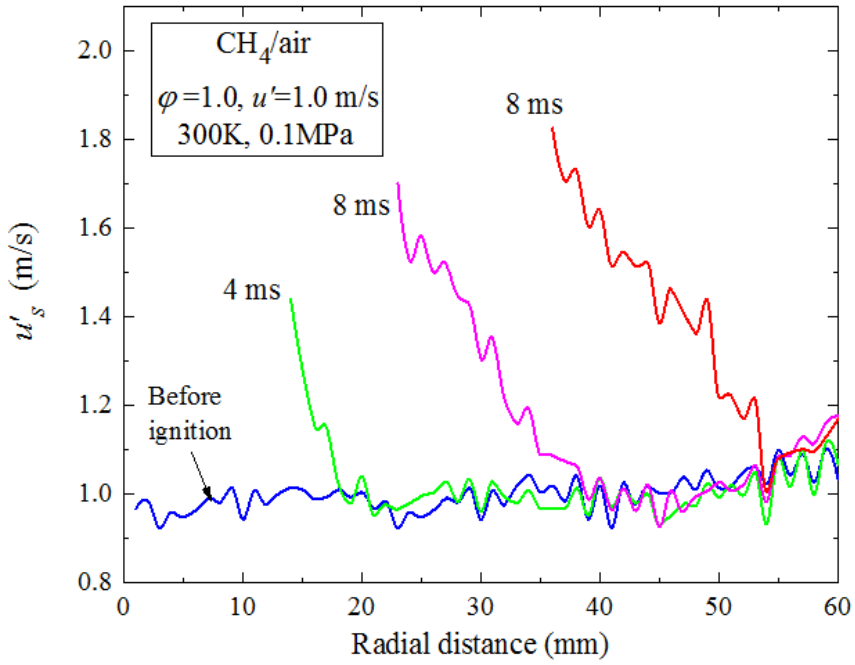

Figure C.5: Variation of spatial rms velocity, u'_s, with the radial distance. Same conditions of Fig. C.4.

The affected distance, due flame propagation, was measured from the tip of the flame front, at a given time, to the point at which the velocity profile is nearly identical with that of the velocity profile before ignition. Figure C.6 shows the affected distance for only one experiment, using methane/air flame, φ = 0.8, 1.0 and 1.3, at 300 K, 0.1 MPa and u'= 1 m/s. Symbols show the measured values of the affected distance and solid curves are the best fit curves for these symbols. For all equivalence ratios, the affected distance is nearly constant up to a flame radius ~ 20 mm. Beyond this radius, the affected distance increases significantly. This might be associated with the increase in flame speed and burning velocity of the mixture with flame growth. Although, the values of the affected distance in Fig. C.6 are highly useful, as it shows the effect of the flame on the flow ahead of it. These values are approximated values due to neglecting the effect of the gases within the area between the tip circle and the flame front, see Fig. C.3.

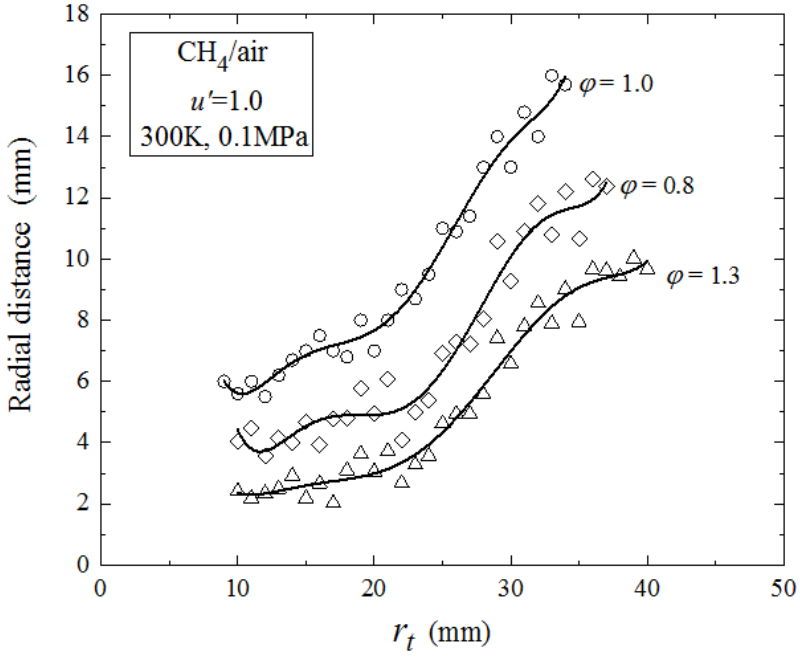

Figure C.6: Affected radial distance due to flame propagation.

Appendix D

D.1 Introduction

This Appendix presents some Matlab scripts written as part of this work. Explanatory notes are provided within the scripts where necessary, to illustrate to the user the required inputs etc.. These scripts do not work “automatically”; they usually require the user to specify the numbers of images to be processed and to change the file directory manually etc..

D.2 Flame Edge Detector Script

A script to read in a sequence of images in a folder and trace the flame edge, if present. This process returns white flame edges on a black ground and saves it under a different name in the current directory. It also calculates the mean flame radius and save it in a text file.

```
% script M-File: DrawSparkLine.m
clear all
close all
% IMPORTANT
% A - Current MATLAB Folder should contain the folder(s) including
the
% images of the explosion(s) ONLY.
% B - Images should be 12-bit greyscale bitmaps.
% C - Last image in each folder should be just before the flame
reaches the
% windows edge

%% delete_pre_flame function
% This small script deletes all images prior to kernel formation.
Use only
% if they haven't been deleted manually!!
delete_pre_flame;
clear all;

%% Imagerotation function
% In order for the function to work properly the bomb window should
appear
% at roughly plus or minus 25 pixels from the centre of image.
imagerotation;
clear all
close all
format short e
%% User Input
disp(' ');
% User prompt to enter pixel sixe. Make sure pixel size is correct
as it
% will be used for filtering out some noise later in the script and
also
```

```
% for determining the flame radius!!!
pixsize = input('Enter pixel size in mm = ');
disp(' ');
disp(' ');
disp('|-------------------------------------------------------------
|');
disp('| Enter threshold adjustment for first image.
|');
disp('| VALUES SHOULD BE BETWEEN 0.2 TO 0.6 depending on the image
|');
disp('| quality. The clearer the edge of the flame, the
|');
disp('| smaller the adjustment value required. A value of 0.4-0.5
|');
disp('| should be OK for most cases.
|');
disp('|-------------------------------------------------------------
|');
disp(' ');
% Variable for first image threshold adjustment. The higher the
value
% entered the lower the resulting threshold.
inimthres = input('Enter first image threshold adjustment value
(inimthres) = ');
if (inimthres < 0.2 || inimthres > 0.6)
    disp(' ');
    disp('|-----------------------------------------|');
    disp('|Bad value! Accepted values are 0.2 to 0.6! |');
    disp('|-----------------------------------------|');
    disp(' ');
    inimthres = input('Enter value = ');
    if (inimthres < 0.2 || inimthres > 0.6)
        return
    end
end

disp(' ');
disp('|-------------------------------------------------------------
|');
disp('| Enter constant threshold value for early flame images.
|');
disp('| ACCEPTABLE VALUES ARE NOW BETWEEN 0.01 AND 0.3. Now the
|');
disp('| darker the flame the higher the value used. Use 0.2-0.3 for
|');
disp('| high pressure dark flames and 0.025 to 0.075 for low
|');
disp('| pressure bright flames.
|');
disp('|-------------------------------------------------------------
|');
disp(' ');
% Variable for constant threshold of early images to be processed.
% The variable early_imthres is vital for the success rate of the
script!!!
early_imthres = input('Enter value for constant thresholding of
early flame images (early_imthres) = ');

disp(' ');
disp('|-------------------------------------------------------------
|');
```

```
disp('| Enter 2nd constant threshold value for early flame images.
|');
disp('| ACCEPTABLE VALUES ARE NOW BETWEEN 0.01 AND 0.3. Now the
|');
disp('| darker the flame the higher the value used. Use 0.2-0.3 for
|');
disp('| high pressure dark flames and 0.01 to 0.03 for low pressure
|');
disp('| bright flames.
|');
disp('|-------------------------------------------------------------
|');
disp(' ');
% Variable for constant threshold of early images to be processed.
% The variable early_imthres_2 is vital for the success rate of the
script!!!
early_imthres_2 = input('Enter 2nd value for constant thresholding
of early flame images (early_imthres_2) = ');

disp(' ');
disp('|-------------------------------------------------------------
|');
disp('| Enter threshold adjustment for mid-late flame images.
|');
disp('| ACCEPTABLE VALUES ARE NOW BETWEEN 0.2 AND 0.9. The darker
|');
disp('| the flame the lower should be the value used. Values of
|');
disp('| 0.3-0.4 should be OK for high pressure dark flames. For low
|');
disp('| pressure bright flames use 0.6-0.7!!
|');
disp('|-------------------------------------------------------------
|');
disp(' ');
% Variable for threshold adjustment of mid-late images. The higher
the
% value entered the lower the resulting threshold. The variable
imthres
% is vital for the success rate of the script!!!
imthres = input('Enter mid-late flame image threshold adjustment
value (imthres) = ');
if (imthres < 0.2 || imthres > 0.9)
    disp(' ');
    disp('|-----------------------------------------|');
    disp('|Bad value! Accepted values are 0.2 to 0.9! |');
    disp('|-----------------------------------------|');
    disp(' ');
    imthres = input('Enter value = ');
    if (imthres < 0.2 || imthres > 0.9)
        return
    end
end

%% Main Program Body
% Calls function CheckDirectory to obtain number of directories and
files
% in the current MATLAB directory.
[dirlist, filelist] = CheckDirectory(cd,0);
[rdirlist, cdirlist] = size(dirlist);
```

```
% Perform batch processing of images for all directories in current
% directory
for d = 1:cdirlist
    [dirlist, filelist] = CheckDirectory(cd,0);
    % Obtain dir name
    [pathstrdir,namedir] = fileparts(dirlist{d});
    dirname = fullfile(pwd,filesep,namedir);
    % Change to dir number d
    cd(dirname);

    % Check number of files inside directory d
    [dirlist, filelist] = CheckDirectory(cd,0);
    [rfilelist, cfilelist] = size(filelist);

    % Calls function initial_image. Reads and thresholds initial
image.
    % Then converts it into greyscale with the spark plug extruding
tip
    % appearing as grey and the rest of the image as black. Initial
image
    % is filelist{3} since the first two files inside the directory
are
    % reserved by Windows.
    inifname = filelist{3};
    [initial,rimsize,cimsize,initialbw,initialgrey] =
initial_image...
    (inifname,inimthres);

    % Starts processing of every image inside the current dir d
    for i = 1:(cfilelist-3)
        % Picks filelist(i+3) as the first image is before spark
ignition
        [pathstr,name,ext] = fileparts(filelist{i+3});
        filename = strcat(name);
        imfname = filelist{i+3};
        % Call function current_image. The function converts image i
        % initially into binary with the use of the greythresh
function and
        % then makes it black%white as class uint8. See
current_image.m for
        % further details.
        [im,imsub,flamebw,flamebw255,flameinigrey] =
current_image...

(imfname,initial,i,cfilelist,imthres,early_imthres,initialgrey);

        % Calls function ez_filtparam to approximately identify the
        % spark plug position using the first image after ignition.
The
        % coordinates identified here will then be used to filter
out
        % unneccesary noise.
        if i == 1
            [iniy,inix,width,left,right,bottom] = ez_filtparam...
                (flamebw,pixsize);
        end

        if i <= round(0.15*cfilelist)
        % Call function current_image_2. Performs same actions as
function
```

```
        % current_image but here thresholding takes place within a
zoomed
        % area around the spark plug. Necessary for better
binarisation of,
        % primarily, initial stages of combustion.
        [flamebw,flamebw255,flameinigrey] = current_image_2...

(imfname,initial,early_imthres_2,initialgrey,width,left,right,...
                bottom,flamebw,flamebw255,flameinigrey);
        end

        % Call function left_difmatrix. The function scans each
image row
        % from left to right and looks for points satisfying the
condition
        % pixel(i+1) - pixel(i) = 255 - 150 (i.e. white - grey). The
points
        % satisfying this condition can only be points of contact
between
        % the left side of the grey spark plug and the white flame.
        [difmatrixleft,lpointrow,lpointcol] =
left_difmatrix(rimsize,...
            flameinigrey,left,bottom,right);

        % Call function right_difmatrix. Does the same as
left_difmatrix
        % but it now scans from right to left looking for points of
contact
        % between spark plug and flame on the right bank of the
spark plug.
        [difmatrixright,rpointrow,rpointcol] =
right_difmatrix(rimsize,...
            flameinigrey,left,bottom,right);

        [difmatrix,rlpointrow,clpointrow,rrpointrow,crpointrow] =...

final_difmatrix(difmatrixleft,difmatrixright,lpointrow,...
            rpointrow);

        if isempty(lpointrow) == 0 && isempty(rpointrow) == 0

            [m,c,x,y,flamebw] =...
            join_spark_line(lpointrow,rpointrow,lpointcol,...
            rpointcol,flamebw);

        end

        flamebw = imfill(flamebw,'holes');% fill black islands
inside flame
        flamebwbin = logical(flamebw);
        pixelnumber = flamebwbin(flamebwbin == 1);
        [pixelarea,yy] = size(pixelnumber);
        pixelradius = (pixelarea/pi)^(0.5);
        mmradius = pixelradius * pixsize;
        radiifile = strcat(namedir,'radii','.dat');
        fid = fopen(radiifile,'a');
        fprintf(fid, '%4.5f\n',mmradius);
        fclose(fid);
        fid = fopen(radiifile,'r');
        fclose(fid);
```

```
        check_radius = dlmread(radiifile);
        max_radius = max(check_radius);
        if max_radius > 74, break, end % Since the window radius is
150mm,
% there is no need to proceed any
% further than 74mm in radius
% considering that none of the
% flames will be perfectly circular

        ext2 = '.tif';
        filename = strcat(filename,ext2);
        flamebw = double(flamebw);
        imwrite(flamebw,filename);
        delete(strcat(name,ext));
        clear dif* fl* im imsub;
    end     %end image processing loop for i = 1:(cfilelist-3)

    delete(filelist{3});
    radii = dlmread(radiifile);
    [A,B] = butter(2,0.5,'low');
    radii_filt = filtfilt(A,B,radii);
    imagenumber = reshape(1:(cfilelist-3),cfilelist-3,1);
    figure1 = figure('Color',[1 1 1],'FileName','Flame Radius.fig');
    axes1 = axes('FontSize',18,'Parent',figure1);
    box on
    axis(axes1,[1 cfilelist-3 0 radii(end)+(0.05*radii(end))]);
    xlabel(axes1,'Image Number','FontSize',22);
    ylabel(axes1,'Flame Radius(mm)','FontSize',22);
    hold(axes1,'all');
    plot(imagenumber, radii,'Color',[0 0 1],'LineWidth',3,...
        'Parent',axes1);
    plot(imagenumber, radii_filt,'Color',[1 0 0],'LineWidth',2,...
        'Parent',axes1);
    print  -dmeta 'Flame Radius.emf'
    hgsave('Flame Radius')
    radiifiltfile = strcat(namedir,'radii_filt','.dat'); % Save
radii data file
    fid = fopen(radiifiltfile,'a');
    fprintf(fid, '%4.5f\n',radii_filt);
    fclose(fid);
    cd('..');
    close all;
    clear init* pixelnumber;
end     %end directory loop for d = 1:cdirlist

close all;
```

D.3 Gas Velocity Script

A script to read in a sequence of flame contour images in a folder and convert it to a Cartesian coordinates. The second part of the code is to derive the gas velocity ahead of flame front..

```
%%/edge coordinate record
% script M-File: Flame_Contour.m
% The script reads the flame contours for a sequence of flame and
%convert it to points and detect the closest vector.
% images belonging to the same experiment.

q1 = 'D:\Matlab\Matlab
work\processing\CH4\010_CH4_1.1_298_L33_1m_10im\images\'
for i = 1:a-3

%         q2 = sprintf('PIVlab_comp_00%d.bmp', i);
%         q3 = sprintf('PIVlab_mask_00%d.bmp', i);
        q4 = sprintf('CH4.4wj2whc1.%04d.txt', i);
%         q12 = horzcat(q1, q2);
%         q13 = horzcat(q1, q3);
        q14 = horzcat(q1, q4);
%         im1{i} = imread(q12);
%         im11{i} = imread(q13);
%         im111{i} = imread(q14);
        A = importdata(q14);
        PIVDATA{i} = (A.data);
        clear A
end

for i = 1:a-3
    PIVX{i} = round(PIVDATA{i}(:,1)./PPF.*10000);
    PIVY{i} = round(PIVDATA{i}(:,2)./PPF.*10000);
    PIVUx{i} = PIVDATA{i}(:,3);
    PIVUy{i} = PIVDATA{i}(:,4);
    PIVVO{i} = PIVDATA{i}(:,5);
    PIVData{i}(:,1) = PIVX{i};
    PIVData{i}(:,2) = PIVY{i};

end

for i = 2:a-2
    [size1 size2] = size(XYI{:,i});
    for ii = 1:size1

        if XYI{:,i}(ii,1) <= SCx
        if mod(XYI{:,i}(ii,1),2) == 0
            Xclosest{i}(ii,1) = XYI{:,i}(ii,1);
        else
            Xclosest{i}(ii,1) = XYI{:,i}(ii,1)-1;
        end
        end

        if XYI{:,i}(ii,1) > SCx
        if mod(XYI{:,i}(ii,1),2) == 0
            Xclosest{i}(ii,1) = XYI{:,i}(ii,1);
        else
            Xclosest{i}(ii,1) = XYI{:,i}(ii,1)+1;
```

```
        end
        end

        if mod(XYI{:,i}(ii,2),2) == 0
            Yclosest{i}(ii,1) = XYI{:,i}(ii,2);
        else
            Yclosest{i}(ii,1) = XYI{:,i}(ii,2)-1;
        end

            XYclosest{i}(ii,:) = [Xclosest{i}(ii,1)
Yclosest{i}(ii,1)];

    end

end

for i = 2:a-2
    [size1 size2] = size(XYI{:,i});
    for ii = 1:size1
        if XYI{:,i}(ii,2) <= SCy
           XYClosest{i}(ii,:) = XYclosest{i}(ii,:);
        else
            XYClosest{i}(ii,:) = [0 0];
        end
    end
    XYClosest{i}( ~any(XYClosest{i},2), : ) = [];
end

for i = 2:a-2
    [size1 size2] = size(XYClosest{:,i});
    for ii = 1:size1
        [tf, index{i}(ii,1)] = ismember(XYClosest{i}(ii,:),
PIVData{1},'rows');
    end
    index{i}( ~any(index{i},2), : ) = [];
end

for z = 1:p
    XYsector{z} = [SCx,SCy];
    for x = 1:512
        for y = 1:512
            if masksector{z}(y,x) == 1
                XYsector{z} = [XYsector{z};x,y];
            end
        end
    end
    XYsector{z}(1,:) = [];
end

for i = 2:a-2
    [size1 size2] = size(XYClosest{:,i});
    XYCS{i,z}(1,:) = [SCx,SCy];
    Indexsector{i,z} = 0;
    for z = 1:p
        for ii = 1:size1
            if ismember(XYClosest{i}(ii,:), XYsector{1,z},'rows') ==
1
                XYCS{i,z} = [XYCS{i,z}; XYClosest{i}(ii,:)];
                Indexsector{i,z} = [Indexsector{i,z};
index{i}(ii,:)];
```

```
            end
        end
        XYCS{i,z}(1,:) = [];
        Indexsector{i,z}(1,:) = [];
        [INDEXsector{i,z},m1,n1] = unique(Indexsector{i,z},'first');
        [c1,d1] =sort(m1);
        INDEXsector{i,z} = INDEXsector{i,z}(d1);
    end
end

for z = 1:p
    theta1(z) = (theta(z))+step/2;
end

for i = 2:a-2
    for z = 1:p
        [size1 size2] = size(INDEXsector{i,z});
        for ii = 1:size1
            UV{i,z}(ii,:) = PIVDATA{i-1}(INDEXsector{i,z}(ii),3:4);
        end
        UV{i,z} = UV{i,z}(~any(isnan(UV{i,z}),2),:);
        [S1 S2] = size(UV{i,z});
        Vectorsector{i,z} = [mean(UV{i,z}(:,1)),mean(UV{i,z}(:,2))];
        Vectorsectorlength{i,z} =
((Vectorsector{i,z}(1))^2+(Vectorsector{i,z}(2))^2)^0.5;
        Vectorsectorangle{i,z} =
atand(Vectorsector{i,z}(2)/Vectorsector{i,z}(1));
        if Vectorsectorangle{i,z} <= 0
            Vectorsectorangle{i,z} = Vectorsectorangle{i,z} +180;

        end
        Vectorangle{i,z} = abs(theta1(z)-Vectorsectorangle{i,z});
        BVsector(i,z) = Sectorspeed(i-1,z)-
Vectorsectorlength{i,z}*cosd(Vectorangle{i,z});
        averageBVspeed(i) = sum(BVsector(i,:))/p;
    end
end

for i = 2:a-2

    imshow(BWI{i})
    for z = 1:p
        if maskpoint(z,1) <= SCx
        txt{i,z} =horzcat(sprintf('%.2f',
BVsector(i,z)),'\rightarrow');
        text(SCx-R{i,z}*cosd(theta(z)+5),SCy-
sind(theta(z)+5)*R{i,z},txt{i,z},'Color','white','HorizontalAlignmen
t','right');
        end
        if maskpoint(z,1) > SCx
        txt{i,z} =horzcat('\leftarrow', sprintf('%.2f',
BVsector(i,z)));
        text(SCx-R{i,z}*cosd(theta(z)+5),SCy-
sind(theta(z)+5)*R{i,z},txt{i,z},'Color','white','HorizontalAlignmen
t','left');
        end

        txt2{i} =horzcat('Average Speed (m/s) = ',
sprintf('%.2f',averageBVspeed(i)));
```

```
        txt3{i} =horzcat('Average radius (mm) = ',
sprintf('%.2f',averageradius(i-1)));

text(5,15,txt2{i},'Color','white','HorizontalAlignment','left');

text(5,30,txt3{i},'Color','white','HorizontalAlignment','left');

    end
%     saveas(gcf,sprintf('BWII%d',i),'fig');
%     openfig(sprintf('BWII%d',i));
drawnow
    frame = getframe();
    bwi{i} = frame2im(frame);
    imshow(bwi{i});
     imwrite(bwi{i},sprintf('ZBVBWI%d.bmp',i))
%     saveas(gcf,sprintf('BWII%d',i),'bmp')
%     imwrite(BWI{k},sprintf('BWII%d.bmp',k));
end
```

D.4 Effective rms Turbulent Velocity Script

A script to calculate the effective rms turbulent velocity.

```
% code to determine u'k/u'
close all;
clear all;
clc;
fileID = fopen('x.txt','r');
formatSpec = '%f %f';
sizeSnr = [2 Inf];
Snr = fscanf(fileID,formatSpec,sizeSnr);
Snr = Snr';
Sn = Snr(:,2);
%Sn = Sn.*1000;
ru = Snr(:,1);
up = input('\nEnter the value of u_prime in meters, u_p = ');
L = input('\nEnter the value of integral length scale in meters, L =
');
nu = input('\nEnter the value of kinematic viscosity in m2/sec, nu =
');
ul = input('\nEnter the value of laminar burning velocity in m/s, ul
= ');
nk = (2*ru)/(L*1000);
R_L = (up*L)/nu;
R_La = 4 * (R_L.^0.5);
%Ke1 = (2*ru)/1000;
j = 1;

for j = 1:numel(nk)

Ke1(j,:)= (((32*3.14159)/((15.^0.25).*nk(j,:))).*(R_La.^-1.5));

%j = j+1;

end
```

```
 nkG = 0.133*((up/ul).^-3);

Ke2 = ((32*3.14159)/((15.^0.25)*nkG))*(R_La.^-1.5);

syms z ;

f = (((0.01668*(R_La.^2.5))+(3.74*(R_La.^0.9))-(70*(R_La.^-
0.1))))/(1+(((0.127*(R_La.^1.5)).*z).^(5/3))+(((1.15*(R_La.^0.622)).
*z).^(4))+(((1.27*(R_La.^0.357)).*z).^(7)));

i = 1;

j = 1;

for Ke11 = 1:numel(Ke1)

 Ke12 = Ke1(j,:);

 a = int(f,Ke12,Ke2);

 b = double(a);

% a(i,:) = int(f,ru,Ke2);

%b = abs(b);

 c = (((15.^0.5)/R_La)*b).^0.5;

 upk_upinf(i,:)= double(c);
 %upk_upinf  = vpa(b, 5);

 i=i+1;

 j = j+1;
 end
 %Ke3 = 0.38;
Ke3 = ((32*3.14159)/((15.^0.25).*19))*(R_La.^-1.5);

Ke4 = 2*3.14159;
k = 1;
a1 = int(f,Ke3,Ke4);

b1 = double(a1);

up_upinf(k,:) = (((15.^0.5)/R_La)*b1).^0.5;

%up_upinf(i,:) = double(b1);

k = k +1;
 upk_up = upk_upinf/u
figure, plot (nk,upk_up);
end
```

D.5 Liquid Fuel Volumes Script

The following script was written to calculate the required amount of liquid fuel, based on the experimental conditions.

```
% A script to calculate liquid fuel volumes to add to the vessel
% could also be used for fuel constituents, including
% oxygen and/or nitrogen-containing fuels

% DOI: 17.02.2016

clear all
close all
clc

% Request some information from the user. Note that a bomb volume of
30.372
% litres has been assumed

if (exist('Variablefd_Fuel_KM8652.mat')==2)
    load('Variables_Fuefl_KM8652.mat');
else
disp('This program requests values for a fuel with the following
formula: CxHyOzNv');
disp('This code is for liquid fuels only! Press "any" key to
continue');
fueldensity = input('Density of the fuel in (kg/m3) = ');
cx = input('Enter the proportion of carbon in the fuel, x = ');
hy = input('Enter the proportion of hydrogen in the fuel, y = ');
oz = input('Enter the proportion of oxygen in the fuel, z = ');
nv = input('Enter the proportion of nitrogen in the fuel, v = ');
T = input('Initial bomb temperature (in K) = ');
Pbar = input('Starting pressure (in bar) = ');
%save('Variables_Fuel_KMfg652');
end
lambda = (input('Required value of lambda (ie. 1/phi) = '));
P = Pbar*100000;

% CxHyOzNv + (m-(z/2))(O2 + 3.76N2) --> xCO2 + yH2O + ((3.76(m-
(z/2))*(v/2))N2

% Other information

V= 0.030372 ;
%V = 0.030575; % bomb volume in m3
R = 8.314; % Universal gas constant in kJ/kg.K
molmassc = 12.011;
molmassh = 1.0079;
molmasso = 15.994;
molmassn = 14.0067;

% Calculate the oxygen to fuel ratio (m)

m = cx + (hy/4) - (oz*0.5);

% n = PV/RT

% Total number of moles in the original mixture in the bomb
```

```
n = (P*V)/(R*T);

% Moles of fuel required
% Fuel mole fraction

ENM = (1/lambda)+(m*4.76); % Number of moles in the equation
FMF = (1/lambda)/ENM;
MFR = n*FMF;

% Molar mass of fuel

Mr = (cx*molmassc)+(hy*molmassh)+(oz*molmasso)+(nv*molmassn);
%Mr = ((cx)+(hy)+(oz)+(nv));

% Mass of fuel required

massfuel = MFR*Mr;

% Volume of fuel required

VF = massfuel/fueldensity;

disp('The required number of ml of fuel at pressure is:')

VFml = VF*1000

disp('The required quantity of fuel at 1 bar in ml is:')

VF1ml = VFml/Pbar

% P = nrt/V - calculate partial pressure of fuel for injected
quantity
 disp('The pressure generated by the added fuel is (in mbar):');

Pa = ((MFR*R*T)/V)/100
```

D.6 Radiation Correction Script

A script to correct the laminar burning velocity, based on the study of (Yu et al., 2014).

```
%Script to do radiation corrections
clear all
clc
B=dlmread('ula.txt');
To=300;
Po=1.0;
So=0.01;
prompt = 'Enter value of P ';
P = input(prompt);
prompt2 = 'Enter value of T ';
Tu = input(prompt2);
[x y] = size(B);
for i= 1:x
```

```
    R(i,1)=0.82*((B(i,1)/So)^(-1.14))*(Tu/To)*((P/Po)^(-0.3));
    Sln(i,1)=(R(i,1)*B(i,1))+B(i,1);
end
Sl=[Sln,B,R*100]
```

D.7 Burned Gas Density Correction Script

A script to correct the laminar burning velocity, due to it not having an adiabatic value for the burned gas density.

```
% To calculate LE number
 global mw
 global cnms
 global lrho
 global cpv
 global cpl
 global Tdeg

 % dummy variable to hold actual Tdeg
 Temp = Tdeg;

 % changes temperature to degree Kelvin if user inputted another T
scale
 %T = at(T);

 % reassigns Tdeg to Kelvin to prevent redundant temperature
conversions in
 % subsequent program calls
 Tdeg = 'K';

 % calculation for dilute binary liquid solution
 if (state == 'l')

  % vector of association parameters for solvent. see BSL page 530
  psi_b = [2.6 1.9 1.5 1.0];

  % calculates thermal conductivity of solvent in units of
kg*m/s^3/K
  k = klcalc(T,2,mw,cnms,lrho);

  % checks if insufficient/erroneous data
  if ((isnan(lrho(2)) == 1) | (k <= 0) | (imag(k) ~= 0) )
  fprintf('\n\nLiquid conditions exceed program capabilities.\n')
  Le = 'NaN';
  else % assume density of dilute solution = density of solvent
  rho = lrho(2); % density of solvent in units of kg/m^3
  mu = liqmucalc(T,2)*10^3; % viscosity of solvent in units of cP
  VtildeA = mw(1)*1000/lrho(1); % molar volume of solute in units of
cm^3/mole
```

```
  % choose appropriate psiB in order to calculate mass Diffusivity
  if strcmp('methane',cnms(2,1:5))
  psiB = psi_b(1);
  elseif strcmp('octane',cnms(2,1:8))
  psiB = psi_b(2);
  elseif strcmp('ethanol',cnms(2,1:7))
  psiB = psi_b(3);
  elseif strcmp('n-butanol',cnms(2,1:7))
  psiB = psi_b(4);
  else
  fprintf('\n\nWarning! Assuming psiB = 1. Only works for
unasscoiated solvents!\n')
  psiB = psi_b(4);
  end

  % calculates diffusivity using Eqn 17.4-8 in units of m^2/s
  Dab = (7.4e-8) * sqrt( psiB*mw(2))*T/(mu*VtildeA^(0.6) ) /
(100^2);

  % calculates heat capacity per mass in units of J/mol/K
  [nrow,ncol]=size(cpl);
  if nargin<2
  index = 1:nrow;
  end
  Tsp = T.^(0:(ncol-1));
  cp = cpl(index,:)*Tsp';
  cp(2);

  % calculates the Lewis number for dilute binary liquid solution
  Le = k/(rho*cp(2)*Dab)*mw(2)/1000;

  end

 % calculation for low density binary gas mixture
 elseif (state == 'v')

  % calculates thermal conductivity in units of W/m/K
  k = mixkt(molefrxn,T);

  R = 8.314; % universal gas constant in units J/mol/K

  % calculates molecular weight of gas mixture in units of g/mol
  mw_mixture = molefrxn(1)*mw(1) + molefrxn(2)*mw(2);

  % assume ideal gas law
  % calculates density of mixture in units of g/m^3
  rho = P/(R*T)*mw_mixture;

  % calculates binary diffusivity in units of m^2/s
  Dab = dcalc(P/1000,T,index);
```

```
  % calculates heat capacity per mass in units of J/mol/K
  [nrow,ncol]=size(cpv);
  if nargin<2
  index = 1:nrow;
  end
  Tsp = T.^(0:(ncol-1));
  cp = cpv(index,:)*Tsp';

  % calculates the average heat capacity of the gas mixture in units
of
  % J/mol/K
  cp_avg = molefrxn(1)*cp(1) + molefrxn(2)*cp(2);

  % calculates the Lewis number for low density binary gas mixtures
  Le = k/(rho*cp_avg*Dab)*mw_mixture;

 else % if a typo was entered for the state

  fprintf('\n\nInvalid state.\n')

 end

 % returns temperature scale to user's original choice of
temperature scale
 Tdeg = Temp;

Part II
% Stretch/Lewis Number correction
clear all
clc
clear all
q1 = 'H:\001_Work\work home\Laminar\Laminar_updated\'
Sn_R=dlmread('R_Sn.txt');
R=Sn_R(:,1);
Sn=Sn_R(:,2);
for ia=1:size(Sn)
alfa(ia)=(2/(R(ia)/1000))*Sn(ia)';
end
alfa=alfa';
figure
scatter(alfa,Sn)
grid on
xlabel('alfa (1/s)')
ylabel('Sn (m/s)')
hold off
prompt = 'Enter value of Lewis number ';
Le = input(prompt);
prompt2 = 'Enter value of Th diffusivity ';
D = input(prompt2);
prompt3 = 'Enter value of Tad ';
Tad = input(prompt3);
Sn2=Sn.^2;
```

```
[x y] = size(Sn);
for i= 1:x
   Rt(i,1)=(D/Sn2(i,1))*((1/Le)-1)*alfa(i,1);
   tf(i,1)=(Rt(i,1)*Tad)+Tad;
end
tadmax=max(tf)
tadmin=min(tf)
tfmean=mean(tf)
figure
plot(R,tf)
grid on
title('Stretch and Lewis number effects')
xlabel('Flame Radius (mm)')
ylabel('Tf (K)')
hold off
```

D.8 Integral Length scale script

The following script was written to calculate the integral length scales for each individual PIV velocity map.

```
clear;clc;[dirlist]=CheckDirectory(cd,0);dirnum=size(dirlist,2);
for d=1:dirnum
[dirlist]=CheckDirectory(cd,0);cd(dirlist{d})
[pathstrdir,namedir]=fileparts(dirlist{d});
[dirlist,filelist]=CheckDirectory(cd,0);filenum=size(filelist,2);
ii=0;Part_name=char(namedir);Part_name=Part_name(:,1:end);
for i=1:(filenum-2)
F=loadvec(i);
if i==1
[row_vx,col_vx]=size(F.vx);
end
U=reshape(F.vx,[],1);row=length(U);V=reshape(F.vy,[],1);count=0;
for k=1:row
if U(k)~=0
count=count+1;U_in(count)=U(k);V_in(count)=V(k);
end
end
if count>0
    ii=ii+1;clear U
V;F.vx(F.vx==0)=NaN;F.vy(F.vy==0)=NaN;U_mean=mean(U_in);
clear U_in;V_mean=mean(V_in);clear V_in;Fluc=F;Fluc.vx=F.vX-U_mean;
Fluc.vy=F.vY-
V_mean;clearF;COR_trans_Y=corrf(vec2scal(Fluc,'ux'),'y','norm');
ils_trans_Y(ii,1)=COR_trans_Y.is0;R_trans_Y{ii}=COR_trans_Y.f';
clear COR_trans_Y;COR_trans_X=corrf(vec2scal(Fluc,'uy'),'x','norm');
ils_trans_X(ii,1)=COR_trans_X.is0;R_trans_X{ii}=COR_trans_X.f;
clear COR_trans_X;COR_long_X=corrf(vec2scal(Fluc,'ux'),'x','norm');
ils_long_X(ii,1)=COR_long_X.is0;R_long_X{ii}=COR_long_X.f;
if ii==1
r_x=COR_long_X.r;
end
clear COR_long_X;COR_long_Y=corrf(vec2scal(Fluc,'uy'),'y','norm');
ils_long_Y(ii,1)=COR_long_Y.is0;R_long_Y{ii}=COR_long_Y.f';
```

```
if ii==1
r_y=COR_long_Y.r;
end
clear COR_long_Y Fluc
end
end
R_long_X_mat=cell2mat(R_long_X);ils_long_X_mean=mean(ils_long_X);
ils_long_X_SD=std(ils_long_X);
ils_long_X_mean_2SD=ils_long_X_mean+2*ils_long_X_SD;
ils_long_X_mean_n2SD=ils_long_X_mean-2*ils_long_X_SD;
n_ils_long_X=length(ils_long_X);
for k=1:n_ils_long_X
n_ils_long_X=length(ils_long_X);n=0;R_long_X_new={};
for j=1:n_ils_long_X
if ils_long_X(j)>=ils_long_X_mean_n2SD
if ils_long_X(j)<=ils_long_X_mean_2SD
n=n+1;ils_long_X_new(n,1)=ils_long_X(j);R_long_X_new{n}=R_long_X_mat
(:,j);
end
end
end
clear
ils_long_XR_long_X_mat;R_long_X_mat_new=cell2mat(R_long_X_new);
R_long_X_mat=R_long_X_mat_new; clear R_long_X_new R_long_X_mat_new;
ils_long_X=ils_long_X_new;n_ils_long_X_new=length(ils_long_X_new);
clear ils_long_X_new;ils_long_X_mean=mean(ils_long_X);
ils_long_X_SD=std(ils_long_X);
ils_long_X_mean_2SD=ils_long_X_mean+2*ils_long_X_SD;
ils_long_X_mean_n2SD=ils_long_X_mean-2*ils_long_X_SD;
if n_ils_long_X_new==n_ils_long_X
long_X=ils_long_X_mean;break
end
end
fname=strcat(Part_name,'_long_X.txt');save(fname,'long_X','-ascii')
fname=strcat(Part_name,'_long_X_all.txt');save(fname,'ils_long_X','-
ascii')
R_long_X_mat=[r_x,R_long_X_mat];fname=strcat(Part_name,'_R_long_X.da
t');
save(fname,'R_long_X_mat','-ascii');clear R_long_X_mat
R_long_Y_mat=cell2mat(R_long_Y);ils_long_Y_mean=mean(ils_long_Y);ils
_long_Y_SD=s
td(ils_long_Y);
ils_long_Y_mean_2SD=ils_long_Y_mean+2*ils_long_Y_SD;
ils_long_Y_mean_n2SD=ils_long_Y_mean-2*ils_long_Y_SD;
n_ils_long_Y=length(ils_long_Y);
for k=1:n_ils_long_Y
n_ils_long_Y=length(ils_long_Y);n=0;R_long_Y_new={};
for j=1:n_ils_long_Y
if ils_long_Y(j)>=ils_long_Y_mean_n2SD
if ils_long_Y(j)<=ils_long_Y_mean_2SDn=n+1
ils_long_Y_new(n,1)=ils_long_Y(j);R_long_Y_new{n}=R_long_Y_mat(:,j);
end
end
end
clear ils_long_Y
R_long_Y_mat;R_long_Y_mat_new=cell2mat(R_long_Y_new);
R_long_Y_mat=R_long_Y_mat_new;clear R_long_Y_new R_long_Y_mat_new;
ils_long_Y=ils_long_Y_new;n_ils_long_Y_new=length(ils_long_Y_new);
clear ils_long_Y_new;
ils_long_Y_mean=mean(ils_long_Y);ils_long_Y_SD=std(ils_long_Y);
ils_long_Y_mean_2SD=ils_long_Y_mean+2*ils_long_Y_SD;
```

```
ils_long_Y_mean_n2SD=ils_long_Y_mean-2*ils_long_Y_SD;
if n_ils_long_Y_new==n_ils_long_Y
long_Y=ils_long_Y_mean;break
end
end
fname=strcat(Part_name,'_long_Y.txt');save(fname,'long_Y','-ascii')
fname=strcat(Part_name,'_long_Y_all.txt');save(fname,'ils_long_Y','-
ascii')
R_long_Y_mat=[r_y',R_long_Y_mat];fname=strcat(Part_name,'_R_long_Y.d
at');
save(fname,'R_long_Y_mat','-ascii');clear R_long_Y_mat
R_trans_X_mat=cell2mat(R_trans_X);ils_trans_X_mean=mean(ils_trans_X)
;
ils_trans_X_SD=std(ils_trans_X);
ils_trans_X_mean_2SD=ils_trans_X_mean+2*ils_trans_X_SD;
ils_trans_X_mean_n2SD=ils_trans_X_mean-2*ils_trans_X_SD;
n_ils_trans_X=length(ils_trans_X);
for k=1:n_ils_trans_X
n_ils_trans_X=length(ils_trans_X);n=0;R_trans_X_new={};
for j=1:n_ils_trans_X
if ils_trans_X(j)>=ils_trans_X_mean_n2SD
if ils_trans_X(j)<=ils_trans_X_mean_2SDn=n+1
ils_trans_X_new(n,1)=ils_trans_X(j);R_trans_X_new{n}=R_trans_X_mat(:
,j)
end
end
end
clear ils_trans_X
R_trans_X_mat;R_trans_X_mat_new=cell2mat(R_trans_X_new);
R_trans_X_mat=R_trans_X_mat_new;clear R_trans_X_new
R_trans_X_mat_new
ils_trans_X=ils_trans_X_new;n_ils_trans_X_new=length(ils_trans_X_new
);
clear ils_trans_X_new;ils_trans_X_mean=mean(ils_trans_X);
ils_trans_X_SD=std(ils_trans_X);
ils_trans_X_mean_2SD=ils_trans_X_mean+2*ils_trans_X_SD;
ils_trans_X_mean_n2SD=ils_trans_X_mean-2*ils_trans_X_SD;
if n_ils_trans_X_new==n_ils_trans_X
trans_X=ils_trans_X_mean;break
end
end
fname=strcat(Part_name,'_trans_X.txt');save(fname,'trans_X','-
ascii')
fname=strcat(Part_name,'_trans_X_all.txt');save(fname,'ils_trans_X',
'-ascii')
R_trans_X_mat=[r_x,R_trans_X_mat];fname=strcat(Part_name,'_R_trans_X
.dat');
save(fname,'R_trans_X_mat','-ascii');clear R_trans_X_mat
R_trans_Y_mat=cell2mat(R_trans_Y);ils_trans_Y_mean=mean(ils_trans_Y)
;
ils_trans_Y_SD=std(ils_trans_Y);
ils_trans_Y_mean_2SD=ils_trans_Y_mean+2*ils_trans_Y_SD;
ils_trans_Y_mean_n2SD=ils_trans_Y_mean-2*ils_trans_Y_SD;
n_ils_trans_Y=length(ils_trans_Y);
for k=1:n_ils_trans_Y
n_ils_trans_Y=length(ils_trans_Y);n=0;R_trans_Y_new={};
for j=1:n_ils_trans_Y
if ils_trans_Y(j)>=ils_trans_Y_mean_n2SD
ifils_trans_Y(j)<=ils_trans_Y_mean_2SDn=n+1
ils_trans_Y_new(n,1)=ils_trans_Y(j);R_trans_Y_new{n}=R_trans_Y_mat(:
,j)
```

```
end
end
end
clear ils_trans_Y
R_trans_Y_mat;R_trans_Y_mat_new=cell2mat(R_trans_Y_new);
R_trans_Y_mat=R_trans_Y_mat_new;clear R_trans_Y_new
R_trans_Y_mat_new;
ils_trans_Y=ils_trans_Y_new;n_ils_trans_Y_new=length(ils_trans_Y_new
);
clear ils_trans_Y_new;ils_trans_Y_mean=mean(ils_trans_Y);
ils_trans_Y_SD=std(ils_trans_Y);
ils_trans_Y_mean_2SD=ils_trans_Y_mean+2*ils_trans_Y_SD;
ils_trans_Y_mean_n2SD=ils_trans_Y_mean-2*ils_trans_Y_SD;
if n_ils_trans_Y_new==n_ils_trans_Y
trans_Y=ils_trans_Y_mean;break
end
end
fname=strcat(Part_name,'_trans_Y.txt');save(fname,'trans_Y','-
ascii')
fname=strcat(Part_name,'_trans_Y_all.txt');save(fname,'ils_trans_Y',
'-ascii')
R_trans_Y_mat=[r_y',R_trans_Y_mat];fname=strcat(Part_name,'_R_trans_
Y.dat');
save(fname,'R_trans_Y_mat','-ascii');clear R_trans_Y_mat
cd('..'); end
```

D.9 Spatial Mean and rms Turbulent Velocities Script

The following script was written to calculate the spatial mean and rms turbulent velocities for each individual PIV velocity map.

```
clear;clc;[dirlist]=CheckDirectory(cd,0);dirnum=size(dirlist,2);
for d=1:dirnum
[dirlist]=CheckDirectory(cd,0);cd(dirlist{d})
[pathstrdir,namedir]=fileparts(dirlist{d});
[dirlist,filelist]=CheckDirectory(cd,0);filenum=size(filelist,2);ii=
0;
Part_name=char(namedir);Part_name=Part_name(:,1:end-5);cols=5:2:73;
for i=1:(filenum-2)
F1=loadvec(i);F=truncf(F1);
Vx_m_per_image{i}=Ux(cols);Vx_rms_per_image{i}=ux_rms(cols);
Vy_m_per_image{i}=Uy(cols);Vy_rms_per_image{i}=uy_rms(cols);
S_m_per_image{i}=S(cols);S_rms_per_image{i}=s_rms(cols);clear F
end
S_rms_m=mean(S_rms_mat,2);
R_Vx=[R,Vx_m_mat,Vx_rms_mat,Vx_m_m,Vx_rms_m];
clear Vx_m_mat Vx_rms_mat Vx_m_m Vx_rms_m
R_Vy=[R,Vy_m_mat,Vy_rms_mat,Vy_m_m,Vy_rms_m];
clear Vy_m_mat Vy_rms_mat Vy_m_m Vy_rms_m
R_S=[R,S_m_mat,S_rms_mat,S_m_m,S_rms_m];clear RS_m_mat S_rms_mat
S_m_m S_rms_m
fname=strcat(Part_name,'_Vx.dat');save(fname,'R_Vx','-ascii')
fname=strcat(Part_name,'_Vy.dat');save(fname,'R_Vy','-ascii')
fname=strcat(Part_name,'_S.dat');save(fname,'R_S','-ascii')
clear R_Vr R_Vt R_S R_Vx R_Vy;cd('..');
end
```

Appendix E

E.1 Introduction

This Appendix provides more information about the effect of the spark plasma on the flame propagation. Ignition energy was varied and its effect on the flow field, flame instability and Markstein length of stoichiometric methane/air mixture at atmospheric pressure was investigated. The radius at which the flame approaches a spherical self-sustaining configuration is, in general, a function of the ignition energy and hence assigning a unique or universal radius beyond which no effect of the spark is inappropriate. The affected distance by a spark plasma discharge, in the presence and absence of chemical reactions, was presented for ignition energies 0.4, 1, 16, 36 and 53 mJ. The ignition energies reported in the present work were calculated based upon breakdown currents and voltages measured in air, under standard conditions (T = 298 K, P = 0.1 MPa), and may not be identical to those in the methane/air mixtures at given experimental conditions. More details about the calculation of the spark ignition energy can be found in (Lawes et al., 2016).

E.2 Spark Plasma Effect

A stable flame takes time to be independent of the initiating spark plasma. Bradley et al. (1996) have suggested less effect of the spark plasma beyond a flame radius, r_u, of 6 mm. In the present work, the local flow field induced by a spark plasma discharge was first investigated in quiescent air under atmospheric conditions. Energies of 0.4, 1, 16, 36 and 53 mJ have been employed. Figure E.1 shows Mie scattering raw images of the spark, at atmospheric conditions, for each energy.

Figure E.2 shows raw images of the spark plasma and corresponding velocity vectors maps for 0.4 mJ. For clarity, only half vectors are displayed in Fig. E.2. Such figure shows that the spark plasma acts like a turbulent flame pushing the unburned gases ahead of it in a non-consistent manner. To calculate the affected distance by the spark plasma, the mean gas velocity around the spark plasma has been calculated within annulus area of thickness 0.94 mm (~ size of the minimum IA), moving from the tip of the spark plasma in the radial direction to the inner surface of the vessel. Figure E.3 shows an example of the velocity profiles ahead of the spark plasma at different instants for spark

energy 0.4 mJ. The velocity is maximum near the tip of the spark plasma and decrease away from it. An increase in the air velocity has been observed near the inner surface of the bomb. Singh et al. (2018) have suggested that differences observed in the flow structures induced by the spark may arise due to a shock wave.

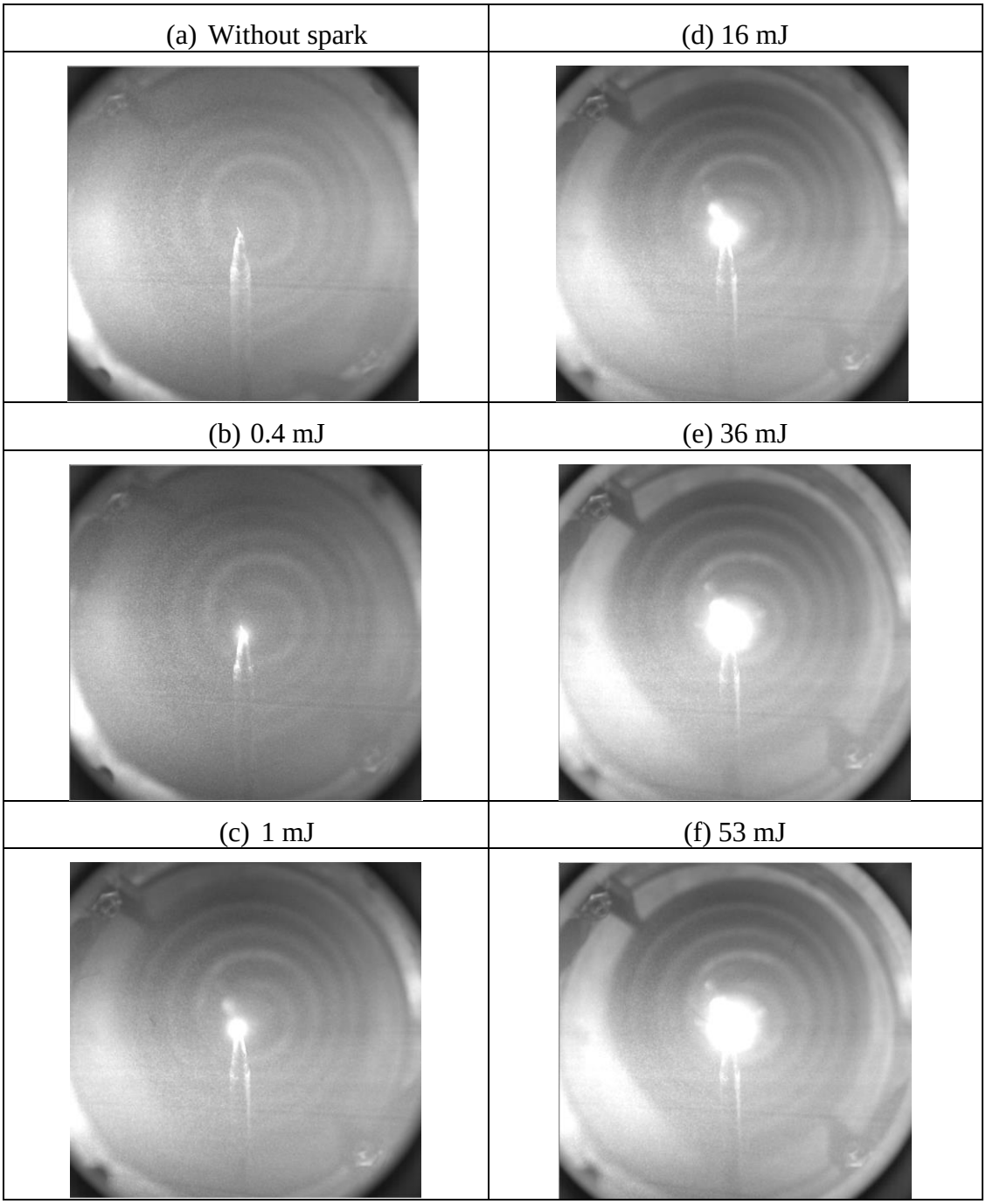

Figure E.1: Shows Mie scattering raw images of the spark, using different spark energies, (a) Without spark, (b) 0.4 mJ, (c) 1.0 mJ, (d) 16 mJ, (e) 36 mJ and (f) 53 mJ.

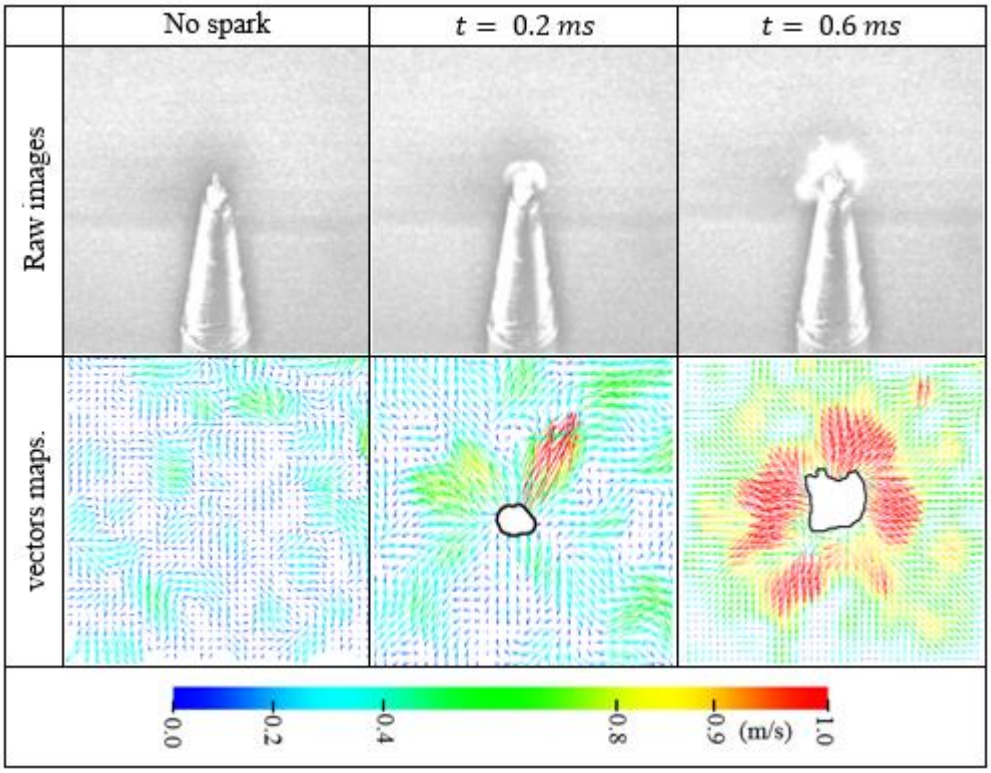

Figure E.2: Shows raw images of the spark plasma and the croosponding vector maps for spark energy 0.4 mJ.

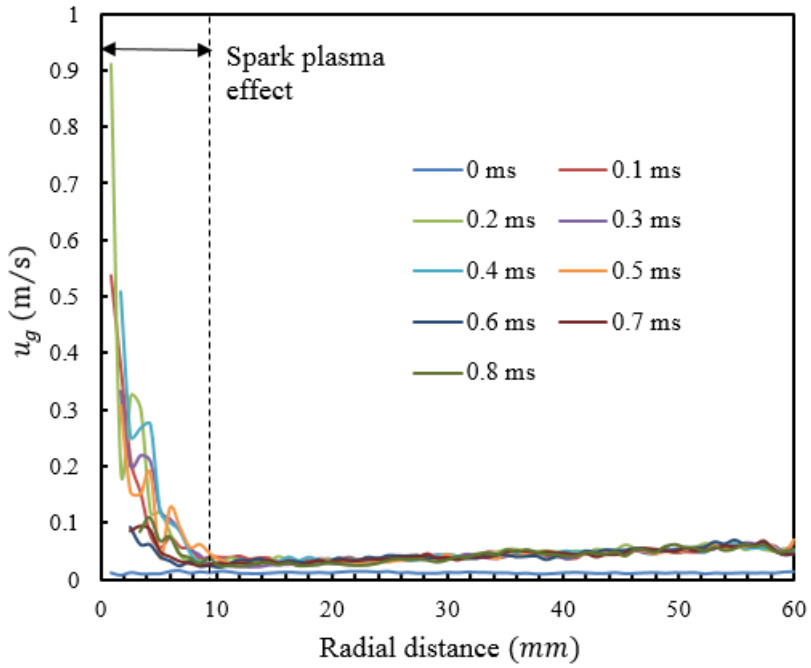

Figure E.3. Shows the effect of the spark plasma on the gas velocity.

Figure E.4 shows the maximum diameter of the spark plasma, D_{max}, and the affected distance (AD), in the absence of chemical reactions with only air in the vessel at 0.1 MPa and 300 K. The size of the spark plasma increases with the increase of spark energy. This causes a significant increase in the affected distance which reaches a maximum value of 37.5 mm at an energy 53 mJ. This distance represents nearly 49% of the measurement volume.

The effect of the spark energy on the unstretched laminar burning velocity and Markstein length was investigated using stoichiometric CH_4/air mixture at 0.1 MPa and 300K. The flame raw images showed that the spark plasma never disappears and persist for a long time until the flame passes the window edge, compared to its life time (~ 0.8 ms) in air. Dissociation of the spark plasma has been observed for energies less than 16 mJ, before it disappears. The only logical reason for that is that spark plasma consumes part of the mixture to survive. Increasing the spark energy also deforms the flame. That is because the flame initially propagates in a non-quiescent environment, within the affected distance of the initiating spark plasma.

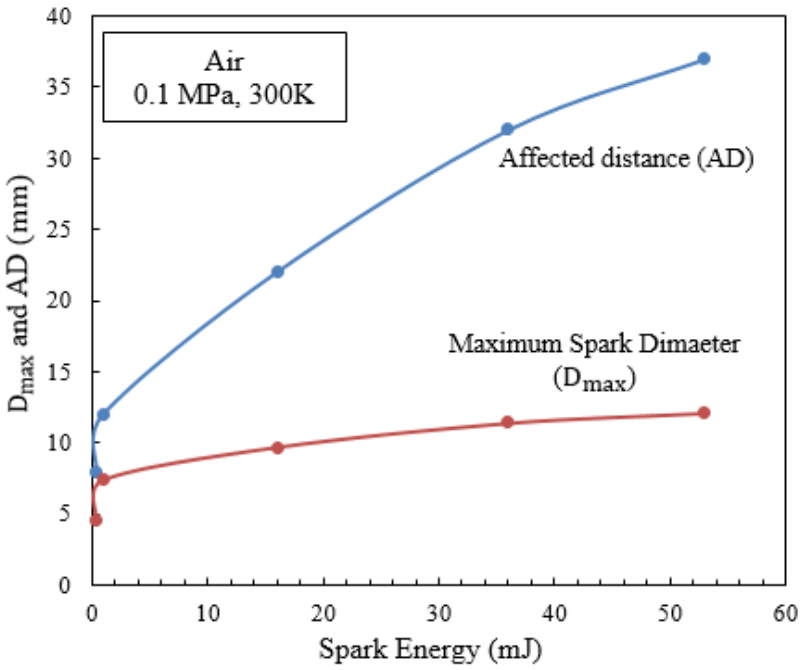

Figure E.4. Shows the maximum diameter of the spark plasma and the affected distance.

Figure E.5 shows the effect of stretch rate, α, on the stretched flame speed, S_n, for stoichiometric CH_4/air mixture at 0.1 MPa and 300K, using spark energies 0.4,16 and 53 mJ. Increasing spark energy causes a reduction in the flame stable, developed regime. The beginning of this regime, at which the flame is not affected by spark, was a function of the spark energy. For spark energies 0.4, 16 and 53 mJ, the flame radius, which represents the beginning of the stable regime, was 8, 12 and 17mm, respectively. The spark energy also affects the onset of instability and Markstein length. In Fig. E.5, the onset of instability regime is indicated by *. As the spark energy increases, the flame becomes unstable rapidly. This reduction in the stable regime, causes a difficulty to measure Markstein length accurately. Figure E.6 shows that Markstein length is increasing with the increase in the value of the spark energy. This changes the extrapolated unstretched flame speed and hence the unstretched burning velocity. Similar effect has been obtained by (Lawes et al., 2016) for *i*-octane and methane/air mixtures at 358 and 0.3 MPa. The current results suggest that it is inappropriate to assign a unique or universal radius beyond which spark effect are not important, as this radius is a function of the ignition energy and the mixture under investigation. The persisting of spark plasma also changes the measured stretched flame speed. So that it is recommended to directly compare the measured stretched flame speed, instead of extrapolated ones, with 1-D simulation results predicted by kinetics so that the uncertainty associated with spark energy and extrapolation can be eliminated.

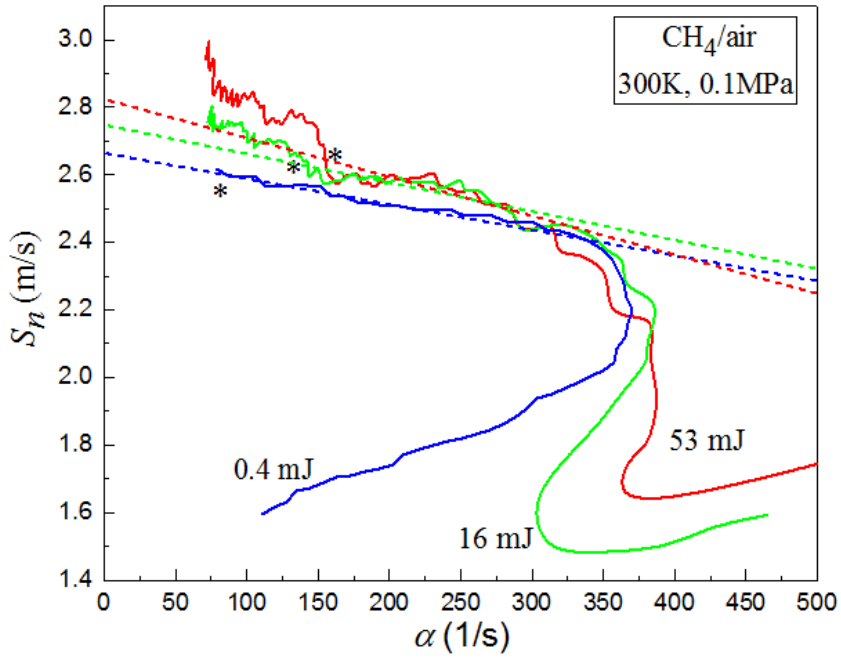

Figure E.5: $S_n - \alpha$ curves for stoichiometric methane/air mixture at 0.1 MPa and 300K, using three different spark energies 0.4, 16 and 53 mJ.

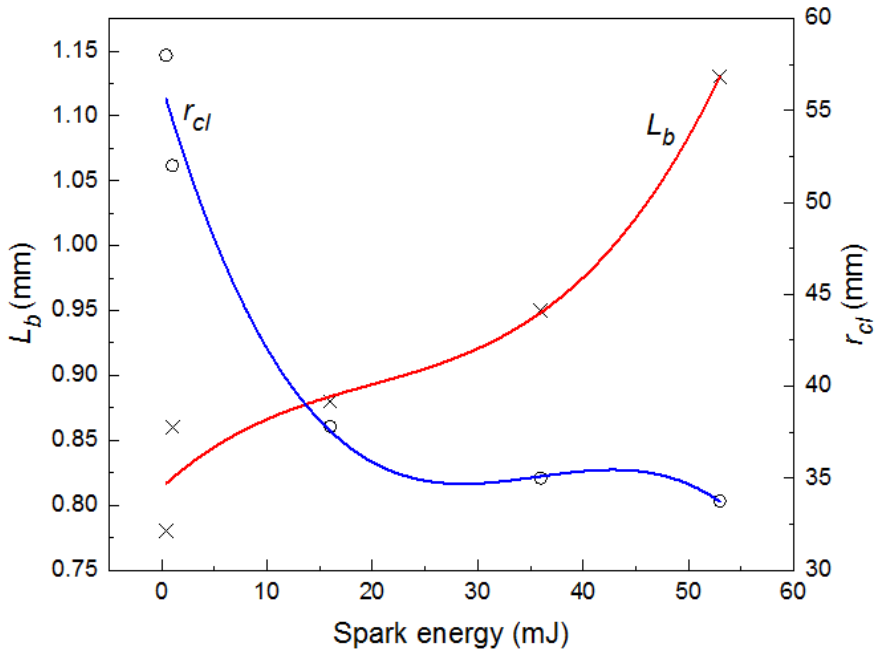

Figure E.6: Influence of spark energy on r_{cl} and L_b.

The End.